NASA Conference Publication 3101

Fourth International Symposium on Long-Range Sound Propagation

Compiled by
William L. Willshire, Jr.
Langley Research Center
Hampton, Virginia

Proceedings of a symposium sponsored by the National Aeronautics and Space Administration, the University of Mississippi, and the Open University of England and held at Langley Research Center
Hampton, Virginia
May 16–17, 1990

NASA
National Aeronautics and Space Administration
Office of Management
Scientific and Technical Information Division
1990

PREFACE

The outdoor propagation of sound remains an important topic of research. Some of the earliest recorded experiments in acoustics dealt with the propagation of sound. The reason for the continuing interest in sound propagation is that sound propagation is an aspect of many acoustic problems. In recent history, during the decade of the 70's, outdoor sound propagation research was largely driven by aircraft noise certification issues. Propagation distances of interest were typically on the order of a mile. The effects of finite impedance boundaries, ground effects, were identified as important to the problem, and much theoretical and experimental work was done on ground effects. Today, propagation distances of interest are an order of magnitude larger. Propagation problems of interest include refraction due to speed of sound gradients and scattering due to turbulence. Applications of long-range sound propagation technology range from en route aircraft noise to the acoustic detection of aircraft. In 1981, the University of Mississippi and the Open University of England co-sponsored a symposium which dealt with issues of particular interest to outdoor, long-range propagation. Approximately every 2 years since the first, the University of Mississippi and the Open University of England have co-sponsored with a third institution a similar symposium on long-range sound propagation. The Fourth International Symposium on Long-Range Sound Propagation was held at the NASA Langley Research Center, Hampton, Va., on May 16–17, 1990. The purpose of the meeting was to exchange information on current research, identify areas needing additional work, and coordinate activities as much as possible. The list of attendees which follows includes representatives from most groups with active research programs in the area.

The meeting was divided into three sessions: ground effects on propagation, infrasound propagation, and meteorological effects on sound propagation. The symposium ended with an open discussion and plans for a future meeting. This report consists of a list of attendees with addresses, a meeting agenda, and a compilation of the presentations made at the symposium.

The hosts would like to express their appreciation to the participants for attending and for sharing their knowledge and expertise.

Henry E. Bass
Professor of Physics
The University of Mississippi
Oxford, Mississippi

Keith Attenborough
Reader in Acoustics
The Open University
Milton Keynes, United Kindgom

William L. Willshire, Jr.
Aero-Space Technologist
NASA Langley Research Center
Applied Acoustics Branch
Hampton, Virginia

CONTENTS

FOURTH INTERNATIONAL SYMPOSIUM ON LONG-RANGE SOUND PROPAGATION

ATTENDEES

Dr. Donald G. Albert
USA CRREL
72 Lyme Road
Hanover, NH 03755-1290
(603) 646-4459

Dr. Keith Attenborough
Department of Engineering Mechanics
The Open University
Walton Hall
Milton Keynes MK7 6AA
ENGLAND
44-908-653947

Dr. Gordon E. Baird
Department of Physics and Astronomy
University of Mississippi
University, MS 38677
(601) 232-7048

Dr. Henry E. Bass
Physical Acoustics Research Laboratory
University of Mississippi
University, MS 38677
(601) 232-5840

Dr. Yves Berthelot
School of Mechanical Engineering
Georgia Institute of Technology
Atlanta, GA 30332
(404) 894-7482

Dr. Richard K. Brienzo
MIT Lincoln Laboratory, M207
244 Wood Street
Lexington, MA 02173
(617) 981-2530

Dr. Simon N. Chandler-Wilde
Department of Civil and Transport Engineering
University of Bradford
Richmond Road, Bradford
West Yorkshire BD7 1DP
ENGLAND

Mr. H. A. Corriher, Jr.
GIRI-RIAL-MAD-CRB
Georgia Institute of Technology
Atlanta, GA 30332-0800

Ms. Amy Chrestman
USAE Waterways Experiment Station
ATTN: CEWES-EN-A
3909 Hallsferry Road
Vicksburg, MS 39180
(601) 634-2149

Dr. Gilles Daigle
Division of Physics
National Research Council
Ottawa, ON K1A OR6
CANADA
(613) 993-6188

Dr. Jim D. Eckard
GIRI-RIAL-MAD-CRB
Georgia Institute of Technology
Atlanta, GA 30332-0800
(404) 894-3662

Dr. Kenneth E. Gilbert
National Center for Physical Acoustics
University of Mississippi
P.O. Box 847
University, MS 38677

Dr. Ralf Grobe
Universitat Oldenburg
Fachbereich Physik
Post Fach 2503
D-2900 Oldenburg
FEDERAL REPUBLIC OF GERMANY
49-441-7983569

Dr. Logan E. Hargrove
Physics Division-Code 1112
Office of Naval Research
800 North Quincy Street
Arlington, VA 22217-5000
(202) 696-4221

Dr. James Hunter
Astronomy Department
211 SSRB
University of Florida
Gainesville, FL 32611
(904) 392-1078

Dr. Helmut Klug
Universitat Oldenburg
Fachbereich Physik
Post Fach 2503
D-2900 Oldenburg
FEDERAL REPUBLIC OF GERMANY
49-441-7983565

Dr. Sung M. Lee
Keweenaw Research Center
Michigan Technological University
Houghton, MI 49931
(906) 487-2327

Dr. Walt McBride
Planning Systems, Inc.
115 Christian Lane
Slidell, LA 70458
(504) 649-0450

Dr. Paul Mutschlecner
Los Alamos National Laboratory
Mail Stop F665
Los Alamos, NM 87545
(505) 667-7672

Dr. John M. Noble
Commander/Director
U.S. Army Atmospheric Science Lab
ATTN: SLCAS-AS-M (John Noble)
White Sands Missile Range, NM
88002-5501
(505) 678-3751

Mr. Robert O. Olsen
U.S. Army Atmospheric Science
Laboratory
ATTN: DELAS-AS-M
White Sands Missile Range, NM
88002-5501
(505) 678-1939

Dr. Gervasio Prado
MS 5120
Textron Defense System
201 Lowell Street
Wilmington, MA 01887
(508) 657-1799

Dr. Richard Raspet
Physical Acoustics Research Laboratory
University of Mississippi
University, MS 38677
(601) 232-5840

Major J. S. Robertson
Department of Mathematics
USMA
West Point, NY 10996-1786
(914) 938-3322

Dr. J. C. Rogers
Electrical Engineering Department
Michigan Technological University
Houghton, MI 49931
(906) 487-2164

Mr. David Schein
Northrop Corporation, B-2 Division
W942/IN
8900 East Washington Blvd.
Pico Rivera, CA 90660-3737
(213) 942-3617

Dr. Edward Shalis
Countermeasures Branch
Tank-Automotive Command
Warren, MI 48090

Mr. Lou Sutherland
Wyle Laboratories
128 Maryland Street
El Segundo, CA 90245
(213) 322-1763, ext 2224

Dr. David Swanson
Applied Research Laboratory
Penn State University
University Park, PA 16802
(814) 863-1585

Dr. Dennis W. Thomson
Department of Meteorology
Penn State University
506 Walker Bldg.
University Park, PA 16802
(814) 863-1585

Mr. Stephen Tooms
Department of Engineering Mechanics
The Open University
Walton Hall
Milton Keynes MK7 6AA
ENGLAND

Dr. William K. Van Moorhem
Mechanical and Industrial
Engineering Department
University of Utah
Salt Lake City, UT 84112
(801) 581-7687

Dr. Martin West
Department of Applied Acoustics
University of Salford
Salford M5 4WT
ENGLAND
44-061-7455000

Dr. Rodney W. Whitaker
Los Alamos National Laboratory
Mail Stop F665
Los Alamos, NM 87545
(505) 667-7672

Dr. Michael White
CERL-EN
Box 4005
Champaign, IL 61820
(217) 373-6751

Mr. William L. Willshire, Jr.
NASA-Langley Research Center
Mail Stop 460
Hampton, VA 23665
(804) 864-5270

Mr. Keith Wilson
Department of Meteorology
Penn State University
506 Walker Bldg.
University Park, PA 16802
(814) 863-1034

FOURTH INTERNATIONAL SYMPOSIUM ON LONG-RANGE SOUND PROPAGATION

AGENDA

Tuesday, May 15, 1990

1700-1900

Happy Hour - Radisson Hotel

1900-2200

Transportation Leaves for Mitty's
No Host Dinner

Wednesday, May 16, 1990

0830

Bus Leaves for NASA Langley Research Center

0900-0905

Welcoming Address
David G. Stephens, Division Chief
Acoustics Division, NASA Langley Research Center

0905-0930

Welcome from Hosts, Introduction, and Statement of Goals

0930-0950

Louis C. Sutherland — Long Range Sound Propagation - A Review of Some Experimental Data

SESSION ON GROUND EFFECTS ON PROPAGATION

0950-1010

F.H. Zhong and W. K. Van Moorhem — Propagation of a Plane Wave Parallel to an Impedance Surface

1010-1030

Gilles Daigle and Tony Embleton — Air-Ground Interference: Surface Waves, Surface Impedance, and Acoustic-to-Seismic Coupling Coefficient

1030-1100

COFFEE

1100-1120

James M. Sabatier and W. Patrick Arnott — Calculation of Impedance Resonances for a Layered Poro-elastic Soil

1120-1140

Richard Raspet and Mark Sprague — Exponentially Varying Ground Models and Their Interpretation

1140-1200

Donald G. Albert — Measured Sound Propagation Over a Variable Seasonal Snow Cover

1200-1310

LUNCH - Follow Bill Willshire to the Cafeteria

1310-1330

J.S. Robertson, P.J. Schlatter, W.L. W.L. Siegmann, and M.J. Jacobson — Numerical Modeling of Long-Range Sound Propagation over Variable Impedance Boundaries

1330-1350

S. N. Chandler-Wilde, J.N.B. Harriott, and D.C. Hothersall — Long Range Propagation Over Discontinuous Impedances

1350-1400

Edward V. Shalis — ADRPM-VII Applied to the Long Range Acoustic Detection Problem

1400-1420

Gervasio Prado, James Fitzgerald, Anthony Arruda, and George Parides — Vehicular Sources in Acoustic Propagation Experiments

1420-1440

J.C. Rogers and S.M. Lee — Acoustic Backscattering from Natural Vegetation (Model Measurements)

1440-1500

Stephen Tooms and Keith Attenborough — Using a Fast Fourier Method to Model Sound Propagation in a Stratified Atmosphere Over a Stratified Porous-Elastic Ground

1500-1515

COFFEE

1515-1535

Dennis W. Thomson — An Overview of Current Studies in Atmospheric Acoustics at Penn State

1535-1555

William L. Willshire, Jr. and Donald P. Garber — Long-Range Vertical Propagation

1555-1625

Discussion of Research Problems and Plans Related to Surface Effects

INFRASOUND PROPAGATION

1625-1645

Rodney Whitaker — Infrasonic Observations of Large Scale HE Events

1645-1700

Discussion of Research Problems and Plans Related to Impulsive and Low Frequency Sound

1700

Bus Leaves for Hotel

1800-1900

No Host Social Hour - Radisson Hotel

1900-2100

Bus leaves for Evening Meal at Fisherman's Wharf. Meals are Prepaid. Drinks must be purchased individually.

2100

Bus Leaves for Hotel

Thursday, May 17, 1990

0815

Bus Leaves for NASA Langley Research Center

0845-0855

Administrative Details

0855-0915

Paul Mutschlecner — A First Order Wind Correction Scheme for Infrasonic Observations

METEOROLOGICAL EFFECTS ON SOUND PROPAGATION

0915-0935

Helmet Klug — Meteorological Effects on Long Range Outdoor Sound Propagation

0935-0955

Richard K. Brienzo — Effect of Wind and Temperature Gradients on Received Acoustic Energy

0955-1015

Keith Wilson — Comparison of FFP Predictions with Measurement of a Low Frequency Acoustic Signal Propagated in the Atmosphere

1015-1035

Martin West and R.A. Sack — New Correction Procedures for the Fast Field Program which Extend its Range

1035-1050

COFFEE

1050-1110

Kenneth E. Gilbert, Xiao Di, Lintao Wang, and Richard Raspet — Comparison of Parabolic Equation and Distorted-Wave Born Approximation Calculations for Turbulent Scattering in an Upward-Refracting Atmosphere

1110-1130

Ralf Große — Wave propagation Through Random Media: A Local Method of Small Perturbations Based on the Helmholtz Equation

1130-1150

Robert O. Olsen, John M. Noble, James Luers, and Mark Dietenberger — Noise Assessment and Prediction System

1150-1210

Walt McBride	Scattering of Sound by Atmospheric Turbulence: Predictions in a Refractive Shadow Zone

1210-1230

John M. Noble, Henry E. Bass, and Richard Raspet	Effects of Large Scale Wind Drive Turbulence on Sound Propagation

1230-1330

LUNCH - Follow Bill Willshire to the Cafeteria

1300

First Bus to Hotel

1330-1400

Discussion of Meteorological Effects and Future Research Plans

1400-1500

PLANS FOR FUTURE COLLABORATION AND MEETINGS

1500

Second Bus to Hotel

1800

Social Hour for Diehards - Radisson Hotel

1900

No Host Dinner for Diehards

LONG-RANGE SOUND PROPAGATION – A REVIEW OF SOME EXPERIMENTAL DATA

Louis C. Sutherland
Consultant in Acoustics
27803 Longhill Dr.
Rancho Palos Verdes, CA 90274

SUMMARY

Three experimental studies of long range sound propagation carried out or sponsored in the past by NASA are briefly reviewed to provide a partial prospective for some of the analytical studies presented in this symposium. The three studies reviewed cover (1) a unique test of two large rocket engines conducted in such a way as to provide an indication of possible atmospheric scattering loss from a large low-frequency directive sound source, (2) a year-long measurement of low frequency sound propagation which clearly demonstrated the dominant influence of the vertical gradient in the vector sound velocity towards the receiver in defining excess sound attenuation due to refraction, and (3), a series of excess ground attenuation measurements over grass and asphalt surfaces replicated several times under very similar inversion weather conditions.

INTRODUCTION

Experimental data on long range sound propagation sound from three unique programs carried out over the last 25 years that were conducted or sponsored by NASA can provide a useful background for some of the analytical models treated in this symposium. These measurement programs are very briefly reviewed here to insure that the existence of these data may be more widely known to researchers in the field of long range sound propagation. The sources of the data are identified for the reader who may wish to pursue the information in more detail.

EXPERIMENTAL DATA ON PROPAGATION OF LOW FREQUENCY ROCKET NOISE AT LONG RANGES.

On March 24, 1964 at approximately 1340 CST, the NASA George C. Marshall Space Flight Center, in Huntsville, Alabama conducted a static test firing of a Saturn S-I first stage rocket booster on a test stand for which the deflected exhaust blast was directed due north. This rocket consists of a cluster of eight engines with a total thrust of about 1.5 million lbs. Seven minutes later, a static test of a Saturn F-I rocket engine (a single chamber rocket engine with the same total thrust), was conducted on the same basic test stand but with the deflected exhaust blast directed due south. Major results of acoustic measurements conducted out to a distance of 15 Km along a line of microphone stations on a 45° azimuth line from the test stand towards the city of Huntsville, as shown in Figure 1, were reported by Tedrick.[1] However, most of the detailed results presented here are contained in an internal NASA Memo.[2] Also shown in Figure 1 are the vertical sound velocity profiles measured in this direction at the time of each test firing and the resulting calculated sound ray paths in this same direction. The sound velocity profiles differ slightly in the first 2 Km but the resulting ray paths differ significantly. Based on a comparison of the ray paths for the two firings, one would expect to see a greater refraction loss for the second test due to the greater upward refraction of the sound ray for this test. As will be shown, precisely the opposite condition prevailed.

Not shown here are the same type of sound profiles and ray paths for a 226° azimuth direction – essentially 180° from those shown in Figure 1. The results were very similar – minor differences in sound profiles and a ray path for the second test showing more upward refraction in this direction than for the first test – again suggesting a greater refraction loss for the second test.

Although the two rocket boosters have a very different geometry, the resultant total sound power levels and spectra are very similar[1] and, as shown in Figure 2, the directivities for the overall sound pressure level at a distance of 1000 ft from the engines are very similar when the different direction of the exhaust blast for the two tests is recognized. In the direction of the microphone positions, the overall sound levels of the two rocket engines differ by about 12 dB at a 1000 ft radius. Figure 3 shows the values of excess attenuation in octave bands, including any air absorption, for the S-I test, as a function of octave band center frequency with distance as a parameter. It was convenient, for this plot, to use 1.6 Km as a reference distance for evaluating excess attenuation. The data show, roughly, the expected trend of increasing excess attenuation with distance and frequency. Figure 4 shows the same data for the S-I test re-plotted as a function of distance where the values of excess attenuation have been averaged over pairs of adjacent octave bands to simplify the data presentation. Figure 5 shows the same information for the F-I test.

However, it is not the purpose of this review to examine the absolute values for the excess attenuation for each test but rather examine the difference in excess attenuation between the two tests. This is shown in Figure 6 in terms of the excess attenuation for the S-I test (i.e., maximum lobe of noise along the measurement direction towards Huntsville) minus the excess attenuation along the same line, for the F-I test (i.e., maximum lobe of noise in opposite direction).

The excess attenuation along this same path decreased between the two tests, conducted only 7 minutes apart. This decrease is most significant for a distance of 9 Km and is more dependent upon frequency at this distance than at any other point. This decrease in excess attenuation could be attributed to a change in sound refraction between the two tests. However, as suggested by the sound velocity profiles and calculated ray paths in Figure 1, this effect would have been expected to be just the opposite from what was observed – i.e., an increase in excess attenuation due to the expected increase in refraction loss for the second test. An alternative hypothesis is that the decrease in excess attenuation could be attributed to the effect of scattering by atmospheric turbulence. This scattering would tend to increase the apparent excess attenuation in the measurement direction for the first test (i.e., remove energy from the main sound lobe in this direction) and decrease the excess attenuation for the second test by adding back-scattered energy to the weaker lobe in this direction.

This hypothesis, admittedly not proven, is consistent with the observations and with theoretical predictions.[3,4] Further research is needed to more fully evaluate and experimentally validate sound attenuation by atmospheric turbulence. Practical applications include definition of correct excess attenuation models for the directive sound fields of jet aircraft and long range warning sirens.

LONG-TERM MEASUREMENT OF EXCESS ATTENUATION WITH REFRACTION

The second sound attenuation program was conducted at the NASA Mississippi Test Range over a one year period by Tedrick and Polly.[5] The program utilized the pure tone siren/horn sound source system shown in Figure 7 mounted on a 60 ft. tower to propagate pure tone signals at 40, 80, 120 and 160 Hz at distances up to 3 Km over a flat terrain heavily covered with a deciduous rain forest. Over 29,000 excess attenuation measurements were made over the one year test period. The results were correlated with the vertical gradient of vector sound velocity from the source to the receiver as measured over the first 300 meters above the ground. Typical results for two distances are shown in Figure 8 in terms of the excess attenuation at 160 Hz as a function of this sound velocity gradient. As for all of the frequencies and distances measured, the data collapsed in the form illustrated. At any given frequency and distance, the mean excess attenuation was essentially constant when the sound velocity gradient was equal to, or greater than zero and decreased approximately linearly as the gradient decreased below zero.

The mean excess attenuation, A_o for sound velocity gradients equal or greater than zero varied linearly with distance and systematically with frequency as shown on Figure 9 which is taken from Ref. 5. Although the excess attenuation includes air absorption, the latter is a relatively small part of the observed

excess attenuation which is believed to be predominantly ground attenuation. Note that the intercept value of A_0 for zero distance is roughly proportional to frequency but the rate of increase with distance increases only slightly with frequency.

For negative sound velocity gradients, Tedrick and Polly showed that the slope of the plot of excess attenuation versus sound velocity gradient increased linearly with distance and approximately linearly with frequency (see Figure 10).

While the above presents a very simplified definition of the data trends, it has substantial face validity on the basis of the very large number of measurements involved and should provide useful benchmarks for comparison with the latest theoretical models for ground attenuation in the presence of refraction.

Another result from this long term test program was the determination of the statistical distribution in the magnitude of focusing amplification (i.e., excess attenuation which is positive) corresponding to sound attenuation less than inverse square spreading loss. While very likely a site-specific statistic, the distribution data shown in Figure 11, developed from tabular data in Ref. 5, shows that this focusing anomaly increases with distance for values of the anomaly less than about 15 dB. Note that in this case, the data cover a much longer propagation range and indicate that, on rare occasions, anomalous increases in level above that predicted by spherical spreading loss of up to 30 dB were observed.

GROUND ATTENUATION MEASUREMENTS FOR INVERSION CONDITIONS OVER GRASS AND ASPHALT SURFACES.

The final test program mentioned here was sponsored by NASA and is fully described in Ref. 6. Copies of the full report may be available through NASA, Langley. The program involved the measurement of ground attenuation over asphalt and grass surfaces on, or next to, an aircraft runway at NASA's Wallops Island facility. The tests were conducted with an elevated loudspeaker source located at 2.5, 5, and 10 meters above each of the surfaces. For most of the tests, the weather conditions corresponded to a mild inversion condition that was replicated several times for each measurement source elevation/ground surface condition. The basic test geometry and microphone array employed is illustrated in Figure 12. Note that at one distance (225 meters), microphones were located essentially at the ground surface, and at 1.2 and 10 meters. At 450 meters, microphones were located at 1.2 and 10 meters. (Note that for the tests over grass, a small strip of asphalt existed along the "grass" path between the 450 and 675 m positions.)

Along with the excess attenuation measurements, the mean weather conditions were evaluated extensively with meteorological instrumentation on 7 and 10 meter towers and a captive weather balloon repeatedly raised to and lowered from a height of 100 m. For the sake of brevity, only a small fraction of the available excess attenuation data are shown here in Figure 13. The figure shows, for two distances, the two surfaces and three source heights, the arithmetically averaged excess attenuation for one third octave bands of noise from 50 to at least 3200 Hz for the four to six replications of nominally very similar inversion conditions. Each excess attenuation measurement was based on an energy average of sound levels over a 15 second period. The standard deviation of the excess attenuation values over the four to six replications for each measurement condition and frequency was normally much less than 1.5 dB.

The results show the characteristic increase in excess attenuation due to ground absorption at frequencies in the range of 125 to 630 Hz depending on the surface and measurement distance. The excess attenuation data are augmented by some very limited measurements of surface impedance employing the simple technique developed by Piercy and Embleton.[7] Thus, these data provide another, and, in some aspects more complete, set of measurements of ground attenuation in the presence of documented refraction conditions than had been available previously. They offer a useful set of measurements for comparison with corresponding theoretical models.

CONCLUSIONS

Results from three different NASA conducted or NASA sponsored tests of long range sound propagation have been very briefly reviewed. The objective has been to identify these unique sources of data, two of which are over 25 years old, for the benefit of modelers of long range sound propagation who may not be aware of their existence. They offer potentially useful data sets for comparison with theoretical models for the evaluation, respectively of: scattering attenuation by atmospheric turbulence, long range ground propagation under a wide range of defined refraction conditions, and ground attenuation over two surfaces for nearly identical mild inversion conditions. As further advances are made in theoretical models, new and more sophisticated measurements will be required to validate the theory.

REFERENCES

1. Tedrick, R.N. "Acoustical measurements of static tests of clustered and single-nozzle rocket engines," J. Acoust. Soc. Amer. 36:2027-2032, 1964.

2. Polly, R. "Acoustic levels resulting from F-I Test TFW-016 and Saturn Test SA-19," Memorandum R-Test-ICA-73-64, Acoustics Section, Components Instrumentation Branch, Test Laboratory NASA GCMSFC, Huntsville, Alabama, April 16, 1964.

3. Sutherland, L. C. "Scattering attenuation of sound in the lower atmosphere," J. Acoust. Soc. Amer. 49:129(A), 1971.

4. Brown, E.H. and Clifford, S.F. "On the attenuation of sound by turbulence," J. Acoust. Soc. Amer. 60:788-794, 1976.

5. Tedrick, R.N. and Polly, R. "Measured acoustic propagation parameters in the Mississippi Test Operations area," NASA TM X-1132, August 1965.

6. Sutherland, L.C. and Brown, R. "Static tests of excess ground attenuation at Wallops Flight Center," NASA CR-3435, June 1981.

7. Piercy, J.E. and Embleton, T.F.W. "Excess attenuation or impedance of common ground surfaces characterized by flow resistance," J. Acoust. Soc. Amer. 65(S1), S63(A), 1979.

BACK-TO-BACK TESTS OF S-I & F-I ROCKETS AT NASA, MSFC - HUNTSVILLE

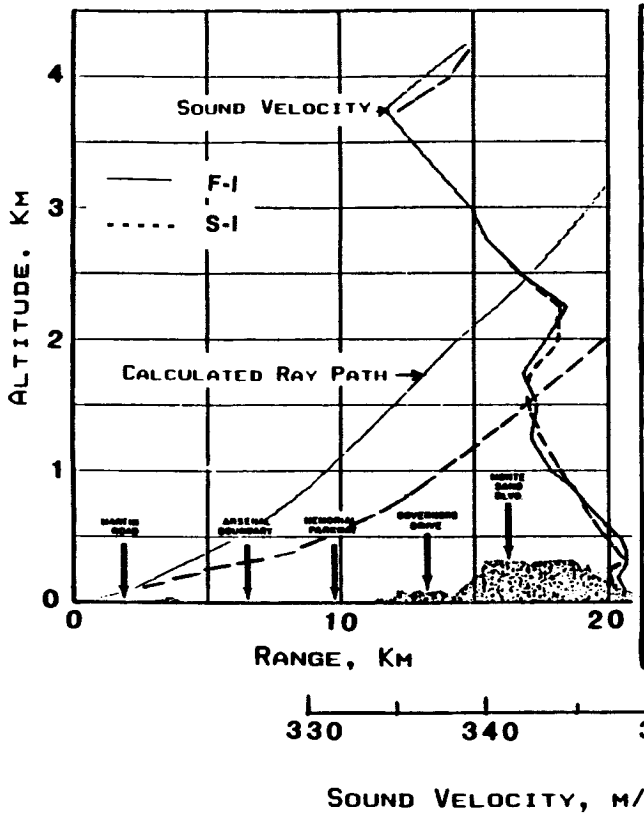

Figure 1A. Sound Velocity Profile

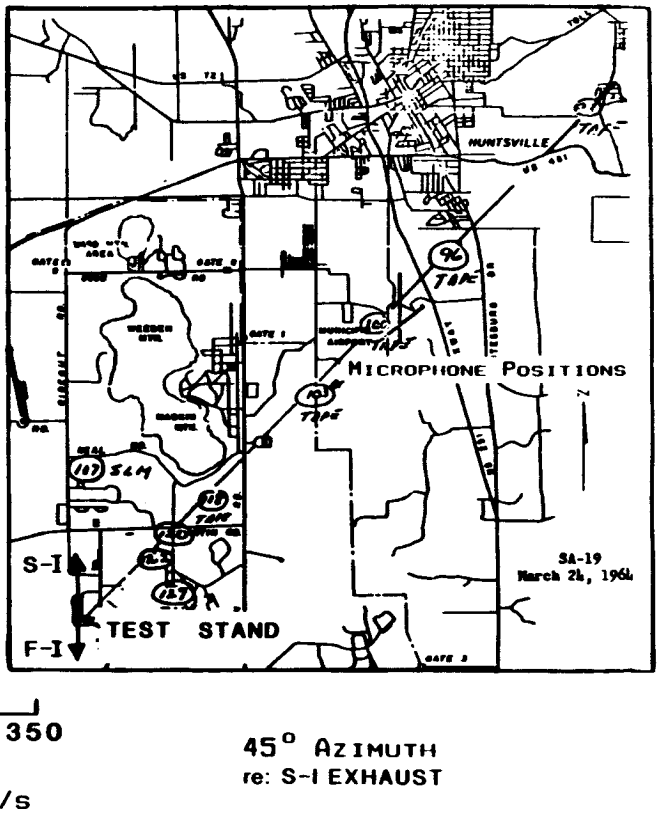

Figure 1B. Microphone Positions

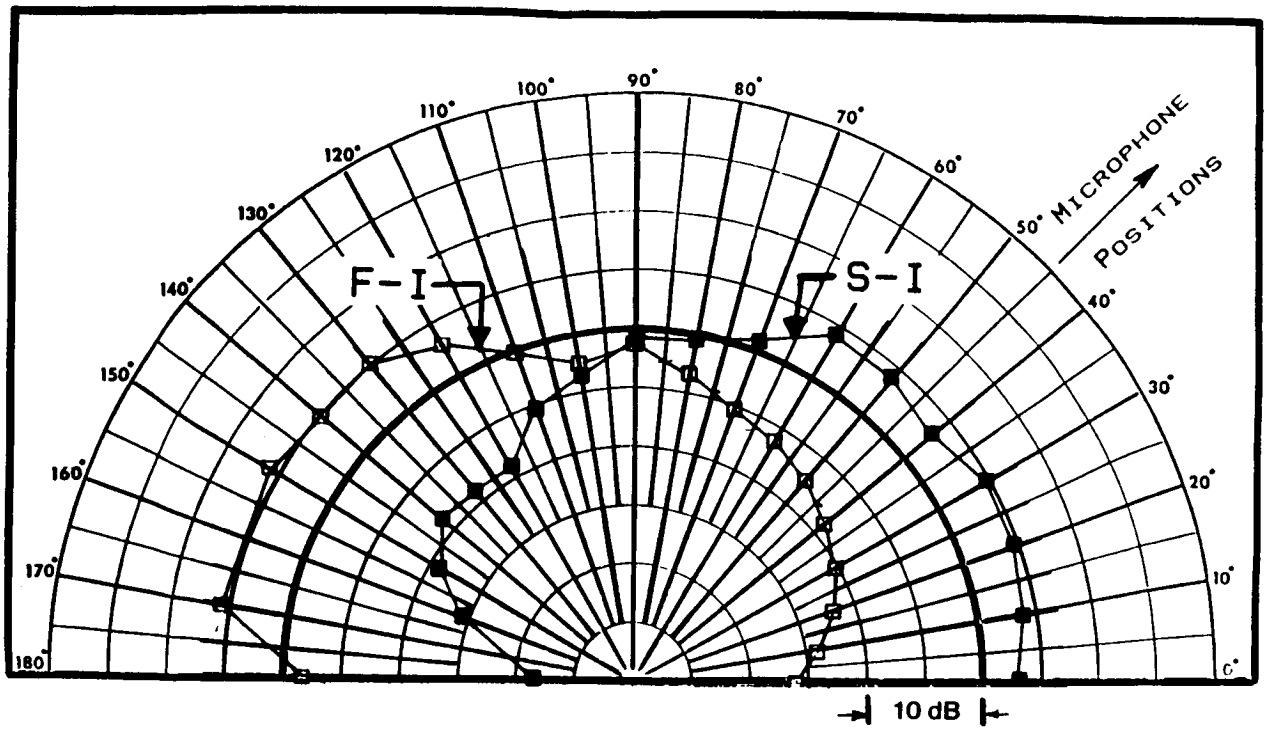

Figure 2. Directivity of S-I and F-I Rockets

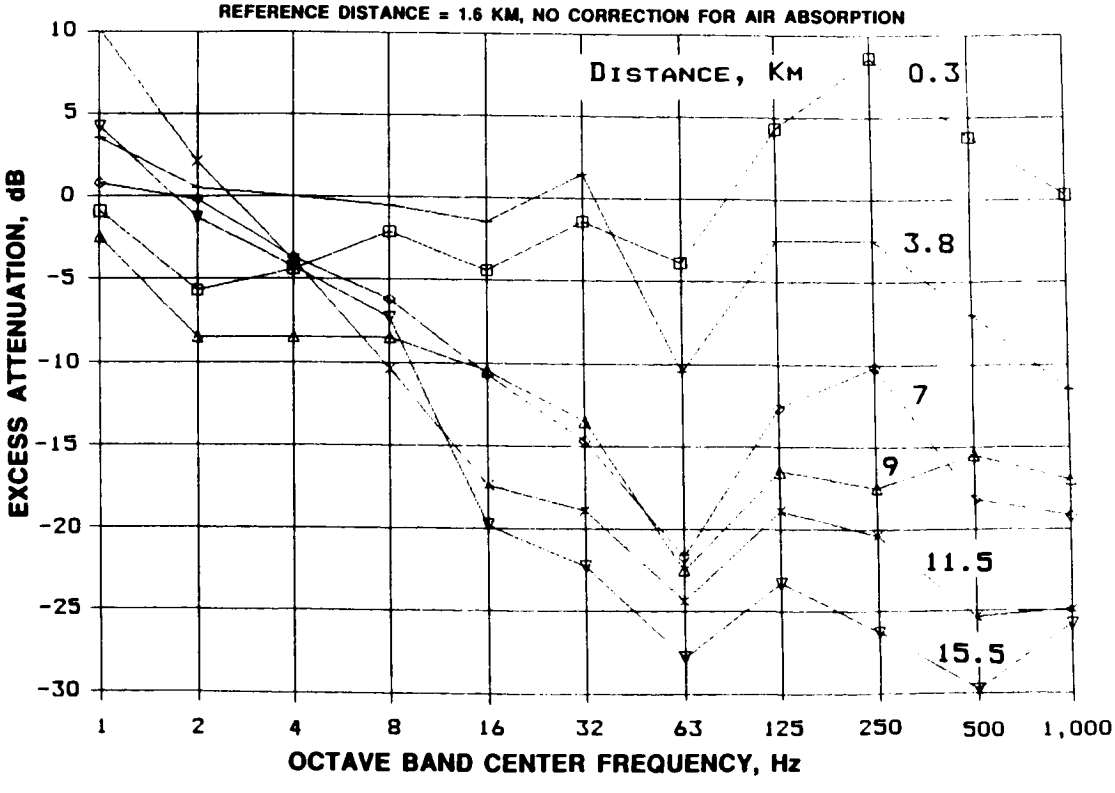

Figure 3. Excess Attenuation (S-I) Versus Frequency

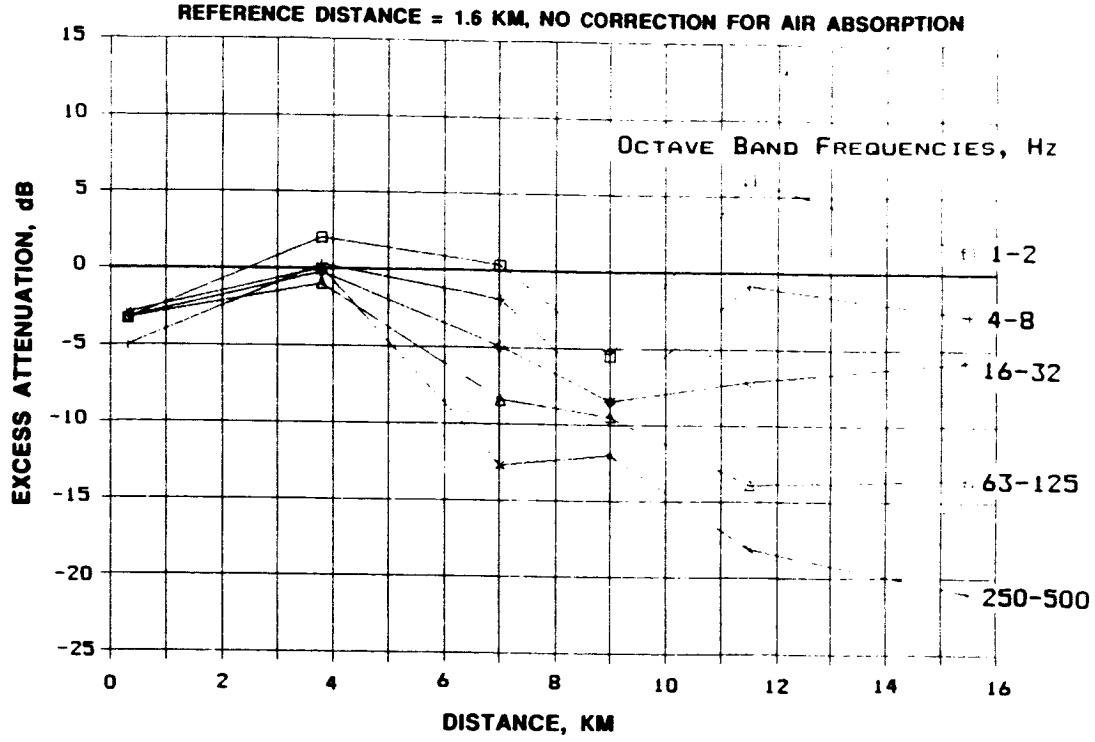

Figure 4. Excess Attenuation Versus Distance (S-I)

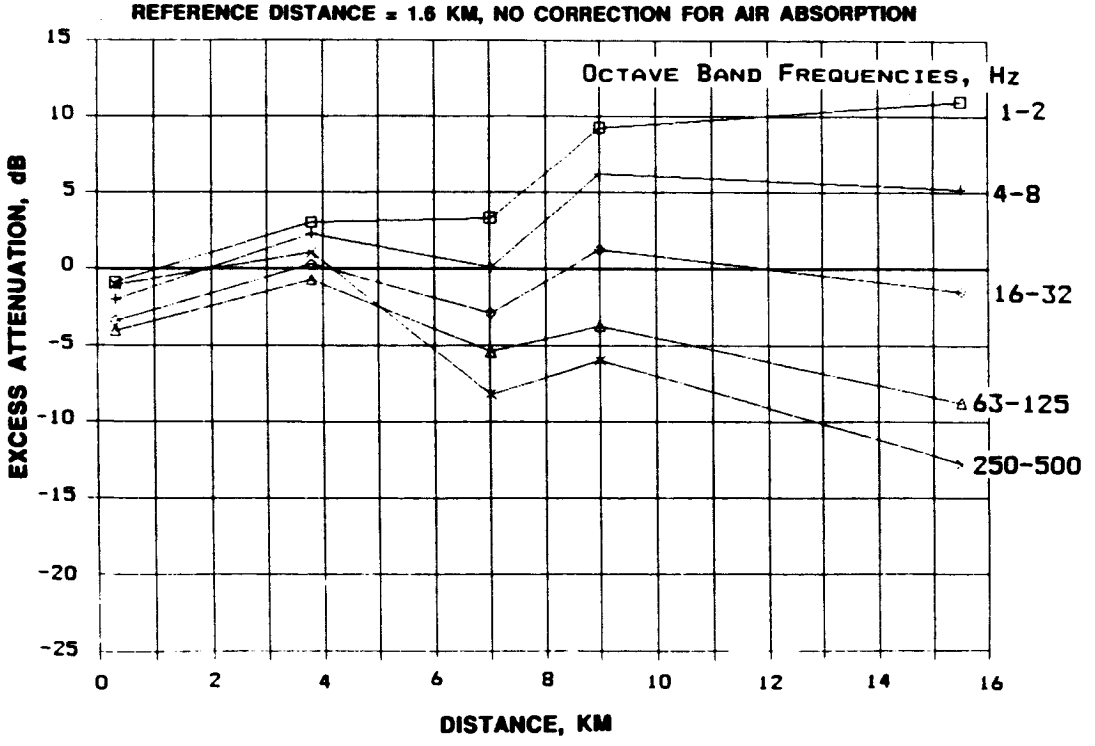

Figure 5. Excess Attenuation Versus Distance (F-I)

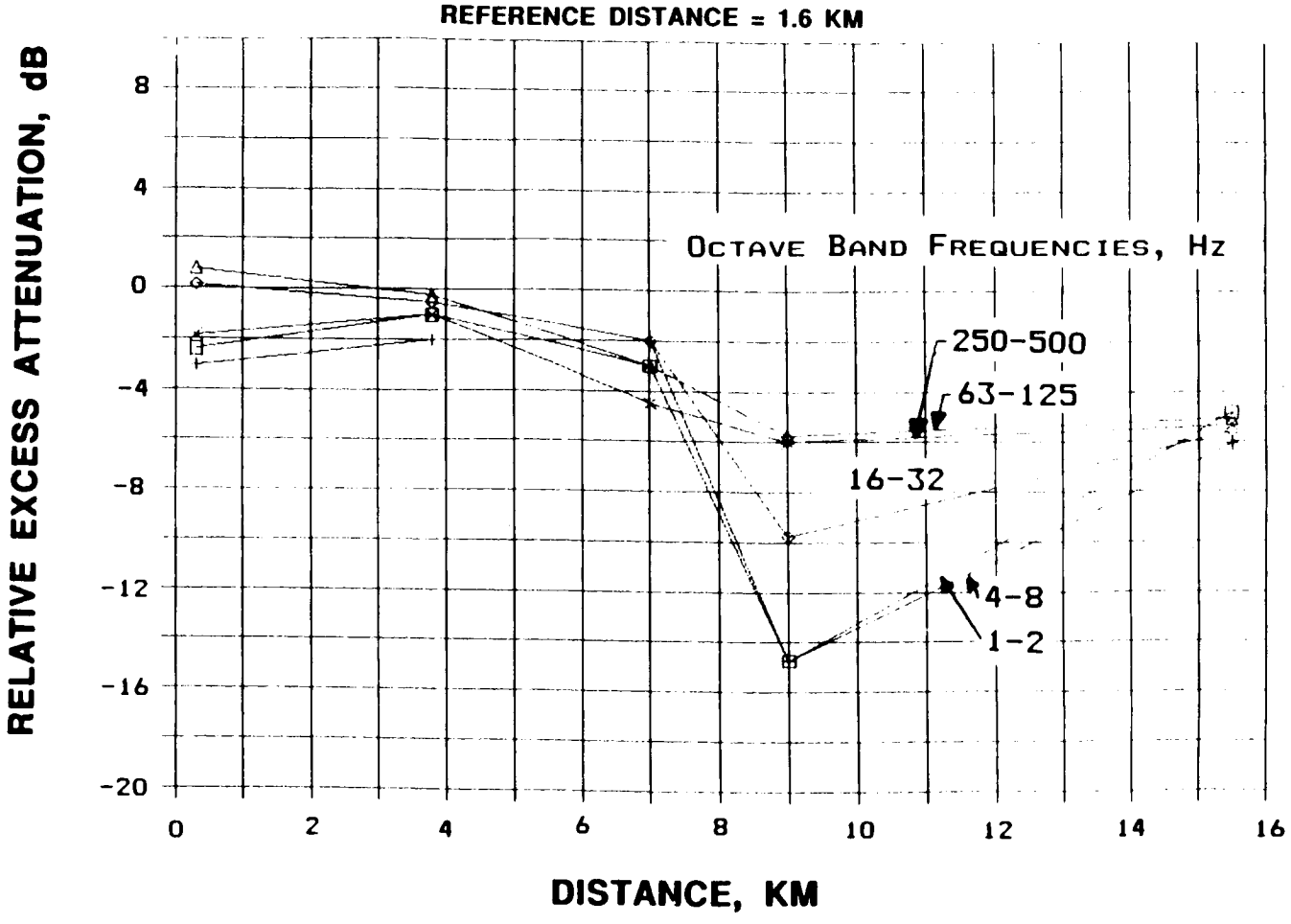

Figure 6. Relative Excess Attenuation (S-I) (F-I)

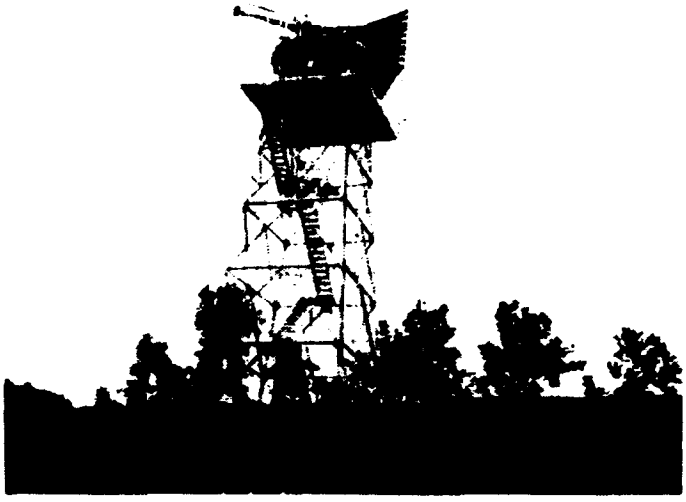

12.5 FT. DIAM. HORN ON 60 FT TOWER

Figure 7. Study of Sound Refraction at the Mississippi Test Range (from Tedrick and Polly, NASA TM X-132, 1965).

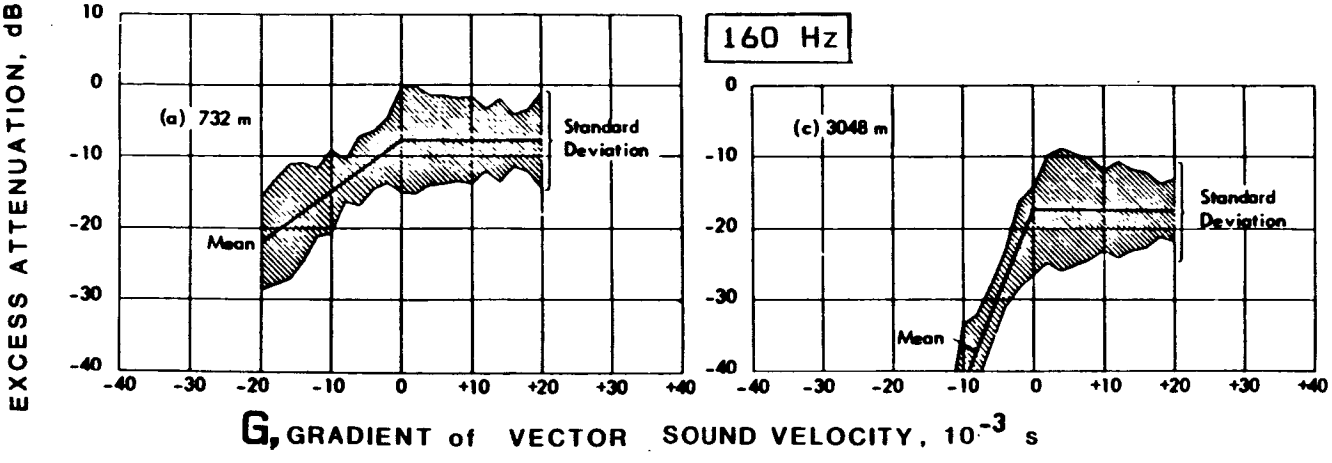

Figure 8. Attenuation in Excess of Inverse Square Loss

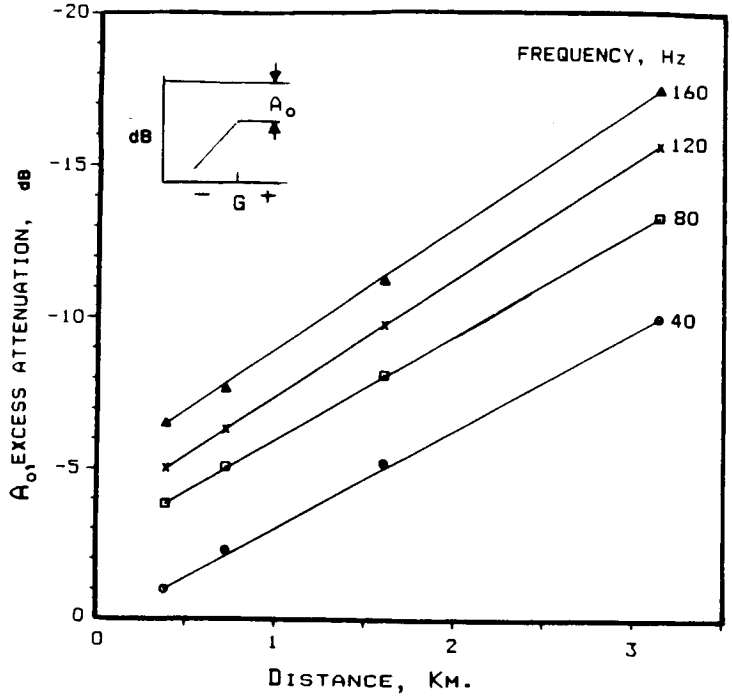

Figure 9. Excess Attenuation for Positive Sound Velocity Gradient

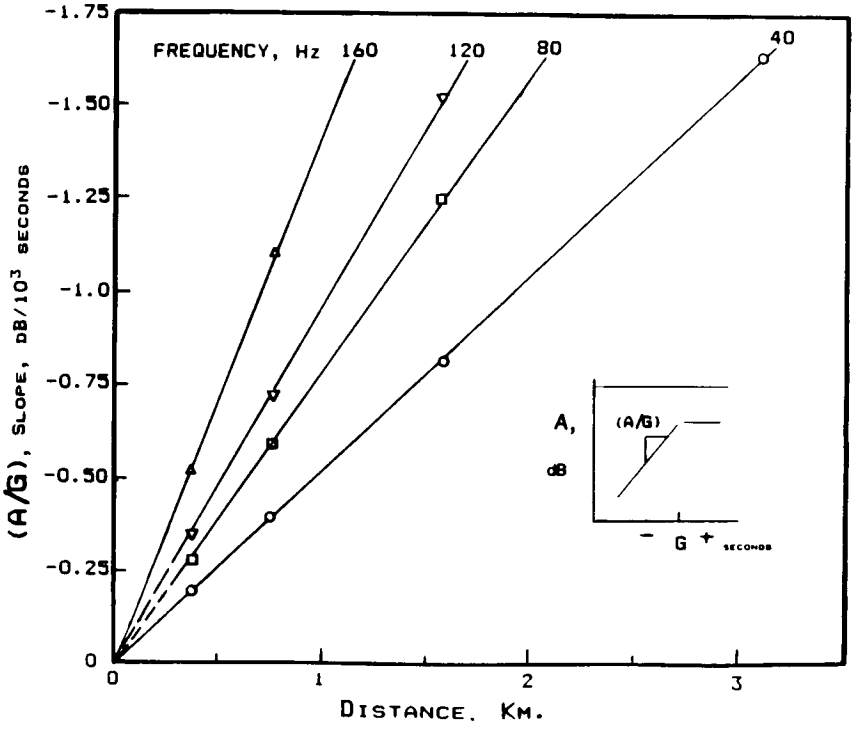

Figure 10. Slope of Excess Attenuation for Negative Sound Velocity Gradient

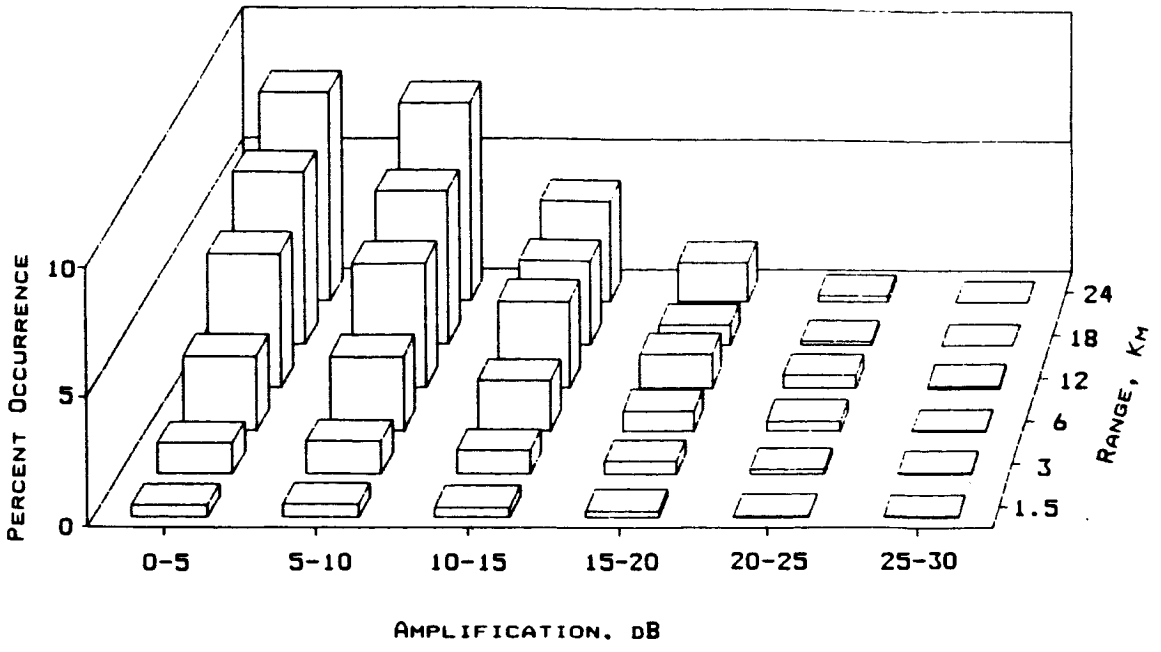

Figure 11. Distribution of Focusing Amplification by Range and Magnitude of Amplification

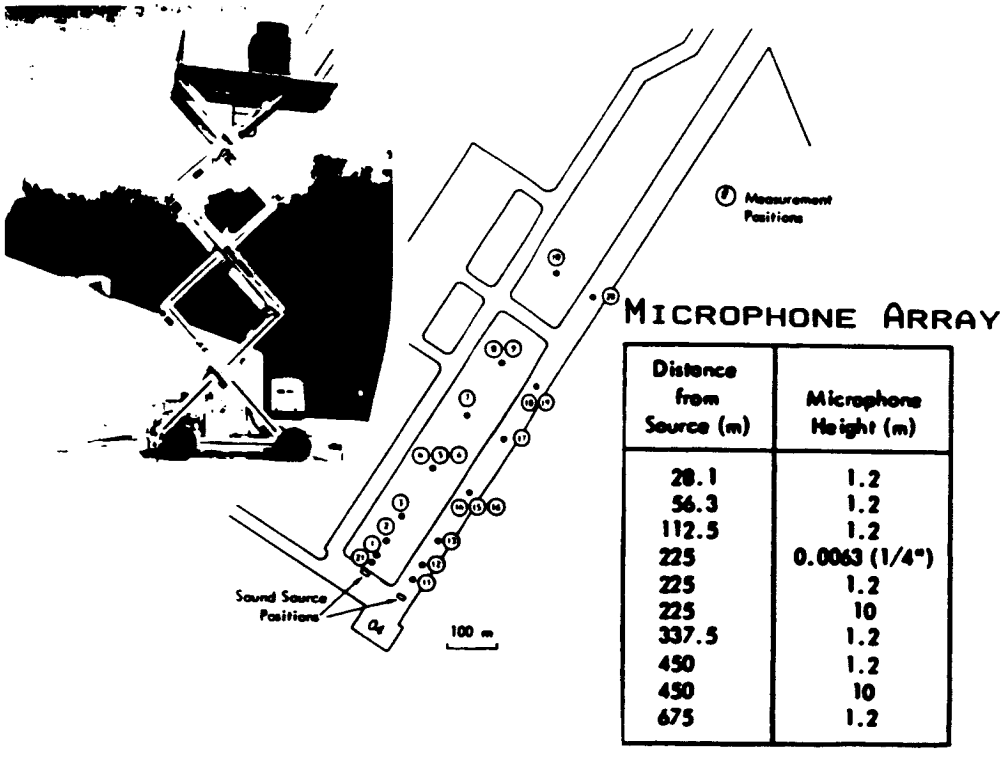

Distance from Source (m)	Microphone Height (m)
28.1	1.2
56.3	1.2
112.5	1.2
225	0.0063 (1/4")
225	1.2
225	10
337.5	1.2
450	1.2
450	10
675	1.2

Figure 12. Ground Attenuation Measurements at Wallops Island (Taken from Sutherland and Brown, NASA CR-3435, 1981)

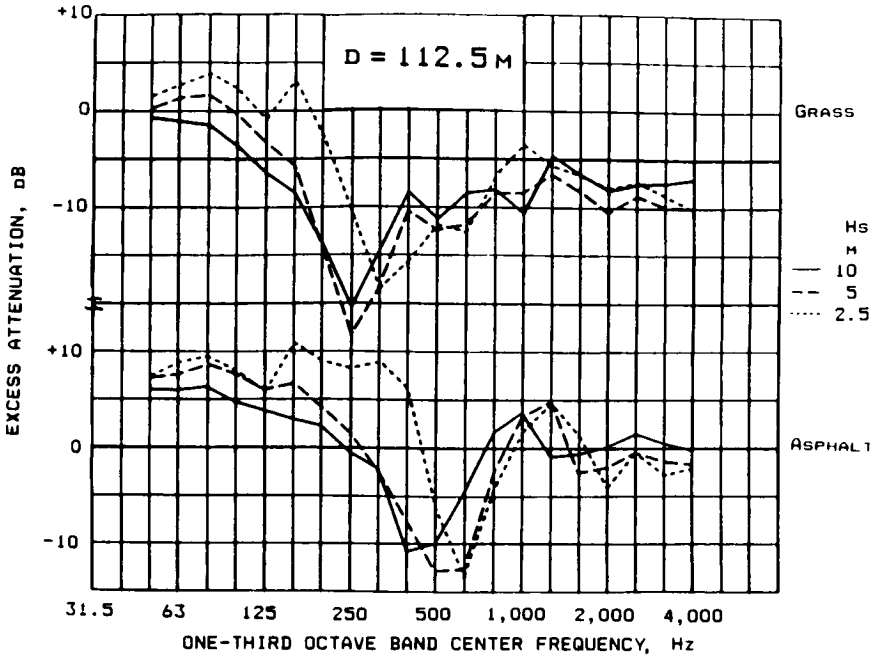

Figure 13A. Excess Ground Attenuation Corrected for Air Absorption (D = 112.5m)

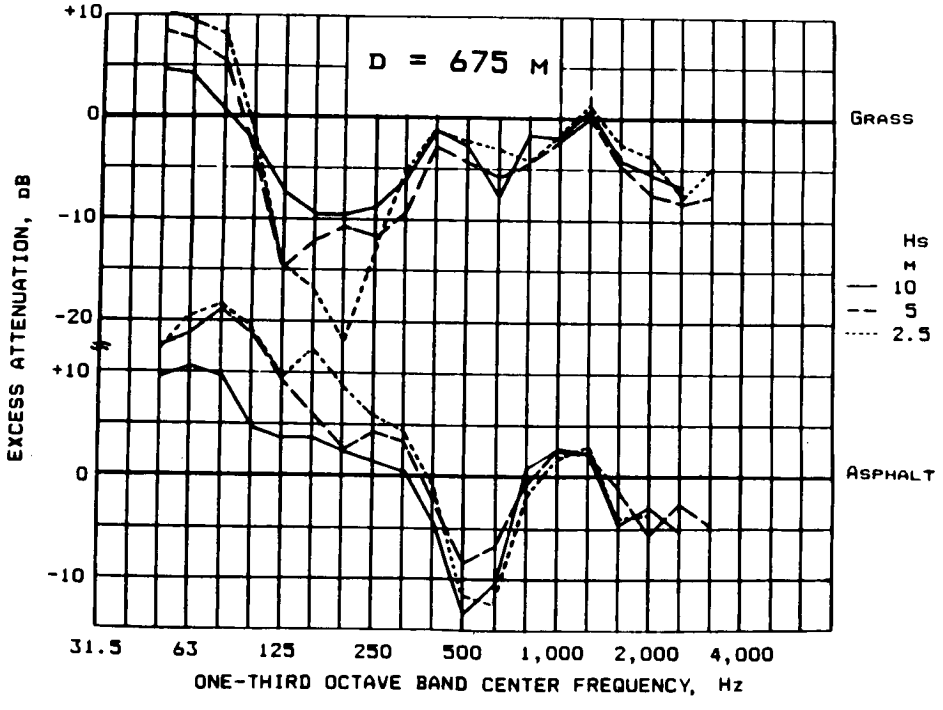

Figure 13B. Excess Ground Attenuation Corrected for Air Absorption (D = 675m)

ON THE PROPAGATION OF PLANE WAVES ABOVE AN IMPEDANCE SURFACE

F. H. Zhong and W. K. Van Moorhem
Department of Mechanical Engineering
University of Utah
Salt Lake City, Utah 84112

ABSTRACT

The propagation of grazing incidence plane waves along a finite impedance boundary is investigated. A solution of the semi-infinite problem, where a harmonic motion, parallel to the boundary, is imposed along a line perpendicular to the boundary, is obtained. This solution consists of quasiplane waves, waves moving parallel to the boundary with amplitude and phase variations perpendicular to the boundary. Several approximations to the full solution are considered.

INTRODUCTION

Mathematical modeling of the propagation and reflection of harmonic plane waves above a finite impedance plane surface is a fundamental topic in acoustics. In the case where the angle between the normal to the wavefront and the surface is not zero an analytic solution is very easy to obtain. This solution consists of the incident plane wave propagating toward the surface plus a reflected plane wave propagating away from the surface at the same magnitude of the angle between its normal and the surface as the incident wave. The amplitude of the reflected wave is given by a reflection coefficient that is expressed in terms of incident angle and the specific impedance of the surface. However at zero incident angle (the wave normal parallel to the surface), complete cancellation of the incident and reflect waves occurs in this model and a zero solution results. Most acoustic texts claim that this situation is not possible [1-3].

McAninch[4] recently has investigated a related situation where a plane wave source is generating waves that would move parallel to a surface if its impedance was infinite but where the surface impedance is not infinite quasiplane waves result. McAninch's investigation, however, uses the parabolic approximation where only waves traveling in one direction are allowed. This paper approaches the same problem without the assumption of parabolic approximation.

FORMULATION OF THE PROBLEM

The governing acoustic wave equation for harmonic waves can be put in the form

$$(\nabla^2 + k^2)\,\phi = 0 \tag{1}$$

where the time dependent part of the potential, $e^{-i\omega t}$, has been separated from the spatial part of the potential, $\phi(x,y)$. When an impedance boundary exists, the solution of equation (1) must also satisfy the boundary condition

$$\phi_y + \gamma\phi = 0 \tag{2}$$

on y=0. Here the subscript y indicates a partial derivative with respect to y.

For a unique solution, some extra constraints must be introduced. One is to assume that ϕ will not be affected by the ground impedance as y approaches infinity, the second is that the acoustic pressure at x=0 is given by

$$\phi(0,y) = 1 \tag{3}$$

EXACT SOLUTION

We assume that the solution of (1) has the form of

$$\phi = e^{ikx} + f(x,y) \tag{4}$$

where e^{ikx} can be considered as a solution without the boundary condition given by (2). Substituting (4) into (1),(2) and (3) we get a new governing equation and set of boundary conditions

$$(\nabla^2 + k^2) f = 0 \tag{5}$$

$$f_y(x,0) + \gamma f(x,0) = -\gamma e^{ikx} \tag{6}$$

$$f(0,y) = 0 \tag{7}$$

and

$$\lim_{y\to\infty} f(x,y) = 0 \tag{8}$$

Equation (8) results from the first uniqueness condition listed above.

The sine transform,

$$F(\lambda,y) = \int_0^\infty f(x,y) \sin(\lambda x)\, dx \tag{9}$$

is equivalent to the Fourier transform of an even function and will be applied here. The inverse transform is given by

$$f(x,y) = \frac{2}{\pi} \int_0^\infty F(x,y) \sin(\lambda x)\, d\lambda \tag{10}$$

Applying (9) to (5) and (6) we have

$$\frac{\partial^2 F}{\partial y^2} - (\lambda^2 - k^2) F = 0 \tag{11}$$

and

$$F_y(\lambda,0) + \gamma F(\lambda,0) = -\gamma \frac{\lambda}{\lambda^2 - k^2} \tag{12}$$

Here, it is assumed that k is a complex number with a very small positive imaginary part.

Solving (11) and making use of the given boundary conditions, yields

$$F(\lambda,y) = A(\lambda,0)\, e^{-my} \tag{13}$$

$$A(\lambda,0) = -\frac{\gamma\lambda}{(\lambda^2 - k^2)(\gamma - m)} \tag{14}$$

where $m = \sqrt{(\lambda^2-k^2)}$. Since the solution is required to remain finite, $Re\sqrt{(\lambda^2-k^2)} > 0$. Substituting (13) and (14) into (10) yields the inverse transform of $F(\lambda,y)$ as

$$f(x,y) = -\frac{2\gamma}{\pi}\int_0^\infty \frac{\lambda}{(\lambda^2 - k^2)(\gamma - m)}\, e^{-my} \sin(\lambda x)\, d\lambda \tag{15}$$

For convenience, substitute the identity

$$\sin(\lambda x) = \frac{e^{i\lambda x} - e^{-i\lambda x}}{2i} \tag{16}$$

into (15), yielding

$$f(x,y) = -\frac{\gamma}{i\pi}(I_1 - I_2) \tag{17}$$

where

$$I_1 = \int_0^\infty \frac{\lambda e^{-my}}{(\lambda^2 - k^2)(\gamma - m)}\, e^{i\lambda x}\, d\lambda \tag{18}$$

$$I_2 = \int_0^\infty \frac{\lambda e^{-my}}{(\lambda^2 - k^2)(\gamma - m)}\, e^{-i\lambda x}\, d\lambda \tag{19}$$

In order to evaluate the above two integrals, introduce the complex variable $\Lambda = \lambda + is$ and define the contour integrals

$$I_{CI} = \int_{CI} \frac{\Lambda e^{-My}}{(\Lambda^2 - k^2)(\gamma - M)}\, e^{i\Lambda x}\, d\Lambda \tag{20}$$

$$I_{CII} = \int_{CII} \frac{\Lambda e^{-My}}{(\Lambda^2 - k^2)(\gamma - M)}\, e^{-i\Lambda x}\, d\Lambda \tag{21}$$

First evaluate the integral I_{CI} where the contour is shown in Figure 1 along with the branch lines which extend from the imaginary axis to the points $\Lambda = \pm k$. The value of this contour integral is determined by the residue within the contour. Writing

$$\gamma = \alpha + i\beta \tag{22}$$

it is clear a pole exists within the contour only when $\alpha > 0$ (since $\mathrm{Re}\sqrt{\Lambda^2 - k^2} > 0$, $\gamma - \sqrt{\Lambda^2 - k^2} = 0$ only when $\mathrm{Re}(\gamma) = \alpha > 0$), and this pole is at $\Lambda = \sqrt{(k^2 + \gamma^2)}$. It is easy to determine the residue at this pole to be

$$\mathrm{Res}\left(\sqrt{k^2 + \gamma^2}\right) = -\frac{e^{-\gamma y + i\sqrt{k^2+\gamma^2}\, x}}{\gamma} \tag{23}$$

and

$$I_1 = I_{C1} = -I_{C2} - I_{C3} - I_{C4} - I_{C5} - I_{C6} + \begin{cases} 2\pi i\, \mathrm{Res}\left(\sqrt{k^2 + \gamma^2}\right) & \alpha > 0 \\ 0 & \alpha < 0 \end{cases} \tag{24}$$

when $R \to \infty$, I_{C2} will vanish, while

$$I_{C3} = -\int_0^\infty \frac{s}{(s^2 + k^2)\left(\gamma - i\sqrt{s^2 + k^2}\right)} e^{-i\sqrt{s^2+k^2}\, y} e^{-s x}\, ds \tag{25}$$

$$I_{C4} = \int_0^k \frac{\lambda}{(\lambda^2 - k^2)\left(\gamma - i\sqrt{k^2 - \lambda^2}\right)} e^{-i\sqrt{k^2-\lambda^2}\, y} e^{i\lambda x}\, d\lambda \tag{26}$$

$$I_{C5} = -\frac{\pi i}{\gamma} e^{i k x} \tag{27}$$

$$I_{C6} = -\int_0^k \frac{\lambda}{(\lambda^2 - k^2)\left(\gamma + i\sqrt{k^2 - \lambda^2}\right)} e^{i\sqrt{k^2-\lambda^2}\, y} e^{i\lambda x}\, d\lambda \tag{28}$$

Substituting the above integrals into (24), yields

$$I_1 = \int_0^k \frac{\lambda}{(\lambda^2 - k^2)} \left\{ \frac{e^{i\sqrt{k^2-\lambda^2}\, y}}{\left(\gamma + i\sqrt{k^2 - \lambda^2}\right)} - \frac{e^{-i\sqrt{k^2-\lambda^2}\, y}}{\left(\gamma - i\sqrt{k^2 - \lambda^2}\right)} \right\} e^{i\lambda x}\, d\lambda$$

$$+ \int_0^\infty \frac{s\, e^{-i\sqrt{s^2+k^2}\, y}}{(s^2 + k^2)\left(\gamma - i\sqrt{s^2 + k^2}\right)} e^{-s x}\, ds + \frac{i\pi}{\gamma} e^{i k x} \tag{29}$$

$$+ \begin{cases} -\frac{i 2\pi}{\gamma} e^{-\gamma y} e^{i\sqrt{k^2+\gamma^2}\, x} & \alpha > 0 \\ 0 & \alpha < 0 \end{cases}$$

The value of integral I_2 is much easier to evaluate. We choose a contour in the fourth quadrant, since there is no pole within the contour. I_2 can then be written as

$$I_2 = \int_0^{\infty} \frac{s\, e^{i\sqrt{s^2+k^2}\, y}}{(s^2+k^2)(\gamma+i\sqrt{s^2+k^2})} e^{-sx}\, ds \tag{30}$$

Here it must be recalled that there is a branch line along the imaginary axis. Subtracting I_2 from I_1 yields

$$I_1 - I_2 = \frac{i\pi}{\gamma} e^{ikx}$$

$$+ \int_0^{k} \frac{\lambda}{(\lambda^2 - k^2)} \left\{ \frac{e^{i\sqrt{k^2-\lambda^2}\, y}}{(\gamma+i\sqrt{k^2-\lambda^2})} - \frac{e^{-i\sqrt{k^2-\lambda^2}\, y}}{(\gamma-i\sqrt{k^2-\lambda^2})} \right\} e^{i\lambda x}\, d\lambda$$

$$+ \int_0^{\infty} \frac{s}{(s^2+k^2)} \left\{ \frac{e^{-i\sqrt{s^2+k^2}\, y}}{(\gamma-i\sqrt{s^2+k^2})} - \frac{e^{i\sqrt{s^2+k^2}\, y}}{(\gamma+i\sqrt{s^2+k^2})} \right\} e^{-sx}\, ds \tag{31}$$

$$+ \begin{cases} -\frac{i2\pi}{\gamma} e^{-\gamma y} e^{i\sqrt{k^2+\gamma^2}\, x} & \alpha > 0 \\ 0 & \alpha < 0 \end{cases}$$

By substitution of $\lambda=\sqrt{k^2-t^2}$ and $s=-i\sqrt{k^2-t^2}$, the above two integrals can be combined into one. The final result is

$$f(x,y) = \begin{cases} -e^{ikx} + P - K & \alpha > 0 \\ -e^{ikx} - K & \alpha < 0 \end{cases} \tag{32}$$

where

$$P = 2e^{-\gamma y} e^{i\sqrt{k^2+\gamma^2}\, x} \tag{33}$$

and

$$K = \frac{2\gamma}{\pi} \int_0^{\infty} \frac{(t\ \mathrm{Cos}(ty) - \gamma \mathrm{Sin}(ty))}{t(\gamma^2+t^2)} e^{i\sqrt{k^2-t^2}\, x}\, dt \tag{34}$$

P is called the surface wave, and it both decays with increasing height y, and also decays with the distance x due to the imaginary part of γ.

ASYMPTOTIC EXPANSION VALID FOR SMALL RECEIVER HEIGHTS

1. Soft boundary case

Integral K can be asymptotically evaluated for large x using the saddle-point method. This method is discussed by Morse and Feshbach[5] and will not be discussed here. Actually we can use some of conclusions from Wenzel [6] since we have the same factor $\sqrt{k^2 - t^2}$ as occurred there.

The steepest-descent path has been shown in [6] to be given by

$$T = t + i\,s \tag{35}$$

where

$$s = -\frac{t}{\sqrt{1 + \frac{t^2}{k^2}}} \tag{36}$$

and $t > 0$. Again using the residue theorem, integral K can be transformed into the integral L. Note that $i\gamma$ is not in the region of concern since $\beta \geq 0$. Thus

$$K = \begin{cases} P + L & -i\gamma \in D \\ L & -i\gamma \notin D \end{cases} \tag{37}$$

where D is the region between positive real axis and curve $s = -t\,(1 + t^2/k^2)^{-1/2}$, P is the surface wave given in (33) and

$$L = \frac{2\gamma}{\pi} \int_{SDP} \frac{T\ \mathrm{Cos}(Ty) - \gamma\ \mathrm{Sin}(Ty)}{(\gamma^2 + T^2)\,T}\ e^{i\sqrt{k^2 - T^2}\ x}\ dT \tag{38}$$

Substituting (37) into (32), we have

$$K = \begin{cases} P + L & -i\gamma \in \Gamma \\ L & -i\gamma \notin \Gamma \end{cases} \tag{39}$$

The region Γ in γ plane is bounded by the curve $\beta \geq 0$, $0 \leq \alpha = \beta(1 + \beta^2/k^2)^{-1/2}$. The region Γ is called the surface wave region in the far field (shown in Figure 2), which is same as that of reference [6]. When $\gamma \in \Gamma$, we can easily show $\mathrm{Re}\sqrt{k^2 + \gamma^2} \geq k$,that means, if the surface wave exists,its propagation speed is less than the speed of sound in free space. It is also found that $\mathrm{Im}\sqrt{k^2 + \gamma^2}$ has a close relationship to the quantity $(\alpha\,\beta/k)$ so that a large imaginary part of γ and low frequency of the source can make the surface wave decay very quickly.

Expanding each expression in (38) around the saddle point T=0 and integrating each term, we get

$$L = \frac{1}{\gamma}\sqrt{\frac{2k}{i\pi x}}\, e^{ikx}\left\{(1-\gamma y)+\frac{ik}{\gamma^2 x}\left(1-\gamma y+\frac{\gamma^2 y^2}{2}-\frac{\gamma^3 y^3}{6}\right)+O(x^{-2})\right\} \tag{40}$$

This asymptotic expansion is not uniformly valid. The conditions for its validity are

$$|\gamma|\sqrt{\frac{x}{k}} >> 1 \tag{41}$$

and

$$k\left|\frac{y^2}{2}-\frac{\gamma y^3}{6}\right|\frac{1}{x} << 1 \tag{42}$$

Extremely small $|\gamma|$ will not satisfy conditions (41) and (42), so another asymptotic method has to be developed.

The total solution under the condition of large x can be obtained by substituting (39) into (4) yielding

$$\phi = \begin{cases} P - L & \gamma \in \Gamma \\ -L & \gamma \notin \Gamma \end{cases} \tag{43}$$

where P and L are given in (33) and (40). If we neglect the surface wave, we can get an explicit equation for the wave above ground in the far field as

$$\phi = \frac{1}{|\gamma|}\sqrt{\frac{2k}{\pi x}\left((1-\alpha y)^2+(\beta y)^2\right)}\; e^{i\left(kx+\frac{3\pi}{4}+\theta\right)} \tag{44}$$

where $\theta = -\arctan(\beta y / (1-\alpha y))$. Furthermore, if the receiver is on the ground, the above expression can be written as

$$20 \text{ Log } \phi = 20 \text{ Log } a - 10 \text{ Log } x \tag{45}$$

with $a = (1/|\gamma|)(2k/\pi)^{1/2}$. This result shows that the acoustic pressure level drops 10dB when the distance increases 10 times or 3 dB per doubling of distance.

2. Hard boundary case

As mentioned before, the asymptotic expansion given in (40) is not uniformly valid in γ, with the method failing for small $|\gamma|$. An alternative method is developed in this section which is valid in the small $|\gamma|$ case. The method is almost the same as that used in evaluating L except the factor $1/(\gamma^2 + T^2)$ in (38) will not be expanded. After changing variables (38) becomes

$$L = \frac{\gamma(1-\gamma y)}{\pi i}\sqrt{\frac{2x}{ik}}\, e^{ikx}\int_0^\infty \left(\frac{x\gamma^2}{2ik}-t^2\right)^{-1} e^{-t^2}\, dt \tag{46}$$

Making use of the formula

$$\int_0^\infty (z^2 - t^2)^{-1}\, e^{-t^2}\, dt = \begin{cases} \frac{\pi}{2iz} e^{-z^2}\, \mathrm{erfc}(-iz) & \mathrm{Im}(z) > 0 \\ \frac{\pi}{2iz} e^{-z^2}\, (\mathrm{erfc}(-iz) - 2) & \mathrm{Im}(z) < 0 \end{cases} \tag{47}$$

and neglecting the terms of order γ^2, yields

$$L = \begin{cases} -e^{ikx}\left[1 + \gamma\left(\frac{2}{\sqrt{\pi}}\sqrt{\frac{ix}{2k}} - y\right)\right] & \mathrm{Im}\left(\frac{\gamma}{\sqrt{i}}\right) > 0 \\ -e^{ikx}\left[1 + \gamma\left(\frac{2}{\sqrt{\pi}}\sqrt{\frac{ix}{2k}} - y\right) - 2(1 - \gamma y)\right] & \mathrm{Im}\left(\frac{\gamma}{\sqrt{i}}\right) < 0 \end{cases} \tag{48}$$

The conditions $\mathrm{Im}(\gamma/\sqrt{i}) > 0$ and $\mathrm{Im}(\gamma/\sqrt{i}) < 0$ can be identified as $\alpha < \beta$ and $\alpha > \beta$ respectively. $\alpha = \beta$ is the line which divides these two regions in γ plane. This is exactly the bounding curve $\alpha = \beta(1 + \beta^2/k^2)^{-1/2}$ obtained previously provided that $|\gamma| \to 0$. Recognizing this relation,we substitute (48) into (43) and rewriting surface wave approximately as $P = 2(1 - \gamma y)\, e^{ikx}$, finally get the total field expression as

$$\phi = e^{ikx}\left\{1 + \gamma\left[\frac{2}{\sqrt{\pi}}\sqrt{\frac{ix}{2k}} - y\right]\right\} \tag{49}$$

the condition for the validity of the above expansion is

$$|\gamma|\, y << 1 \tag{50}$$

and

$$|\gamma|\sqrt{\frac{x}{k}} << 1 \tag{51}$$

although x can't be small because of the nature of the saddle point method.

ANOTHER ASYMPTOTIC EXPANSION VALID FOR LARGE RECEIVER HEIGHT

The asymptotic expansions obtained above have their limitations in application. For example, they require the receiver's location to be near the ground. In this section we will derive a asymptotic expansion which is valid for large $R = \sqrt{x^2+y^2}$ (except for small y) . The idea is similar to that of Chien and Soroka [7].

By using the identity $\sin(\lambda x) = (e^{i\lambda x} - e^{-i\lambda x})/2i$ and transformation $\lambda = k \sin(z)$, (15) becomes

$$f(x,y) = \frac{\gamma}{i\pi} \int_C \frac{\mathrm{Tan}(z)}{\gamma + ik\,\mathrm{Cos}(z)}\, e^{ik(y\,\mathrm{Cos}(z) + x\,\mathrm{Sin}(z))}\, dz \tag{52}$$

The contour C is shown in Figure 3. In order to get an expansion in terms of the variable $R = \sqrt{x^2+y^2}$, we transform the Cartesian coordinate system into the polar coordinate system by

$$x = R \operatorname{Sin} \theta \tag{53}$$

and

$$y = R \operatorname{Cos} \theta \tag{54}$$

Substituting into (52), yields

$$f(x,y) = \frac{\gamma}{i\pi} \int_C \frac{\operatorname{Tan}(z)}{\gamma + i \operatorname{Cos}(z)} e^{i k R \operatorname{Cos}(z-\theta)} dz \tag{55}$$

the saddle point for the function i k R Cos(z-θ) is at z = θ and the path of steepest descent is found to be given by

$$\operatorname{Cos}(u-\theta) \operatorname{Cosh}(v) = 1 \tag{56}$$

where z = u + i v, by considering Im (i k R Cos (z - θ))=Im (i k R). This path, denoted as C' is shown in Figure (3). Deforming contour C into C', adding the possible poles (Cos z = i γ / k), we have

$$f(x,y) = Q + H\left(-\operatorname{Re}\left(1 - \frac{i\gamma}{k} \operatorname{Cos}\theta - \sqrt{1 + \frac{\gamma^2}{k^2}} \operatorname{Sin}\theta\right)\right) P \tag{57}$$

where Q is defined by (54) but with the contour C changed to C', H is Heavyside step function and P is the surface wave given in (33). The condition for the existence of pole is explained in reference [7], and will not be repeated here. In the limit of θ approaching π/2 the condition for the existence of the pole in the present case is equivalent to the condition for the existence of the pole in (39).

Q can be evaluated asymptotically with a method similar to that used in evaluating L, i.e. to expand each term around the saddle point θ and then integrate them with suitable transformation of the variable . The result is

$$Q = \sqrt{\frac{2}{i\pi k R}} \frac{\gamma \operatorname{Tan}\theta}{i(\gamma + i \operatorname{Cos}\theta)} e^{ikR} \left\{1 + \frac{1}{ikR}\left[1 + \frac{ik \operatorname{Cos}\theta}{2(\gamma + ik \operatorname{Cos}\theta)} + \frac{ik}{(\gamma + ik \operatorname{Cos}\theta)\operatorname{Cos}\theta}\right]\right\} \tag{58}$$

The conditions for the validity of the above expansion are

$$kR >> 1 \tag{59}$$

and

$$\frac{\frac{\operatorname{Cos}^2\theta}{2} + 1}{|\gamma + i \operatorname{Cos}\theta| R \operatorname{Cos}\theta} << 1 \tag{60}$$

It is clear that θ cannot be too close to $\pi/2$. This limitation is complimentary to the asymptotic expansions obtained previously (for small y). Substituting into (4) yields

$$\phi = e^{ikx} + Q + H\left(-\mathrm{Re}\left(1 - \frac{i\gamma}{k}\cos\theta - \sqrt{1 + \frac{\gamma^2}{k^2}}\sin\theta\right)\right)P \qquad (61)$$

In the limit $R\to\infty$, Q and P will vanish , with the result that only the plane wave term remains.

Equation (38) can be evaluated accurately by numerical methods as well as by asymptotic expansions. Calculations show that the results match quite well when y is small. Figure 4 gives the amplitude of acoustic pressure on the ground versus the distance to the receiver obtained by numerical integration and from (44). Figures 5a, b and c show the amplitude of acoustic pressure versus the receiver height for several receiver locations as obtained from the asymptotic expansions, (40) and (61). These figures are similar to the results obtained by McAninch [4].

CONCLUSIONS

The acoustic field of a plane wave at grazing incident to a finite impedance has been theoretically investigated. Exact numerical and asymptotic expansions are developed, which are very similar to those found by Wenzel [6] for a point source and by McAninch [4] using the parabolic approximation to the wave equation. When y is small, the incident wave is indeed canceled, but the result is not zero due to the existence of a surface wave and the wave denoted as L. Near the ground, the acoustic pressure decays as $x^{-1/2}$ (assuming the surface wave is neglected). The asymptotic expansion for large distance R shows that the acoustic pressure decays as $R^{-1/2}$ when $R\to\infty$ and when the receiver is not close to the surface only incident wave exists.

REFERENCES

[1] Dowling, A. P., and J. E. Ffowes Williams, *Sound and Sources of Sound,* (Ellis Horwood Ltd., Chichester, 1983), p. 83.

[2] Morse, P. M., *Vibration and Sound,* (American Institute of Physics, Woodbury, N.Y., 1983), pp. 366-368.

[3] Rudnick, I., "The Propagation of an Acoustic Wave along a Boundary." J. Acoust. Soc. Am., **19**, 348-356, (1947).

[4] McAninch, G. L., "Propagation of Quasiplane Waves Along an Impedance Boundary." AIAA 26th Aerospace Sciences Meeting Paper 88-0179 (1974).

[5] Morse,P. M and H. Feshbach, *Methods of Theoretical Physics*, (McGraw-Hill,New York, 1953), p. 441.

[6] Wenzel, A. R., "Propagation of Waves along an Impedance Boundary." J. Acoust. Soc. Am., **55**, 956-963 (1974).

[7] Chien,C.F. and W.W. Soroka, "Sound Propagation Along an Impedance Plane." J. Sound and Vibration, **43** ,(1), 9-20, (1975).

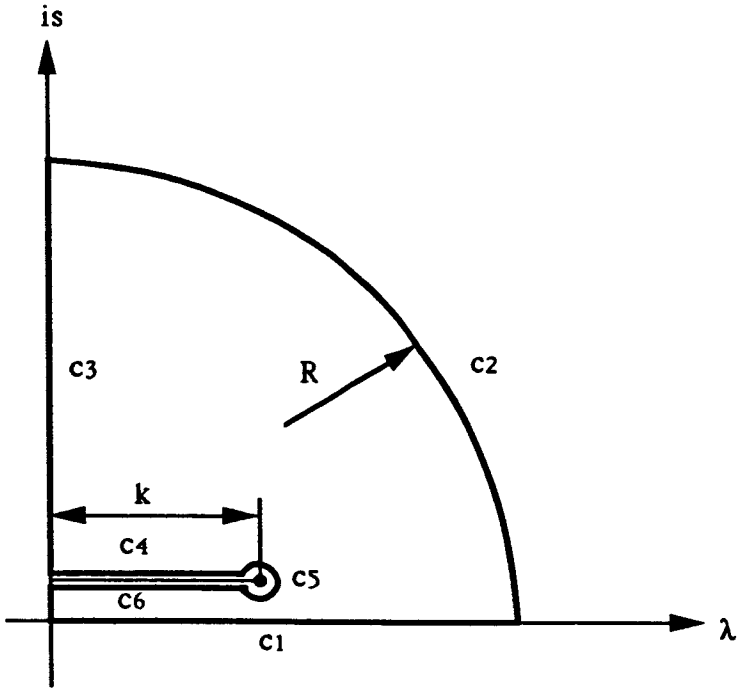

Figure 1. Integration path for the integral I_1 in the complex Λ plane.

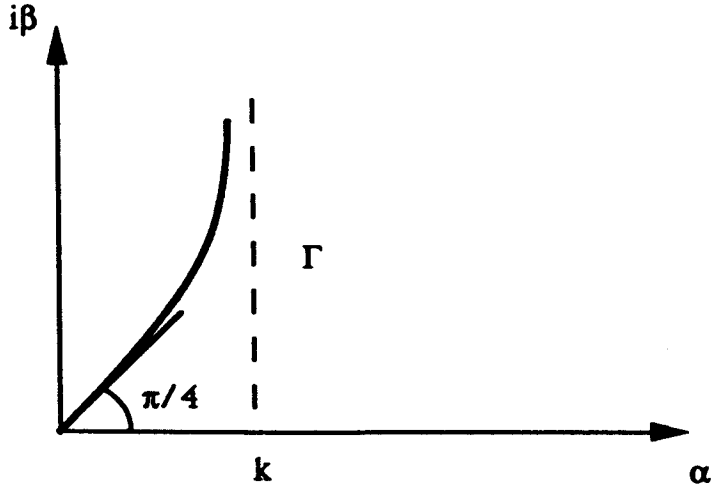

Figure 2. The region Γ in the γ plane.

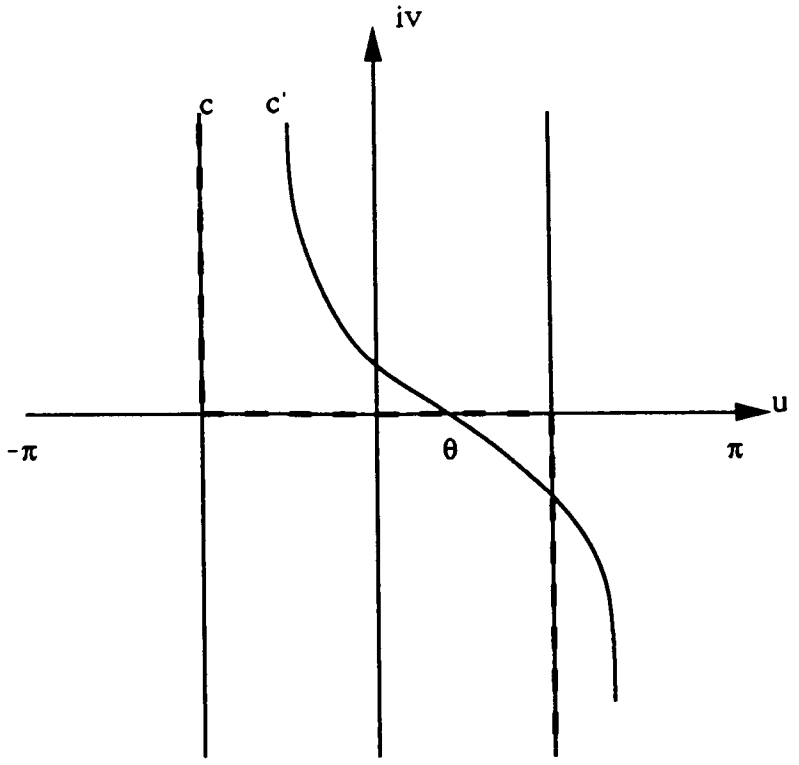

Figure 3. The u-v plane, showing the integration contour C and the steepest descent path C'.

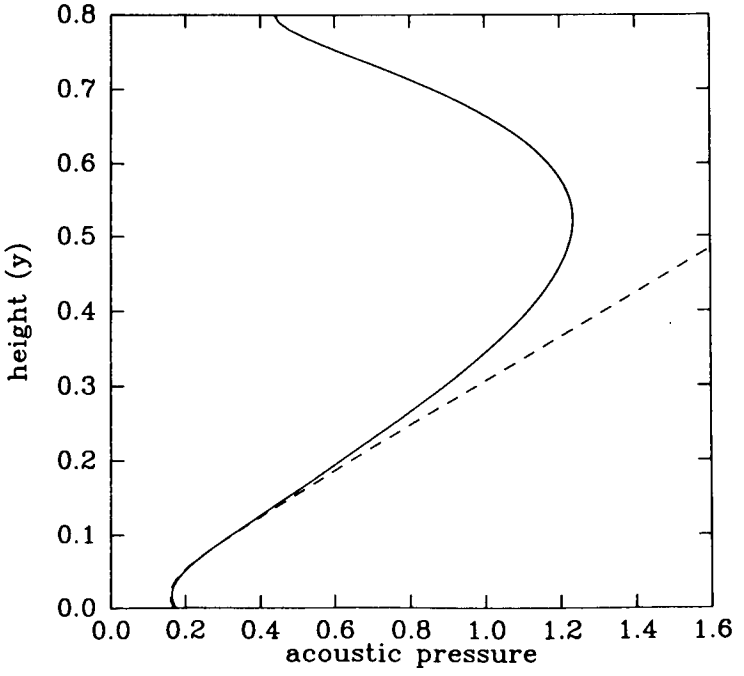

Figure 4. Comparison between a numerical result and the asymptotic result, (44), for the parameters, $k = 18.313$ and $\gamma = 6.935 + i\ 19.015$.

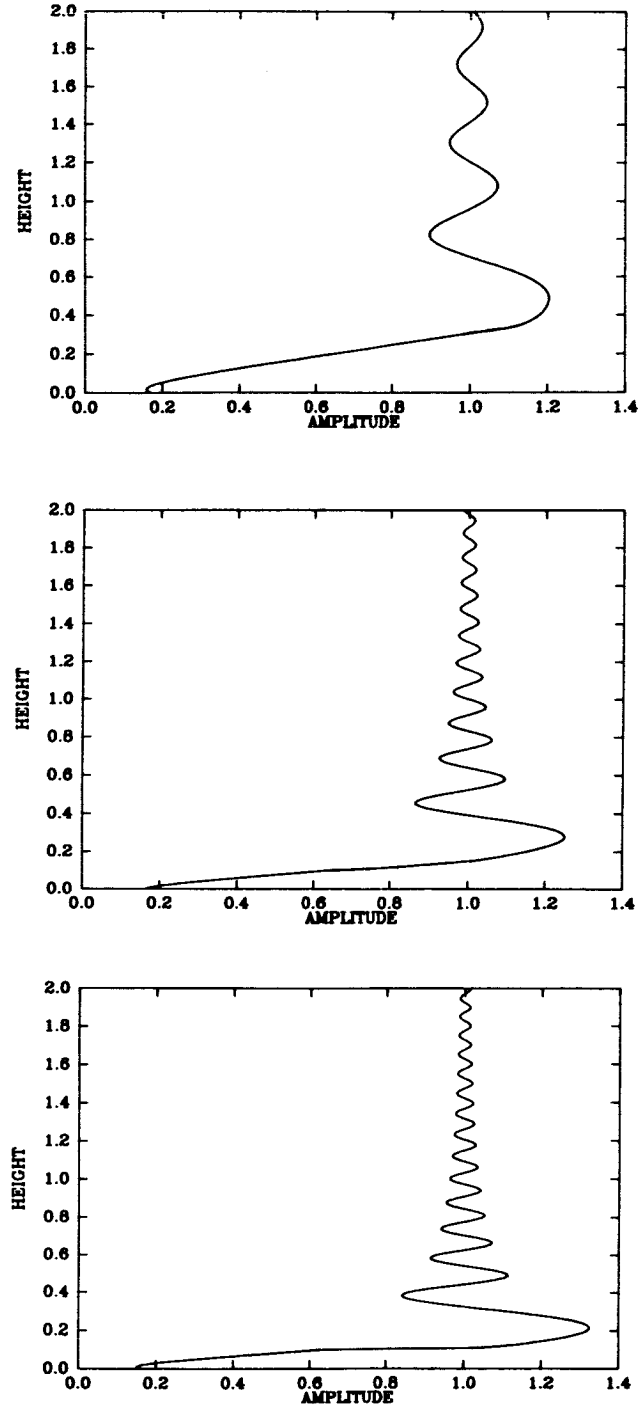

Figure 5. Amplitude of the acoustic pressure versus the receiver height for different parameters:
(a) f = 1000 Hz; γ = 6.935 + i 19.015.
(b) f = 2000 Hz; γ = -5.031 + i 35.932.
(c) f = 4000 Hz; γ = 18.038 + i 37.002.

AIR-GROUND INTERFACE: SURFACE WAVES, SURFACE IMPEDANCE AND ACOUSTIC-TO-SEISMIC COUPLING COEFFICIENT

Gilles Daigle and Tony Embleton
Division of Physics
National Research Council
Ottawa CANADA K1A 0R6

ABSTRACT

In atmospheric acoustics, the subject of surface waves has been an area of discussion for many years. The existence of an acoustic surface wave is now well established theoretically. The mathematical solution for spherical wave propagation above an impedance boundary includes the possibility of a contribution that possesses all the standard properties for a surface wave. Surface waves exist when the surface is sufficiently porous, relative to its acoustical resistance, that it can influence the airborne particle velocity near the surface and reduce the phase velocity of sound waves in air at the surface. This traps some of the sound energy in the air to remain near the surface as it propagates. Above porous grounds, the existence of surface waves has eluded direct experimental confirmation (pulse experiments have failed to show a separate arrival expected from the reduced phase speed) and indirect evidence for its existence has appeared contradictory. In PART I of this paper the experimental evidence for the existence of an acoustical surface wave above porous boundaries is reviewed. Recent measurements including pulse experiments will also be described.

A few years ago the acoustic impedance of a grass-covered surface was measured in the frequency range 30 to 300 Hz. In PART II of this paper further measurements on the same site are discussed. These measurements include core samples, a shallow refractive survey to determine the seismic velocities, and measurements of the acoustic-to-seismic coupling coefficient.

PART I

INTRODUCTION

In atmospheric acoustics, the subject of surface waves above porous grounds has been an area of discussion for many years. The existence of an acoustic surface wave is now well established theoretically. The mathematical solution for spherical wave propagation above an impedance boundary includes the possibility of a contribution that possesses all the standard properties for a surface wave. These include cylindrical spreading in the horizontal direction, exponential decay in amplitude with height above the ground, and a reduced phase speed.

However, above natural porous ground surfaces, the existence of an acoustic surface wave has eluded direct experimental confirmation. Pulse experiments have failed to show a separate arrival from the direct pulse as expected from the reduced phase speed. Further, indirect evidence for its existence has appeared contradictory.

The experimental evidence for surface waves has been mostly restricted to careful indoor measurements, using sources of continuous sound and model surfaces composed of a thin layer of porous material or comblike structures. The reduced phase speed and cylindrical spreading of the surface wave are expected to produce a total sound pressure level in excess of that which would be measured over an acoustically hard boundary.

In this paper the experimental evidence for the existence of an acoustical surface wave above porous boundaries is reviewed. In addition, some recent measurements including pulse experiments will also be discussed.

FIGURE 1

At this point it is useful to distinguish between body waves and boundary waves. Acoustic waves propagating through the body of the fluid are referred to as body waves. The effect of boundaries upon these waves is secondary in that the existence of the waves is in no way tied to the presence of the boundaries. The role of boundaries is strictly extrinsic. On the other hand, boundary waves depend upon the existence of boundaries to support them and the role of the boundaries here is intrinsic.

In atmospheric acoustics, the field from a point source above a porous ground is commonly described in terms of direct, reflected, ground, and surface waves. Obviously ground and surface waves are closely related but their fundamental origins differ, as does their behavior during propagation. Ground waves exist because curved wave fronts strike different parts of the ground at different angles of incidence and because the reflection coefficient of finite-impedance ground is also a function of angle of incidence. Ground waves exist unless the ground is infinitely hard or infinitely soft or unless the incident wave fronts are plane, that is, the source can be considered infinitely far away. Ground waves can exist in the absence of surface waves.

Surface waves exist when the ground surface is sufficiently porous, relative to its acoustical resistance, that it can influence the airborne particle velocity near the surface and reduce the phase velocity of sound waves in air at the surface. In its simplest terms, the condition for its existence is when the imaginary component of the surface impedance is a spring-like reactance and is greater than the resistive component. This traps some of the sound energy in the air, regardless of the shape of the incident sound field, to remain near the surface as it propagates from the source to the receiver. Surface waves can exist in the absence of ground waves. The existence of a surface wave in the absence of wavefront curvature has been shown theoretically by McAninch and Myers (AIAA 1988). They demonstrate the presence of a surface wave in the solution for plane waves at grazing incidence to a finite impedance boundary. Further, Raspet and Baird (JASA 1989) have demonstrated that the surface wave can exist independent of the acoustic body wave in the half-space above the surface by examining the limit as the upper half-space becomes incompressible.

The equation on the top part of this figure represents a particular representation for the total field above an impedance plane. The field is broken up into a direct wave, a perfect reflected wave, a diffracted wave that accounts for the phase change on reflection and the effects of the spherical wave fronts, and a surface wave. The surface wave exists if $Im(Z) > Re(Z)$ and is zero otherwise. The surface wave is characterized by cylindrical spreading in the horizontal plane, exponential decay with increasing height above the ground, and a reduced phased speed $v < c$.

Theory which predicts the acoustical characteristics of rigid porous materials in terms of their microstructure indicates that the resistive and reactive components of the surface

impedance are equal in the case of a homogeneous porous ground (Attenborough, JSV 1985). Therefore, no surface wave can exist above such grounds. On the other hand, if the microstructural properties of the ground vary with depth (such as a varying porosity), the reactive component of the impedance exceeds the resistive component and the surface wave can exist.

A specific example of a surface whose reactive component of impedance exceeds the resistive component is a thin porous layer above an acoustically hard backing. We note that in the case of a ground where the porosity varies with depth at a rate α, the impedance is equivalent to the impedance of a porous layer with an effective thickness equal to $2/\alpha$ (Donato, JASA 1977).

FIGURE 2

The consequence and origin of the reduced phase speed of the surface wave are illustrated in this figure. Far from the ground, there is horizontal particle motion associated with the propagating body wave, as shown in A. Due to the alternating compression and rarefaction cycles, the air molecules at the ground are entrained in vertical particle motion as shown in C. Just above the surface of the ground in the fluid, the resulting particle motion is therefore elliptical, as shown in B.

The elliptical particle motion results in a reduced phase speed and the resulting lag causes the wavefronts to be "bent" towards the ground, giving rise to enhanced sound energy close to the surface. The increased sound energy associated with the surface wave close to the ground is at the expense of less sound energy at heights above the surface wave thickness. This will be illustrated in some of the following figures.

FIGURE 3

This figure shows experimental evidence measured outdoors over natural ground surfaces. The points in (a) are measurements obtained by Rasmussen above grass covered ground. The sound pressure levels in this figure, and all of the following figures, are plotted relative to free field. Hence, these results suggest sound pressure levels in excess of the +6 dB expected at lower frequencies. The solid curve is the best prediction that can be achieved by assuming the ground to be a semi-infinite half plane. Rasmussen calculated the dashed curve by assuming a porous layer 0.01 m thick. Equivalently, the same result can be obtained by assuming a ground with its porosity varying with dept at a rate given by $\alpha = 2/0.01 = 200\ m^{-1}$. This is a more likely physical model for natural ground surfaces (Donato, JASA 1977).

We note that the behavior of Rasmussen's measurements is consistent with the behavior of the classic measurements of Parkin and Scholes (JSV 1965) of the propagation of jet engine noise above grass covered airport ground.

In (b), the points were measured above a well defined layer (8 cm) of snow above frozen ground. The dashed curve was calculated by assuming a layer of snow infinitely thick. The solid curve accounts for the layer. Although the measurements show the enhanced dip that is predicted around 300 Hz (Chien and Soroka, JSV 1975), the behavior of the measurements at the lower frequencies indicate that the surface wave is absent. These results have contributed to the controversy concerning the existence of surface waves above natural ground surfaces. It has been suggested (Attenborough, JSV 1988) that the situation is complicated by the existence of seismic quarter-wavelength resonances in the low frequency range as a result of the elasticity of the porous surface layer.

FIGURE 4

The short dashed curve on this slide is the sound pressure levels predicted for propagation at grazing incidence above an infinitely thick surface of porous felt. The propagation distance is 2 m. There is no surface wave and this curve represents the ground wave. The open squares are measurements obtained above a thick layer of felt.

The upper two curves are calculated from different versions of the same theory in the case of a layer of felt of thickness 0.003 m. In this case the surface wave Φ_S exists. The difference between the two curves is attributed to numerical precision and is not significant for the discussion here.

The solid points are measurements made by Thomasson above a layer of felt. The open circles are our own measurements and confirm the results of Thomasson. Both theory and experiment clearly indicate sound pressure levels in excess of the +6 dB expected from inverse square law above a perfectly rigid ground.

FIGURE 5

The open points are measurements made as a function of height above the same layer of felt and shown for two frequencies. The solid points were obtained by Thomasson for the same two frequencies. The solid and broken curves are the predictions calculated from two versions of the same theory. The broken curves are the predictions in the case of an infinitely thick layer.

The dotted lines drawn at +6 dB show the levels expected in the case of a perfectly rigid ground. Both theory and measurements show the existence of the enhanced sound levels at heights below 10 cm resulting from the existence of the surface wave. In addition, the slightly reduced levels above about 10 cm, especially at 2 kHz, is observed.

FIGURE 6

In this figure, the porous layer is replaced by a comblike surface consisting of overhead lighting panels (Donato, JASA 1978). The panels are molded plastic: there is a square array of solid ribs at 1.13 cm spacing; the sheet is 2.26 cm thick, open on top and bottom surfaces. The sheet is laid on a hard floor.

Results of measurements are shown for two frequencies and two distances of propagation. The solid points clearly show significantly enhanced sound levels close to the surface, especially at 800 Hz, and the expected reduced level at higher heights.

The open points are the results above a rigid surface and the solid lines are drawn at +6 dB.

FIGURE 7

These results are similar to the ones on the previous slide but the first four meters of the propagation path are acoustically rigid while the remainder consist of the comblike surface.

The solid points to the left are measurements made above the rigid surface. The open points on the right were measured 5 m from the source, hence after 1 m of propagation above the ceiling panels.

The behavior of the results at 5 m suggest that a surface wave has developed over the

1 m of panel. We note that the panels are located about 12 wavelengths from the source. Therefore the surface wavelike behavior is exhibited when the curvature of the wavelength is significantly reduced. This is consistent with the theory of McAninch and Myers.

FIGURE 8

The solid points on the top part of this figure are the results measured at grazing incidence above the comblike surface as a function of frequency for a distance of 1 m. The behavior of these results is identical to those measured above the layer of felt.

The solid curve on the bottom part of the figure shows the predicted surface wave velocity, v (Brekhovskikh, Sov. Phys. Acoust. 1959). The straight line at about 340 m/s indicates the speed of the body wave in air. Beyond about 1.5 kHz there is a sufficient difference between the surface wave velocity v and the body wave velocity c, that it should be possible to observe the surface as a separate arrival using a short pulse of sound propagating over a distance of a few meters.

FIGURE 9

The traces shown here are of a 2.1 kHz tone burst measured after propagation above the comblike surface at various distances up to 1.5 m. The arrow immediately below the last three traces indicates the arrival of the surface wave relative to the body wave predicted from the solid curve on the previous slide.

The observed behavior of the measured pulses as a function of distance is not inconsistent with expectations. In the absence of a surface wave all the traces would have the appearance of the top trace.

FIGURE 10

This figure shows the traces at different receiver heights for three distances of propagation (the source is on the ground). At a distance of 0.1 m, the surface wave has not yet had time to develop and the trace does not change with height.

At the other two distances, the exponential decay of the second arrival as a function of height is clearly illustrated and is indicative of a surface wave.

PART II

INTRODUCTION

A few years ago the acoustic impedance of a grass-covered surface was measured (Daigle and Stinson, JASA 1987) in the frequency range 30 to 300 Hz by measuring the pressure, phase and phase-gradient in the sound field along a vertical line directly below a loudspeaker suspended some 7 m above the surface. Recent core samples showed that this ground consisted of a layer of silt of uniform texture and almost constant thickness (1.6 +/- 0.3 m) over bedrock -- a ground structure of ideal simplicity for acoustical study. Seismic velocity measurements were consistent with this simple structure, and indicated a layer thickness (1.9 +/- 0.3 m) reasonably in agreement with the core sample.

The calculated quarter-wavelength-layer-thickness frequency is then about 45 Hz. Direct measurement of the acoustic-to-seismic coupling coefficient at normal incidence shows

maxima in the admittance of the surface at about 50 and 135 Hz. (Several other maxima exist at apparently unrelated frequencies.) At oblique angles of incidence the admittance spectrum is of similar shape but shifts upwards in frequency by about 10%.

A number of minima in the admittance spectrum are also present and should correspond with maxima in the acoustic reflection coefficient; however, the correspondence was found to be poor. Probable explanations of the discrepancies could be that the ground exhibits in reality a more complex structure than our current understanding allows or that different measurements were over slightly different areas of the ground and detected different thicknesses of the supposedly constant thickness silt layer.

FIGURE 11

This figure illustrates the original measurements. A pure tone is radiated spherically from a loudspeaker suspended resiliently from a support. Wavefronts are reflected at the ground surface and interfere with the incoming waves to produce an interference field. Two closely spaced microphones were moved together along a track that was perpendicular to the surface and directly below the source. By comparing the signals from the two microphones with each other and with the electrical signal to the source, one can determine the amplitude, phase and phase gradient of the field along the line of measurement. The locations where one of these three parameters becomes inaccurate are usually those where the other two parameters can be measured with enhanced precision. In this way the magnitude and phase of the reflection coefficient can be obtained reasonably accurately down to 30 Hz.

FIGURE 12

This figure shows the results. Although the individual points show some scatter there are definite trends and several peaks, or resonances are clearly evident. For example there is some confidence in the peaks at around 95, 130 and 200 Hz. These seismic resonances are consistent with the theoretical work and measurements of Sabatier, Bass and others at the University of Mississippi.

In 1989 a seismic survey team drilled one or two core samples on our exact site. It was discovered that our site was almost ideal from an acoustical point of view. Apart from the top few centimeters of grass and its roots, the ground was a layer of silt of uniform consistency and almost constant thickness (1.6 +/- 0.3 m) lying directly over bedrock.

FIGURE 13

Time-of-flight measurements along the surface are shown in this figure. These were made by hitting a heavy metal disk lying on the ground with a hammer, and receiving the signal with a geophone. The sound speed in the silt layer is calculated to be 330 m/s (almost the same as the speed in air) and in the rock about 2000 m/s. From the break-point on this curve the thickness of the layer is calculated as 1.9 +/- 0.3 m. The $v = 330$ m/s part of this plot does not pass through the origin but intersects the ordinate at about $t = 3.8$ ms. This time delay is related to the slow sound speed through the top few centimeters of soil and grass-roots, but we were not able to measure the break-point due to the soil-silt interface. The calculated quarter-wavelength-layer-thickness resonance for the silt layer is about 45 Hz.

FIGURE 14

The acoustic-to-seismic transfer function was measured using a Mark Products L-21A

geophone pushed into the ground surface and a collocated microphone 10 cm above the surface. The two signals were analyzed and compared using a Bruel and Kjaer Model 2032 Dual Channel Signal Analyzer. The acoustic-to-seismic transfer function was found for various angles of incidence ranging from normal to about 87^{o}. Those for normal incidence and for 84^{o} are shown in Figure 14. Measurements at oblique incidence show a) larger surface admittance, b) smoother curves, and c) an upward shift in frequency by about 10%, compared with the admittance spectrum for normal incidence.

Quarter-wavelength resonances in the silt layer should lead to maxima in the acoustic-to-seismic admittance spectrum at roughly 45, 135 and 225 Hz, and minima at 90 and 180 Hz. The only apparent agreement seems to be maxima at about 50 and 135 Hz and a minimum at about 85 Hz. Although the results could suggest a peak around 225 Hz and a dip at a frequency slightly greater than 180, the measurements are inconclusive. The peaks at about 70, 105 and 180 Hz appear to be completely unrelated to the silt layer. Some of this structure could be due to the thin layer of topsoil and grass roots.

Maxima in the acoustic reflection coefficient of the surface, Figure 12, should be related to the minima of the surface admittance spectrum, Figure 14. The match between these two spectra is far from satisfactory. However, the peaks of the reflection coefficient at about 95 and 195 Hz are not inconsistent with the dips in the admittance spectrum at roughly the same frequencies and are predictable, within experimental, from the thickness of the layer found from the core sample or the refractive survey. The peak at about 135 Hz in the reflection coefficient is unrelated, but the admittance spectrum does suggest a dip at about this frequency.

Clearly, although our current understanding allows us to explain many aspects of these measurements, there are other features of this rather simple ground structure that require additional elucidation. Certainly more work is required before we can accurately predict the acoustical behavior of more realistic and complex ground structures.

ACKNOWLEDGEMENT

The refractive survey and measurements of the acoustic-to-seismic transfer function were carried out by C. Verhaegen (Katholieke Universiteit Leuven, Belgium) during a one month stay as a guest scientist in our laboratory at the National Research Council. We would also like to acknowledge the technical assistance provided by R. St-Denis.

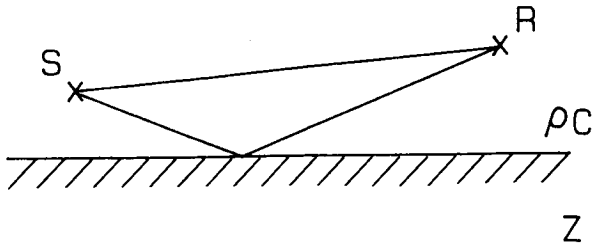

Total field

① $$\Phi = \Phi_D + \Phi_R + \Phi_d + \Phi_s$$

$$\Phi_s = \begin{cases} \text{Surface wave} & \text{if } Im(Z) > Re(Z) \\ 0 & \text{otherwise} \end{cases}$$

$$\Phi_s \propto \frac{1}{\sqrt{r}} e^{-\alpha h + i\beta r}$$

Surface wave velocity

Fig. 1

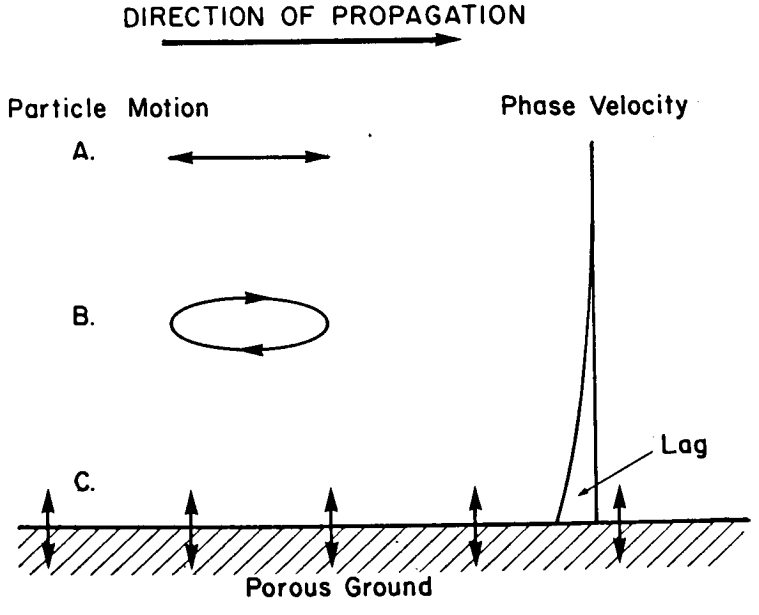

ORIGIN OF THE SURFACE WAVE

Fig. 2

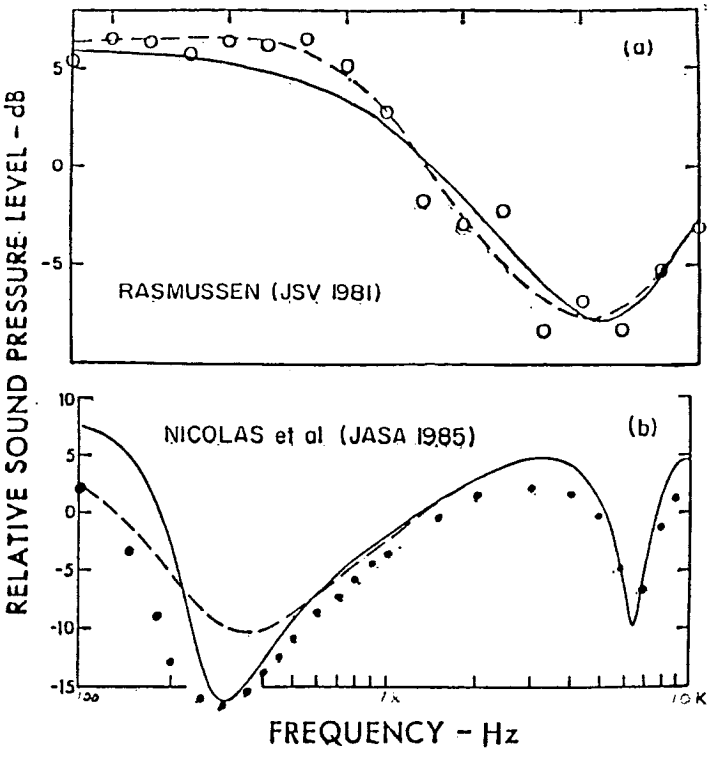
(a)
RASMUSSEN (JSV 1981)
NICOLAS et al (JASA 1985)
(b)
RELATIVE SOUND PRESSURE LEVEL - dB
FREQUENCY - Hz

Fig. 3

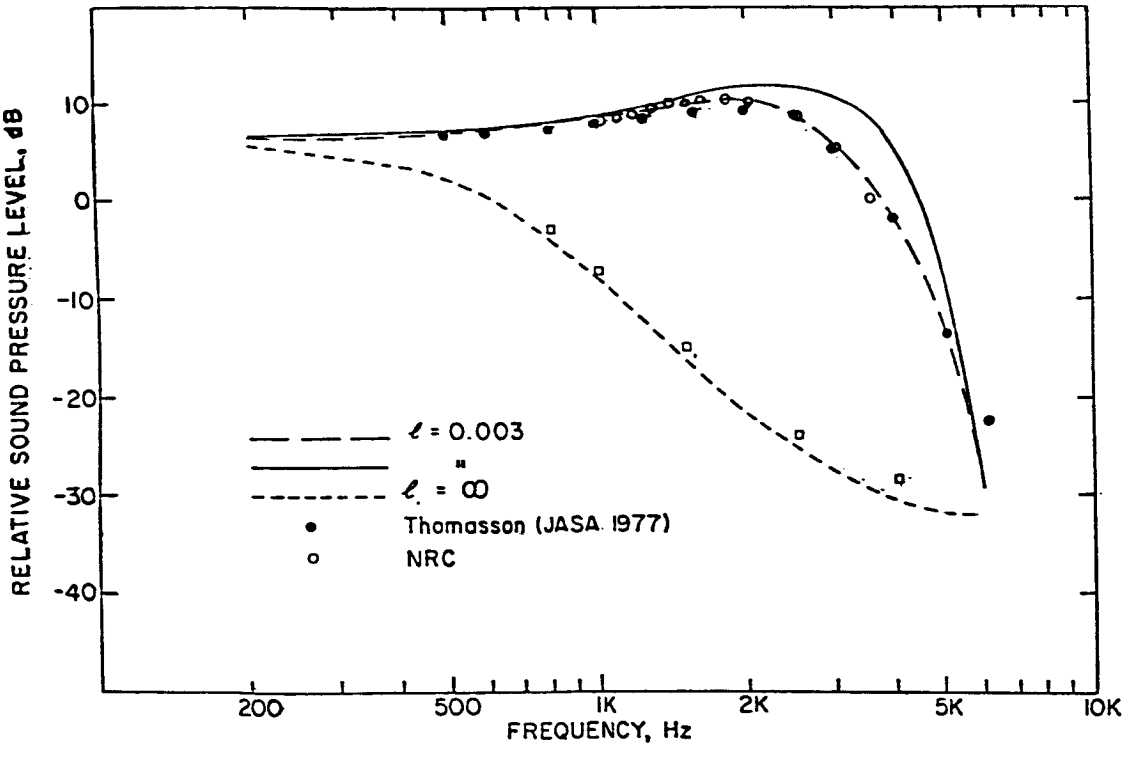
RELATIVE SOUND PRESSURE LEVEL, dB
FREQUENCY, Hz
ℓ = 0.003
ℓ = ∞
Thomasson (JASA 1977)
NRC

Fig. 4

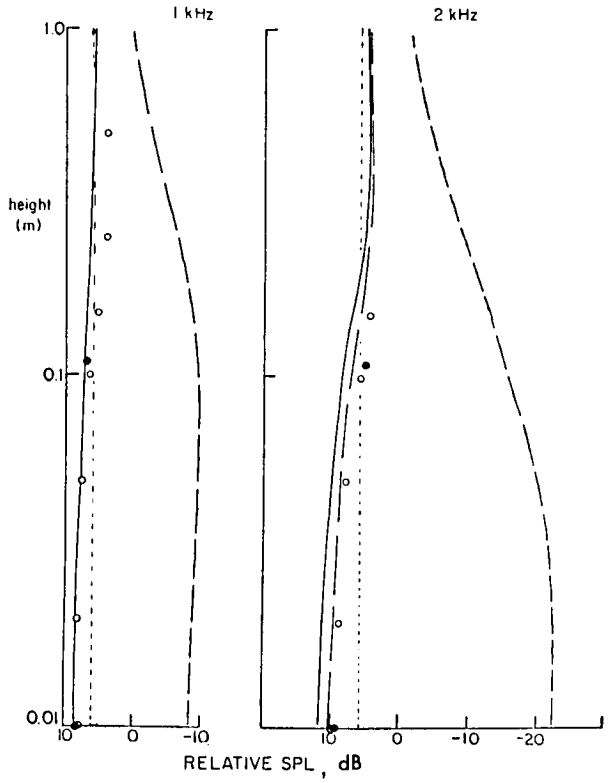

Fig. 5

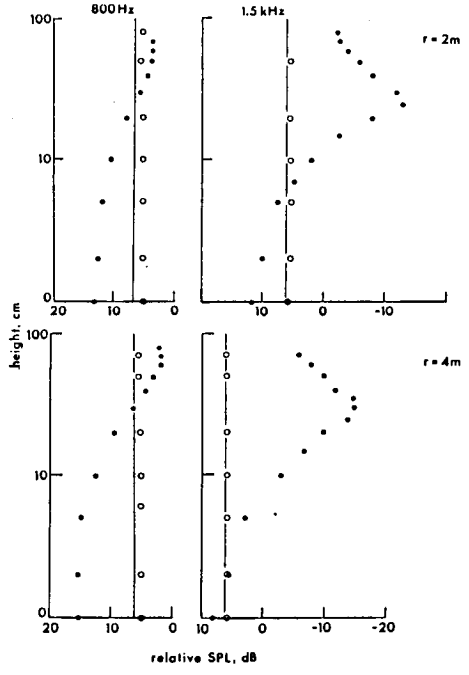

Fig. 6

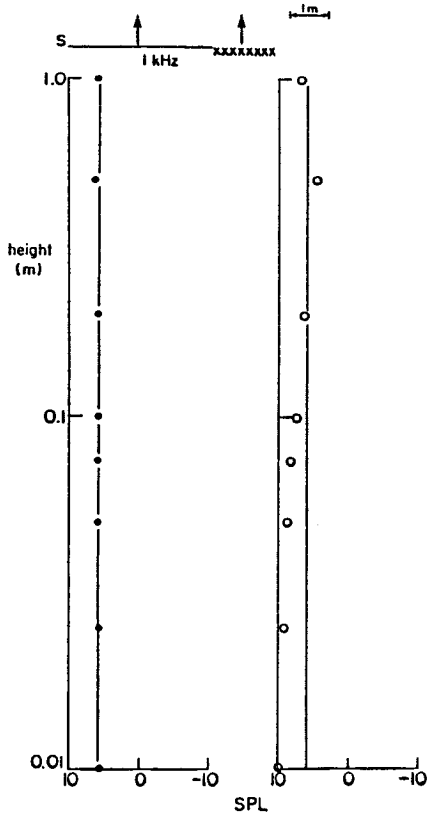

Fig. 7

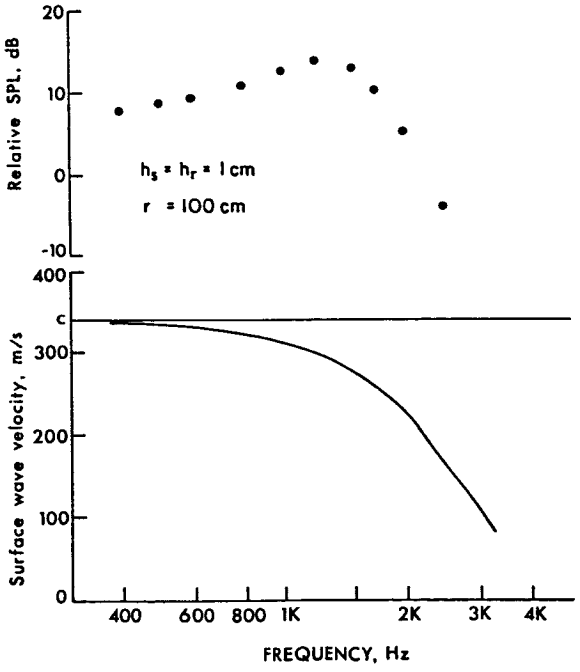

Fig. 8

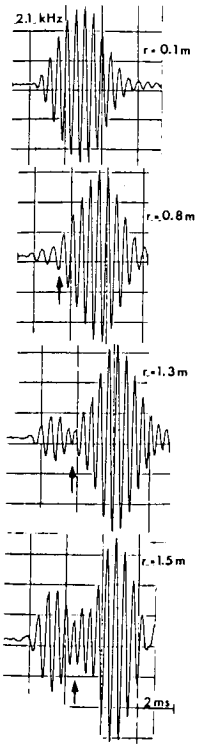

Fig. 9

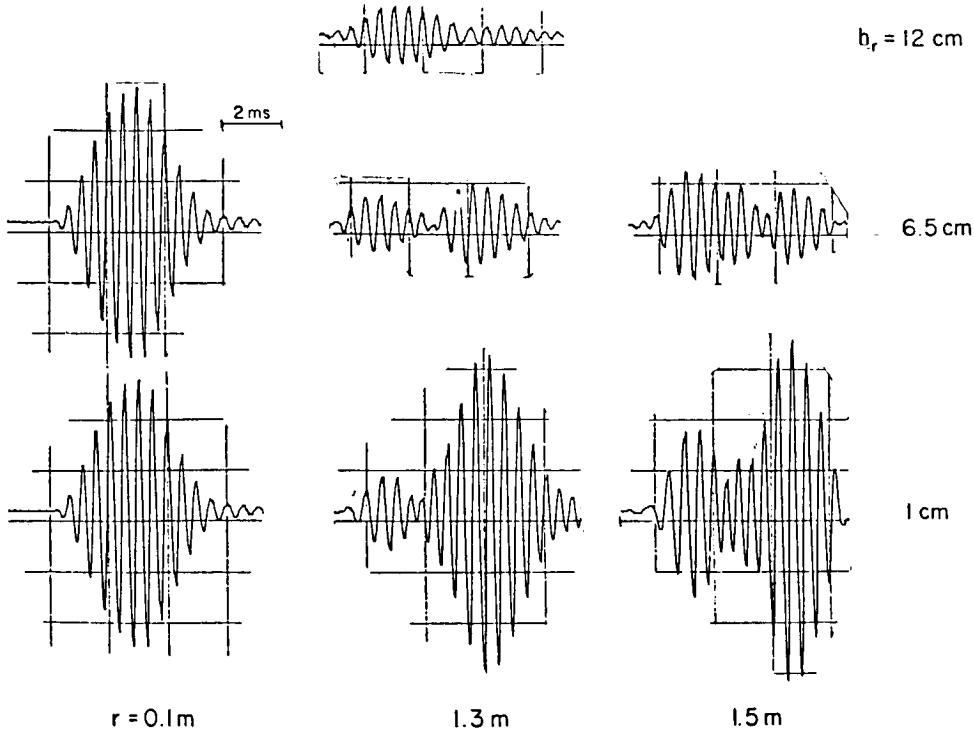

Fig. 10

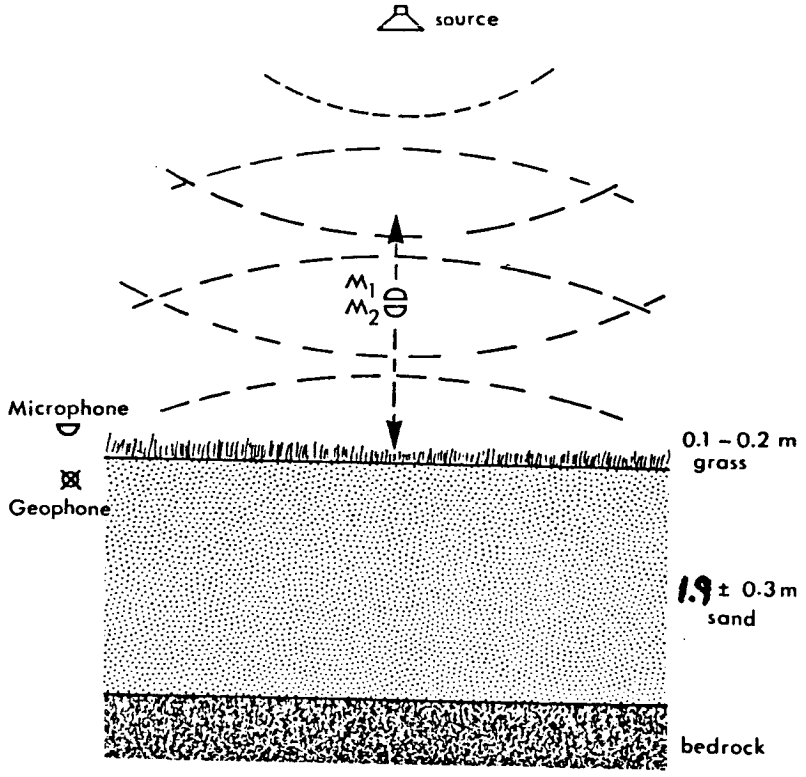

Fig. 11

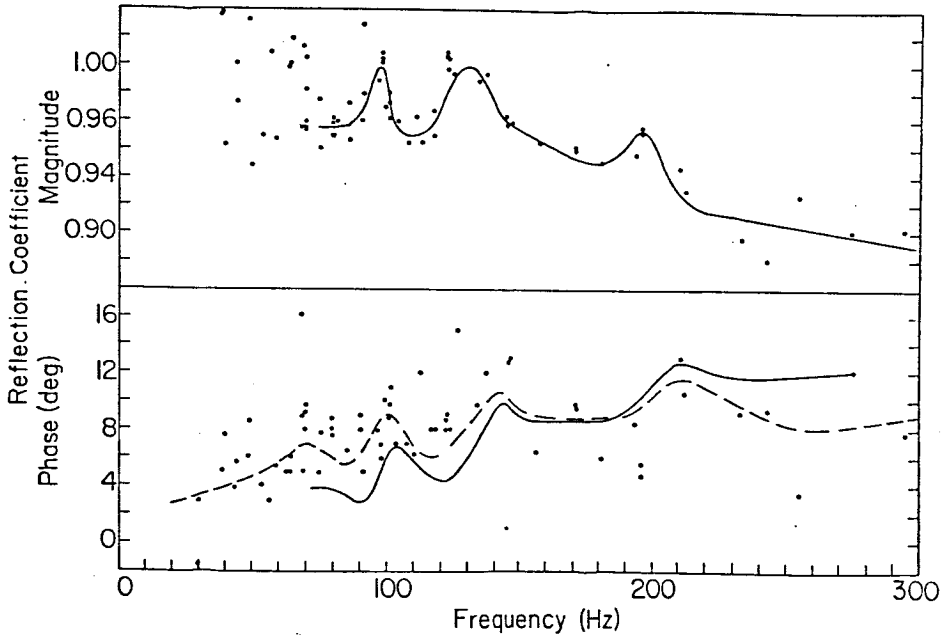

DAIGLE & STINSON(JASA 1987)

Fig. 12

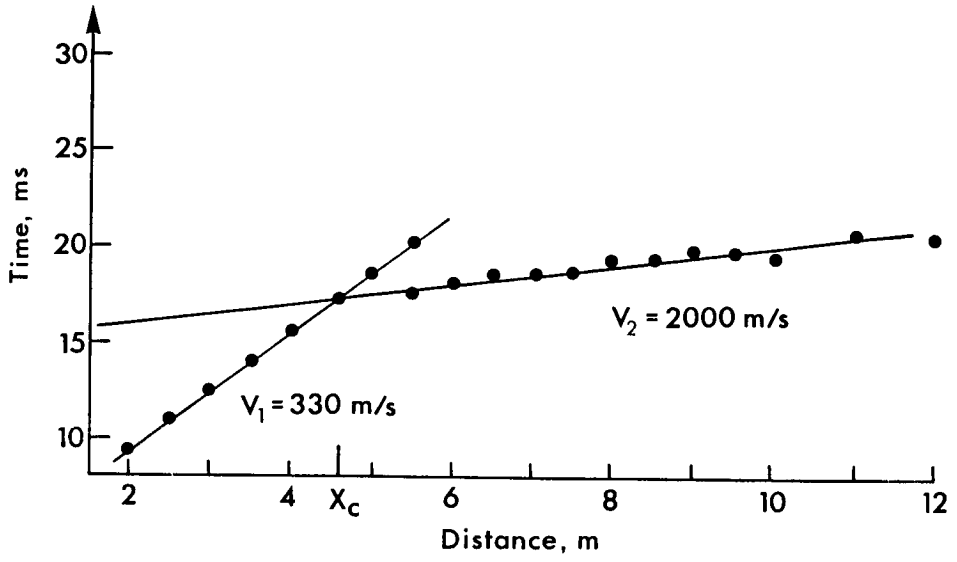
30
25
20
15
10
Time, ms
V_2 = 2000 m/s
V_1 = 330 m/s
2
4
X_c
6
8
10
12
Distance, m

Fig. 13

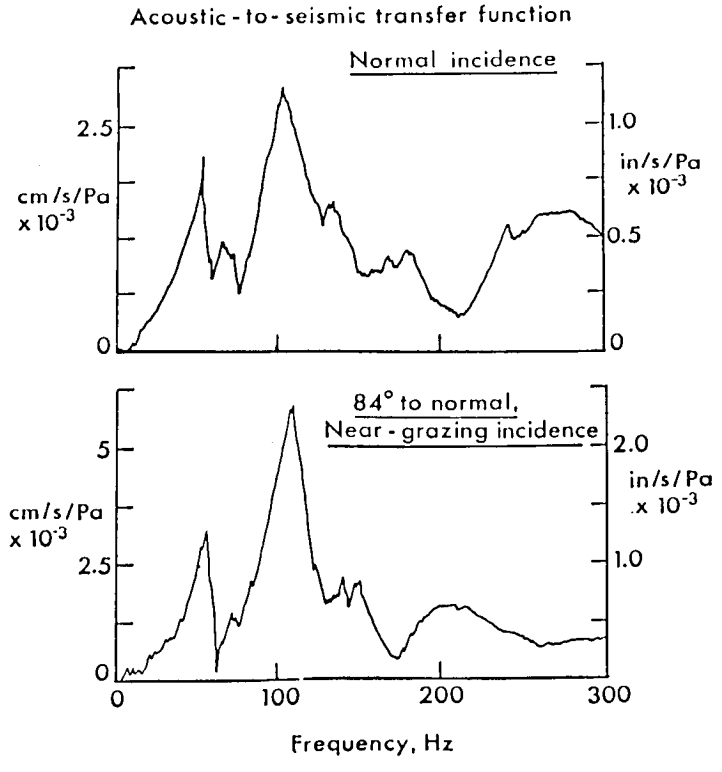
Acoustic - to - seismic transfer function
Normal incidence
2.5
0
cm/s/Pa
x 10^{-3}
1.0
0.5
0
in/s/Pa
x 10^{-3}
84° to normal,
Near - grazing incidence
5
2.5
0
cm/s/Pa
x 10^{-3}
2.0
1.0
in/s/Pa
x 10^{-3}
0
100
200
300
Frequency, Hz

Fig. 14

EXPONENTIAL GROUND IMPEDANCE MODELS AND THEIR INTERPRETATION

Richard Raspet and Mark Sprague

Department of Physics and Astronomy, University of Mississippi, University, MS 38677

SUMMARY

In this paper we compare the results of Donato's exponentially varying ground model, Attenborough's exponentially varying ground model and the rigid backed thin layer model. We show that these models produce similar results for slow variations. For rapid variations the results are quite different but the basic theory used is only correct for the thin layer model. These results suggest that the exponentially varying models are not necessary for fitting ground impedance data.

INTRODUCTION

Donato proposed an exponentially varying ground model to be used for the interpretation of ground impedance data.[1] Attenborough has demonstrated that the exponential variation chosen by Donato results in model grounds with increasing porosity with depth and has derived a ground model which has a decreasing porosity with depth.[2]

In this paper we examine the behavior of both these models in the limit of large and small variation and compare the results to the rigid backed layer model.[3] To facilitate this we have reduced the solutions to their simplest forms and have employed Attenborough's low frequency/high flow resistivity results for numerical comparison.

I. GROUND MODELS

A. Rigid Backed Layer

A layer of porous material of thickness d overlying an acoustically rigid surface has a surface impedance of the form:

$$Z(0) = i\, Z_c \cot(kd) \qquad (1)$$

where Z_c is the impedance of a seminfinite half space of the porous material and k is the complex wave number in the porous material.

B. Donato's Exponential Model

Donato has derived a impedance model for a material whose porosity times wave number decreases exponentially with depth. Attenborough has demonstrated that for natural grounds this implies that the porosity increases exponentially with depth and the wave number decreases exponentially with depth. This will not commonly occur in natural ground surfaces but may be a useful model in some cases. With the notation above Donato's formula becomes

$$Z(0) = i Z_c \frac{J_0(2k/\alpha)}{J_1(2k/\alpha)} ; \tag{2}$$

α is the exponential varation of the square of the complex wave number

$$k(z)^2 = k(0)^2 e^{-\alpha z}. \tag{3}$$

C. Attenborough's Exponential Model

Attenborough's solution for a porous material whose porosity decreases exponentially with depth and wave number increases exponentially with depth is given by

$$Z(0) = i Z_c \frac{H_0^{(2)}(2k/\alpha)}{H_1^{(2)}(2k/\alpha)} ; \tag{4}$$

where

$$k(z)^2 = k(0)^2 e^{\alpha z}. \tag{5}$$

II. BEHAVIOR OF THE IMPEDANCE AND WAVE NUMBER

It will be useful in the interpretation of these models to have a specific formulae for the wave number and impedance of a homogeneous porous material. For this paper we will use Attenborough's low frequency approximation:

$$Z_c = \frac{kc}{\gamma \Omega \omega} = .218\left(\frac{\sigma_e}{f}\right)^{1/2} (1 + i). \tag{6}$$

σ_e is the effective flow resistivity of the material, γ is the ratio of specific heats and c is the speed of sound in air.[2]

III. BEHAVIOR OF THE GROUND MODELS IN THE LIMIT OF LARGE AND SMALL ARGUMENTS

A. Rigid Backed Layer

i) Limit as $d \rightarrow 0$.

For a thin layer $d \rightarrow 0$ and Eq. (1) becomes

$$Z(0) = \lim_{d\rightarrow 0} i Z_c \cot(kd) = i \frac{Z_c}{kd} - i \frac{Z_c kd}{3} \tag{7}$$

If we use Eq. (6) to relate Z_c and k for low frequency we find

$$Z(0) = \frac{4\pi(.218)^2 \gamma\Omega d\sigma_e}{3c} + i \frac{1}{\gamma\Omega k_0 d}. \tag{8}$$

where k_0 is ω/c. Note that the imaginary term approaches infinity as $k_0 d$ goes to zero, while the real part depends only on the layer thickness and the surface flow resistance. This form is displayed by Attenborough.[2]

ii) Limit as $d \rightarrow \infty$

As $d \rightarrow \infty$ the model should recover the result for the homogeneous half space. The cotangent can be expanded in terms of the exponents of the real and imaginary parts of kd.

$$\lim_{d\rightarrow\infty} \cot(kd) = \lim_{d\rightarrow\infty} = \frac{e^{i k_1 d} e^{-k_2 d} + e^{-ik_1 d} e^{+k_2 d}}{2} / \frac{e^{i k_1 d} e^{-k_2 d} - e^{-ik_1 d} e^{k_2 d}}{2i} \tag{9}$$

where

$$k = k_1 + i k_2.$$

k_2 must be positive so that

$$Z(0) = i Z_c (-i) = Z_c, \tag{10}$$

and the original condition is recovered.

B. Donato's Exponential Model

i) Limit as α becomes small

As α becomes small the medium approaches a homogeneous media. If we take the limit of Eq. (2) for small α and large $2k/\alpha$ we find

$$Z(0) \approx i Z_c \frac{\sqrt{\frac{2\pi\alpha}{2k}} \cos\left(\frac{2k}{\alpha} - \frac{\pi}{4}\right)}{\sqrt{\frac{2\pi\alpha}{2k}} \cos\left(\frac{2k}{\alpha} - \frac{\pi}{2} - \frac{\pi}{4}\right)} = i Z_c \cot\left(\frac{2k}{\alpha} - \frac{\pi}{4}\right). \tag{11}$$

This is like the impedance of a thin layer of thickness $2/\alpha$ with an additional $-\pi/4$ phase change. The next correction term is of order $\alpha/2k$. A pressure release backed thin layer would have a phase change of $-\pi/2$. As $\alpha \rightarrow 0$, the cotangent term will approach -i as in Section A-ii) and $Z(0) = Z_c$ as expected.

ii) Limit as $\alpha \rightarrow \infty$

In the limit as $\alpha \rightarrow \infty$, the argument becomes small and the ascending series may be used to evaluate the Bessel functions.

$$Z(0) \approx i Z_c \frac{1}{\frac{k}{\alpha}} - i \frac{Z_c k}{2\alpha}. \tag{12}$$

The behavior of this solution is very similar to Eq. 7. We have a rapidly increasing imaginary part and a constant real part as the frequency decreases for fixed d and σ_e. The imaginary parts are identical if the rigid backed layer has a thickness $1/\alpha$, while the real parts are equal if the rigid backed layer thickness is given by $1.5/\alpha$.

C. Attenborough's Exponential Model

i) Limit as $\alpha \rightarrow 0$

The asymptotic expansions can be employed for the Hankel functions giving

$$Z(0) \approx i Z_c \frac{\sqrt{\frac{2}{\pi}\frac{\alpha}{2k}}\, e^{-i(2k/\alpha - \pi/4)}}{\sqrt{\frac{2}{\pi}\frac{\alpha}{2k}}\, e^{i\frac{\pi}{2}}\, e^{-i(2k/\alpha - \pi/4)}} \approx i Z_c e^{-i\pi/2} = Z_c. \tag{13}$$

The Attenborough model recovers the homogeneous half space surface impedance as $\alpha \rightarrow 0$.

ii) Limit as $\alpha \rightarrow \infty$

The small argument formulae for the Hankel functions are inserted in Eq. (4) to give

$$Z(0) = Z_c\left[\left(\frac{\pi}{2} - i\varepsilon\right)\frac{2k}{\alpha} - i\frac{2k}{\alpha}\ln\left(\frac{k}{a}\right)\right], \tag{14}$$

where $\varepsilon = .5772$.

This result is not easily interpreted in terms of a layered model. The behavior of this solution is best illustrated by use of Eq. (6) to yield

$$Z(0) = 5.923\ln\left|\frac{k}{\alpha}\right| + 3.419 + i\,13.955 \tag{15}$$

As $\alpha \rightarrow \infty$ the impedance of the Attenborough model has a large negative real part tending to $-\infty$ and a constant imaginary part. This puzzling result indicates that the surface is not absorbing energy and has a reflection coefficient greater than one! In a gross sense the behavior is physical. The reflection coefficient approaches one as the impedance becomes infinite. The only problem is that the surface cannot be generating acoustic energy.

iii) Limit for $2k/\alpha > 1$, α not infinite

A third limit is developed by Attenborough as useful for computation and comparison with data. This form is developed for α small enough that the leading term in asymptotic series for the Hankel functions may be used. For $2k/\alpha > 1$

$$\frac{H_0^{(2)}(2k/\alpha)}{H_1^{(2)}(2k/\alpha)} \approx -i\frac{\left(1 + \frac{i}{8}\frac{\alpha}{2k}\right)}{\left(1 - \frac{i}{8}3\frac{\alpha}{2k}\right)} \cong -i\left\{1 + \frac{i\alpha}{4k}\right\} \tag{16}$$

and

$$Z(0) = Z_c\left\{1 + \frac{i\alpha}{4k}\right\} \tag{17}$$

Using Eq. (6) to relate k and Z_c gives us

$$Z(0) = Z_c + \frac{ic}{4\gamma\omega}\left[\frac{\alpha}{\Omega}\right]. \tag{18}$$

Defining $\alpha_e = \alpha/\Omega$ and inserting numerical values from Eq. (6) gives us Attenborough's form:

$$Z(0) = .218\left(\frac{\sigma_e}{f}\right)^{1/2} + i\left[.218\left(\frac{\sigma_e}{f}\right)^{1/2} + 9.74\left(\frac{\alpha_e}{f}\right)\right] \tag{19}$$

The next terms in the asymptotic series are on the order of 7% of the last term in Eq. (19) when the argument of the Hankel function is one.

Note that we can recover Eq. (13) by letting α approach zero. Also note that the second term in Eq. (17) is very similar to the form for the imaginary part of the impedance of a thin rigid backed layer. Compare

$$i Z_c \frac{\alpha}{4k} \text{ and } \frac{i Z_c}{kd} . \tag{20}$$

The second term in Eq. (17) is the imaginary part of the impedance of a thin layer of effective thickness $d_e = 4/\alpha$. The imaginary parts dominate the impedance for large α.

IV. NUMERICAL RESULTS

To calculate numerical values for the three impedance models we set

$$kd = 2k/\alpha = x(1 + i). \tag{21}$$

Then, using Eq. (6), we solve for f and Z_c in terms of x:

$$f = \left[\frac{\alpha x c}{4\pi\gamma\Omega\,(.218)}\right]^2 \frac{1}{\sigma_e}, \tag{22}$$

and

$$Z_c = \frac{4\pi\gamma\Omega(.218)^2\sigma_e}{\alpha\, x\, c}\,(1 + i) . \tag{23}$$

We use the following typical values of γ, Ω, σ_e, and α based on our experience and that of Attenborough:

$\gamma = 1.4$

$\Omega = 0.4$

$\sigma_e = 120{,}000$ MKS rayls

$\alpha = 40.\ m^{-1}$; d = 5 cm.

Then, we calculate impedances using Eqs. (1), (2) and (4) for x = 0 to 5. The results are plotted in

Fig. 1 (rigid backed layer), Fig. 2 (Donato's formula), and Fig. 3 (Attenborough's solution). The imaginary parts of the impedance are multiplied by -1 so the plots of the real part are usually on the positive side of the vertical axis and the imaginary parts are on the negative side. The plots are nearly identical for values of x greater than one. For the variables above, x = 1.0 corresponds to 654 Hz.

Figure 4 displays the normal reflection coefficient calculated from Eqs. (1,2, and 4). The behavior is similar for all the models. Better agreement can be achieved between any two models by the choice of the equivalent depth of the exponential variation.

V. DISCUSSIONS AND CONCLUSIONS

The surface impedance predicted by each of the three models above approaches the homogeneous half-space impedance as the variation of wave number becomes small or the layer depth becomes large in the rigid backed model.

As the exponential variations become larger the impedance formula can be approximated as a constant or slowly varying real and imaginary part plus an imaginary term which is proportional to α/ω or $1/\omega d$.

For very rapid variations, the expansion of Attenborough's solution results in a non-physical solution (Eq. 13).

The basic assumption in the derivation of Eq. (6) and it's more exact analogues, is that the gradients of the variables with respect to the propagation direction are much smaller than gradients of the variables normal to the direction of propagation.[4] The result that the reflection coefficient is greater than one for small variable x is probably due to the error in Eq. (6) rather than any physical error in the theory leading to Eq. (4).

By the same reasoning, Donato's formula should be inaccurate for small values of the variable x. There is no physical problem with the thin rigid backed layer since the porous layer is homogeneous and Eq. (6) should hold. For the variables we have chosen, there appears to be little practical reason to employ the exponential models to fit ground data, while there appears to be a significant theoretical reason for not using the exponential models in the region where they vary significantly from the rigid backed layer.

At very low frequencies, the impedance translation theorem can be employed to calculate the impedance of an impedance backed layer. This model has sufficient flexibility to fit most data without the theoretical difficulties of the Donato or Attenborough models.

REFERENCES

1. R.J. Donato, "Impedance models for grass covered ground," J. Acoust. Soc. Am. 61, 1449-1452 (1977).

2. K. Attenborough, "Acoustical impedance models for outdoor ground surfaces," J. Sound Vib. 99, 521-544 (1985).

3. All expansions are from Handbook of Mathematical Functions, edited by M. Abramowitz and I.A. Stegun (Dover Publications, Inc., New York, 1970).

4. H. Tijdeman, "On the propagation of sound waves in cylindrical tubes," J. Sound Vib. 39, 1-33 (1975).

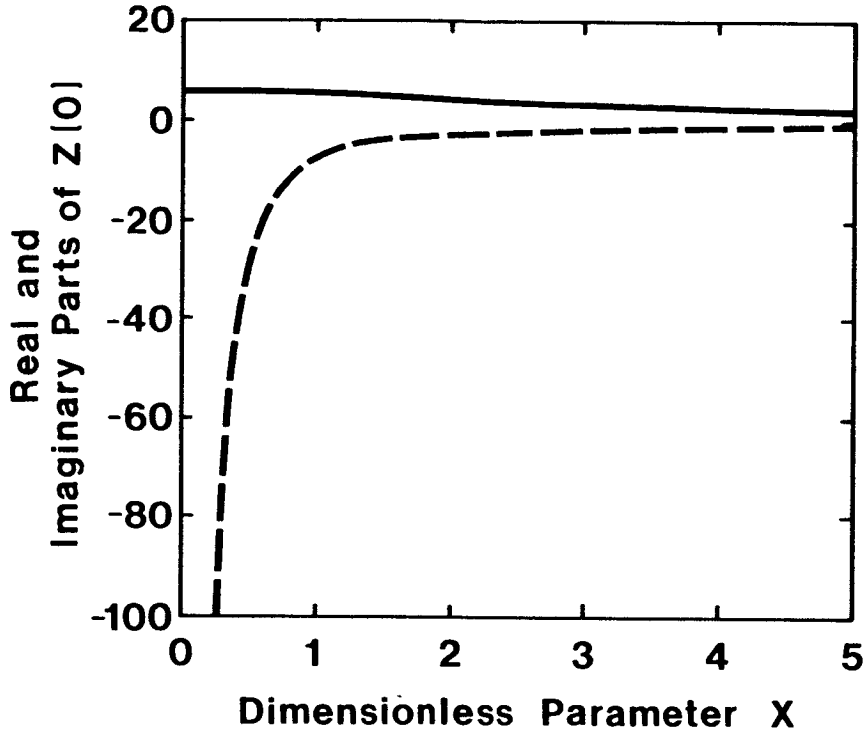

Figure 1. The real and imaginary part of the ground impedance versus the parameter x for the thin rigid backed layer. The imaginary part is multiplied by negative one for display purposes.

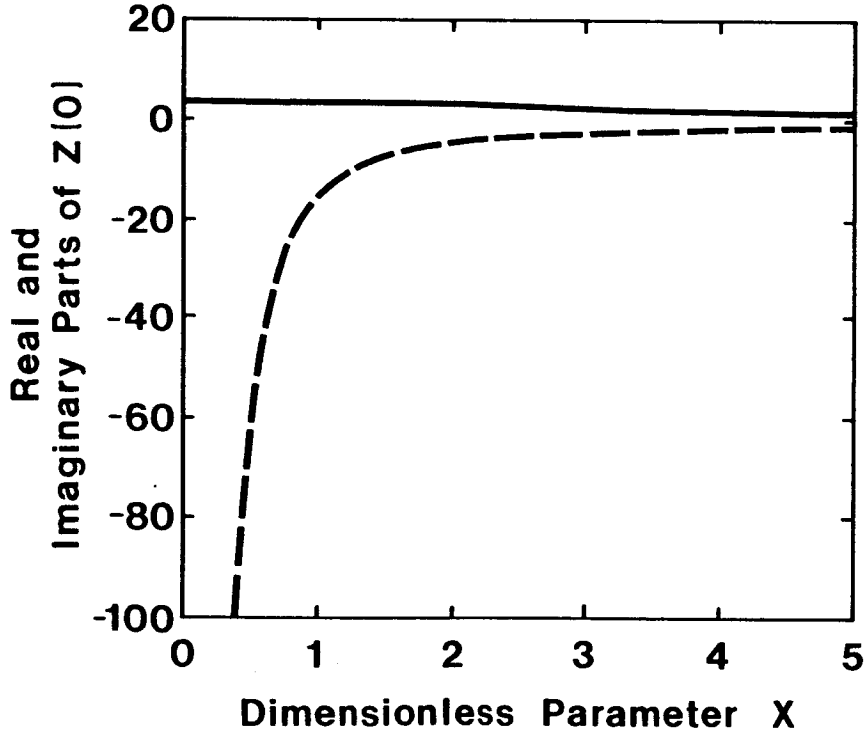

Figure 2. The real and imaginary parts of the ground impedance versus the parameter x for Donato's exponentially varying model.

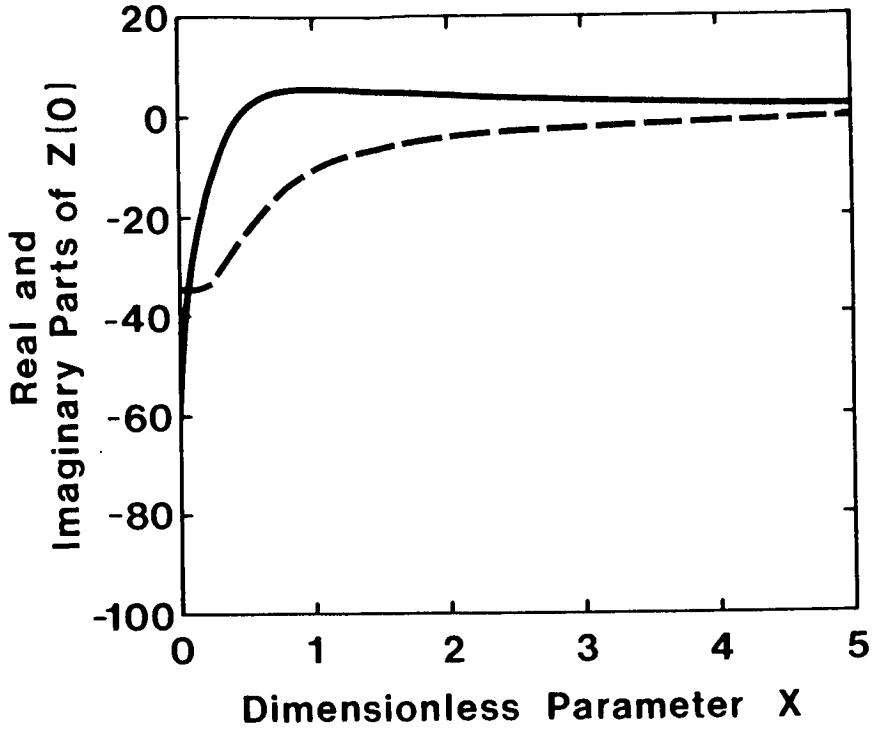

Figure 3. The real and imaginary parts of the ground impedance versus the parameter x for Attenborough's exponentially varying model.

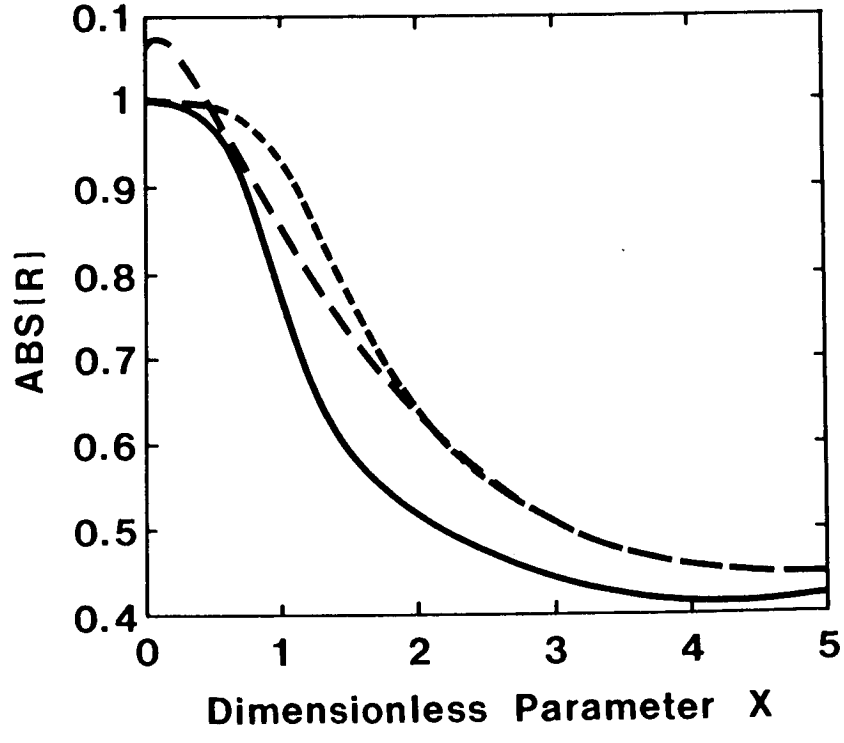

Figure 4. The absolute value of the reflection factor for normal reflection for the three models versus the parameter x—thin layer,-----Donato,— —Attenborough.)

PRELIMINARY ANALYSIS OF MEASURED SOUND PROPAGATION OVER VARIOUS SEASONAL SNOW COVERS

Donald G. Albert
US Army Cold Regions Research and
Engineering Laboratory
Hanover, NH 03755-1290

ABSTRACT

Measurements of acoustic pulse propagation in the 5- to 500-Hz frequency band were conducted under various snow cover conditions during the 1989–1990 winter in New Hampshire. The objective was to determine the effect of snow cover thickness and other snow properties on the absorption of acoustic pulses. Blank pistol shots were used as the source of the acoustic waves, and geophones and microphones in an 80-m-long linear array served as receivers. Snow thicknesses ranged from 0.05 to 0.35 m, and densities varied from 100 to 350 kg m^{-3} during the 10 separate measurement days. Preliminary analysis indicates that the peak pulse amplitude decayed in proportion to $\sim r^{-1.7}$ for most conditions and that the acoustic-to-seismic ratios varied from about 4 to 15 x 10^{-6} m s^{-1} Pa^{-1}. Theoretical waveforms were calculated for propagation in a homogeneous atmosphere using Attenborough's model of ground impedance. An automatic fitting procedure for the normalized experimental and theoretical waveforms was used to determine the effective flow resistivity of the snow covers, and gave values of 10 to 35 kN s m^{-4}, in agreement with earlier results.

INTRODUCTION

Absorption of sound energy by the ground is important in understanding noise propagation through the atmosphere. It affects predictions of traffic, industrial, or blasting noise levels, which are becoming increasingly important in mitigating or preventing community noise problems and assessing environmental impacts of various activities. In previous work it has been shown that a snow cover has a large effect on acoustic pulse propagation, causing increased attenuation and marked waveform changes compared with propagation over grassland (Ref. 1). Those measurements were for a single snow cover, so measurements were undertaken during the 1989–1990 winter to investigate additional snow covers and to examine the effect of snow cover thickness and other snow properties on pulse propagation. This paper reports on the experimental approach, preliminary results of data analysis, and first steps towards an automatic inversion procedure to determine acoustically the properties of the snow cover.

EXPERIMENTAL MEASUREMENTS

As in previous measurements, a .45 caliber blank pistol held and fired 1 m above the surface was used as the source of the acoustic waves. The receivers were a linear array of 4.5-Hz Mark Products Model L-15B geophones and Globe Model 100C low frequency microphones. Two Bruel & Kjaer Type 4165 microphones were used to record the source pulse. Both types of microphones have a flat response in the frequency band of interest. A Bison Model 9048 recording system was used to acquire 48 channels of data at a 5-kHz rate. The bandwidth of the measurements is estimated as 5–500 Hz and is limited mainly by the source output.

In the fall of 1989, vertical and horizontal component geophones were installed along a relatively flat 80-m-long line. A few geophones were also buried 0.5 m deep in the soil 30 and 60 m away from the location of the source. During the winter, just before each measurement period, geophones and microphones were installed at the snow surface and probe microphones (Ref. 2) were inserted into the snow. A number of pistol shot responses were then recorded, and these sensors were removed after that day's measurements were completed. Only the surface sensors will be discussed in this paper.

On the days that acoustic experiments were conducted, a snow characterization pit was dug and the temperature, density, grain size, and crystal type were determined for each layer present. Snow and frost depths were also recorded.

Meteorological data were collected using a Campbell Scientific Model 21X data logger. Temperatures were measured within the ground and snow and at heights of 0.01, 0.03, 0.1, 0.3, 1, 3, and 5 m in the air. Wind speeds at 1- and 3-m heights were also recorded, along with relative humidity and barometric pressure. Measurements were taken every minute, but averages, variations (minimum, maximum, and standard deviation), and instantaneous values were recorded every 10 and every 30 minutes during the acoustic experiments. Values were recorded every 4 hours during the rest of the winter.

ACOUSTIC WAVEFORM ANALYSIS

Figure 1 shows the waveforms recorded on nine separate days by the Globe 100C low frequency surface microphones a distance of 60 m from the source. The positive peak amplitudes of these pulses, along with the air temperature, snow depth, and snow density (for the surface layer) are given in Table 1. (Experiment 4 used a different sensor array than the rest of the experiments and has not yet been analyzed.)

TABLE 1. MEASURED AMPLITUDES, ENVIRONMENTAL PARAMETERS, AND BEST FITTING WAVEFORM PARAMETERS FOR THE 1989–1990 WINTER EXPERIMENTS.

Expt No	Date (1989–1990)	Amplitude, (Pa, at 60 m)	Air temp. (°C)	Snow depth (mm)	Snow density (kg/m^3)	Flow resistivity (kN s/m^4)	Change in fitted snow depth (mm)
1	29 Dec	3.1	–12.4	185	170	25	0
2	4 Jan	4.9	3.1	170	260	30	0
3	10 Jan	4.3	1.3	140	280	35	–50
4	19 Jan	17.0	–3.0	50	210	—	—
5	22 Jan	2.0	–5.3	190	100	10	+50
6	31 Jan	2.2	–2.8	350	140	10	0
7	8 Feb	1.9	3.0	280	150	10	+50
8	6 Mar	3.3	–4.0	140	340	35	–50
9	15 Mar	16.1	14.3	0–60	350	—	—
10	12 Apr	16.7	3.2	0	300	—	—

Note: The snow cover was continuous for all of the experiments except for experiment number 4 (9/10 of the ground was covered), experiment number 9 (5/10 covered), and experiment number 10 (no snow).

The two largest arrivals were recorded on days when there was little or no snow cover present, and have amplitudes about five times larger than the pulses recorded when snow was present. The waveforms recorded over snow are all elongated to various degrees, and exhibit relatively stronger low frequency content than those recorded without snow present.

In Reference 1, a method of calculating theoretical acoustic pulse waveforms from known surface properties was developed and verified. The procedure is briefly outlined here. For a monofrequency source in the air and a receiver on the surface, the acoustic pressure a slant distance *(r)* away from the source is given by

$$P/P_0 = 1/kr\, e^{ikr}\,(1 + Q)$$

where P_0 is a reference source level, k is the wave number in air, Q is the image source strength representing the effect of the ground, and $e^{-i\omega t}$ is suppressed. At high frequencies ($kr >> 1$), Q can be written as (Ref. 3 and 4)

$$Q = R_p + (1 - R_p)\, F(w)$$

where R_p is the plane wave reflection coefficient, F is the ground wave term, and w is a numerical distance, all of which depend on the specific impedance Z_2 of the ground. The impedance is itself dependent upon frequency; thus, so is Q. [The elongation and relatively stronger low frequency content of the measured waveforms in Figure 1 can be explained theoretically by the decrease in R_p at high frequencies and the

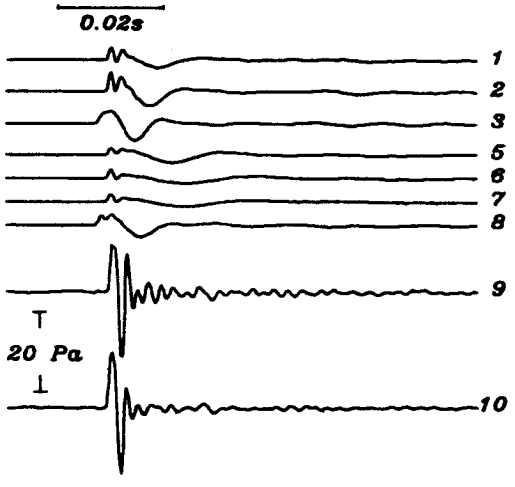

Figure 1. True amplitude, time aligned, low frequency surface microphone waveforms at 60-m range from a .45 caliber pistol shot 1 m high above the snow or ground surface. These waveforms were recorded with the same microphone on nine separate days, and the numbers refer to the measurement days listed in Table 1. The two largest waveforms occurred on days when there was very little or no snow cover present. Note that waveforms 3 and 8 are slightly misaligned in time; the shift is the result of the low frequency portion of the waveform being larger than the direct arrival.

enhancement of $F(w)$ at low frequencies (see Ref. 1, Fig. 4).] By determining Q over the frequency band of interest, an inverse FFT* can be used to construct theoretical pulse waveforms in the time domain. Nicolas et al. (Ref. 5) have shown that an explicitly layered model of the ground must be used to represent thin snow covers, and this was done in the calculations presented here using

$$Z = (Z_3 - i\,Z_2 \tan k_2 d) \,/\, (Z_2 - i\,Z_3 \tan k_2 d)$$

where d is the snow layer thickness, k_2 is the wave number in the layer, and Z_2 and Z_3 are the impedances of the layer and substratum, respectively (Ref. 6).

The impedance Z_2 and wave number k_2 of the snow were calculated using Attenborough's (Ref. 7) four-parameter model. For all of the calculations, the grain shape factor n' was set to 0.5 and the pore shape factor ratio s_f was 0.8. The porosity Ω was determined from the measured density of the snow, and the effective flow resistivity σ was allowed to vary.

A new result presented in this paper is a method of comparing calculated and observed acoustic pulse waveforms. A suite of waveforms were calculated and the best fitting waveform was selected under the L_1 norm criterion (i.e., the sum of the absolute value of the differences between the calculated and observed waveforms over a fixed time window). A least squares criterion, the L_2 norm, was avoided because it heavily weights, and tries to reduce, the maximum misfit. Since the source pulse in the calculations is an assumed one, and not actually measured, I wanted to allow for errors in this assumed pulse to be ignored while accurately fitting the overall, low frequency portion of the measured waveforms accurately.

Eight theoretical waveforms were calculated to fit the observed waveform at $r = 60$ m using the measured snow thickness and porosity, with the effective flow resistivity σ varying from 5 to 40 kN s m^{-4}. Then, for the best σ, four additional waveforms were calculated, with the snow thickness changed by ±0.05- and ±0.1-m increments from the measured thickness to see if the fit could be improved. An example is given in Figure 2.

*Fast Fourier Transform

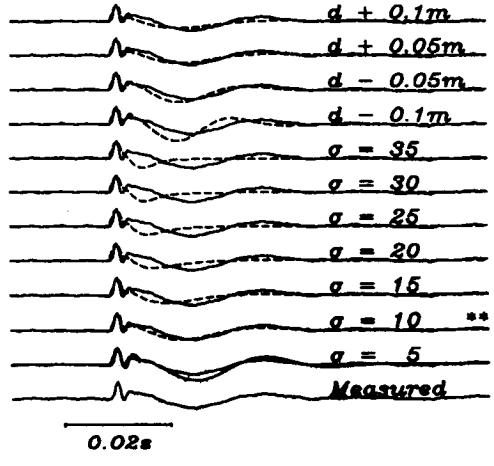

Figure 2. Comparison between normalized measured and calculated waveforms for experiment number 6 (see Table 1) at a range of 60 m. The solid lines are the measured waveform; the dashed lines are calculated waveforms with the indicated effective flow resistivities σ. The measured snow depth d was 0.35 m. Stars mark the best fitting waveform.

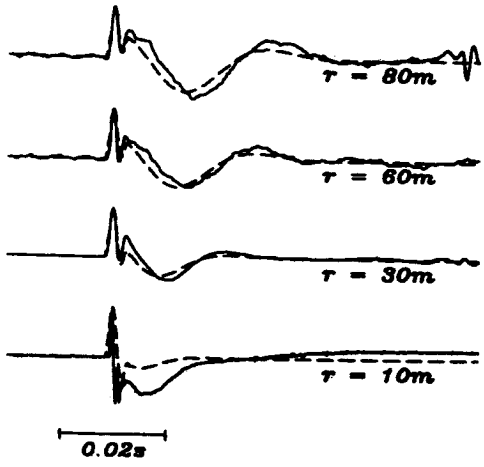

Figure 3. Comparison between normalized measured (solid) and calculated (dashed) waveforms for experiment number 6. The waveforms at all the ranges were calculated using the parameters from the fitting procedure at 60 m. At 10-m range, a Bruel & Kjaer Type 4165 microphone 0.3 m above the snow was used (and the measured waveform shows some evidence of being clipped); the other measurements were made with Globe Model 100C low frequency microphones on the snow surface.

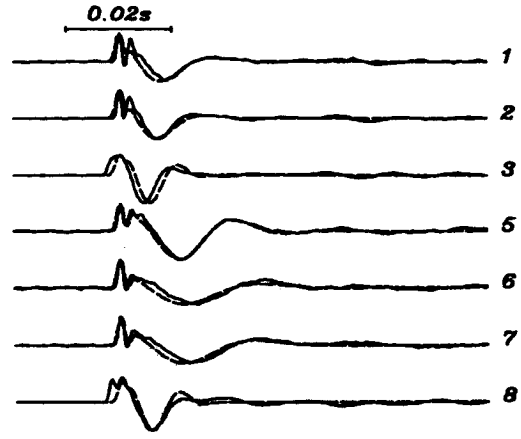

Figure 4. Comparison of normalized measured (solid lines) and calculated (dashed) waveforms at 60 m for propagation over various snow covers. The numbers refer to the experiment numbers given in Table 1, where the best fitting flow resistivities and snow layer thicknesses are listed.

In this case the best fit was obtained for $\sigma = 10$ kN s m^{-4} and the measured snow thickness. Using these best fit values of σ and d, more waveforms were then calculated for different propagation ranges. The comparisons between these waveforms and observations are shown in Figure 3, and the agreement is quite good.

All the measured and best-fit calculated waveforms for snow are shown in Figure 4. The fitting procedure has been able to automatically match waveforms of quite different appearance. The last two columns of Table 1 list the effective flow resistivities and snow depths determined using this fitting procedure. In all cases the snow thickness was within ±0.05 m of the measured thickness, a reasonable variation considering the variation in the actual snow cover thickness across the propagation path.

ADDITIONAL ACOUSTIC MEASUREMENTS

The amplitude decay as a function of range was determined by least squares fitting of the data from the low frequency microphones to

$$A(r) = A(r_0)\, r^{-\alpha}$$

where r is the propagation distance in m, $A(r)$ is the peak amplitude in Pa at range r, $A(r_0)$ is the source amplitude at a reference distance r_0, and α is the distance attenuation exponent. For the data analyzed so far, the results are given in Table 2. Values of α for snow range from 1.6 to 1.9, compared with the expected 1.0 from spherical spreading. For the last two experiments, with little or no snow present, the coefficient is around 1.1.

TABLE 2. RANGE DECAY COEFFICIENT AND ACOUSTIC-TO-SEISMIC COUPLING RATIO MEASURED FOR AIR WAVES.

Expt No.	Date	Range decay coefficient α			Acoustic-to-seismic coupling ratio, m s^{-1} Pa^{-1}		
		No. of points	Value of α	95% confidence interval	No. of points	Value of coupling ratio	95% confidence interval
1	12–29–90	12	−1.60	± 0.30	10	4.01×10^{-6}	± 1.25×10^{-6}
2	1–04–90	13	−1.71	± 0.49	10	6.35	± 5.18
3	1–10–90	18	−1.69	± 0.22	15	3.41	± 0.87
4	1–19–90						
5	1–22–90	8	−1.76	± 0.64	6	5.10	± 5.03
6	1–31–90	18	−1.84	± 0.22	15	15.1	± 2.77
7	2–08–90	16	−1.91	± 0.36	13	5.93	± 1.49
8	3–06–90	18	−1.73	± 0.16	12	4.27	± 1.07
9	3–15–90	11	−1.05	± 0.46	9	6.28	± 2.66
10	4–12–90	30	−1.12	± 0.19	25	10.2	± 1.69

The ratio of induced particle velocity in the snow or soil to incident pressure was determined from the collocated surface vertical component geophones and surface microphones (Table 2). These ratios vary from 3 to 15 × 10^{-6} m s^{-1} Pa^{-1}. Note that some of the values have very poor confidence intervals (e.g., experiments 2 and 5). It is hoped that these values will be better determined when all of the data are analyzed.

CONCLUSIONS

The experiments were successful in obtaining accurate measurements of pulse propagation over a variety of seasonal snow covers. Preliminary values have been presented for the range decay and acoustic-to-seismic coupling coefficients, and more accurate values will be provided when the data analysis is completed. I have also demonstrated a waveform matching procedure that can be used to select the theoretical waveform that best fits the measured data.

Future work will include completing the data analysis, including determination of attenuation coefficients in the snow from the probe microphone recordings, and correlating the acoustic effects with the snow cover properties. A true waveform inversion procedure will also be developed.

ACKNOWLEDGMENTS

These experiments could not have been conducted without the assistance of many of my co-workers. Nancy Greeley provided all the meteorological data, did much of the snow characterization, and assisted with

the experiments. Steve Decato was the primary shooter and provided much additional support. Dave Gaskin helped to arrange for the use of the test site and Jim Cragin provided access to a heated shelter for the equipment and personnel. Their assistance is greatly appreciated. Thanks are also due to LT Karen Faran, Gus Greeley, SSG Tommie Hall, and Mark Moran for their help.

Rapid technical reviews were provided by Steve Arcone and Mark Moran. This work is supported by the Directorate of Research and Development, U.S. Army Corps of Engineers, Projects 4A161102AT24 and 4A762730AT42.

REFERENCES

1. Albert, D.G. and Orcutt, J.A.: Acoustic Pulse Propagation Above Grassland and Snow: Comparison of Theoretical and Experimental Waveforms. **J. Acoust. Soc. Amer. 87**, 93–100 (1990).

2. Attenborough, K., J.M. Sabatier, H.E. Bass, and L.N. Bolen: The Acoustic Transfer Function at the Surface of a Layered Poroelastic Soil. **J. Acoust. Soc. Am. 79**, 1353–1358 (1986).

3. Jordan, E.C. and K.G. Balmain: **Electromagnetic Waves and Radiating Systems**, Second edition, (Prentice-Hall, Englewood Cliffs, NJ, 1968).

4. Stratton, J.A.: **Electromagnetic Theory**. (McGraw-Hill, NY, 1941).

5. Nicolas, J., J.-L. Berry, and G.A. Daigle: Propagation of Sound Above a Finite Layer of Snow. **J. Acoust. Soc. Amer. 77**, 67–73 (1985).

6. Brekhovskikh, L.M.: **Waves in Layered Media.** Second edition (Academic Press, New York, 1980) p. 17.

7. Attenborough, K.: Acoustical Impedance Models for Outdoor Ground Surfaces," **J. Sound Vib. 99**, 521–544 (1985).

LONG-DISTANCE SOUND PROPAGATION OVER DISCONTINUOUS IMPEDANCES

Simon N. Chandler-Wilde, Joseph N. B. Harriott
and David C. Hothersall
Department of Civil Engineering, Bradford University, England.

SUMMARY

A calculation method is presented for sound propagation over an impedance discontinuity in flat ground with a homogeneous, still atmosphere. The method is based on an approximate solution to a two dimensional boundary integral equation formulation of the problem, which expresses the wave field as the solution for homogeneous ground plus an integral over half of the boundary. Through recognising this integral as a generalised Fourier integral, asymptotic methods are applied to evaluate the part of the integral most expensive to compute by numerical quadrature. Single frequency excess attenuation results for propagation from a point source above rigid ground to a receiver above absorbing ground are discussed. The results are applied, with air attenuation and A-weighting, to a notional jet engine noise source; simple trends are noted.

INTRODUCTION

The problem discussed in this paper is propagation from a point source in a homogeneous still atmosphere above flat locally reacting ground. Efficient calculation methods for the wave field above acoustically homogeneous ground are well known (e.g. ref. 1). More recently sound propagation over impedance inhomogeneities has been theoretically examined; a thorough review is given in reference 2. A limitation of the accurate calculation methods is their computational expense.

Here we focus on propagation over a single straight line impedance discontinuity which lies perpendicular to the direct source-receiver propagation path. A development to an existing calculation method is described which significantly reduces the computational expense.

The improved calculation method is applied to grazing incidence propagation from a source above a rigid surface to a distant receiver above absorbing ground. Monofrequency excess attenuation results are examined and some simple trends are observed. The results for a 1·5m high receiver are applied, with air attenuation and A-weighting, to a notional jet engine noise source at 1·5m height. Again some simple trends are noted.

CALCULATION METHOD

Description of the Problem

Figure 1 illustrates the problem. A point source with harmonic time dependence ($e^{-i\omega t}$) is situated over a flat locally reacting surface of infinite extent. The surface is divided by a straight line into two half planes. Each half plane is acoustically homogeneous and characterised by a frequency dependent complex admittance (the inverse of the normalised acoustic surface impedance). We are interested in evaluating the acoustic potential at a point in a vertical half plane that is bounded by the surface, passes through the source and is perpendicular to the line of the admittance discontinuity. For the mathematical description we will use right-handed Cartesian coordinates Oxyz as indicated in Figure 1, the y-axis vertical and the surface in the plane y=0. The source and receiver coordinates are $(0,h_S,0)$ and $(L,h_r,0)$ respectively. The admittance discontinuity is along the line x=X in the surface.

An Existing Calculation Method

First we consider the related problem in which the source is replaced by an infinitely long coherent line source, parallel to the admittance discontinuity. This cylindrical wave propagation problem is mathematically equivalent to the two dimensional problem which is illustrated in Figure 2. From the mathematical expression of this problem as a two dimensional boundary value problem (consisting of the Helmholtz equation and suitable boundary conditions) the following boundary integral equation can be derived (ref. 3):

$$\Phi(\underset{\sim}{t}_2,\underset{\sim}{t}_1) = G_{\beta_2}(\underset{\sim}{t}_1,\underset{\sim}{t}_2) + ik(\beta_1-\beta_2)\int_{-\infty}^{X}\Phi(\underset{\sim}{s},\underset{\sim}{t}_1)G_{\beta_2}(\underset{\sim}{s},\underset{\sim}{t}_2)dx. \qquad (1)$$

In this equation $\underset{\sim}{t}_1=(0,h_S)$ is the source position, $\underset{\sim}{t}_2=(L,h_r)$ is the receiver position, and β_1 and β_2 are the admittances of the two halves of the boundary. The integration is over the interval $\gamma=(-\infty,X]$; this is the part of the boundary with admittance β_1. $\underset{\sim}{s}=(x,0)$ is a point in the boundary. For two points $\underset{\sim}{a}$ and $\underset{\sim}{b}$, $\Phi(\underset{\sim}{a},\underset{\sim}{b})$ denotes the acoustic potential detected by a receiver at $\underset{\sim}{a}$ when insonified by a unit source at $\underset{\sim}{b}$; $G_\beta(\underset{\sim}{a},\underset{\sim}{b})$ (where $\beta=\beta_1$ or β_2) denotes the same quantity in the simple case when the boundary has homogeneous admittance β. Efficient methods for evaluating the solution in this simpler case have already been developed (refs. 4,5).

Equation (1), which describes an inhomogeneous admittance boundary problem, can be solved accurately for $\Phi(\underset{\sim}{t}_2,\underset{\sim}{t}_1)$ by the boundary element method (refs. 3,4,6). We consider here an approximate but less computationally expensive method of solution. To develop this we make the physically plausible assumption that the potential in γ is what it would be if the whole boundary had admittance β_1 (refs. 7,8). Thus $\Phi(\underset{\sim}{s},\underset{\sim}{t}_1)$ in equation (1) is replaced by $G_{\beta_1}(\underset{\sim}{s},\underset{\sim}{t}_1)$, giving the following approximation to $\Phi(\underset{\sim}{t}_2,\underset{\sim}{t}_1)$:

$$\Phi_A(\underset{\sim}{t}_2,\underset{\sim}{t}_1) = G_{\beta_2}(\underset{\sim}{t}_1,\underset{\sim}{t}_2) + i(\beta_1-\beta_2)I(X) \ ,$$

where

$$I(X)= k\int_{-\infty}^{X} G_{\beta_1}(\underset{\sim}{s},\underset{\sim}{t}_1)G_{\beta_2}(\underset{\sim}{s},\underset{\sim}{t}_2)dx \ . \qquad (2)$$

This approximation avoids using the boundary element method.

Using $\Phi_A(\underset{\sim}{t}_2,\underset{\sim}{t}_1)$ we can calculate $Q_A(\underset{\sim}{t}_2,\underset{\sim}{t}_1)$, an approximate cylindrical wave reflection coefficient. Let d and D denote the distances from source and from image source (at $(0,-h_s)$) to receiver, respectively. Assuming a source with unit volume flow rate amplitude,

$$\Phi_A(\underset{\sim}{t}_2,\underset{\sim}{t}_1) = -\frac{i}{4}H_0^{(1)}(kd) + Q_A(\underset{\sim}{t}_2,\underset{\sim}{t}_1)\left[-\frac{i}{4}H_0^{(1)}(kD)\right] \quad ,$$

where $H_0^{(1)}$ is the Hankel function of the first kind of order zero.

For propagation over short distances, the difference $20\log_{10}|\Phi_A(\underset{\sim}{t}_2,\underset{\sim}{t}_1)| - 20\log_{10}|\Phi(\underset{\sim}{t}_2,\underset{\sim}{t}_1)|$, where $\Phi(\underset{\sim}{t}_2,\underset{\sim}{t}_1)$ is calculated by the boundary element method, has been found to be around 0·1dB (ref. 6). This suggests that $Q_A(\underset{\sim}{t}_2,\underset{\sim}{t}_1)$ is an accurate approximation to $Q(\underset{\sim}{t}_2,\underset{\sim}{t}_1)$, the exact cylindrical wave reflection coefficient for the two dimensional problem illustrated in Figure 2. Also, it has been argued that (ref. 6), for a receiver in the far field of the image source ($kD \gg 1$), $Q(\underset{\sim}{t}_2,\underset{\sim}{t}_1)$ is an accurate approximation to the spherical wave reflection coefficent, q, for the three dimensional problem illustrated in Figure 1. If the point source in the three dimensional problem has unit volume flow rate amplitude, then the acoustic potential at the receiver position is

$$\varphi = -\frac{e^{ikd}}{4\pi d} - q\frac{e^{ikD}}{4\pi D} \quad .$$

Replacing q with $Q(\underset{\sim}{t}_2,\underset{\sim}{t}_1)$, which is approximated by $Q_A(\underset{\sim}{t}_2,\underset{\sim}{t}_1)$, we obtain an approximation for φ:

$$\varphi_A = -\frac{e^{ikd}}{4\pi d} - Q_A(\underset{\sim}{t}_2,\underset{\sim}{t}_1)\frac{e^{ikD}}{4\pi D} \quad . \qquad (3)$$

We assume throughout the rest of the paper, without further comment, that this is a good approximation for φ.

The main computational expense in this approximate calculation method is in evaluating the integral I(X). In previous calculations (ref. 6) I(X) was evaluated numerically after first replacing the lower limit of integration, $-\infty$, by a sufficiently large negative value. Unfortunately the integrand in equation (2) is usually highly oscillatory over the range of integration, making numerical integration an expensive process. Here we derive a semi-analytical method of evaluation which deals efficiently with the part of the integral that is most expensive to evaluate numerically.

The Improved Calculation Method

We begin by examining the general behaviour of the integrand in equation (2). We note that, for a receiver at the point $\underset{\sim}{s}$ in the boundary, we can write

$$4iG_\beta(\underset{\sim}{s},\underset{\sim}{t}) = H_0^{(1)}(k|\underset{\sim}{t}-\underset{\sim}{s}|)R_\beta(\underset{\sim}{s},\underset{\sim}{t}) \quad ,$$

where $R_\beta(\underset{\sim}{s},\underset{\sim}{t})=1+Q_\beta(\underset{\sim}{s},\underset{\sim}{t})$, and $Q_\beta(\underset{\sim}{s},\underset{\sim}{t})$ is the cylindrical wave reflection coefficient for a homogeneous surface of admittance β. As x is increased from $-\infty$, the real and imaginary parts of $H_0^{(1)}(k|\underset{\sim}{t}-\underset{\sim}{s}|)$ oscillate in a well defined fashion, while $R_\beta(\underset{\sim}{s},\underset{\sim}{t})$ changes less rapidly. In fact, from the asymptotic expansion of the Hankel function at large argument, we see that if we factorise,

$$G_\beta(\underset{\sim}{s},\underset{\sim}{t}) = e^{ik|\underset{\sim}{t}-\underset{\sim}{s}|}S(\underset{\sim}{s},\underset{\sim}{t}) \quad ,$$

then $S(\underset{\sim}{s},\underset{\sim}{t})$ is smooth as a function of x compared to $e^{ik|\underset{\sim}{t}-\underset{\sim}{s}|}$ when $k|\underset{\sim}{t}-\underset{\sim}{s}|$ is large. This observation suggests that I(X) can be usefully written in the form of a generalised Fourier integral:

$$I(X) = \int_{-\infty}^{X} f(x) e^{ikg(x)} dx \quad , \tag{4}$$

where

$$f(x) = kG_{\beta_1}(\underset{\sim}{s},\underset{\sim}{t}_1)G_{\beta_2}(\underset{\sim}{s},\underset{\sim}{t}_2)e^{-ikg(x)},$$

$$g(x) = g_1(x) + g_2(x),$$

and

$$g_1(x) = |\underset{\sim}{t}_1-\underset{\sim}{s}|, \quad g_2(x) = |\underset{\sim}{t}_2-\underset{\sim}{s}|.$$

Notice that g(x) is the distance from source to receiver via the point $\underset{\sim}{s}$. The location on the boundary of the geometrical reflection point, x_r, is therefore given by $g'(x_r)=0$. When $\underset{\sim}{s}$ is sufficiently distant from $\underset{\sim}{t}_1$, $\underset{\sim}{t}_2$, and $(x_r,0)$, f(x) is a slowly changing function of x compared to $e^{ikg(x)}$. This fact allows us to use simple asymptotic methods to help evaluate I(X).

To introduce the asymptotic analysis we consider first what proves to be the simplest type of configuration to deal with. This has x_r well outside γ, and $\underset{\sim}{t}_1$ and $\underset{\sim}{t}_2$ at least one wavelength from the boundary. For this type of configuration we may integrate I(X) by parts to give

$$I(X) = J_1(X) + R_1(X) \tag{5}$$

where

$$J_1(X) = \frac{f(X)\, e^{ikg(X)}}{ikg'(X)} \quad ,$$

$$R_1(X) = -\int_{-\infty}^{X} \frac{d}{dx}\left[\frac{f(x)}{ikg'(x)}\right] e^{ikg(x)} dx \quad ,$$

and then integrate $R_1(X)$ by parts to give

$$R_1(X) = J_2(X) + R_2(X) \quad ,$$

where

$$J_2(X) = \left[\frac{g''(X)}{g'(X)} - \frac{f'(X)}{f(X)}\right] \frac{f(X)e^{ikg(X)}}{(ikg'(X))^2} \quad ,$$

$$R_2(X) = \int_{-\infty}^{X} \frac{d}{dx}\left[\frac{d}{dx}\left[\frac{f(x)}{ikg'(x)}\right]\frac{1}{ikg'(x)}\right] e^{ikg(x)} dx \quad .$$

If f(x) were completely independent of k, we could apply the Riemann-Lebesgue lemma to show that, for n=1,2,

$$R_n(X) = o(k^{-n}) \quad , \quad k \to \infty \quad .$$

In fact f(x) depends weakly on k, but f(x) approaches a limit independent of k as $k\to\infty$ with other variables fixed (ref. 2, p.585). Thus I(X) has the following asymptotic approximation:

$$I(X) \sim J_1(X) + J_2(X) \quad , \quad k \to \infty \quad .$$

$J_1(X)$ and $J_2(X)$ are the first and second terms in what is approximately an asymptotic expansion of $I(X)$ in inverse powers of k. When k is large enough, $J_1(X) \gg J_2(X)$, so that we can safely approximate

$$I(X) \approx J_1(X). \qquad (6)$$

The above arguments do not tell us how large k should be in any particular case for approximation (6) to be valid. However, it is plausible that $R_2(X) \ll J_2(X)$ when $J_2(X) \ll J_1(X)$. Thus we can estimate the relative error in approximation (6) by the following upper bound on $|J_2(X)/J_1(X)|$:

$$E_r(X) = \left[\frac{g''(X)}{|g'(X)|} + \frac{3}{2}\left[\frac{1}{g_1(X)} + \frac{1}{g_2(X)}\right]\right]\frac{1}{k|g'(X)|} .$$

(To obtain this expression, $|f'(X)/f(X)|$ has been replaced by $(3/2)[1/g_1(X) + 1/g_2(X)]$, which is expected to be an upper bound on $|f'(X)/f(X)|$ in all cases (ref. 2, p.598).) We can estimate the absolute error in approximation (6) by the following upper bound on $|J_2(X)|$:

$$E_a(X) = E_r(X)\,\frac{|f(X)|}{k|g'(X)|} .$$

Both $E_r(X)$ and $E_a(X)$ are infinite at $X=x_r$ and tend to zero as $X \to -\infty$. Moreover, a graphical examination of $E_r(x)$ and $E_a(x)$ suggests that they are monotonic in $(-\infty, x_r)$, for typical geometries, admittance values and frequencies.

We move on to consider configurations for which still $X<x_r$ but $x_r - X$ is small enough for $E_r(X)$ and/or $E_a(X)$ to be unacceptably large. For the moment we require that both the source and receiver are many wavelengths above the boundary. The following breakdown of the integral is used:

$$I(X) = I(\tau) + K , \qquad (7)$$

where K is the integral over a truncated interval $\gamma_T=[\tau, X]$,

$$K = k\int_{\tau}^{X} G_{\beta_1}(\underset{\sim}{s},\underset{\sim}{t}_1)G_{\beta_2}(\underset{\sim}{s},\underset{\sim}{t}_2)dx ,$$

which will be evaluated numerically. We will choose τ so that we can satisfactorily approximate

$$I(\tau) \approx J_1(\tau) . \qquad (8)$$

To reduce the expense in evaluating K numerically we want to choose τ as close to x_r as possible while still insisting that approximation (8) should satisfy certain relative and absolute error criteria. We can uniquely define two upper limits, τ_r and τ_a, for τ by

$$E_r(\tau_r) = 0{\cdot}2 ,$$

$$E_a(\tau_a) = \epsilon , \qquad (9)$$

where ϵ is an arbitrary positive constant. $\tau \leq \tau_r$ ensures that $J_2(\tau)$ is sufficiently small compared to $J_1(\tau)$ for $E_a(\tau)$ to be an accurate estimate of the absolute error in approximation (8). Therefore, if also $\tau \leq \tau_a$, then the absolute error in the approximation (8) is $\leq \epsilon$. Thus by taking τ to be the minimum of τ_r and τ_a we ensure that the error made in replacing $I(\tau)$ by $J_1(\tau)$ in equation (7) is $\leq \epsilon$.

We can now consider the more general configuration in which x_r may be anywhere in relation to X, but the source and receiver remain many wavelengths above the boundary. If X is less than x_r, one of the above calculation methods applies. If X is greater than x_r, reciprocity can be invoked (reflect the problem in the plane x=L/2, then swap the source and receiver) and then one of the above methods applied.

Finally we note why the source and the receiver have so far been kept at least one wavelength above the boundary. If $\underset{\sim}{t}_1$ (or $\underset{\sim}{t}_2$) is very close to γ the approximation (6), which involves neglecting the integral $R_1(X)$ in equation (5), breaks down. This is because, for x in a small range of γ around $\underset{\sim}{t}_1$ (or $\underset{\sim}{t}_2$), f(x) changes rapidly with x. Thus the derivative of f(x) in the integrand of $R_1(X)$ is very large.

To avoid the consequent inaccuracies which may occur when $\underset{\sim}{t}_1$ or $\underset{\sim}{t}_2$ is within one wavelength of γ, an additional criterion is used for the choice of τ. We require τ to be small enough so that the line $x \leq \tau$ in γ is always at least one wavelength from $\underset{\sim}{t}_1$ and $\underset{\sim}{t}_2$.

GRAZING INCIDENCE RESULTS

Monofrequency Excess Attenuation

We can use the method described above for estimating φ_A to examine propagation over flat ground through a homogeneous still atmosphere. The monofrequency excess attenuation over geometrical spreading due to the presence of the ground can be approximated by

$$A_1 = 20\log_{10}\left|\frac{e^{ikd}}{4\pi d\ \varphi_A}\right| \quad \text{dB} \ . \qquad (10)$$

Propagation from a source above rigid ground to a receiver above absorbing ground has been examined. To model this problem β_1 was set to zero and the dependence of β_2 on frequency was calculated by the Delany and Bazley semi-empirical formula (refs. 9,10), with an effective flow resistivity of $10^5 \text{kgs}^{-1}\text{m}^{-3}$. This value was chosen as being a low value for grassland (ref. 11). (It is found that using two or three times this flow resistivity value causes only a small reduction in the magnitude of the A_1 results, and no change in the trends was observed.) Six configurations of source and receiver heights (h_s and h_r) were examined. Specifically, heights of 5m, 1·5m, and 0·5m were used, with $h_s \geq h_r$ in all cases. For each h_s and h_r combination calculations were carried out at four distances: L=250m, 500m, 1km, and 2km.

We will examine the significance of the proportion of rigid ground between the source and receiver. We can define a useful variable, p_r, by

$$p_r = X/L \ .$$

When the impedance discontinuity is between the source and receiver ($0 \leq X \leq L$), p_r gives the proportion of rigid ground between the source and receiver.

A sample of the results examined is shown in Figures 3a and 3b. Plots like those shown were calculated for all the octave band centre frequencies between 100Hz and 5kHz. Notice that, as is of course expected intuitively, when $p_r \leq 0$ or $p_r \geq 1$ the modelled ground behaves as an acoustically homogeneous plan, absorbing or rigid,

respectively. We therefore now concentrate the investigation only on the range $0 \leq p_r \leq 1$.

Figure 4(a) illustrates a simple curve shape that occurs whenever both kh_s and kh_r are small enough. Half of the plots examined were of this type. We see that A_1 increases monotonically with p_r. The gradient of each curve is greatest at the ends of the range of interest, i.e. near $p_r=0$ and $p_r=1$. At low enough frequencies the curves straighten out.

Figure 4(b) illustrates the disintegration of the orderly patterns seen in Figure 4(a) that occurs when h_s, h_r, or the frequency is increased sufficiently. About a third of the plots examined showed this type of disorderly pattern.

Figure 4(c) illustrates a different pattern that sometimes occurs when the source is higher than the receiver, but neither are so high above the boundary that the disorderly pattern seen in Figure 4(b) occurs. In Figure 4(c), A_1 is less dependent on the location of the impedance discontinuity when $p_r \leq 0{\cdot}3$. Notice that the right half of this plot shows the features observed in Figure 4(a). About a sixth of the plots examined showed this pattern.

When the orderly patterns seen in Figure 4(a) and the right hand side of Figure 4(c) occur, there is usually a range of octave band centre frequencies around 1kHz at which some or all of the curves on a plot are separated, in most of the range $0 \leq p_r \leq 1$, by about 3dB. This approximate 3dB increase in A_1 per doubling of L when propagation is over an admittance discontinuity occurs only for a range of values of kL. The start of this inhomogeneous absorbing ground effect corresponds with the start of a 6dB separation of the A_1 curves at $p_r \leq 0$, which occurs when $kL \approx 2300$. This 6dB increase in A_1 per doubling of L is a homogeneous absorbing ground effect which has been predicted theoretically (ref. 12). Figure 5 illustrates these observations. The range of plots examined show that the inhomogeneous ground effect fails to occur when kh_s or kh_r is large. This failure is observed in the left hand side of Figure 4(c).

Jet Engine Noise

We move on to examine the excess attenuation of a notional broad band environmental noise source. A simple spectral shape representative of a jet engine at full thrust is chosen. The free field 1m third octave band sound pressure level is taken as constant up to 200Hz, above which frequency it is reduced by 0·8dB per third octave band. Third octave band excess attenuations due to the presence of the ground are approximated here by A_1 values given by equation (10), using the band centre frequencies. To make the calculation more realistic we include the B.S.5727 (1979) third octave band free field air attenuations for 20°C and 70% relative humidity.

We consider only source and receiver heights of 1·5m so that the simple A_1 pattern illustrated in Figure 4(a) dominates the results. The process of intensity addition over the third octave bands will produce more moderate excess attenuations for the broad band noise than those calculated for monofrequency sound.

The excess attenuation of the broad band source noise caused by the presence of the ground and by air absorption along the propagation path is

$$A_2 = S_1 - (S_2 + 20\log_{10}L) \quad dB(A) \ ,$$

where S_1 is the total A-weighted sound pressure level of the notional source at 1m distance in the free field, and S_2 is the total A-weighted sound pressure level that we calculate at the receiver position.

Figure 6 shows how A_2 depends on p_r and L. We can see that it is not possible to predict the A_2 values at intermediate p_r from a linear interpolation between the values at p_r=0 and p_r=1. Notice however that, in the range $0{\cdot}25 \leq p_r \leq 0{\cdot}75$, A_2 appears to vary linearly with p_r. Also, in this range, A_2 increases by 5dB(A) per doubling of L. This dependence on L is in reasonable agreement with a commonly used 4dB(A) extra attenuation (of perceived noise level) per doubling of receiver distance from an aircraft source very close to the ground (of unspecified admittance) (ref. 13).

At L=1km and 2km, A_2 varies linearly with p_r in the range $0 \leq p_r \leq 0{\cdot}75$. This is useful because it means that $A_2(p_r)$ can be estimated from $A_2(0)$, the value for homogeneous absorbing ground, which is easier to calculate. The simple predictive equation, which is shown in Figure 5 for L=1km and 2km, is

$$A_2(p_r) = A_2(0) - 14{\cdot}7p_r \quad \text{dB(A)} \ , \quad 0 \leq p_r \leq 0{\cdot}75, \qquad (11)$$

Unfortunately we know of no practical results with which to compare this equation.

CONCLUSIONS

An improved calculation method has been presented for sound propagation over a straight line impedance discontinuity in flat ground. The method is restricted to the case when the impedance discontinuity is perpendicular to the direct source to receiver propagation path. The method is derived from an asymptotic analysis at large wavenumber of an approximate solution of a two dimensional boundary integral equation. Accuracy is adequate for the purpose of examining environmental noise propagation in ideal conditions. A limitation of the method is the assumption of homogeneous still air and flat ground.

Results for long distance grazing incidence monofrequency propagation show that the dimensionless heights (height multiplied by wavenumber) of the source and receiver above the ground are as important as the location of the impedance discontinuity. When these dimensionless heights are small enough, the results are very orderly, as illustrated by Figures 4(a) and (c).

Theoretical results for the excess attenuation, including air absorption, of a broad-band A-weighted notional environmental noise source have been examined. A few simple trends have been noted, in particular, equation (11).

REFERENCES

1. Thomasson, S.-I.: Reflection of Waves From a Point Source by an Impedance Boundary. J. Acoust. Soc. Amer., vol. 59, 1976, pp. 780-785.

2. Chandler-Wilde, S. N.: Ground Effects in Environmental Sound Propagation. Ph.D. Thesis, Bradford Univ., England, Dec. 1988.

3. Habault, D.: Sound Propagation Above an Inhomogeneous Plane: Boundary Integral Equation Methods. J. Sound Vib., vol. 100, 1985, pp. 55-67.

4. Chandler-Wilde, S. N.; Hothersall, D. C.: Integral Equations in Traffic Noise Simulation. In Computers in Mathematical Research (N.M. Stephens and M.P. Thorne, editors), Oxford University Press, 1988, pp. 207-235.

5. Chandler-Wilde, S. N.; Hothersall, D. C.: On the Green Function for Two-Dimensional Acoustic Propagation Above a Homogeneous Impedance Plane. Research Rep., Coventry Polytech., England, 1989.

6. Chandler-Wilde, S. N.; Hothersall, D. C.: Sound Propagation Above an Inhomogeneous Impedance Plane. J. Sound Vib., vol. 98, 1985, pp. 475-491.

7. Durnin, J.; Bertoni, H. L.: Acoustic Propagation Over Ground Having Inhomogeneous Surface Impedance. J. Acoust. Soc. Amer., vol. 70, 1981, pp. 852-859.

8. Klein, C.; Myncke, H.: Sound Field Above an Impedance Discontinuity. Proc. 3rd F.A.S.E. Congress, Göttingen, West Germany, Sept. 1982, pp. 471-474.

9. Delany, M. E.; Bazley, E. N.: Acoustical Properties of Fibrous Absorbent Materials. Applied Acoust., vol. 3, 1970, pp. 105-116.

10. Chessell, C. I.: Propagation of Noise Along a Finite Impedance Boundary. J. Acoust. Soc. Amer., vol. 62, 1977, pp. 825-34.

11. Embleton, T. F. W.; Piercey, J. E.; Daigle, G. A.: Effective Flow Resistivity of Ground Surfaces Determined by Acoustical Measurements. J. Acoust. Soc. Amer., vol. 74, 1983, pp. 1239-44.

12. Attenborough, K.: Review of Ground Effects on Outdoor Sound Propagation From Continuous Broadband Sources. Applied Acoust., vol. 24, 1988, pp. 289-319.

13. Davies, L. I. C.: A Guide to the Calculation of NNI. Direct. Operat. Res. Anal. Comm. 7908, 2nd Ed., C.A.A., London, 1981.

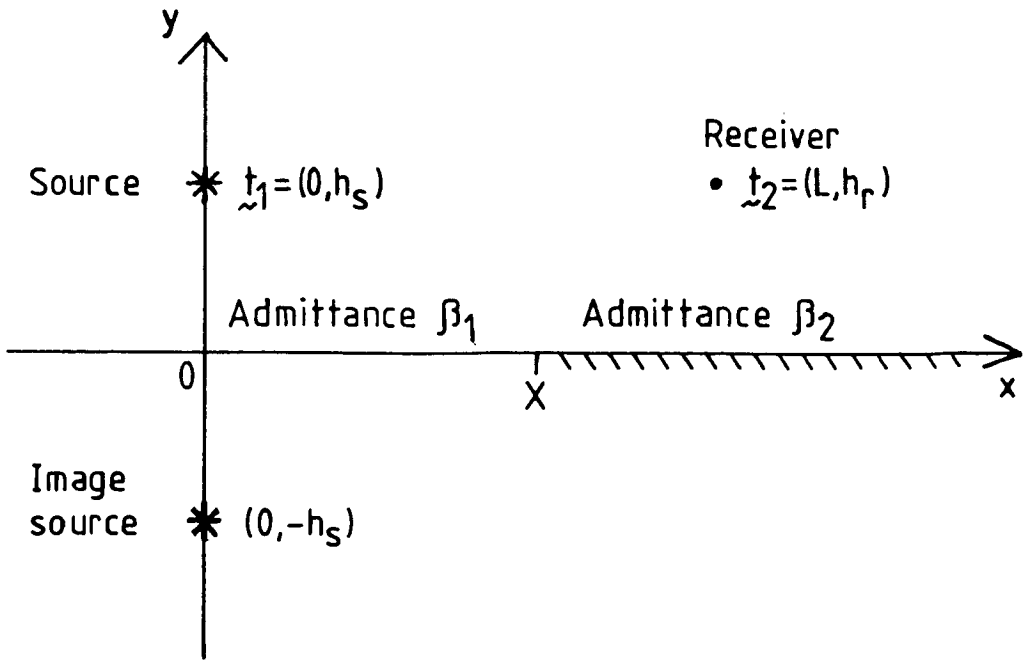

Fig.1 The problem in three dimensions.

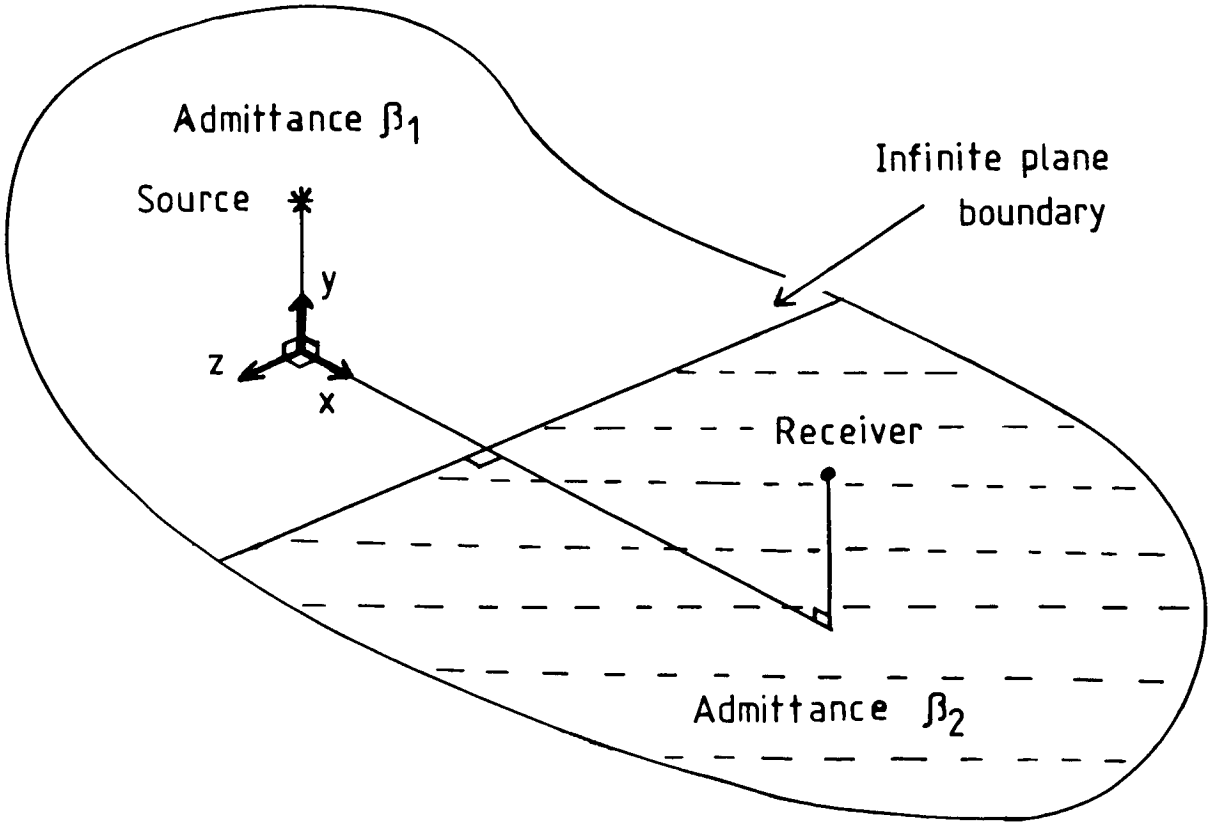

Fig.2 The problem in two dimensions.

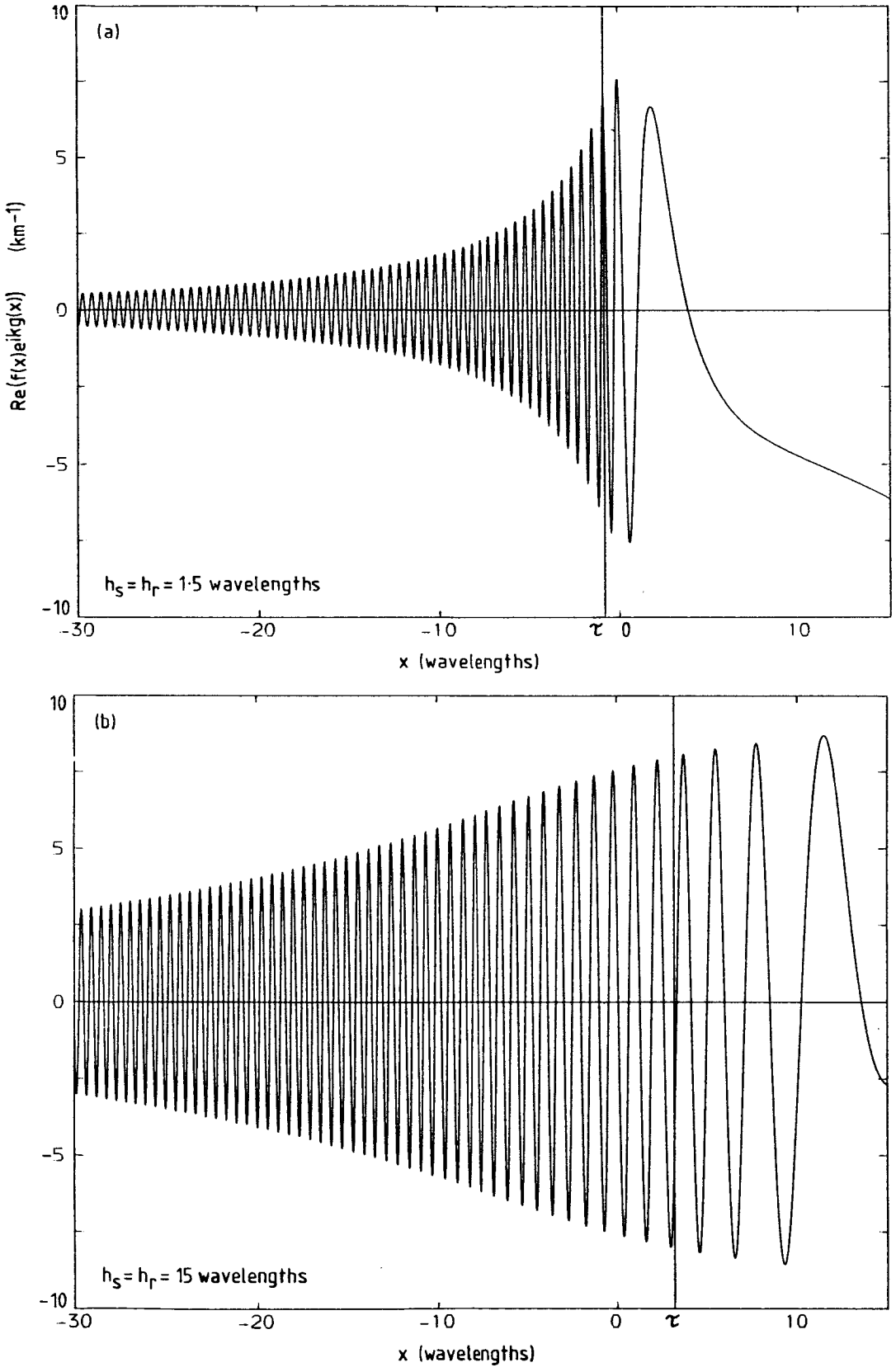

Fig.3 The real part of the integrand in the integral I(X), plotted against x over the range $1 \leq x \leq x_r$. L=30 wavelengths, β_1=0, β_2=0·13603-i0·13456.

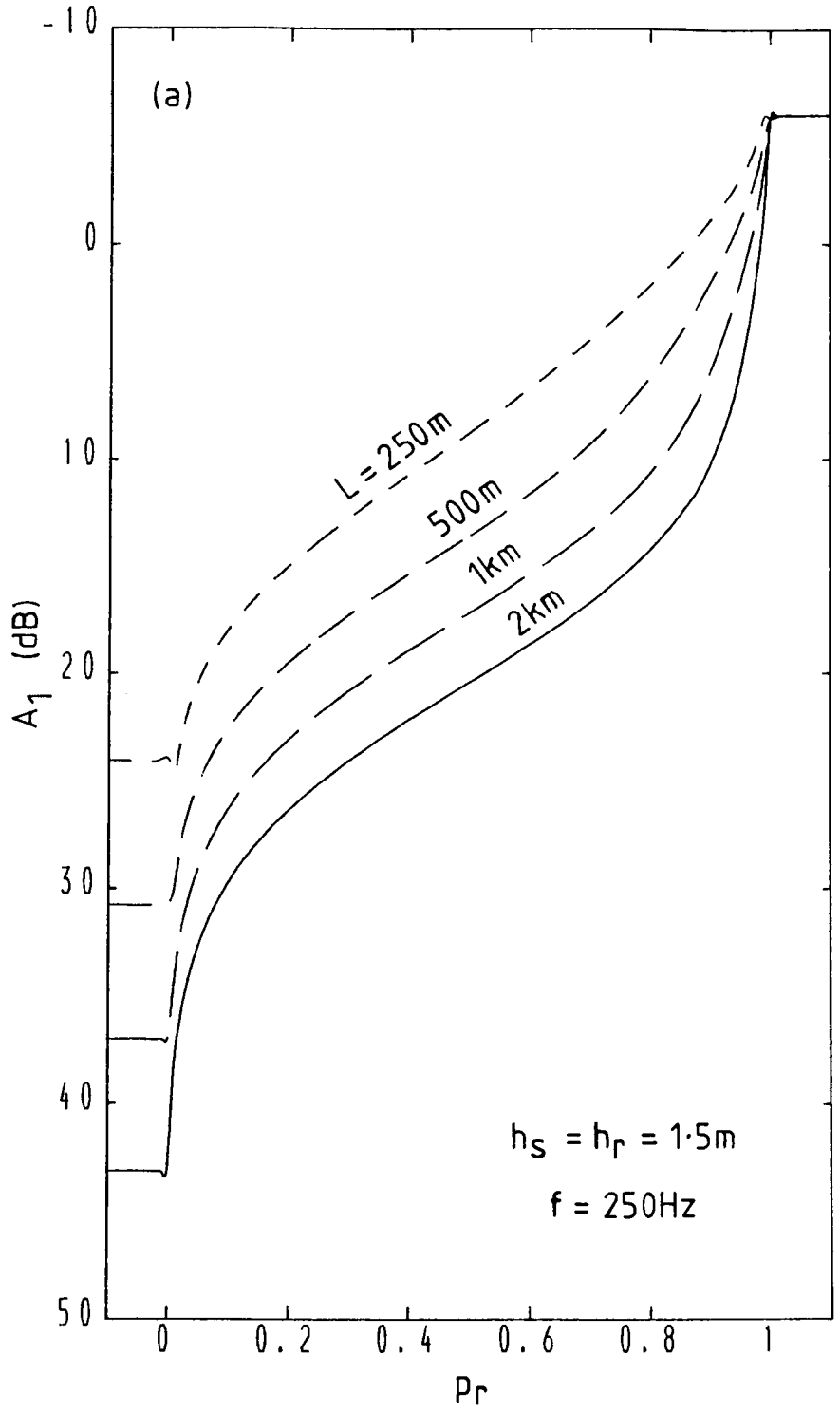

Fig.4a Monofrequency excess attenuation over geometrical spreading at four long distances, plotted against the proportion of rigid ground. h_s=h_r=1·5m, f=250Hz.

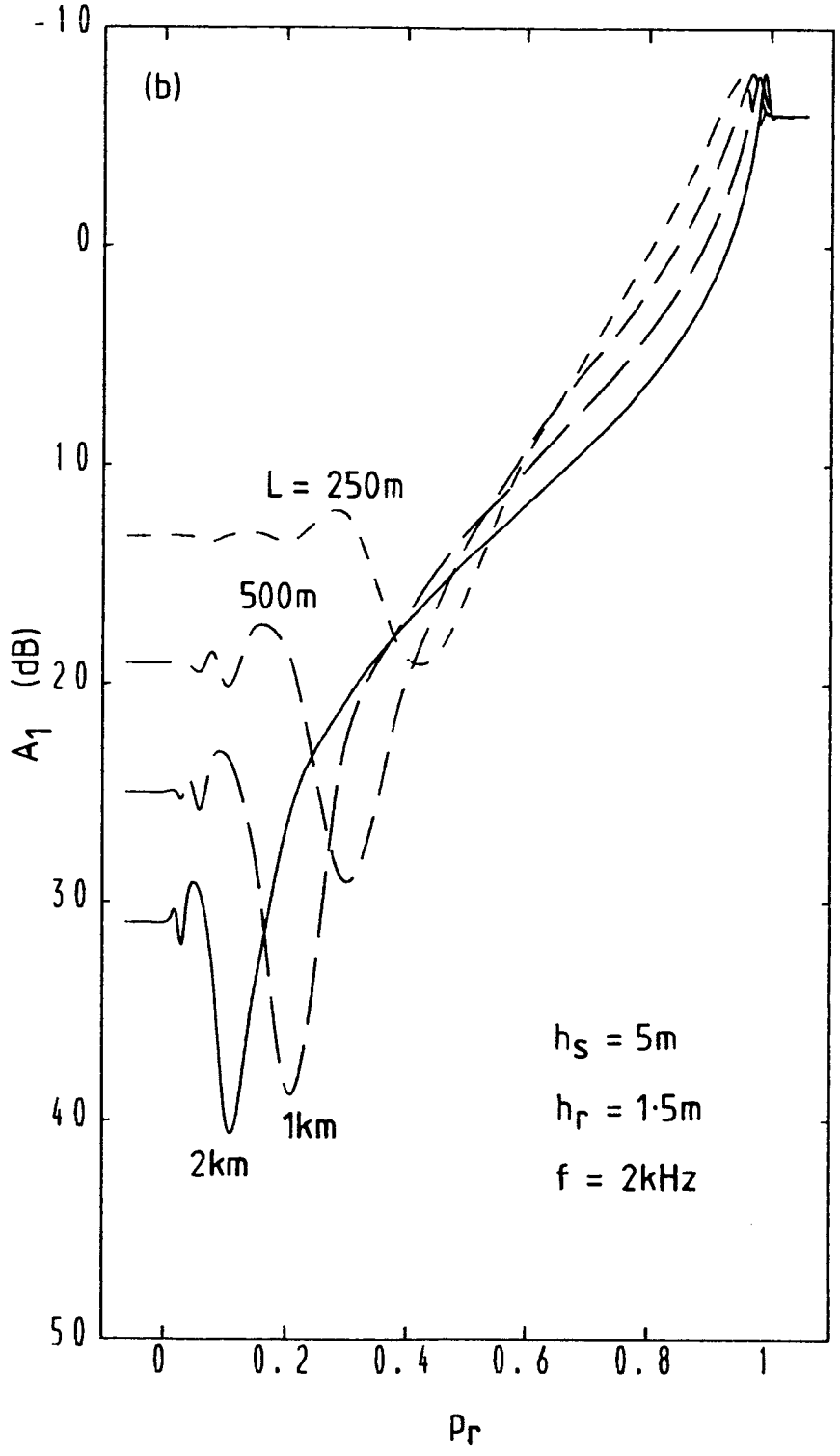

Fig.4b Monofrequency excess attenuation over geometrical spreading at four long distances, plotted against the proportion of rigid ground. h_s=5m, h_r=1.5m, f=2kHz.

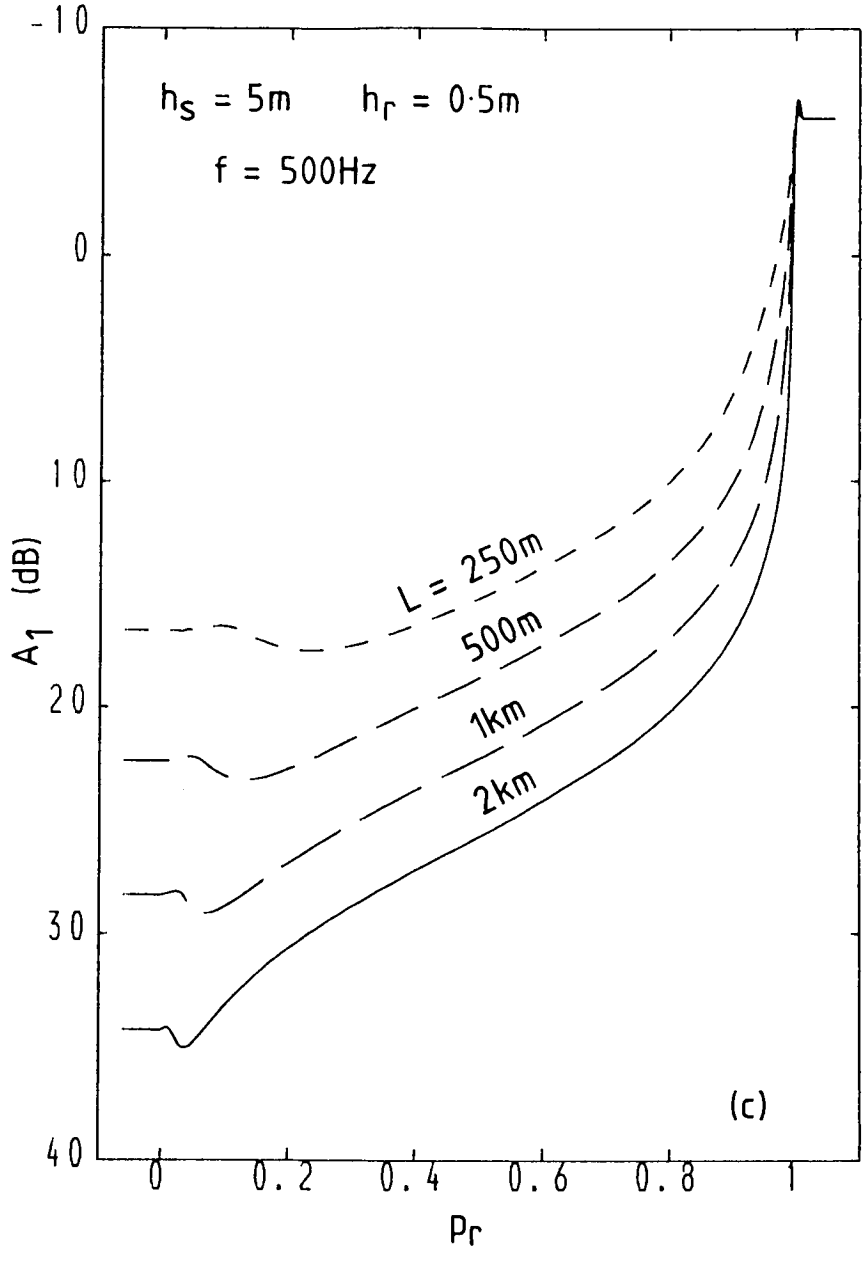

Fig.4c Monofrequency excess attenuation over geometrical spreading at four long distances, plotted against the proportion of rigid ground. h_s=5m, h_r=0.5m, f=500Hz.

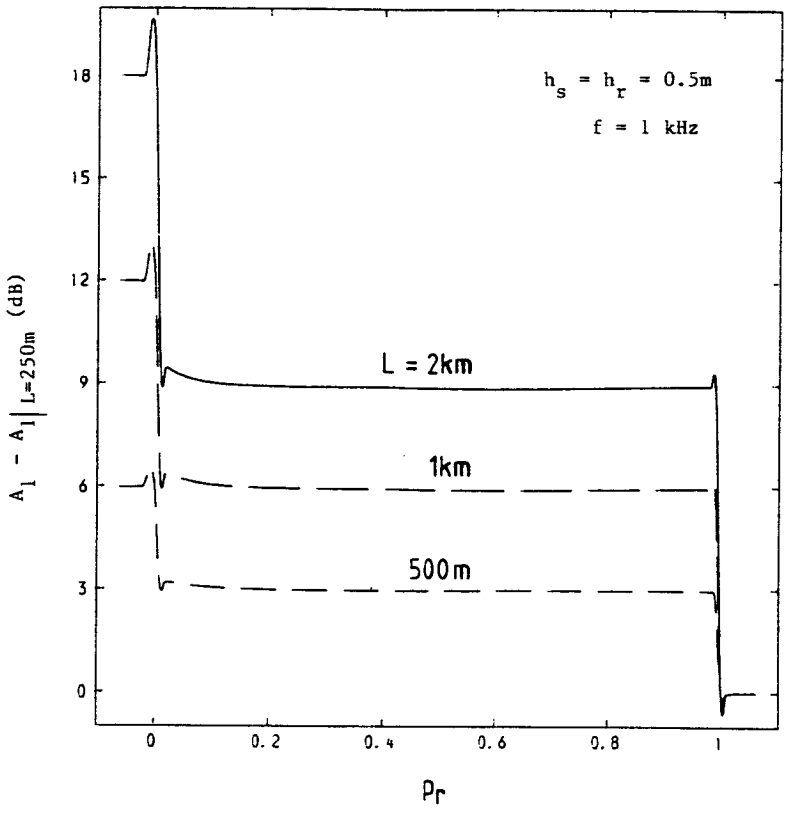

Fig.5 A_1 at L=500,1000,2000m relative to A_1 at L=250m, plotted against p_r.

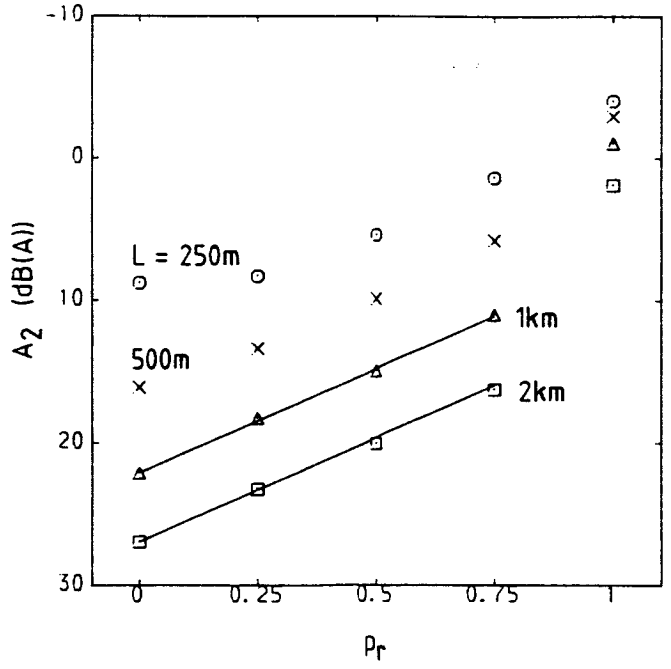

Fig.6 The attenuation of propagated noise from a notional jet engine source, plotted against p_r. Solid lines are equation (11).

ADRPM-VII APPLIED TO THE LONG-RANGE ACOUSTIC DETECTION PROBLEM

Edward Shalis, Gerald Koenig
Countermeasures Branch
Tank-Automotive Command
Warren, Mi 48090

INTRODUCTION

An acoustic detection range prediction model (ADRPM-VII) has been written for IBM PC/AT machines running on the MS-DOS operating system. The software allows the user to predict detection distances of ground combat vehicles and their associated targets when they are involved in quasi-military settings. The program can also calculate individual attenuation losses due to spherical spreading, atmospheric absorption, ground reflection and atmospheric refraction due to temperature and wind gradients while varying parameters effecting the source-receiver problem. The purpose of this paper is to examine the strengths and limitations of ADRPM-VII by modeling the losses due to atmospheric refraction and ground absorption, commonly known as excess attenuation, when applied to the long range detection problem for distances greater than 3 kilometers.

BASIC ASSUMPTIONS OF ADRPM-VII

The basic assumptions of ADRPM-VII are the following:

o ADRPM is based on simplified atmospheric conditions adjusted to a standard day during the seasonal year. In the real world, a standard day does not exist since temporal variations must be allowed for in all environmental propagation measurements. The effect of these variations can only be measured with sound speed profile soundings.

o The noise emitted by the source is omnidirectional, broadband and continuous.

o The primary propagation path is near the surface of the ground.

o All attenuation elements are considered independent of each other with the total attenuation arrived from the summation of its individual parts.

o The ground is defined as a rigid plane or a plane of finite impedance and the model uses a table of values of ground cover loss that is linearly dependent on the distance from the source.

o "The model is developed in the context of a need to estimate noise levels of surface vehicles at distances ranging from tens of meters to hundreds of meters for a relatively wide range of environmental conditions" according to Fidell and Bishop (ref. 1).

ATTENUATION DUE TO REFRACTING ATMOSPHERES

The model calculates propagation loss in a refractive atmosphere by applying a correction term to the reflected and surface wave terms derived from non-refracting atmospheres. This correction term, which is based on ray tracing, considers the existence of shadow zones for upward refraction and an intensity ratio modification for the downward refracting case (ref. 2).

Several representative atmospheres have been chosen from the given meteorological profiles in ADRPM for analysis of the models refractive effects. Average wind velocities u(r), surface roughness parameter z(o), and Monin stability length L are given for each selected profile:

Neutral Profiles: Vertical temperature lapse of -.01 degrees Kelvin per meter and turbulence due to wind only. The following latitude and season was chosen for analysis:

1. Mid-latitude (45°N), summer, with

u(r) = 3.3 mph,
z(o) = 0.15
surface temperature = 73.8°F.

Stable Profiles: A positive temperature gradient and damped turbulence due to thermal inversion only.

1. Mid-latitude (45°N), summer night, with

u(r) = 2.5 mph
z(o) = 0.15
L = 39.65
surface temperature = 62°F
temperature gradient = .02 for 0-40 meters
= .01 above 40 meters

2. Midlatitude (45°N), winter night, with

u(r) = 4.4 mph
z(o) = 0.15
L = 38.6
surface temperature = 21°F
temperature gradient = 0.07 for 0-40 meters
= 0.02 above 40 meters

Unstable Profiles:

1. Midlatitude (45°N), summer daytime, with

u(r) = 3.6 mph
z(o) = 0.15
L = -16.88
surface temperature = 84°F
temperature gradient = -.05 for 0-65 meters
-.02 65-165 meters
-.01 above 165 meters

2. Midlatitude (45°N), winter daytime, with

u(r) = 6.5 mph
z(o) = 0.15
L = -243.5
surface temperature = 36°F
temperature gradient = -.02 for 0-15 meters
= -.01 15-25 meters
= -.004 above 25 meters

A:Attenuation Due To Upward Refraction

The upwardly bending sound energy algorithms have evolved through the efforts of several investigators, with Felt (ref. 3) making the greatest contribution. Felt's ray tracing procedure requires a numerical solution to a differential equation to determine the ray path as a function of the initial angle of propagation. For a specified source height h(s) and receiver height h(r), attenuation is based on the distance to the shadow zone d(s), which is defined by:

$$d(s) = (h(s)/k)^{1/a} + (h(r)/k)^{1/a} \qquad (1)$$

where: h(s) = source height
h(r) = receiver height
d(s) = distance to the shadow zone

and a,k are parameters that are determined from Snell's law of refraction for various meteorological profiles.

The attenuation due to upward refraction is capped by a maximum frequency dependent value that is dependent on the distance to the shadow zone, as determined from equation 1. The value of attenuation A(e) is calculated from:

$$A(e) = A(max)(1- d(s)/d) \qquad (2)$$

For a source to distance receiver d, the model considers two cases:

d < d(s) where the receiver is not in the shadow zone
d > d(s) where the receiver is in the shadow zone

B:Attenuation Due To Downward Refraction

For the downwardly refracting case, a fitting function based on the initial propagation angle α and the distance from the source to where the ray strikes the ground x is given by (ref. 4):

$$\tan \alpha = MX^b \qquad (3)$$

where M,b are determined in much the same way as a,k were determined for the upwardly refracting case in equation 1.

ATTENUATION DUE TO GROUND IMPEDANCE

The attenuation due to the effect of a sound wave interacting with a surface of finite impedance is based on the work by Embleton, Piercy, Olson (ref. 5) and Delany,Bazley (ref. 6). ADRPM-VII calculates the effect of ground impedance based entirely on the coherence of incoming waves. However, the stable conditions assumed for the phase dependent calculations are unlikely to exist for longer ranges since the effect of inhomogeneity on the delicate phase relationships is ignored.

Nevertheless, the theory predicts losses of 50-70 dB for some conditions. Since losses beyond 30 dB are rarely observed, the model handles this empirical discrepancy by decreasing the effects of ground impedance for distances greater than 500 meters.

In addition , the model accounts for a non-uniform surface by requiring a single user supplied parameter. This parameter, h, is the root mean square surface roughness height. Based on reference 6, h yields a smoothness, s, that represents the fraction of the reflected energy that is specularly reflected.

However, the unique topography along the propagation path is not included in the model. This is an important omission since sloping ground can control the phase as well as serve as a barrier by intercepting incoming rays.

RESULTS AND DISCUSSION

Field data of stationary and moving helicopters have been analyzed over ranges from 300 meters to 12 km. The results show a built-in variability of the continuously received signal for ranges between 2 and 5 km. At these source-receiver distances, the refractive atmospheric state, with all its existing temperature and changing wind directions, will have a variable attenuation effect on the propagating rays and consequently produce a variable received signal.

In the field, it remains difficult to determine the unique local sound speed profile for all threat directions, especially since the sound speed profile can change with the next gust of wind or the next reversal of wind direction. This problem of measuring time varying speed profiles occurs at all field locations that we have visited across the United States. However,the meteorological conditions are still determined only at the detector during ground vehicle testing.

The area of the atmosphere that primarily effects ground vehicle vulnerability for the medium detection distances is in constant change due to its turbulance. A wave propagating through this boundary layer is variable in amplitude and is influenced by the daily cycle of stable and unstable meteorological conditions that repeat themselves several times each day. TACOM data shows that noon time provides the largest variation of amplitude, sometimes as much as 7 to 8 dB. The fluctuations are less and also slower during the morning and early part of the evening. In all cases, it is best to obtain sound speed profiles each time that a set of data is

measured, with as many locations as possible, but at least two extreme readings that would cover the source and the projected receiver distance.

For ranges beyond 5 km, field data signals are intermittent, where there may be no signal received for long segments of the propagation path. This behavior is expected, since randomness of atmospheric gradients and changing terrain features are common. The potential of several inversion layers existing is always there when the propagation path is great.

In addition, for distances greater than 5 km, the received signal is fairly constant in level and the sound pressure does not follow the classical spherical divergence law. This variation from spherical spreading may be produced by the large number of multiple ray paths that are possible, with multiple ray arrival producing a mixture of phase that tends to produce a fixed sound pressure level.

Since every sound propagation study in the long range is unique, the model was used to calculate the effect of changing a single parameter on the received signal. For instance, the source receiver geometry and the atmospheric refraction conditions were varied by selecting user parameters available from the program. The results of excess attenuation calculations were then compared for different standard days/nights.

Figure 1 represents the total sound pressure level for the isothermal-no wind condition for short detection distances of 200 meters. This case illustrates the removal of refraction as an attenuation effect since the rays will travel in a straight line, with time of travel between equally spaced distances remaining the same. For low frequencies, especially 20 and 80 Hz, atmospheric absorption can be ignored and the curves illustrate the effect of spherical spreading and ground effects.

The effects due to spherical spreading and atmospheric absorption were removed so that losses due to refraction and ground impedance could be examined more closely. Figure 2 examines the effect of isothermal atmospheres, where the excess attenuation is due to ground effects. Figure 2 shows that the model calculates the ground effect as a linear function of distance.

Both atmospheric and wind refractive effects were investigated for the mid-latitude summer neutral profile for both the downwind and upwind cases, as seen in Figures 3 and 4. The excess attenuation is capped at 1 km and remains fixed for the entire range beyond 1 km. For the upwind case, the cap starts at 2 km and the values remain fixed throughout the remaining ranges. One point should be made at this time; the values of excess attenuation for both cases are too low and refractive effects appear to be missing from 2 km onwards.

The change in the meteorological profile to mid-latitude summer night is shown in Figures 5 and 6 for both wind directions. Again, the values are capped and the excess attenuation due to refraction is too low in value.

Consequently, there is a maximum distance beyond which the model should not be used. This distance is normally 1 km but can be extended to 2 km for atmospheric conditions that are unusually uniform. After 2 km, a model that uses instantaneous atmospheric readings to determine the velocity of sound profile should be used to calculate propagation losses. This latter model should use statistics determined by the defined topography and atmosphere to discuss variations in the received signal amplitude.

CONCLUSION

ADRPM-VII solves the detection problem even though detailed knowledge of temperature, humidity, variation in terrain features and wind gradients are not available to the user. Given these conditions, the model can give misleading information when compared to a model that performs ray tracing refraction based on accumulated local meteorological information.

Perhaps a two model approach is required to solve the long range detection problem. ADRPM can be used for ranges below two kilometers where general meteorological conditions are approximated by readings at no more than two locations and terrain features are determined visually. Beyond two kilometers, a more elaborate model that is based on detailed atmospheric information would take over and perform the analysis.

REFERENCES

1. Fidell,S., Bishop,D., "Prediction of Acoustic Detectability", TACOM Technical Report No.11949, p.9 (1974).

2. Francis, W.P., "An Analysis of the TARADCOM Acoustic Detection Range Prediction Model", TACOM Technical Report No.12467, pp.39-53 (1979).

3. Felt,J., "Modified Acoustic Range Prediction Model (ADRPM-V)", TACOM Technical Report No.12544 (1980).

4. Felt,J., Ibid, p.10

5. Embleton,T.,Piercy,F. and Olson,N., "Sound Propogation Over Ground of Finite Impedance", J. Acoust. Soc. Am.,Vol.59, pp.267-277 (1976)

6. Delany,M.,and Bazley,E., "Monopole Radiation in the Presence of an Absorbing Plane", J. Sound Vib.,Vol.13, pp.269-279(1970)

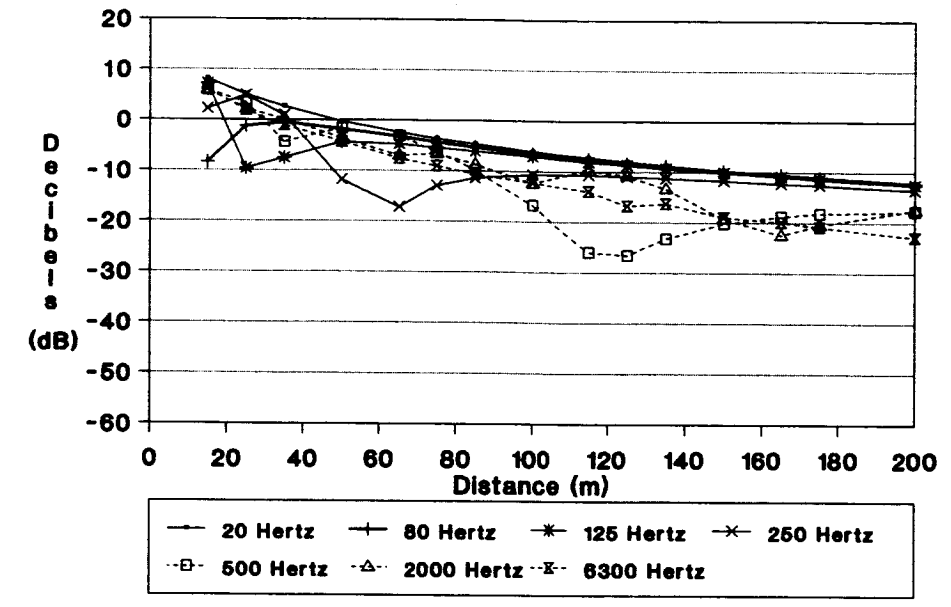

FIGURE 1

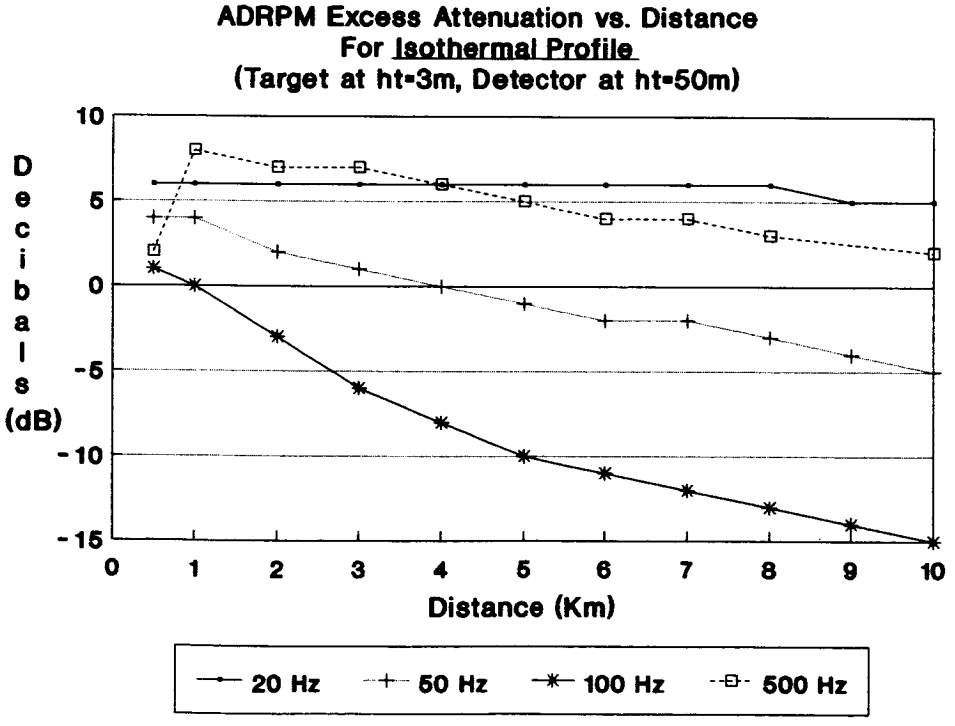

FIGURE 2

C-2

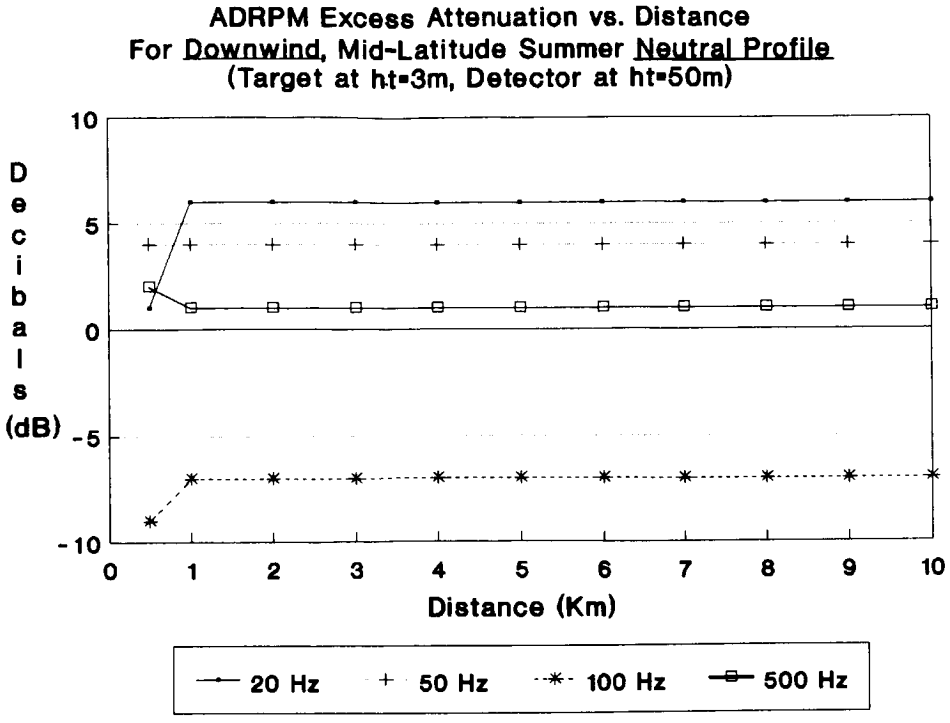

FIGURE 3

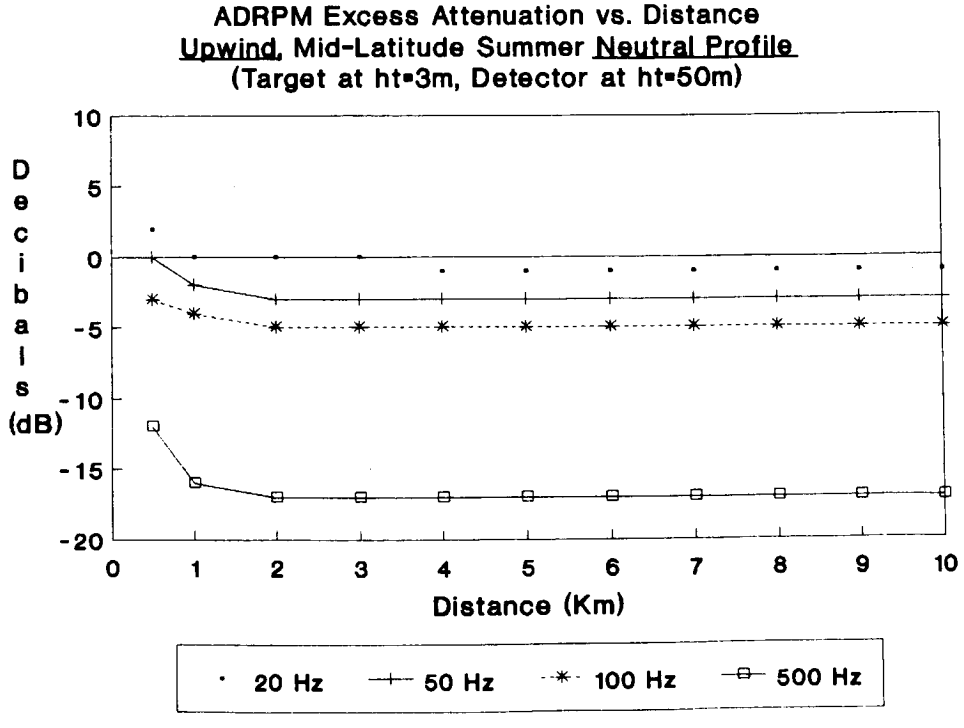

FIGURE 4

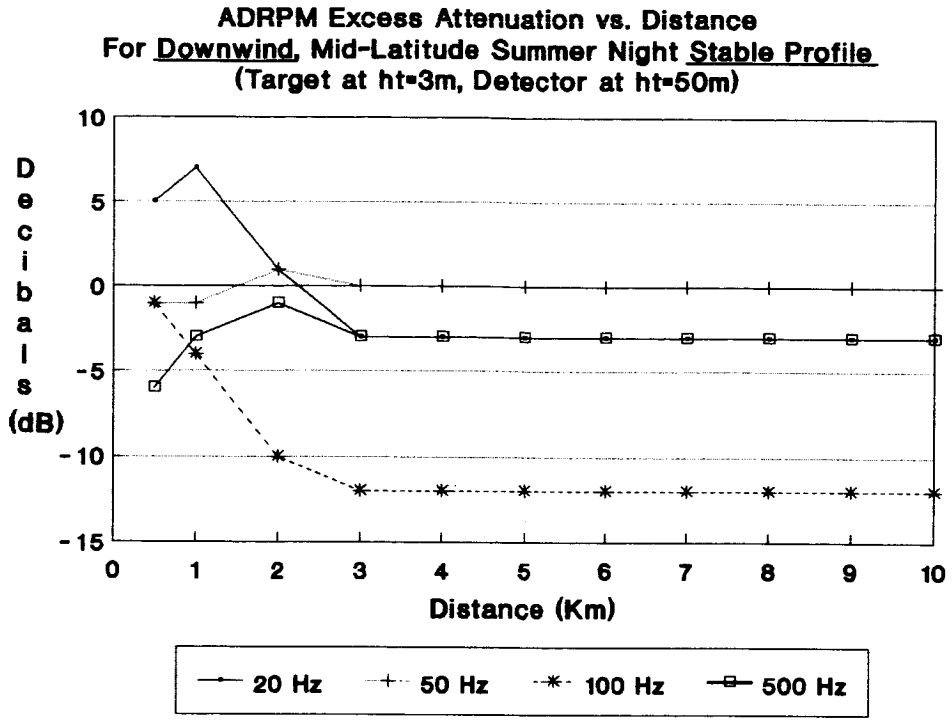

FIGURE 5

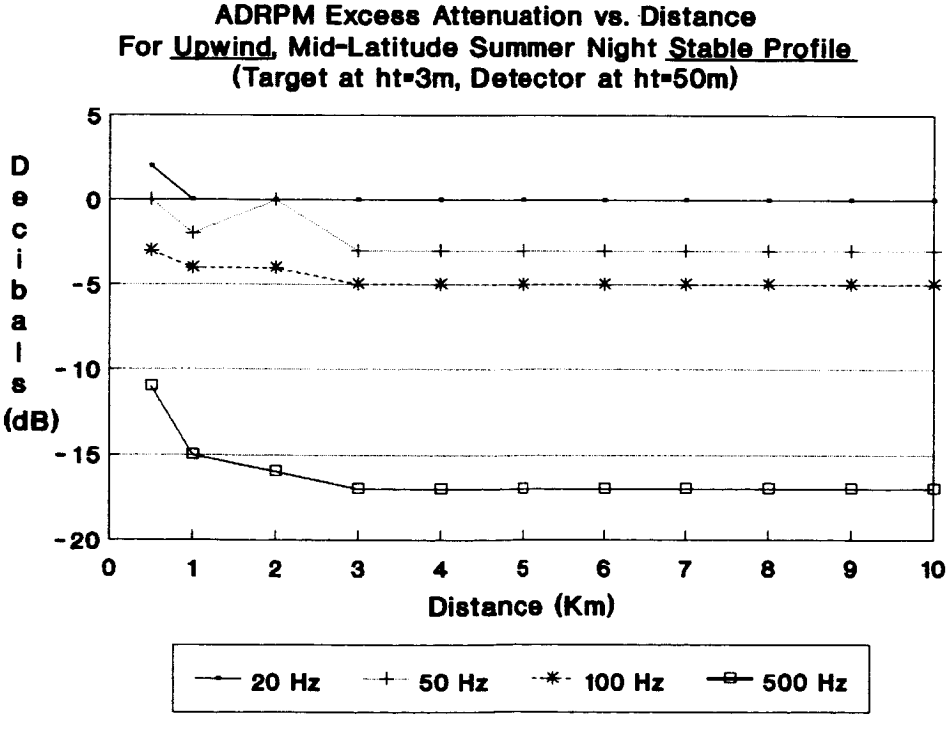

FIGURE 6

Vehicular Sources in Acoustic Propagation Experiments

Dr. Gervasio Prado, James Fitzgerald, Anthony Arruda and George Parides

TEXTRON Defense Systems
201 Lowell St.
Wilmington MA 1887

Abstract

One of the most important uses of acoustic propagation models lies in the area of detection and tracking of vehicles. Propagation models are used to compute transmission losses in performance prediction models and to analyze the results of past experiments. Vehicles can also provide the means for cost effective experiments to measure acoustic propagation conditions over significant ranges. In order to properly correlate the information provided by the experimental data and the propagation models, the following issues must be taken into consideration:

- The phenomenology of the vehicle noise sources must be understood and characterized.
- The vehicle's location or "ground truth" must be accurately reproduced and synchronized with the acoustic data.
- Sufficient meteorological data must be collected to support the requirements of the propagation models.

This paper treats the experimental procedures and instrumentation needed to carry out propagation experiments. Illustrative results are presented for two cases. First, a helicopter was used to measure propagation losses at a range of 1 to 10 Km. Second, a heavy diesel-powered vehicle was used to measure propagation losses in the 300 to 2200 m range.

1. Introduction

The development of acoustic propagation models has made significant advances in recent years resulting in accurate and practical propagation models such as those based on the Fast Field Program and the Parabolic Equation. Given sufficient meteorological data with

which to derive an accurate sound velocity profile, these programs model acoustic propagation losses quite accurately. Progress is also being made in the more difficult problem of modeling the effect of atmospheric turbulence on sound propagation.

A very significant sector of the uses for acoustic propagation models is in detection and tracking problems. In these systems, signals gathered by a microphone array are used to determine the location and track of a vehicle. Both air and ground vehicles are of importance in these applications. Acoustic propagation models play a very important role, being used to either predict performance under new conditions or to analyze the results of an experiment. In this paper we describe the methodology for the analysis of data involving vehicular sources and describe results obtained from two different tests: one, a long range experiment using a helicopter; the second, a mid range experiment, using a heavy, Diesel powered vehicle.

2. Approach

The essential elements necessary for the analysis of propagation data generated by vehicles are: a) a thorough understanding of the phenomenology of the vehicular sources, b) accurate positional data of the target vehicle's trajectory (ground truth data) and c) sufficient meteorological data to reconstruct the propagation conditions.

2.1 Source Phenomenology

In a test where the target vehicle is operating freely it is impractical to monitor the source strength continuously, therefore our knowledge of the source strength must be based on prior knowledge of the source's characteristics and whatever can be inferred by monitoring the observable parameters such as aspect angle or engine RPM. We will consider two types of vehicles, helicopters and heavy diesel powered vehicles.

Helicopters provide an almost ideal source for long range propagation measurements. The noise generated by the main and tail rotors is loud and periodic with a relatively low fundamental frequency. In the spectral domain, helicopter signatures are characterized as families of narrow-band spectral lines. Fundamental frequencies of 10 to 30 Hz are typical. Source levels can reach 144 dB (re 20 micro-Pa in one Hz bands). Helicopters also operate at nearly constant blade rotational speed, as can be appreciated in a spectrogram (Figure 1), where the only frequency variations are those caused by the Doppler effect as the trajectory geometry changes. Strong aspect angle dependencies exist, both in the horizontal and the vertical planes (Figure 2). The amplitude of the rotor noise will also show a velocity

dependency proportional to the 12th power of the blade-tip Mach number (Figure 2). For a full treatment of helicopter noise characteristics, see Reference 1.

Heavy Diesel-powered vehicles are easily detected at short to medium distances. Like helicopters, the spectral characteristics of vehicle noise are dominated by families of narrow-band harmonic components. Unlike helicopters, the frequency history of these components is highly variable. Rapid changes in engine RPM occur in response to operator actions, road conditions and gear changes. The amplitude of these narrow-band components is strongly dependent on engine load and RPM, as shown in Figure 3. From the sensor location, we must be content with observing only engine RPM. A good treatment of ground vehicle noise can be found in Reference 2.

2.2 Vehicle Location Data

Vehicle position data must be collected and synchronized with the acoustic data in order to measure propagation losses. In long range experiments or when the target is moving very fast, acoustic propagation delays must be accounted for.

Helicopters and other aircraft can be tracked accurately with a radar system, if available. A more cost effective approach is to obtain tracking data from an Air Traffic Control facility, if the target is equipped with an ATC Beacon transponder. Such data can be obtained by prior arrangement with the local FAA facility.

Ground targets can be tracked with an RF multilateration system, such as the Motorola Falcon Position Location System (PLS). This system is particularly convenient, since it allows tracking of multiple targets at a one Hz rate with digital data output. As an inexpensive alternative, the position of a ground target can be tracked by maintaining radio contact with one of the vehicle operators, who calls in "marks" as they go by pre-surveyed positions.

Accurate ground truth is a necessity in these kinds of propagation experiments, but it need not be an inordinate expense if the proper procedures are worked out.

2.3 Meteorological Data

Meteorological data is a critical element of the propagation measurement, since it gives us the data necessary to understand the results of our experiment.

The necessary meteorological information consists of sound velocity profiles, pressure and humidity. Sound velocity profiles are the most difficult to obtain. Traditional methods use

balloon sounding; SODAR devices are also being used at a limited number of sites. Tower measurements provide adequate data for short range experiments, and can fill the low altitude gap in the data provided by most balloon soundings.

With progress being made in the modeling on the effects of turbulence on sound propagation, there is a need for more 'fine grained' measurements of the sound velocity profile. These gaps will have to be filled by more dense and frequent measurements of the lower atmosphere.

3. Experiment Descriptions

We will discuss the results of two propagation experiments using vehicular data. In the first a helicopter was tracked from a distance of 10 Km, in the second a diesel powered vehicle was tracked to a distance of 2.2 Km.

3.1 Helicopter Test

A test using a helicopter was made following a nearly radial trajectory starting at a distance of 10 Km. The helicopter flew at a speed of 185 Km and a height of 152 m. At the point of closest approach, it came within a distance of 500 m from the sensor site. The signature recorded by the sensors was shown in the form of a spectrogram in Figure 1. The fourth harmonic was tracked automatically to extract frequency and amplitude data (Figures 4). Positional data was obtained with a radar tracking system and time-synchronized with the acoustic data. The constant speed trajectory allowed us to easily compensate for the propagation delays.

Meteorological data consisted of a balloon sounding made approximately one hour before the test (Figure 5). The Fast Field Program was used to model propagation losses as a function of range, using the sound velocity profiles as input. A two parameter model of the surface acoustic impedance was used, with 300 Rayls of surface flow resistivity and porosity of 0.25.

The results of the measured and modeled transmission losses (TL) are compared in Figure 6. Beyond a range of 4000 m the agreement between experimental and modeled data is quite good. The mean values of the TLs were very close. More important perhaps, the statistics of the variations with respect to their mean levels were also very close. It should be recognized that propagation losses will never be modeled beyond a certain level of precision and that a statistical description of propagation losses is the most realistic outcome given a limited amount of meteorological data. The statistics of signal and noise levels become

specially important in detection problems in order to predict the performance level of specific detection schemes. A study of the statistical properties of long range propagation losses appears to be a very promising area of research.

The measured TL at ranges shorter than 4000m are higher than those predicted by the FFP. Some of the difference can be due to the directivity of the helicopter noise source, which reduces the effective source level as the elevation angle increases, however this effect is smaller than the observed discrepancy. At this point, we must attribute the differences to the inaccuracy of the sound velocity profile used in the FFP relative to the actual conditions at the time of the test. This result just reinforces the importance for accurate and timely meteorological data.

3.2 Ground Vehicle Experiment.

A short to mid range experiment was made using a heavy diesel powered vehicle. The vehicle operated on a road with a nearly radial trajectory starting at a range of 300m and finishing at a range of 2200 m.

The vehicle signature as measured at the sensor location is shown in the form of a spectrogram in Figure 7. An automatic tracking program was used to extract the amplitude and frequency data corresponding to the 6th engine harmonic or Engine Firing Rate; this information is shown in Figure 8.

Lack of sound velocity profile data forced us to model the SVP as that of a 'neutral' atmosphere, that is, a profile matching the nominal atmospheric lapse rate. The neutral atmosphere profile was used as an input to the FFP, producing the TL curve shown in Figure 9, along with the measured TL. The match between the measured and modeled TLs is good at short ranges, but they start to diverge at longer ranges. However, a simplistic model which assumes spherical spreading plus a fairly high absorption term (0.0045 dB / meter) produced an excellent fit to the measured data. We hypothesized that the difference could, in part, be explained by variations in the engine RPM and/or engine load. The noise of heavy diesel powered vehicles is directly affected by engine load and RPM. An attempt was made to compensate for the effect of RPM. This is an imperfect approach, since we should compensate for both the RPM and load, however we do not know of any practical way of inferring load at long distances. The incremental sound pressure level relative to the best fitting model was plotted against the incremental frequency relative to 80 Hz. This result is shown in Figure 10, and shows a clear dependency between SPL and frequency. The SPL figures were then adjusted to a constant 80 Hz (SPL was adjusted downward if the frequency

was more than 80 Hz, upwards if it was less than 80 Hz), producing the curve shown in Figure 11. The corrected TL curve shows a better agreement with the computational models. Some of the extreme variations in TL have also been reduced as a result of the compensation procedure.

4. Conclusions

Two experiments involving a ground vehicle and an aircraft have been analyzed with the help of the Fast Field Program, one of the state of the art acoustic propagation models. By making use of meteorological data as an input to the Fast Field Program and knowledge about the source phenomenology of the vehicles, we were able to obtain a good match between the measured and predicted transmission losses. These results are encouraging and underscore the importance of thoroughly characterizing vehicular sources and of obtaining fine grained meteorological data.

The development of computational models of sound propagation have made dramatic advances in recent years, and their need becomes the driving requirement for data collection in many field experiments.

References

1. F. H. Schmitz and Y.H. Yu, "Helicopter Impulsive Noise; Theoretical and Experimental Status", NASA Technical Memo 84390, Nov. 1983

2. Richard H. Lyon, Lectures in Transportation Noise, Grozier Publishing, Cambridge MA 1973

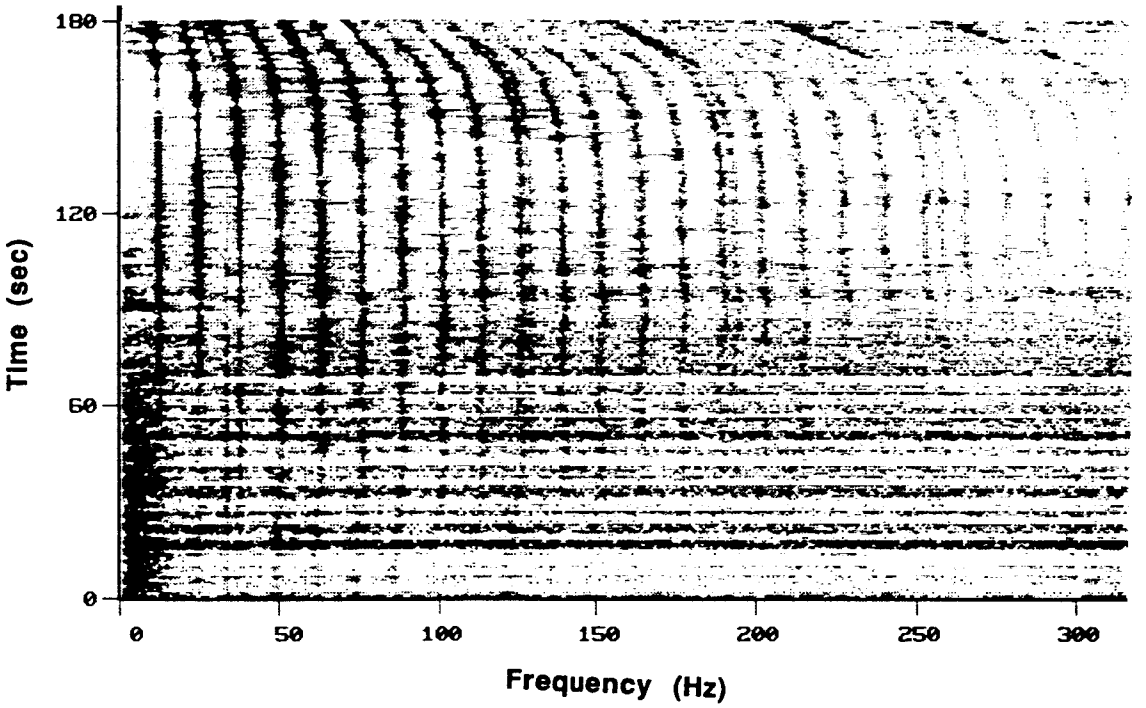

Figure 1 Spectrogram of helicopter signature, recorded during a nearly inbound-radial run.

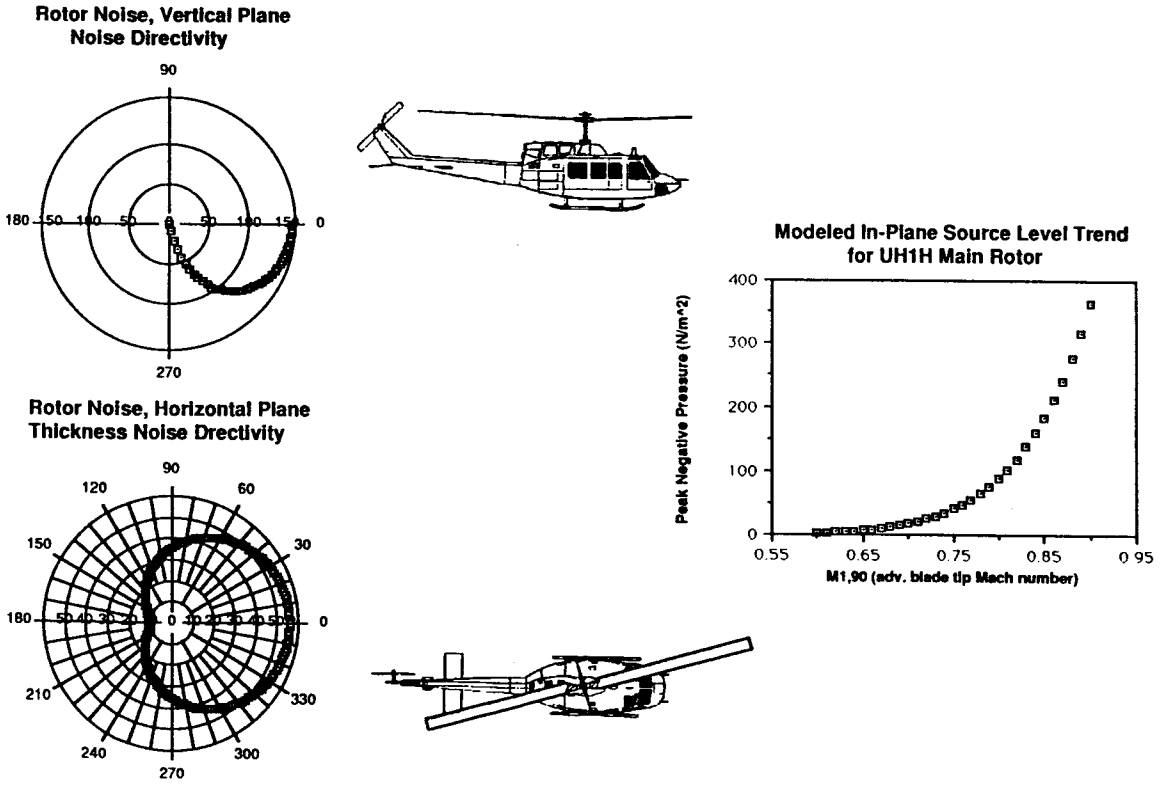

Figure 2 Helicopter noise sources are highly directional and strongly dependent on blade tip velocity (and therefore on helicopter forward speed as well).

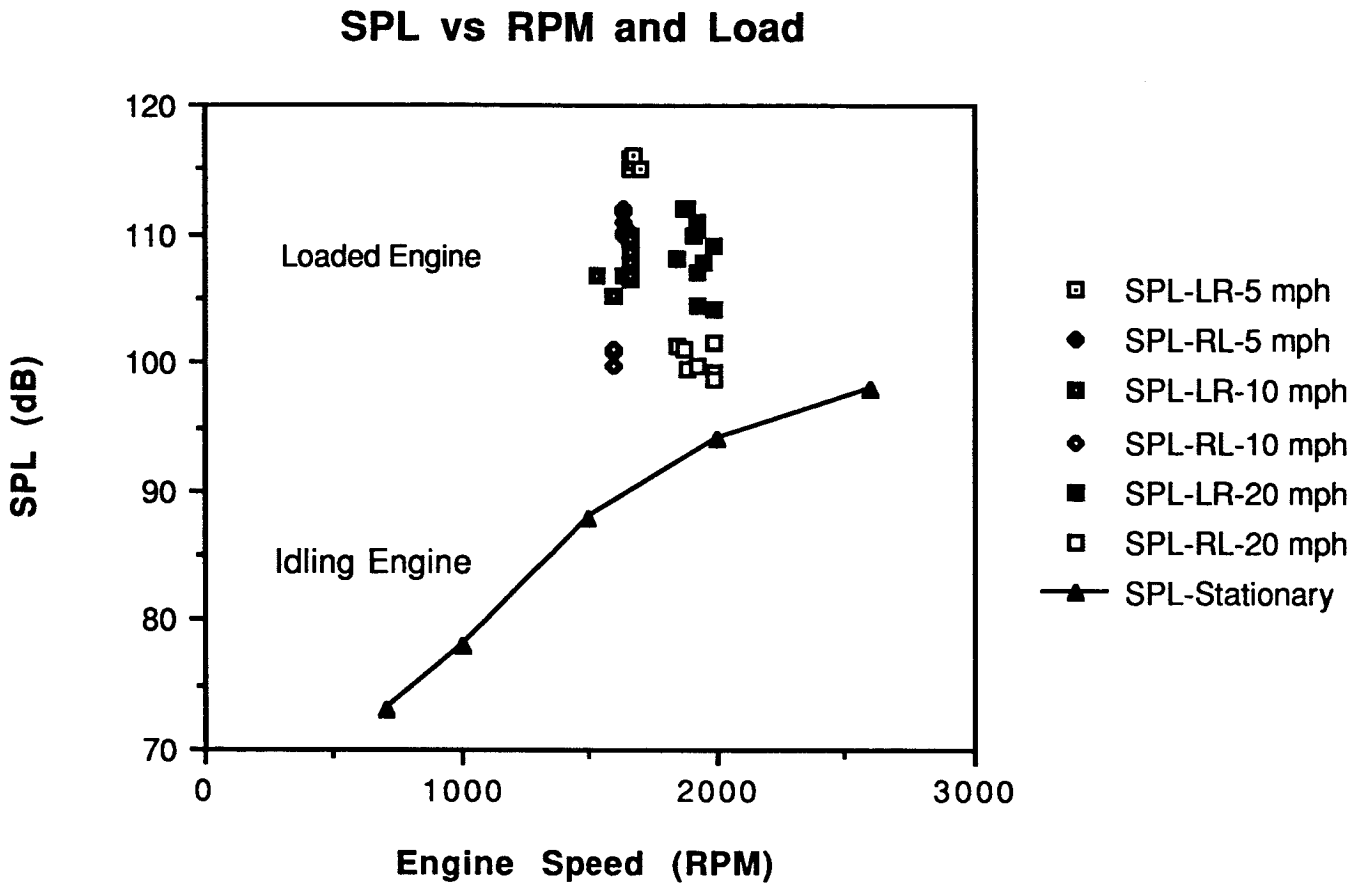

Figure 3 The noise generated by a Diesel-powered ground vehicle is strongly dependent on engine speed (RPM) and load.

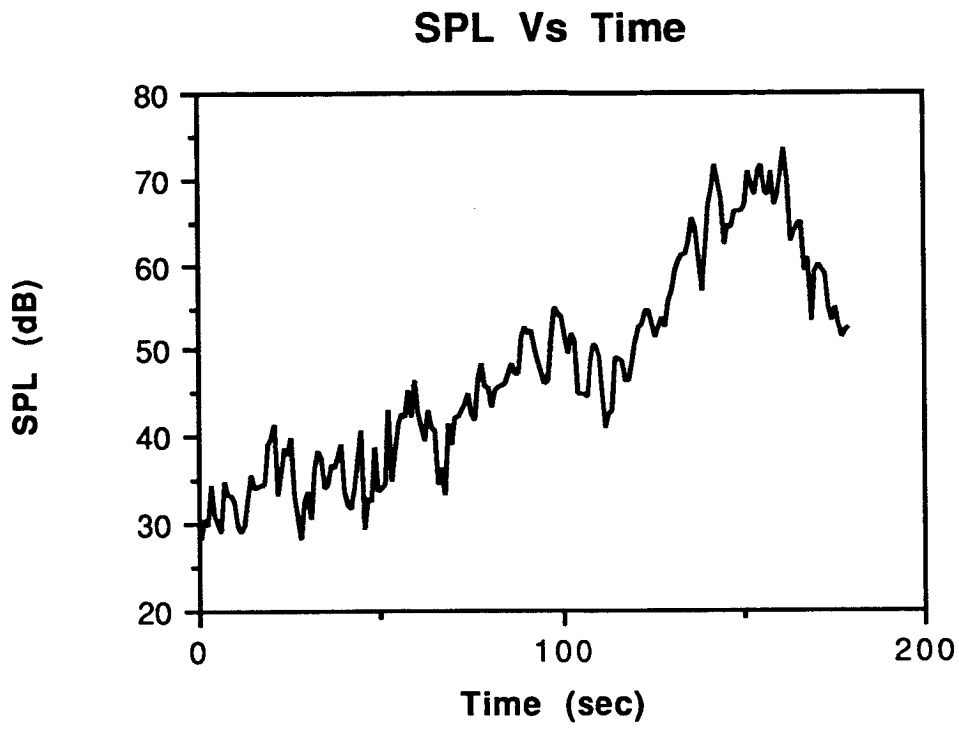

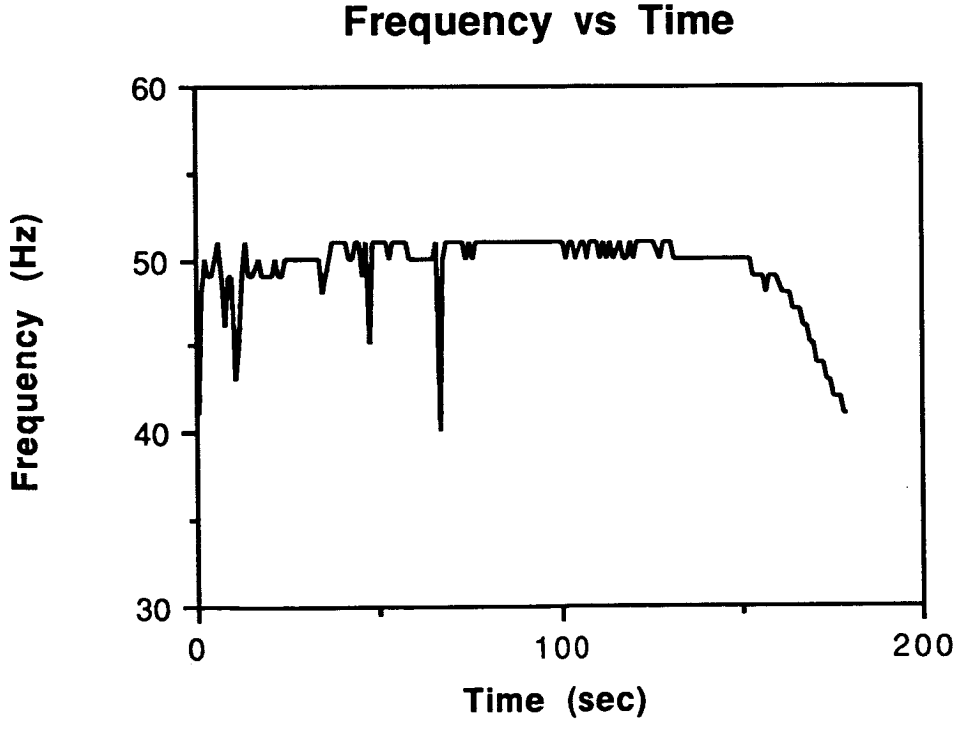

Figure 4 Amplitude and frequency of the fourth harmonic of the helicopter noise signature as a function of time.

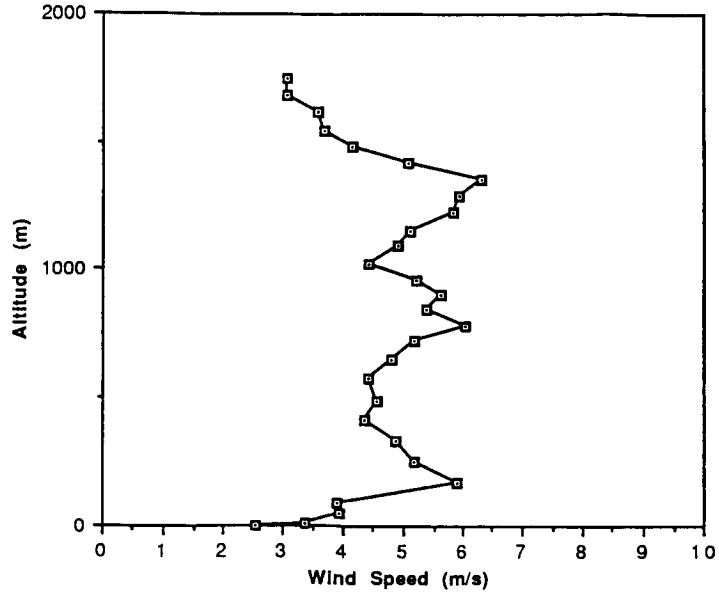

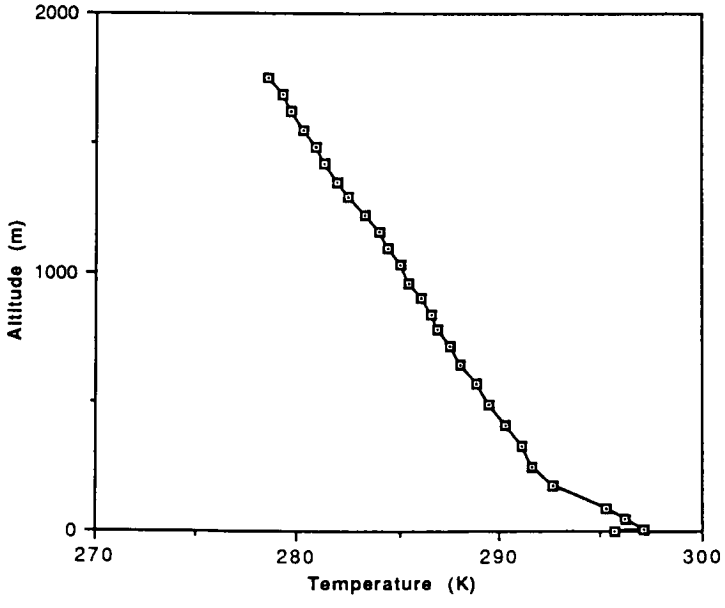

Figure 5 Profiles of temperature and wind velocity prior to the propagation experiment.

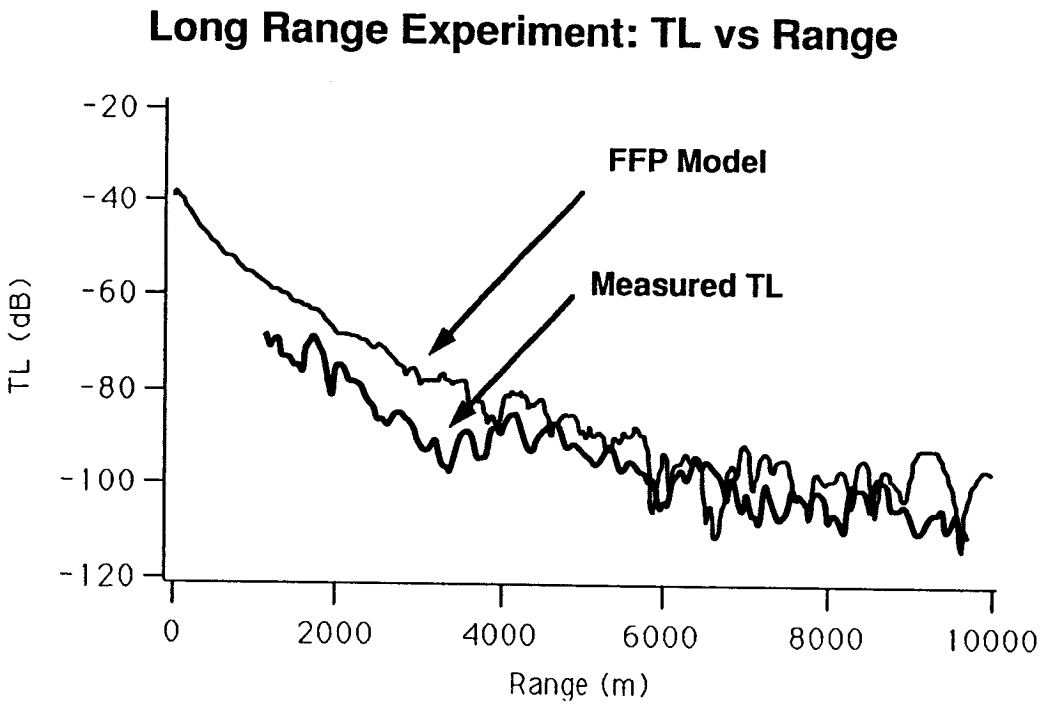

Figure 6 Measured and modeled (using the FFP) transmission losses.

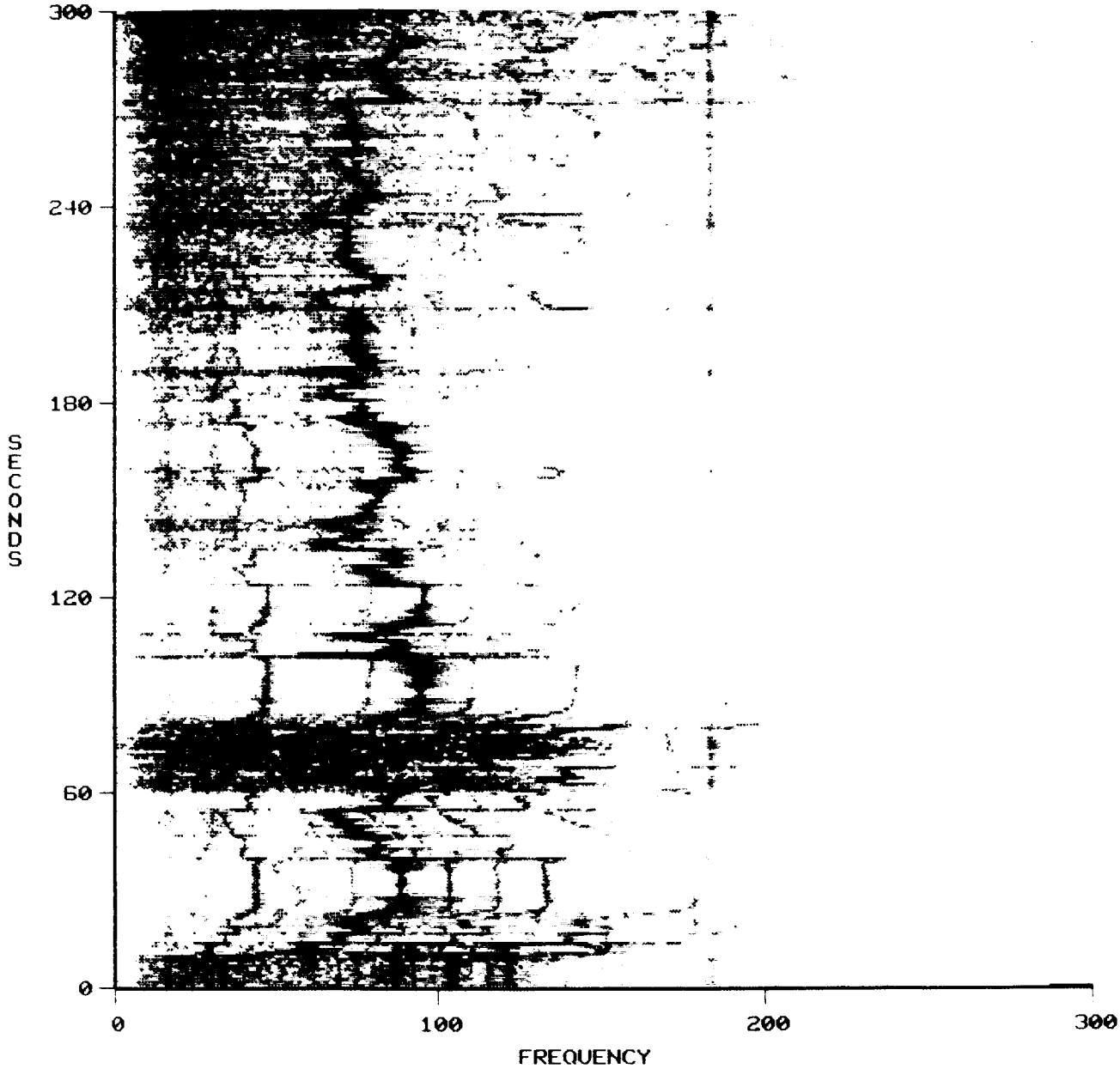

Figure 7 Spectrogram of the acoustic signature of a heavy Diesel-powered vehicle on level ground.

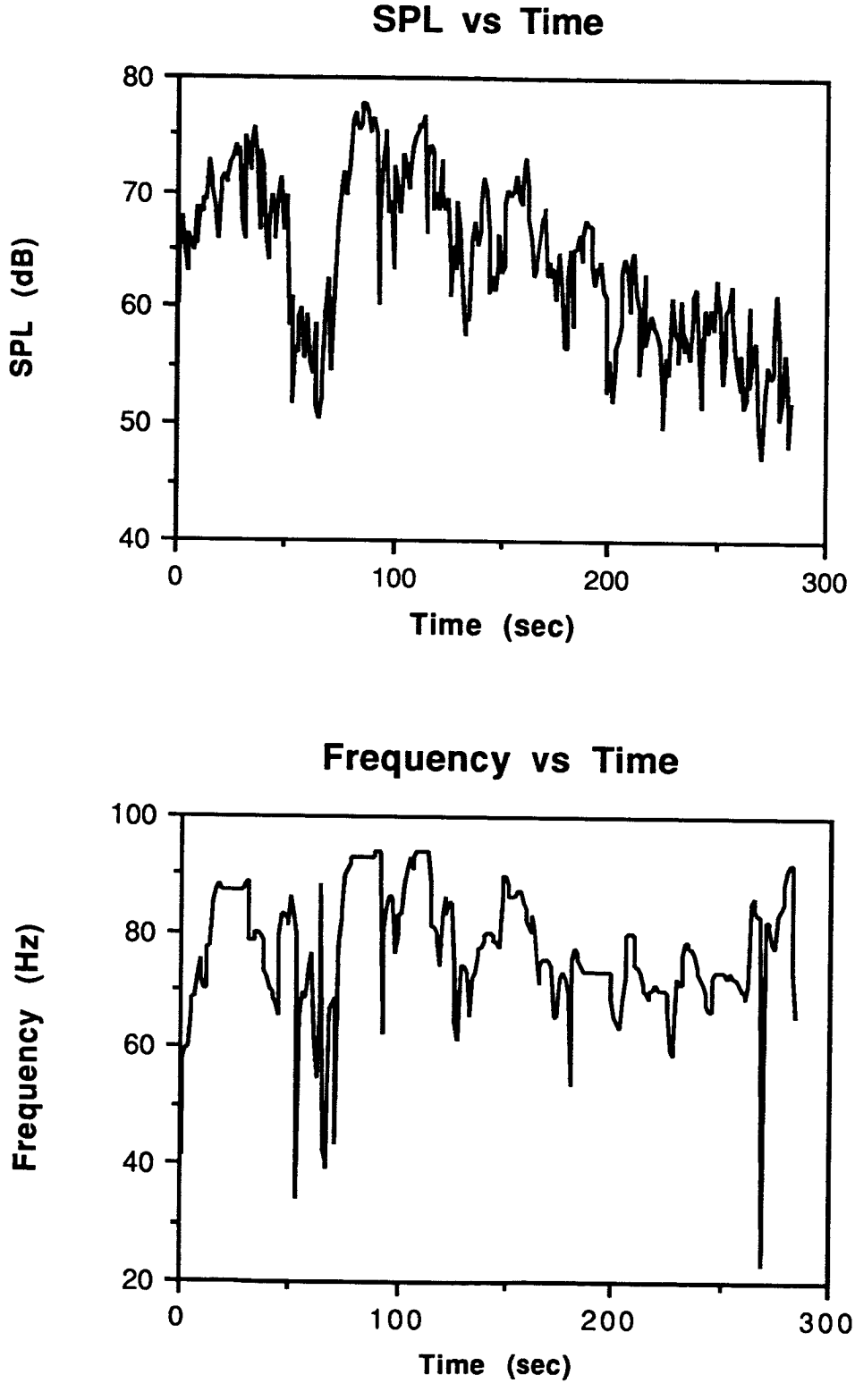

Figure 8 Amplitude and frequency of the main component of the engine noise signature as a function of time.

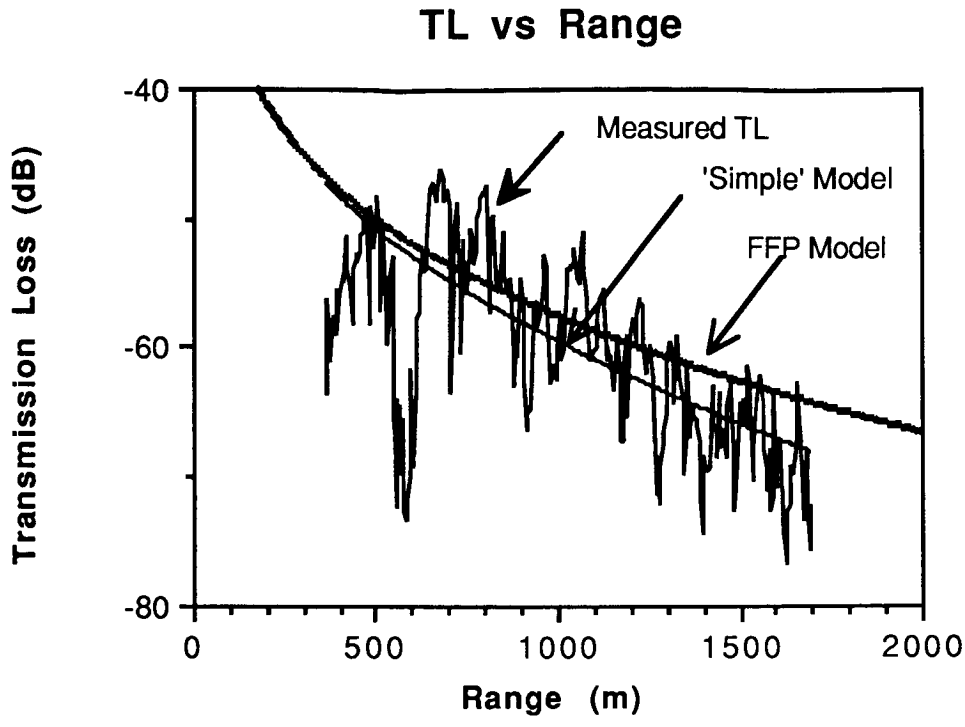

Figure 9 Measured and modeled (using the FFP) transmission losses during outward-bound run.

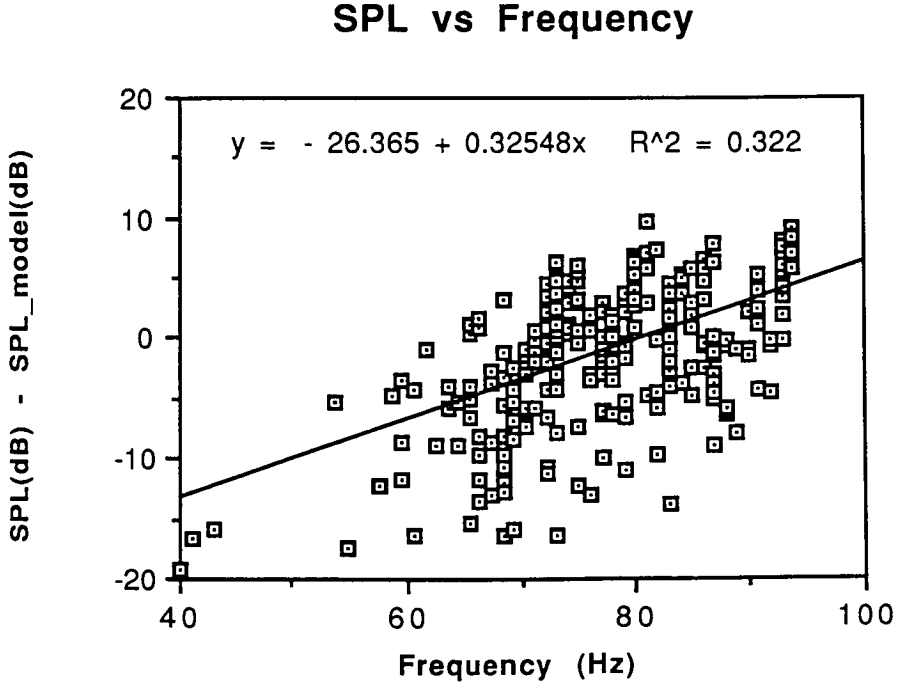

Figure 10 Measured Sound Pressure Level shows a strong dependency on engine RPM. Engine load was not directly observable in this experiment.

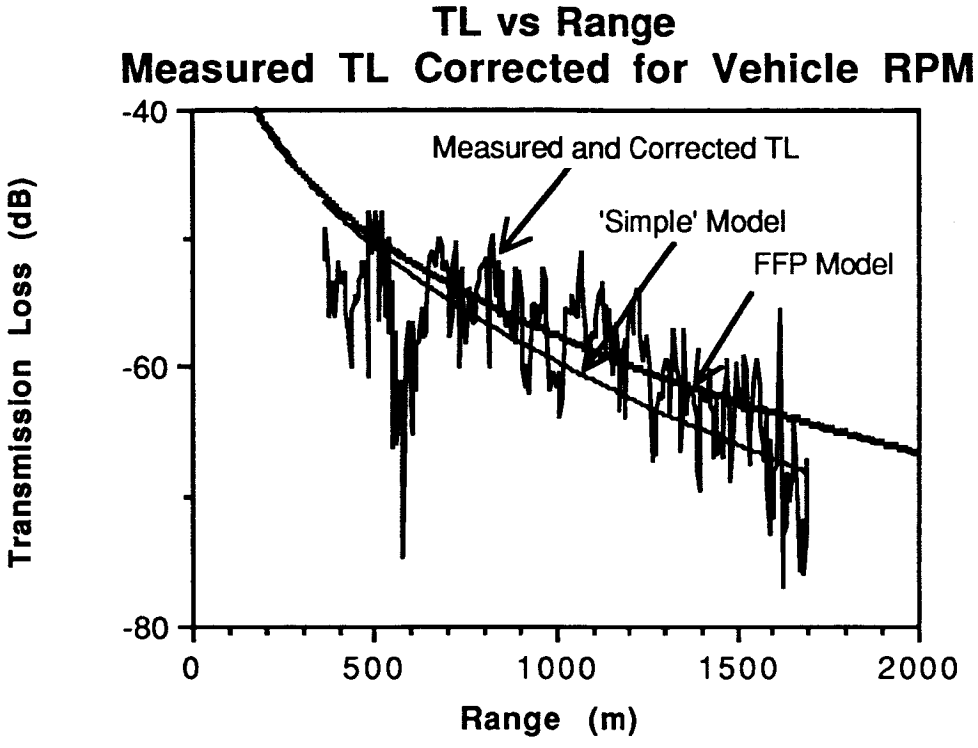

Figure 11 Measured transmission loss, after correcting for the effects of engine RPM variations.

SCATTERING MEASUREMENTS ON NATURAL AND MODEL TREES

James C. Rogers and Sung M. Lee
Michigan Technological University

SUMMARY

The acoustical back scattering from a simple scale model of a tree has been experimentally measured. The model consisted of a trunk and six limbs, each with 4 branches; no foliage or twigs were included. The data from the anechoic chamber measurements were then mathematically combined to construct the effective back scattering from groups of trees. Also, initial measurements have been conducted out-of-doors on a single tree in an open field in order to characterize its acoustic scattering as a function of azimuth angle. These measurements were performed in the spring, prior to leaf development. The data support a statistical model of forest scattering; the scattered signal spectrum is highly irregular but with a remarkable general resemblance to the incident signal spectrum. Also, the scattered signal's spectra showed little dependence upon scattering angle.

INTRODUCTION

Acoustic scattering in forests has often been studied in the context of sound which propagates through forests and thereby suffers attenuation. This attenuation is attractive to those who might consider the acoustic screening effects of forested areas. Thus, sound propagation in forested areas has been considered by many researchers (ref. 1, 2, 3). At least five factors contribute to the attenuation of sound propagating in forests: spherical spreading, atmospheric absorption, foliage absorption, ground loss, and scattering. It appears that scattering is a significant factor in sound attenuation at the middle frequency range (ref. 4, 5). The approach toward studying scattering that we use here is to focus on scattering alone and to particularly include back scattering. In this way only the scattered signal is measured whereas in traditional measurements of attenuation through forests both scattered signals and direct signals are present. In this case it is quite difficult to separate the scattered component from the considerably stronger direct signal component. Since forests are made up of many single trees, back scattering from forests can be considered using single tree scattering processes and extending this to the aggregate effects of many trees.

MODEL TREE BACK SCATTERING MEASUREMENTS IN AN ANECHOIC CHAMBER

Purpose of Measurements

There are several advantages to making back scattering measurements on a simple model tree in an anechoic chamber. If an asymmetrical tree is used the scattered signal will be different for different azimuth angles and synthetic "forest scattering" data can be generated by using an ensemble of these model scattering measurements. Also, it is possible to observe scattering as a function of increasing scattering angle: zero degrees for back scattering and one hundred eighty degrees for forward scattering. The results reported here do not use this capability however. If the tree is elevated on a pedestal the effects of ground reflections are removed, something that is not possible with a natural tree. Finally, the measurements are quite repeatable with no effects from meteorological influences.

Description of Model "Tree"

A tree silhouette was selected that approximately simulates that of a tree in a northern hardwood forest. The basic structure is a trunk, several limbs and a large number of branches as described earlier in Rogers et. al. (ref. 6). In order to utilize a simple construction technique and to facilitate theoretical analysis (something not yet completed), the cylinder shape was used as a basic structure element in our model. Hard wooden cylinders of three diameters were used for fabricating the three basic elements: the trunk, the limbs, and the branches. A single wooden cylinder that is several wavelengths long provides an effective back scattering element with a structured scattering pattern (ref. 7). Figure 1 shows a sketch (not to scale) of the tree and lists the dimensions and numbers of the components. The limbs were randomly distributed around the perimeter of the trunk and were spaced at irregular intervals along its length. The branches were similarly placed on the limbs. The effects of leaves and twigs were ignored. We believe that these will not give significant back scattering contributions in the low and mid frequency range studied.

Back Scattering Measurements and Results

The basic arrangement of the speaker source and receiving microphone in relation to the tree are shown in Figure 1. A single pulse was applied to the speaker through an amplifier, received by the microphone as a "direct" wave, and again received by the microphone as a back scattered signal.

Our small speaker (with a hemispherical cone approximately 0.02m in diameter) did not radiate a great deal of energy and several techniques were used to ensure an adequate signal to noise ratio. The tree was removed from its stand and a "constant

background" measurement was made by coherently time averaging several pulse events; this gave a reliable estimate of the signal which regularly existed in the portion of a time record occupied by the desired scattered signal. This signal was subtracted from all scattering records. Also, coherent time averaging was used in all scattering measurements to reduce the effects of random noise. Using the known geometry it is possible to construct a time window in which the scattered events will appear; such a window was used to exclude all signal outside of the desired scattering events. Finally, the useful spectral content of the source was judged to be from approximately 1 kHz to over 10 kHz. A filter was applied to the scattered signal to permit only those frequencies in the analyzed data.

Figure 2 compares the signal back scattered from the trunk alone, after it has been processed as described above and amplified by a factor of approximately 30, with the "direct" signal. There is a high degree of similarity between the signals as would be expected for back scattering from a single cylinder. The scattered signal is considerably more complex after the limbs and branches are added to the trunk.

After the tree was assembled, twenty four separate back scattering measurements were made. For each the tree was rotated 15 degrees about its vertical axis. The non symmetrical nature of the silhouette produced 24 unique scattering records which were then treated as the back scattering from 24 separate trees.

SYNTHESIS OF BACK SCATTERING FROM A GROUP OF MODEL TREES

Eighteen of the unique back scattering records were used to synthesize the scattering one would measure from a grove of 18 trees. Figure 3 shows a plan view of the grove, to scale, where the distance between the source, the microphone, and the first tree in the grove is indicated. Each original time domain measured back scattered signal was amplitude scaled by a (1/distance) factor to account for the round trip distance from the source to the tree and back to the microphone. Also, each original signal was time delayed by an amount proportional to the round trip distance. Finally all eighteen time domain records were added to simulate the signal back scattered from a grove of trees. Figure 4a shows the composite time domain signal. Two features are apparent: several individual tree scattering events are seen and as time increases in the figure the signal amplitude diminishes in accordance with the (1/distance) spreading factor. Figure 4b presents the spectrum of the composite scattered signal and compares it with the spectrum of a single direct pulse.

Over the useful bandwidth of the signal shown in the figure, approximately 1 kHz to 14 kHz, there is a close resemblance between the average spectrum of the scattered signal and that of the direct signal. There is approximately a 30 dB level difference between the

two spectra and a very irregular character to the scattered signal spectrum as would be expected for a random combination of similar signals. This random spectral appearance is observed even though the model tree did not have a broad distribution of sizes in its structure (in fact, only three different cylinder diameters and lengths were used). We conclude, by comparing the spectrum of the scattered signal from the synthetic grove with that which is produced by an actual forest (not shown here) that a high degree of realism has been achieved with a relatively small number of "trees" in the grove. One further comment about the synthetic scattering record should be made: since we combined individual records of sound scattered from individual trees, we have not allowed multiple scattering between trees. However, each individual tree record naturally incorporates multiple scattering among elements of the tree such as the trunk, limbs and branches. This scattering is probably considerably more important than that between individual trees.

SCATTERING MEASUREMENTS ON A SINGLE TREE IN A FIELD

Purpose and Measurement Arrangement

Scattering within a forest is a complex process; the presence of a large number of individual scattering trees with a wide spatial distribution precludes the study of the process at the level of the individual tree. We have therefore selected an isolated tree located in a uniformly flat grassy field for a series of scattering measurements. Both back scattering and scattering at angles up to 165 degrees from back scattering have been measured. This arrangement permits use of an impulsive source which is desired for separating the scattered signal from the signal which travels directly from the source to the microphone. The source was a simple mechanical device with a barrel and firing pin. It was machined to accept shot shell primers, Winchester part # 209, which are detonated by striking the firing pin.

Figure 5 is a plan view of the measurement arrangement. The source was located at a fixed point 30 meters from the center of the tree and the measurement microphone was located a distance of 15 meters from the tree at a series of points separated by 15 degrees of azimuth. A reference microphone was situated along a line between the source and the tree and 5 meters from the source. The source and measurement microphones were at fixed heights of 1.15 and 1.10 meters respectively. Bruel and Kjaer microphones, type 4155, were used on type 2330 sound level meters for both the reference and measurement microphones. Typical peak direct wave sound levels measured by the reference and measurement sound level meters were 137 dB and 120 dB respectively. At each location three separate shots were fired and the data recorded on a 4 channel digital audio tape recorder with a uniform frequency response from 0 to 10 kHz and a dynamic range of 84 dB.

Ground Impedance Measurements

It is not possible to directly remove the effects of ground reflections from the measurements since the source-ground-tree geometry is quite variable over all of the tree components such as the trunk, limbs, and branches. A level difference measurement was made between two microphones; one was placed at the ground level and the second was elevated 1.15 meters directly over the first. The shot source was located 5 meters away from the pair at an elevation of 1.15 meters. The ratio of the elevated microphone power spectrum to the ground level microphone power spectrum produced a differential spectrum or "transfer function" magnitude characteristic of the interference process between the direct and the reflected wave as described in ref. 4. Using the experimental data found in Donato (ref. 8) and the fact that the real and imaginary parts of the ground impedance are observed to vary approximately as the inverse square root of the frequency, a good fit was found for our experimentally determined differential spectrum with a theoretically predicted differential spectrum. The fit was better at frequencies below 1000 Hz but quite acceptable above that frequency too. We thus have a good estimate of the ground impedance for the field surrounding the tree. A representative value for the magnitude of the ground reflection coefficient at 300 Hz is about 0.8.

The initial scattering investigation sought to minimize the variability of all effects except the azimuth angle which was varied in 15 degree increments as shown earlier. Thus, although the precise effect of the ground reflections on the "insonification function" for the tree is not known, the source-tree geometry was fixed for all of the measurements. Also, the measurement microphone was always maintained at a fixed distance of 15 meters from the tree. The impulsive source proved to be quite repeatable but to reduce the effects of random noise and source variability somewhat, each scattering measurement reported here is the average of three power spectra from three separate measurements. The temperature was approximately 78 degrees F at 1 meter elevation and the wind varied in strength from 0.5 to about 1.5 meters per second.

Results of Scattering Measurements

Figure 6 shows the back scattered (0 degree azimuth angle) signal spectrum. The general shape is characteristic of the source alone in an anechoic environment (without any ground effect present). The spectrum, which is the average of three power spectra, is highly irregular in the same manner as that previously observed in Figure 4b for the synthetic grove of trees. The maple tree used for the outdoor experiment had multiple trunks with dozens of limbs and branches. Since the measurement was made early in the spring there were no leaves on the tree. One can estimate the signal to noise level by examining the background noise spectrum (the average of three noise power spectra) which is also shown on

the figure. There is good signal to noise (about 15 dB to 25 dB) over an approximate frequency range from 0.5 kHz to 9.5 kHz.

The scattered signal spectra at azimuth angles of 45, 90, and 150 degrees are shown in Figures 7, 8, and 9 respectively. Also, the scattered signal at 0 degrees, from Figure 6, is shown in these figures. A principal feature of these plots is that the scattered signal spectrum level varies only a small amount with azimuth angle for the frequency range of the measurements.

DISCUSSION AND CONCLUSIONS

Close examination of Figures 7, 8, and 9 shows that the scattered signal is remarkably similar over all angles of scattering. The insonification of the tree was the same in all cases since the source-tree geometry remained constant so comparison between figures examines only the effects of varying the scattering angle. Only at 150 degrees (Figure 7) does there appear to be a significant variation from the scattered signal at 0 degrees. This deviation is seen in frequencies from approximately 700 Hz to 1200 Hz. The rather narrow frequency range of this feature is perplexing. The scattering record for 165 degrees has been examined in this frequency range. It too shows reduced signal levels over approximately the same frequency range. However, the scattering record at 135 degrees does not display this feature.

The measurements presented here are part of a continuing investigation of scattering by forests. Foliage effects are to be included and additional low frequency data are required. Also, scattering models for trees and forests are required. These should adequately treat azimuth angle, frequency effects and address the problem of ground effects. Finally, the influence of tree variety should be considered on forest scattering.

REFERENCES

1. Frickie, F.: Sound Attenuation in Forests. J. Sound Vibration, vol. 92, no. 1, 1984, pp. 149.

2. Martens, M. J. M.: Noise Abatement in Plant Monocultures and Plant Communities, Applied Acoustics, vol. 14, 1981, pp. 167-189.

3. Burn, S. H.: The Absorption of Sound by Pine Trees, J. Acoust. Soc. Am., vol. 40, no. 3, 1966, pp. 658-661.

4. Price, M. A., Attenborough, K.: Sound Attenuation Through Trees: Measurements and Models, J. Acoust. Soc. Am., vol. 84, no. 5, 1988, pp. 1836-1844.

5. Aylor, D.: Noise Reduction by Vegetation and Ground, J. Acoust. Soc. Am., vol. 51, no. 1, 1972, pp. 197-205.

6. Rogers, J. C., Shen, W., Lee, S. M.: Acoustic Scattering : Measurements on Model Trees and Their Extention to Natural Forests, Acoustics '90, Univ. Southampton, England, Vol. 12 pt. I, 1990, pp 827-834.

7. Rogers, J. C., Lee, S. M.: Sound Scattering from Forests: Considerations and Initial Measurements, Proc. 13th Intl. Congress
on Acoustics, Belgrade, Yu., vol. 3, no. 7, 1989, pp. 217-220.

8. Donato, R. J.: Impedance Models for Grass-Covered Ground, J. Acoust. Soc. Am., vol. 61, no. 6, 1977, pp. 1449-1452.

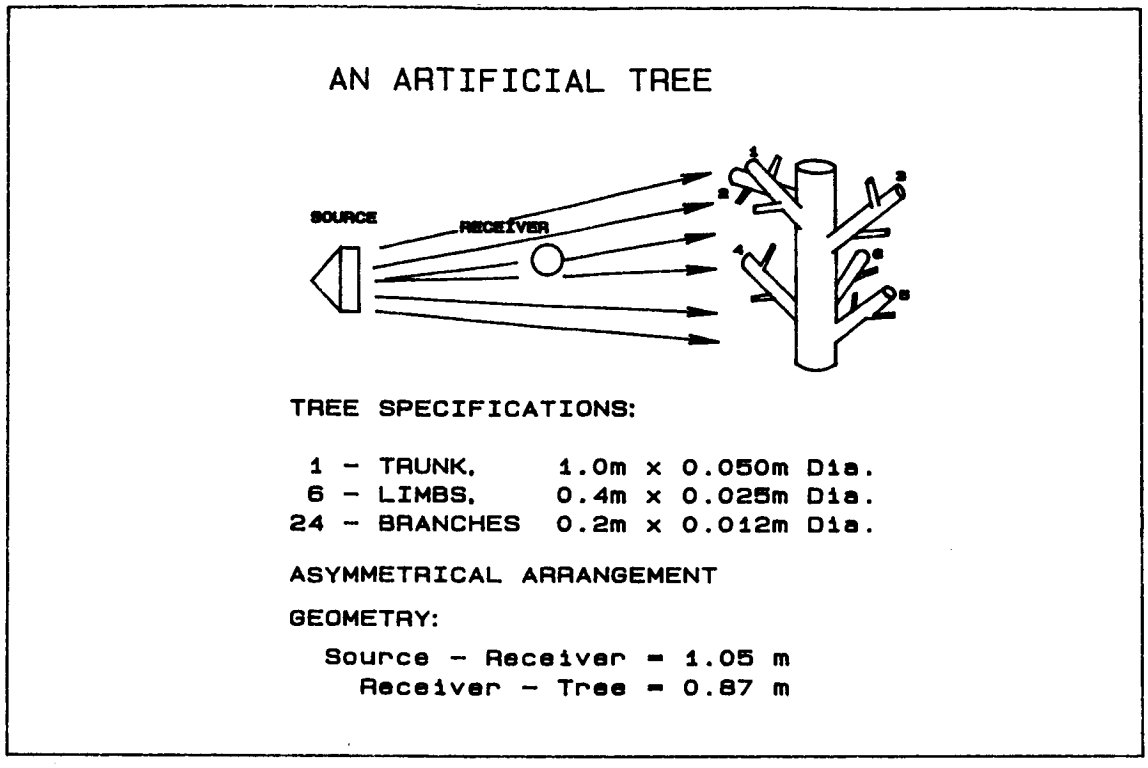

Figure 1. Sketch of model tree (not to scale) with element dimensions and physical arrangement for back scattering measurements in an anechoic chamber.

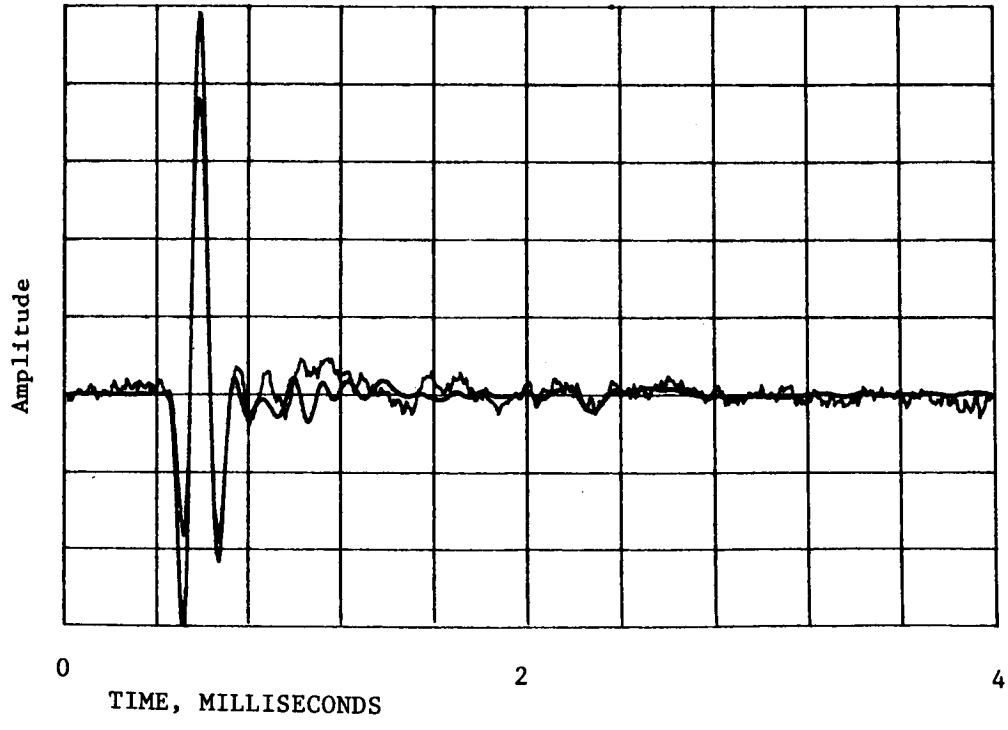

Figure 2. The direct signal (smooth) and the back scattered signal from the trunk alone (noisy and irregular) after amplification by a factor of 30.

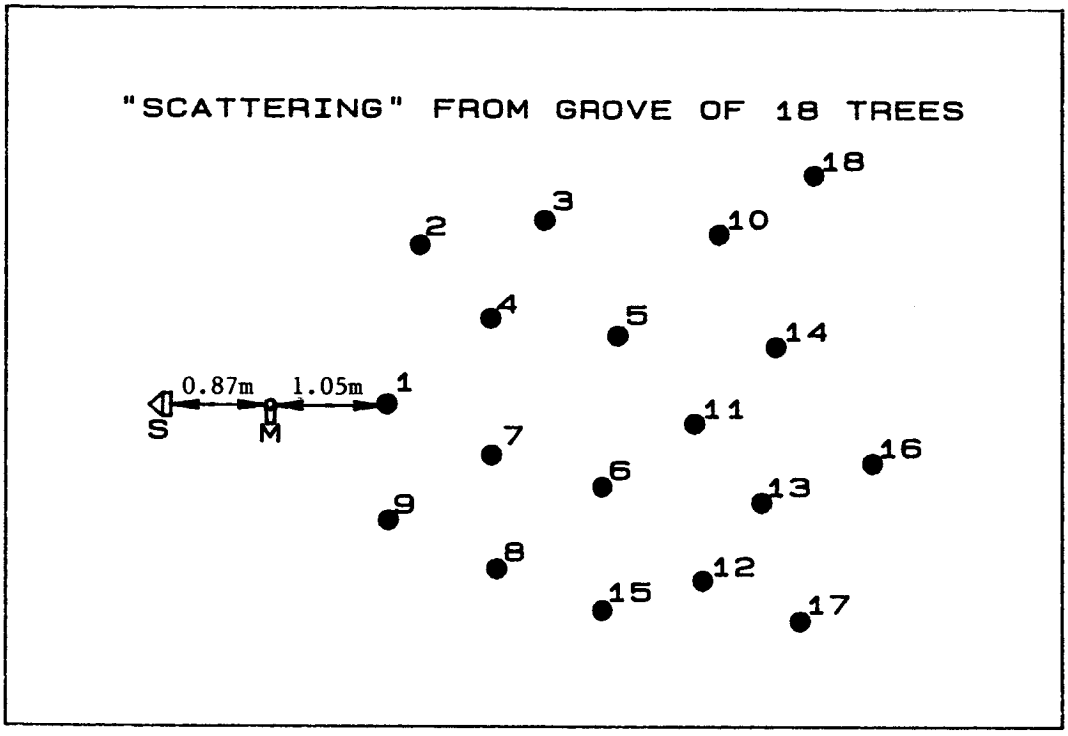

Figure 3. Arrangement of individual trees in synthetic grove of trees (to scale). The source and microphone positions are also to scale. Each tree position contributes an individual time domain scattering event to the synthetic back scattering record as described in the test.

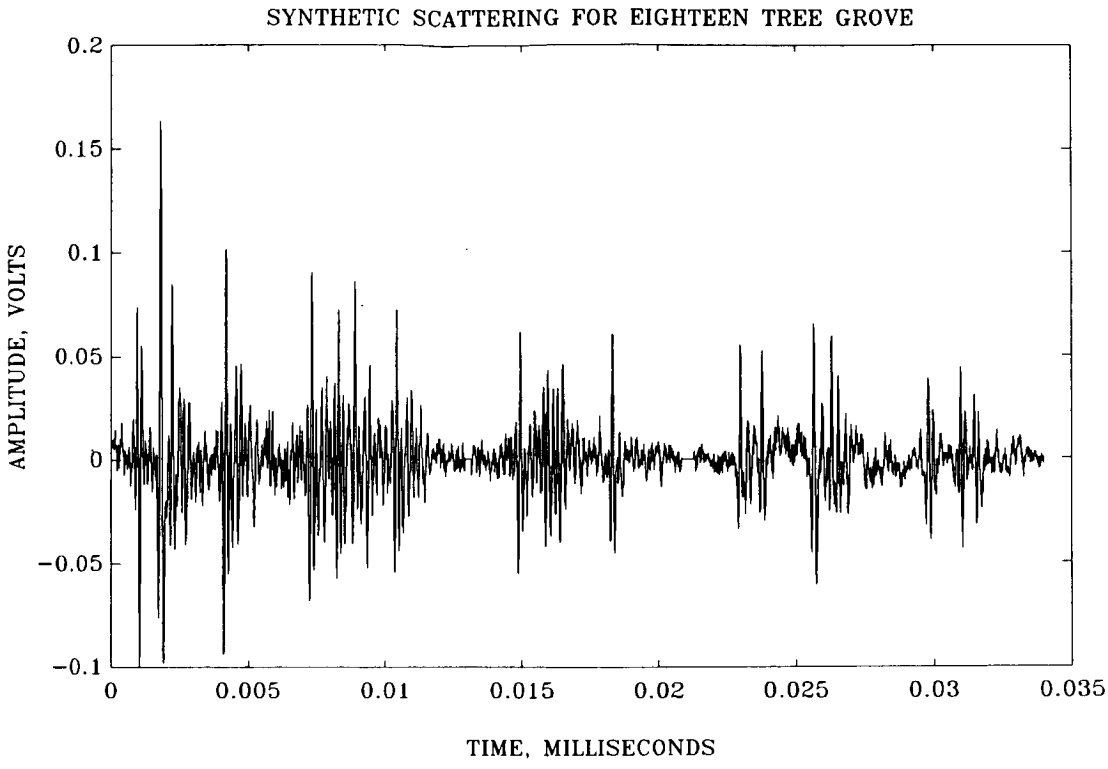

Figure 4. a). Synthetic time domain record constructed for grove of 18 trees shown in Figure 3.

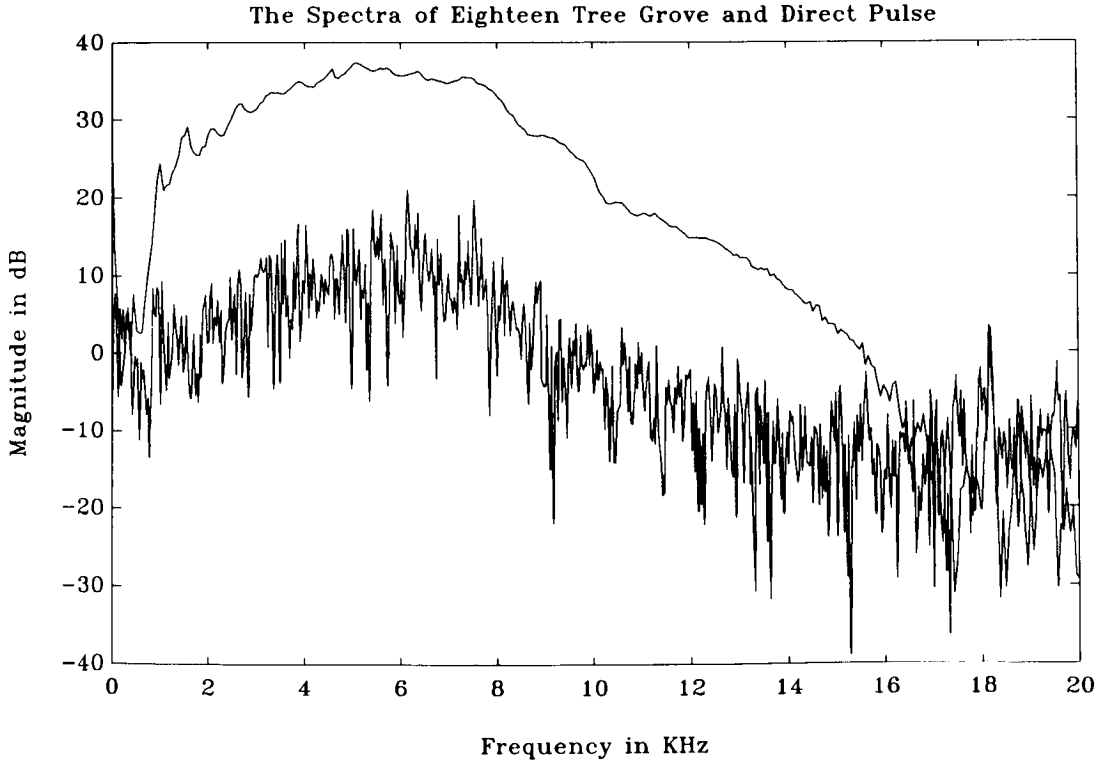

b). Comparison of the direct signal spectrum with that from the synthetic scattering data in a).

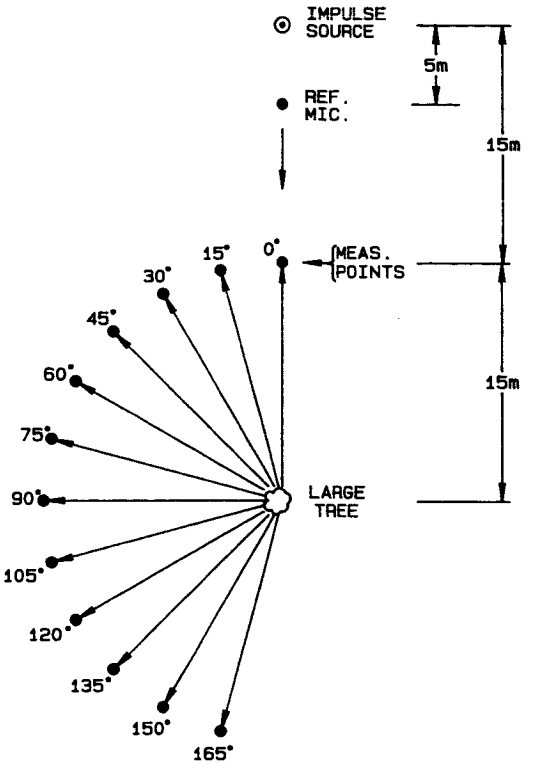

Figure 5. Plan view of scattering measurements made on a single tree in a grassy field.

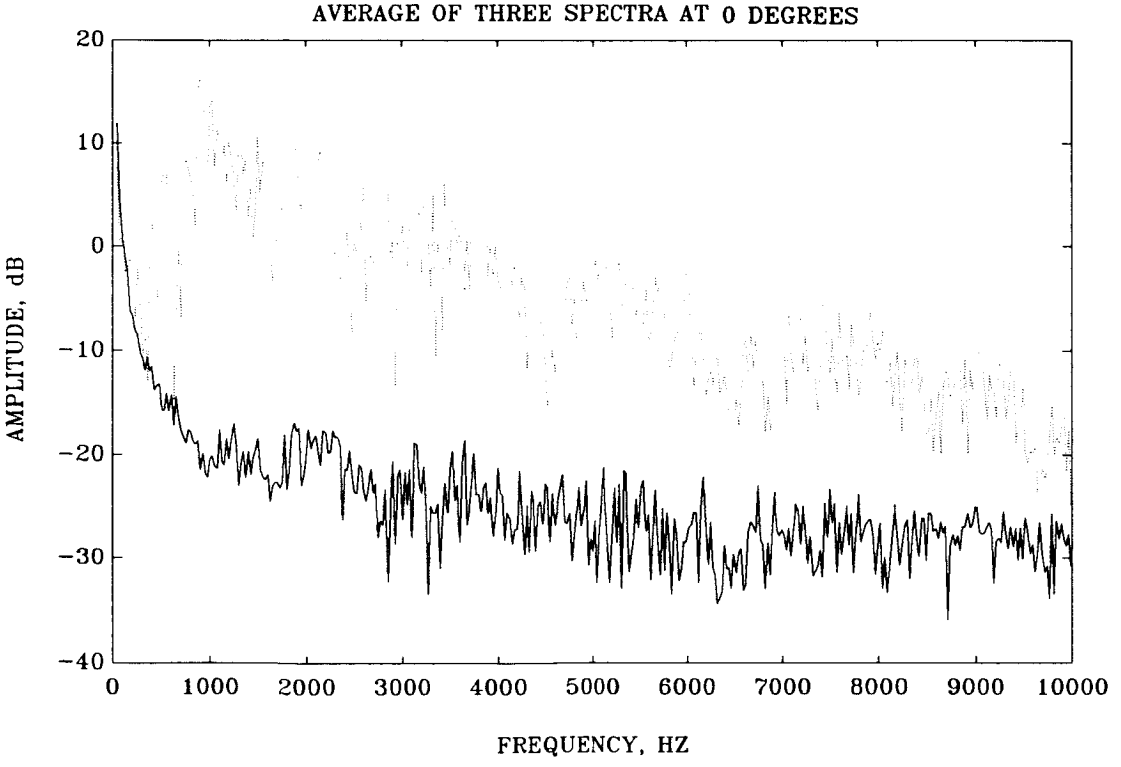

Figure 6. Single tree scattering at 0 degrees (back scattering), dashed line, and background noise spectrum, solid line.

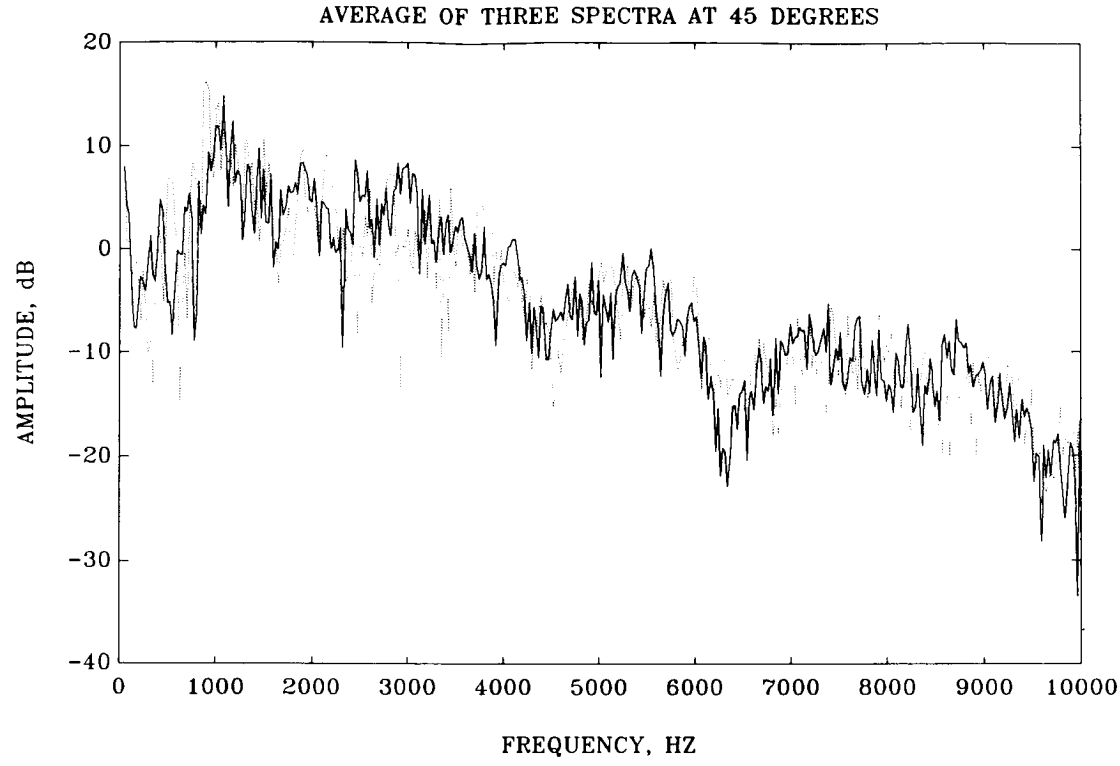

Figure 7. Single tree scattering at 45 degrees, solid line, compared with back scattered spectrum, dashed line.

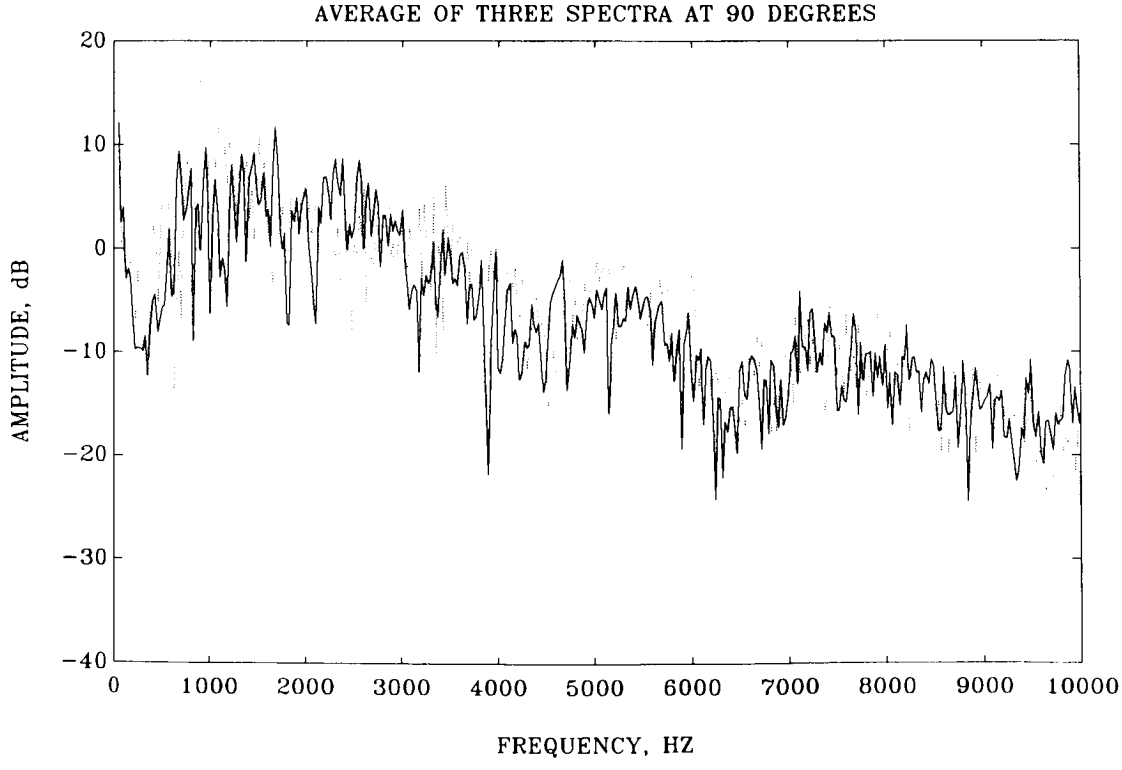

Figure 8. Single tree scattering at 90 degrees, solid line, compared with the back scattered spectrum, dashed line.

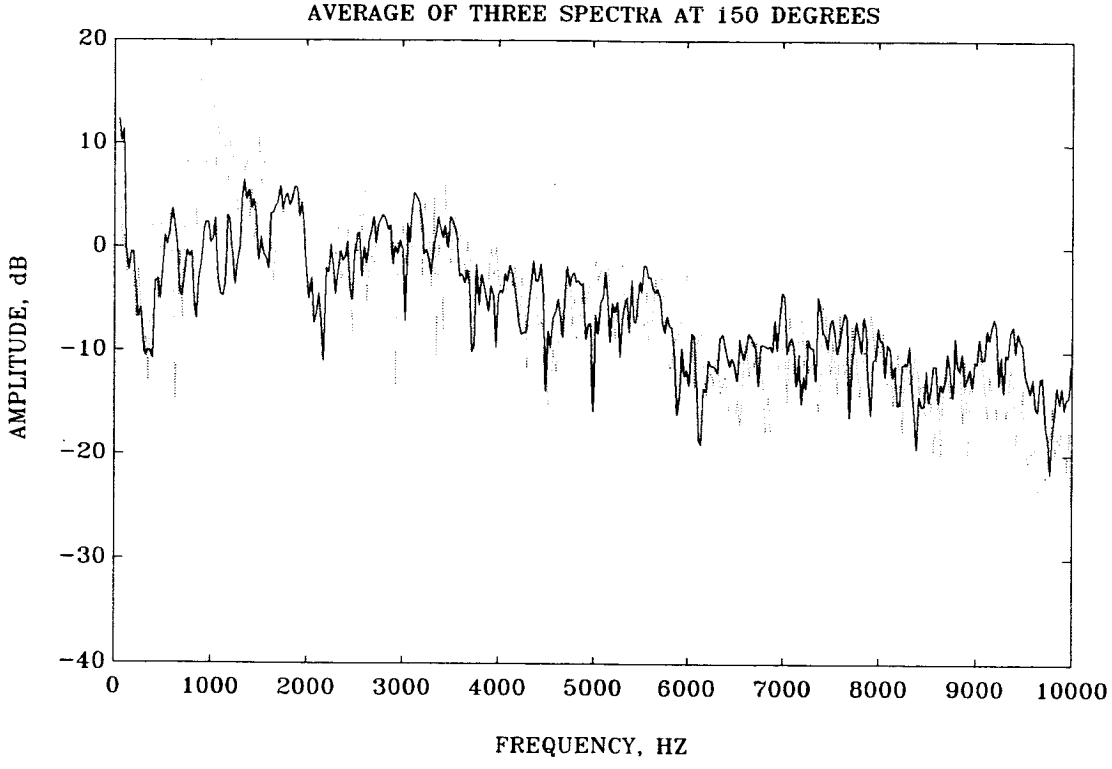

Figure 9. Single tree scattering at 150 degrees, solid line, compared with the back scattered spectrum, dashed line.

Using a Fast Fourier method to model sound propagation in a stratified atmosphere over a stratified porous-elastic ground

S. Tooms and K. Attenborough,
The Open University,
Milton Keynes,
England.

Abstract

Using a Fast Fourier integration method and a global matrix method for solution of the boundary condition equations at all interfaces simultaneously, a useful tool for predicting acoustic propagation in a stratified fluid over a stratified porous-elastic solid has been developed. The model for the solid is a modified Biot-Stoll model incorporating four parameters describing the pore structure corresponding to the Rayleigh-Attenborough rigid-porous structure model.

The method is also compared to another Fast Fourier code (CERL-FFP) which models the ground as an impedance surface under a horizontally stratified air. Agreement with the CERL FFP is good.

The effects on sound propagation of a combination of ground elasticity, complex ground structure, and atmospheric conditions are demonstrated by theoretical results over a snow layer, and experimental results over a model ground surface.

Introduction

The ground has conventionally been modelled for outdoor sound propagation as either an impedance surface or a rigid-porous structure. These approaches have both been highly productive in the case of high density materials. However in reality the ground is poro-elastic. Ground surfaces have hitherto been modelled as such when the interest has been in acoustic to seismic coupling, but there has been little interest in porous-elastic ground models in propagation in the air. For some outdoor ground surfaces (such as snow or forest floors for example) the bulk density of the material is low enough for seismic effects to become important for sound propagation over the surface at some frequencies.

In this paper an FFP propagation model is used to calculate sound pressure levels over a porous-elastic ground surface. The model's predictions are compared to the predictions of other propagation models for the high density, high seismic velocity rigid-porous limit of the porous-elastic ground model. The effects on acoustic propagation of the elasticity of various ground surfaces is then shown by comparison to the rigid frame limit. Using a multiply layered fluid atmosphere the combined effects of meteorology and ground elasticity are examined.

The Biot-Stoll poro-elastic model

The ground model used in this investigation was a modified Biot-Stoll Poro-Elastic model[1,2,3]. Propagation within the material is via three different modes; a fast wave, equivalent to the seismic P wave: a slow wave equivalent to the pore wave in the Rayleigh Attenborough rigid-porous model[4]: and a shear wave equivalent to the seismic S wave. Each wavetype causes vibration in both the solid material and the pore fluid. Attenuation of all three wavetypes is predicted by the theory due to viscous losses on the

pore walls, though it has been shown to underpredict the attenuation in real materials because other loss mechanisms are not taken into account. Hence an extra attenuation is added as an imaginary part of the fast and shear propagation constants.

The Fast Fourier Method

If one applies a Hankel transform in range to the Helmholtz equation one obtains the depth separated wave equation:

$$\left(\frac{d^2}{dz^2} + \left(k^2 - k_m^2(z)\right)\right)\Gamma(k,z) = \bar{h}(k,z), \tag{1}$$

where, for a point source,

$$\bar{h}(k,z) = \frac{1}{2\pi}\delta(z - z_0) \tag{2}$$

Solutions to this equation are depth dependent only and are equivalent to solutions to the wave equation for continuous plane wave incidence. In order to obtain a range dependent solution one must obtain depth dependent solutions to the depth separated wave equation, and then perform the inverse Hankel Transform on the solution to equation 1 , which is in terms of horizontal wavenumber.

The exact range dependent solution is in the form;

$$F_{(x,d)} = \int_{k_h=0}^{\infty} J_\nu(k_h.x).\Gamma(k_h,d).dk_h, \tag{3}$$

where Γ is the depth dependent Greens function.

A large argument approximation to the Bessel function [5] is:

$$J_\nu(z) \simeq \frac{1}{\sqrt{2\pi z}}\left[e^{i(z-\pi\nu/2-\pi/4)} + e^{-i(z-\pi\nu/2-\pi/4)}\right] \tag{4}$$

This approximation together with the replacement of the integration by a finite sum gives the approximate equation for $F_{(x,d)}$:

$$F_{(x_m,d)} \simeq \frac{\delta k N^{1/2}}{2\pi m^{1/2}}\left[e^{-i\pi/4}\sum_{n=0}^{N-1}\Gamma_{(k_n,d)}n^{\frac{-1}{2}}e^{\frac{2i\pi mn}{N}} + e^{i\pi/4}\sum_{n=0}^{N-1}\Gamma_{(k_n,d)}n^{\frac{-1}{2}}e^{\frac{-2i\pi mn}{N}}\right]. \tag{5}$$

This Fourier series approximation can then be improved by corrections to allow for the truncation of the integral to infinity to a finite wavenumber, $k_{h(max)}$, and the avoidance of pole(s) on the real axis[6], which together lead to inaccuracies and oscillations in the result, to give

$$\begin{aligned} F_{(x_m,d)} \simeq \frac{\delta k N^{\frac{1}{2}}}{2\pi m^{\frac{1}{2}}}\Bigg[&e^{-i\pi/4}\sum_{n=0}^{N-1}C_{(k_n,d)}e^{\frac{2i\pi mn}{N}}e^{\frac{2\pi m\alpha}{N}} \\ &+ e^{i\pi/4}\sum_{n=0}^{N-1}C_{(k_{N-n},d)}e^{\frac{2i\pi(N-m)n}{N}}e^{\frac{-2\pi m\alpha}{N}}\Bigg]. \end{aligned} \tag{6}$$

where

$$G_{(k_n,d)} = \Gamma_{(k_n,d)} + \frac{iN\Gamma_{(k_0,d)}}{\alpha\Delta}\left[1 - e^{(\Delta(i\alpha-n)/N)}\right], \tag{7}$$

$$C_{(k_n,d)} = G_{(k_n,d)}.(n - i\alpha)^{-1/2} + G_{(k_{N-1},d)}N^{-1/2}S^*, \tag{8}$$

and S^* is an approximation to the sum,

$$S = \sum_{j=1}^{\infty}(j + [(n - i\alpha)/N])^{-1/2}. \tag{9}$$

The Environment

The environment is assumed to be range independent and to consist of a fluid (air) upper half-space overlying a set of horizontal fluid (air) layers of differing sound speeds and densities. The lowest of these fluid layers is in contact with a ground made up of a set of horizontal elastic porous layers under which is an elastic porous half-space. The number of layers in either fluid or ground can be set to zero.

The Depth Dependent Green's function

The depth dependent Green's function Γ must be solved for the above environment.

In a fluid layer containing a spherical point source the depth dependent Green's function is

$$\Gamma = \left[\frac{1}{\beta_0} e^{i.(h_s-h).\beta_0} + R_{\uparrow}.e^{i.(h_1-h).\beta_0} + R_{\downarrow}.e^{i.(h-h_2).\beta_0}\right]. \tag{10}$$

The $R_{\updownarrow}$ are calculated by solution of the boundary condition equations at the interfaces.

In the porous elastic medium there are three scalar displacement potentials describing propagation in the fluid,

$$\Phi_1 = \int_0^\infty \bar{\Phi}_1 J_0(k_h.r).k_h.dk_h \tag{11}$$

$$\Phi_2 = \int_0^\infty \bar{\Phi}_2 J_0(k_h.r).k_h.dk_h \tag{12}$$

$$\Phi_3 = \int_0^\infty \bar{\Phi}_3 J_0(k_h.r).dk_h, \tag{13}$$

Φ_1 is the longitudinal displacement potential in the solid, Φ_2 is the longitudinal displacement potential in the pore fluid, Φ_3 is the transverse displacement potential in the solid, to which the fluid transverse displacement potential is directly proportional.

In a porous-elastic layer, bounded by interfaces at depths d_1 and d_2, in the absence of a source, the $\bar{\Phi}_i$s at a depth z are given by.

$$\bar{\Phi}_1 = A_{1\downarrow}e^{i(z-d_1)\beta_1} + A_{1\uparrow}e^{i(d_2-z)\beta_1} + A_{2\downarrow}e^{i(z-d_1)\beta_2} + A_{2\uparrow}e^{i(d_2-z)\beta_2} \ , \tag{14}$$

$$\bar{\Phi}_2 = m_1\left(A_{1\downarrow}e^{i(z-d_1)\beta_1} + A_{1\uparrow}e^{i(d_2-z)\beta_1}\right) + m_2\left(A_{2\downarrow}e^{i(z-d_1)\beta_2} + A_{2\uparrow}e^{i(d_2-z)\beta_2}\right) \ , \tag{15}$$

$$\bar{\Phi}_3 = A_{3\downarrow}e^{i(z-d_1)\beta_3} + A_{3\uparrow}e^{i(d_2-z)\beta_3} \ , \tag{16}$$

The m_i are the ratios of the amplitude in the solid and pore fluid for each wavetype, and the $\beta_i = (k_i^2 - k^2)^{1/2}$, where the k_i are propagation constants, and k is the horizontal wavenumber. The depth dependent Green's function Γ for a desired output parameter in the fluid is a function of the $\bar{\Phi}_i$. The $A_{\updownarrow}$ are calculated by solution of the boundary condition equations.

Boundary conditions

Boundary condition equations in cylindrical polar coordinates (r, θ, z) are needed. However the axisymmetric nature of the problem considered here means that there is no θ dependence.

At boundaries between two fluid layers the two boundary conditions are

1. continuity of pressure,
2. continuity of normal particle displacement,

At the interface between the fluid and the porous elastic medium there are four boundary conditions,

1. continuity of total normal stress[3],
2. continuity of normal displacement[3],
3. continuity of fluid pressure[7],
4. continuity of tangential stress,

Six boundary conditions are required at each interface between porous-elastic layers. These boundary conditions are the four above and two others,

5. continuity of normal relative fluid displacement, and
6. continuity of tangential frame displacement.

The range dependent parts of the boundary condition equations are identical on each side of the boundary, therefore only the depth dependent Green's functions of the boundary conditions need to be equated.

The boundary condition equations are solved simultanaeously for the $A_\updownarrow$ and $R_\updownarrow$ at all interfaces. The depth dependent Green's function is then calculated for the desired output parameter (sound pressure level, frame displacement, etc). The range dependent solution is calculated using the FFP method described above.

Comparison to other propagation models

For propagation above a rigid-porous halfspace the model compares well with other propagation models, such as the CERL-FFP (see figure 1)[8], and Attenborough, Hayek, and Lawther's 'exact' analytic model(see figure 2)[7]. Above an extended reaction rigid-porous layer over a non-porous backing agreement with Nicholas-Berry and Daigle's propagation model is good for a wide variety of model surfaces(see figures 3 and 4) [9]. Source and receiver heights are 0.5 and 0.3 metres respectively.

Effects of ground surface elasticity on sound propagation

The largest effects of ground elasticity on sound propagation over it are likely to be where the bulk density of the ground surface is small. The most common ground cover where this is so is a snow layer. Measured normal surface impedance over snow cover sometimes shows low frequency peaks [10,11]. These could be interpreted as seismic resonances in a snow layer. Figure 5 shows the predicted excess attenuation over an 8cm thick snow layer overlying a rigid nonporous halfspace at twenty metres range, using a rigid-porous model, and porous-elastic model. The pore structure and elastic parameters are taken calculated from Sommerfeld[12], Johnson[11] Ishida[10] and Attenborough and Buser[13]. A resonant effect can clearly be seen at about 810Hz in the porous elastic model output which is not present for the rigid-porous model. Figure 6 shows the predicted excess attenuation over the same snow layer at 810Hz as a function of range. This figure demontrates that at this frequency a seismic resonance in the snow layer leads to an apparent hardening of the snow surface at a short range, leading to less attenuation due to ground absorption. The behaviour at longer ranges shows that away from the source the attenuation due to the ground is unaffected by the elastic effects, but the signal amplitude is increased due to the reduced attenuation near to the source.

Combined effects of elasticity and atmospheric sound velocity gradients

Continuous sound velocity gradients can be modelled by thin homogeneous layers as long as the layer thickness is much less than the wavelength of the sound [14]. In figure 7 the combined effect of the logarithmic downward refracting sound velocity gradient(roughness length 5.10^{-3}metres, temperature difference between ground and 4.0 metres 7^o Centigrade) and an elastic surface are shown. The difference between elastic and rigid models remains approximately the same as for no gradient.

Comparison with experiments

In order to test the validity of this porous-elastic propagation model, measurements of the level difference between two vertically separated microphones were made over a thin (4cm) layer of low density foam material. The foam was attached to a non-porous concrete surface. A point noise source was suspended over the foam surface.

The elastic and porous parameters of the foam were separately measured using non-acoustic techniques. The measured level difference was compared to the level difference predicted using both rigid and poro-elastic models. The results are shown in figure 8. The geometry used for this figure was source height 0.2 metres, receiver heights 0.01 and 0.2 metres, and range 0.4 metres. The results show a better agreement with the elastic model than with the rigid model.

Conclusions

An FFP model for propagation over porous-elastic surfaces has been developed. It has been shown that in the rigid frame limit it agrees well with other propagation models. For sound propagation over low bulk density layered materials it has been shown that ground elasticity can have a substantial effect on received sound pressure levels for both real and theoretical results.

Table 1: Material parameters used in the prediction of excess attenuation

Parameter	Unit	Rigid-porous Halfspace	Rigid-porous layer	Snow layer	Foam layer
Flow resistivity σ	MKSraylsm^{-1}	100000	10000	15900	18400
Porosity Ω	-	0.3	0.3	0.804	0.97
Pore shape factor ratio s_p	-	0.5	0.5	0.5	0.5
Grain shape factor n'	-	0.5	0.5	0.5	63.8
Bulk density	kgm^{-3}	-	-	184.0	32.0
P-wave velocity v_p	ms^{-1}	-	-	130.0	79.0
S-wave velocity v_s	ms^{-1}	-	-	90.0	56.0
$\Im(v)/\Re(v)$	-	-	-	0.05	0.085
Grain bulk modulus K_r	Nm^{-2}	-	-	1.10^9	1.10^{10}
Layer depth	m	-	0.1	0.08	0.04

References

[1] M.A. Biot. Theory of propagation of elastic waves in a fluid saturated porous solid. *J.Acoust.Soc.Am.*, 168–191, 1956.

[2] M.A. Biot. Mechanics of deformation and acoustic propagation in porous media. *J.Applied Physics*, 33(4):1482–1498, 1962.

[3] J.M. Sabatier, H.E. Bass, L.M. Bolen, K. Attenborough, and V.V.S.S. Sastry. The interaction of airborne sound with the porous ground: the theoretical formulation. *J.Acoust.Soc.Am.*, 79(5):1345–1352, May 1986.

[4] K. Attenborough. On the acoustic slow wave in air filled granular media. *J.Acoust.Soc.Am.*, 81(1):93–102, Jan. 1987.

[5] M.Abramowitz and I.A.Stegun. *Handbook of Mathematical Functions.* Dover NY USA, 1970.

[6] T.L. Richards. Accurate fft-based hankel transforms for prediction of outdoor sound propagation. *J.Sound and Vib.*, 109(1):157–167, 1986.

[7] K.Attenborough, S.I.Hayek, and J.M.Lawther. Propagation of sound above a porous half-space. *J.Acoust.Soc.Am.*, 68(5):1493–1501, November 1980.

[8] S.J.Franke and G.W.Swenson(Jr). A brief tutorial on the fast field program (ffp) as applied to sound propagation in the air. *Applied Acoustics*, 27(3):203–216, September 1989. Univ of Illinois at Urbana-Champaign.

[9] J.Nicholas, J.L.Berry, and G.A.Daigle. Propagation of sound above a finite layer of snow. *J.Acoust.Soc.Am*, 77(1):67–73, 1985.

[10] T. Ishida. Acoustic properties of snow. *Contributions from the Intensity of Low Temperature Science Series A.*, 20:23–63, 1965.

[11] J.B. Johnson. On the application of biot's theory to acoustic wave propagation in snow. *Cold regions Science and Technology*, 6:49–60, 1982.

[12] R A Sommerfeld. A review of snow acoustics. *Reviews of Geophysics and Space Physics*, 20(1):62–66, February 1982.

[13] K.Attenborough and O.Buser. On the application of rigid-porous models to impedance data for snow. *J.Sound Vib.*, 124(2):315–327, 1988.

[14] S.J.Franke, R.Raspet, and C.H.Liu. Numerical predictions of atmospheric sound pressure levels in shadow zones. *J.Acoust.Soc.Am.*, 83(2):816–820, 1988.

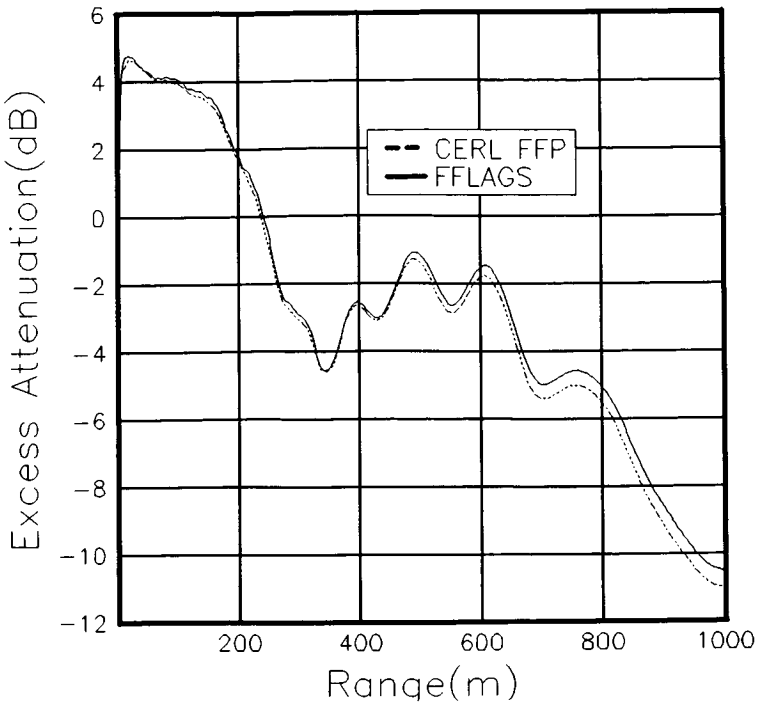

Figure 1 Comparison of CERL FFP and FFLAGS for propagation over a rigid-porous halfspace in a 12 layered atmosphere. Frequency=50Hz.

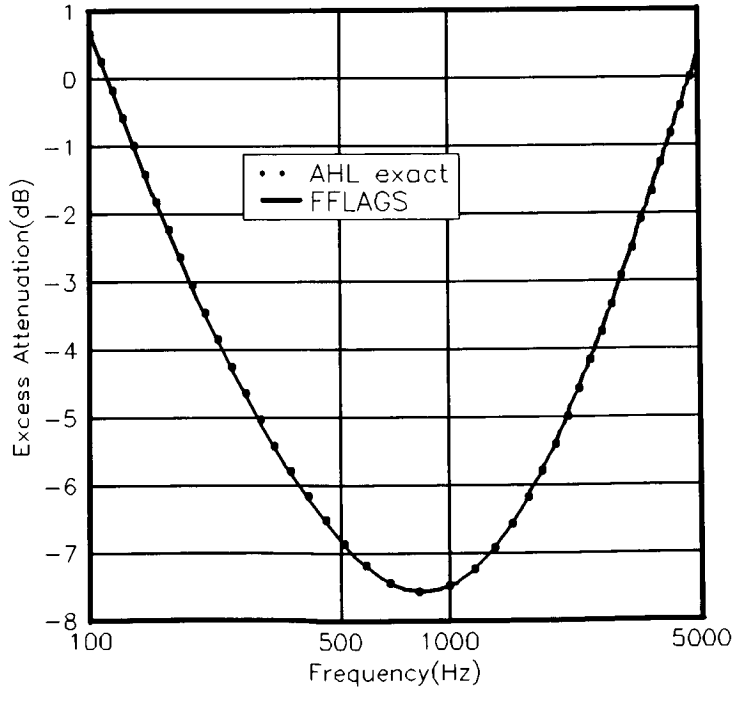

Figure 2 Comparison of FFLAGS to the predictions of Attenborough, Hayek, and Lawther's exact extended reaction model for propagation over an extended reaction rigid-porous halfspace. Range=20 metres.

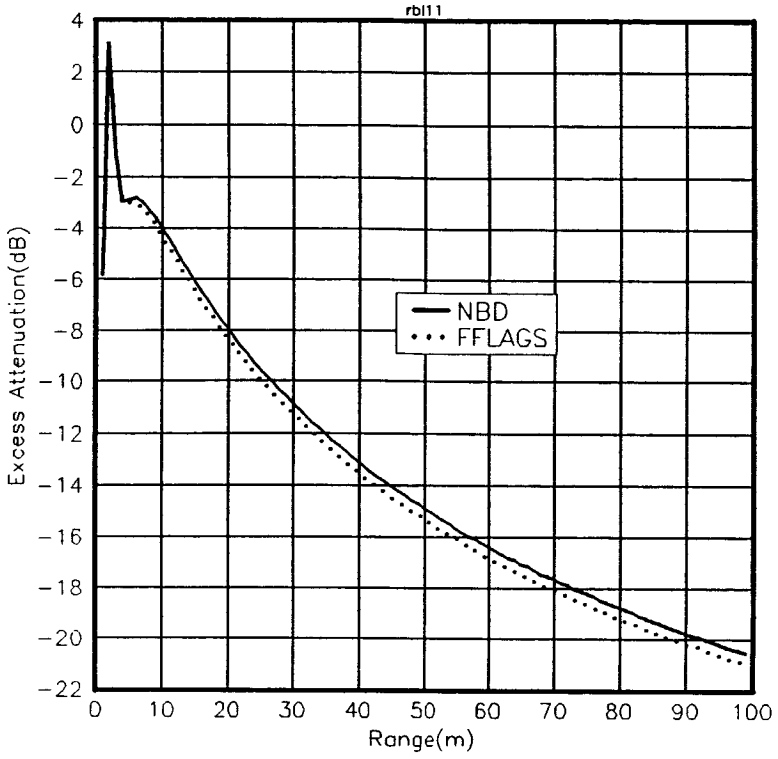

Figure 3 Comparison of Nicholas Berry and Daigle's model for predicted excess attenuation over an extended reaction rigid-backed layer at 100Hz.

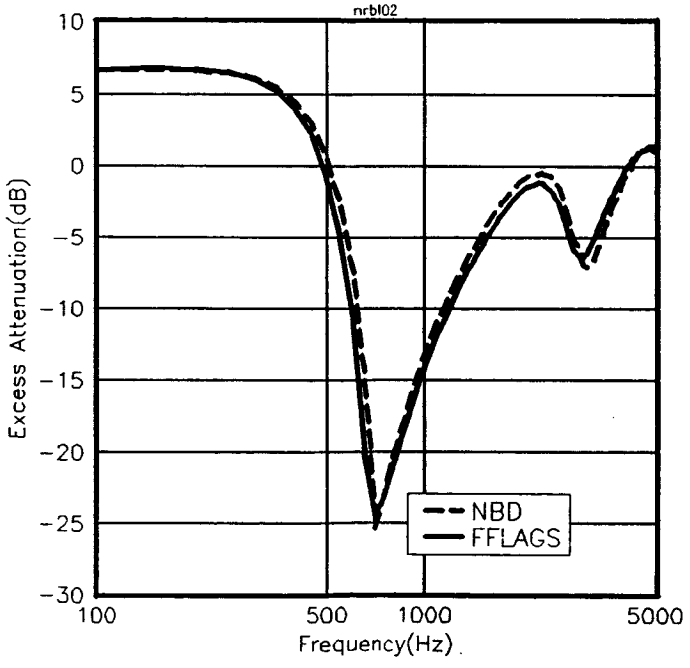

Figure 4 Comparison of FFLAGS to Nicholas Berry and Daigle's model for predicted excess attenuation over an extended reaction rigid backed layer at 20 metres.

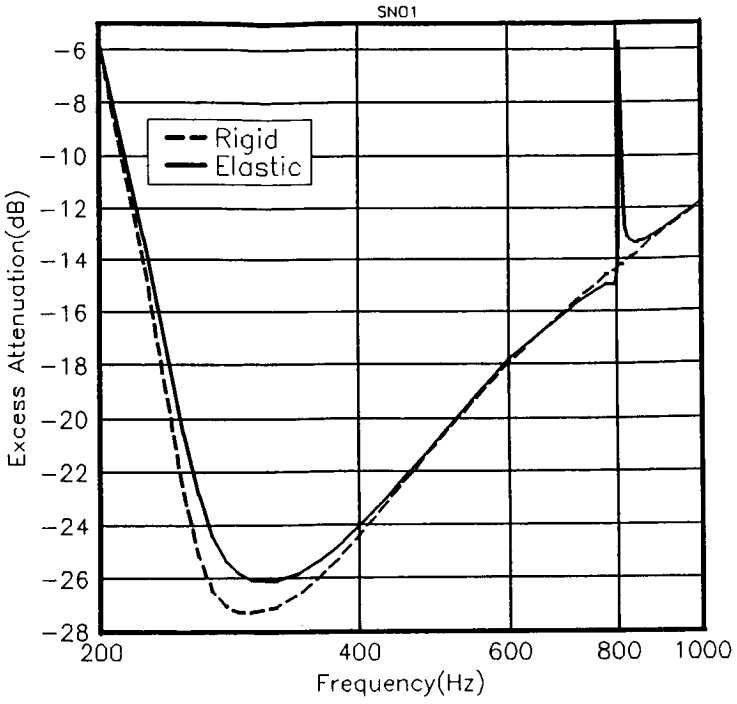

Figure 5 Predicted excess attenuation over thin snow layer using FFLAGS with rigid-porous parameters, and porous-elastic parameters. Range 20 metres.

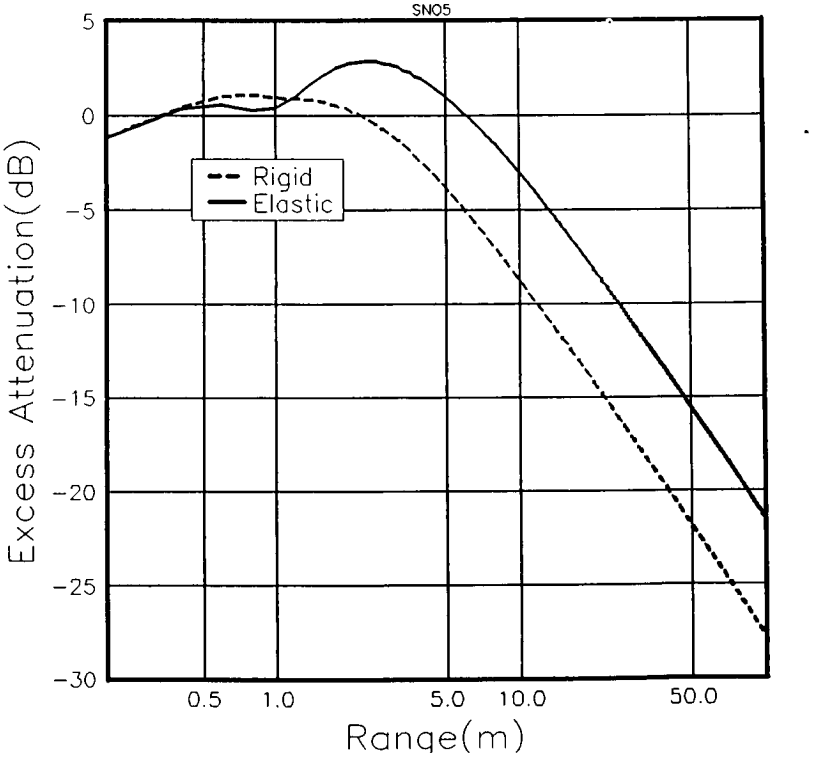

Figure 6 Predicted excess attenuation over thin snow layer at 810Hz. Showing difference between rigid and elastic model at this frequency.

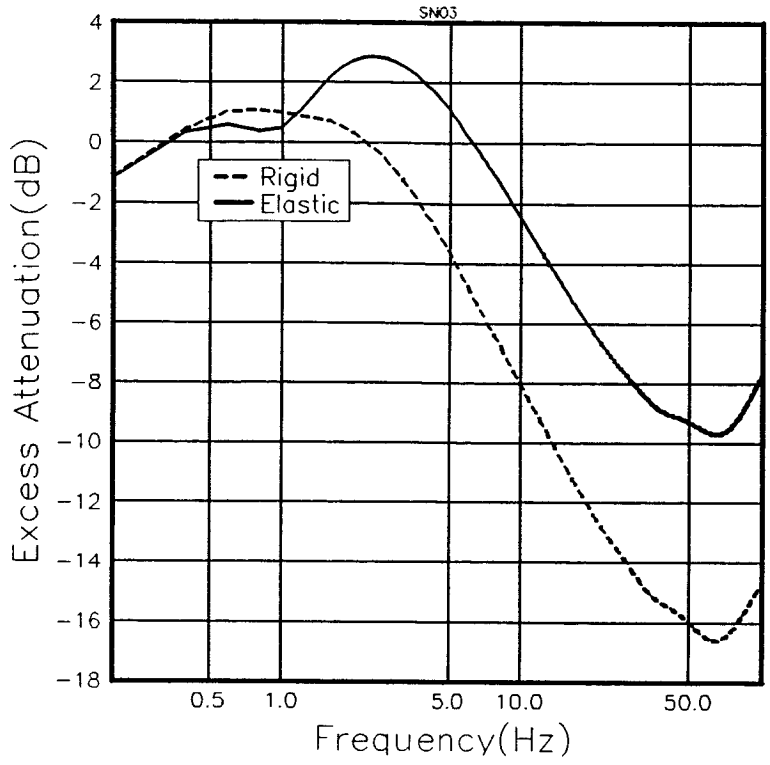

Figure 7 Predicted excess attenuation over thin snow layer at 810Hz in the presence of a downward refracting logarithmic sound velocity gradient.

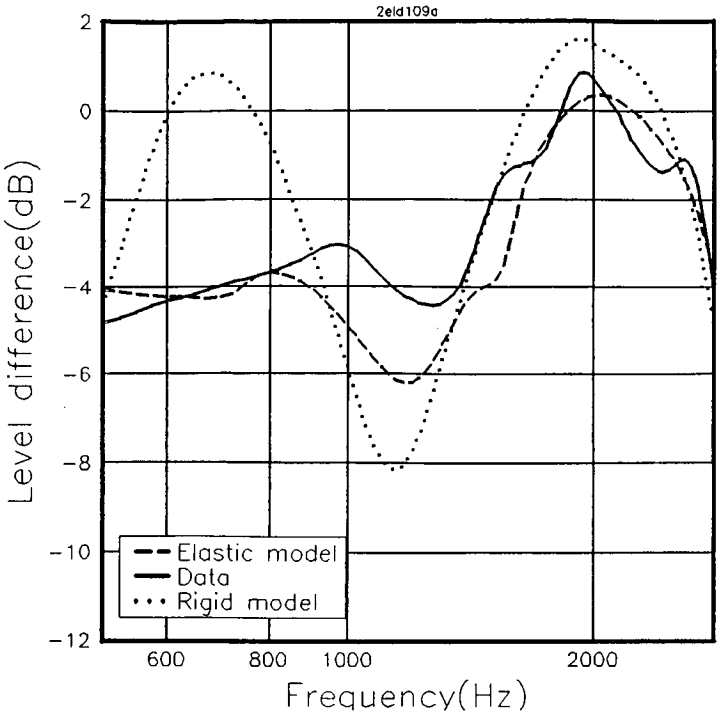

Figure 8 Measured Level difference between two vertically separated microphones (heights 0.2 and 0.01 metres) at a range of 0.4 metres from a point source over a thin (4cm) rigidly backed foam surface. Compared to the predicted level difference using rigid-porous and porous-elastic models, calculated from direct measurement of the pore and elastic parameters of the foam.

LONG-RANGE VERTICAL PROPAGATION

William L. Willshire, Jr.
NASA Langley Research Center
Hampton, VA 23665

and

Donald P. Garber
Lockheed Engineering & Sciences Company
Hampton, VA 23666

Development of the advanced turboprop has led to concerns about en route noise. Advanced turboprops generate low-frequency, periodic noise signatures at relatively high levels. As demonstrated in a flight test of NASA LeRC's Propfan Test Assessment (PTA) airplane in Alabama in October 1987, the noise of an advanced turboprop operating at cruise altitudes can be audible on the ground. The assessment of the en route noise issue is difficult due to the variability in received noise levels caused by atmospheric propagation and the uncertainty in predicting community response to the relatively low-level en route noise, as compared to noise associated with airport operations.

The En Route Noise Test was designed to address the atmospheric propagation of advanced turboprop noise from cruise altitudes and consisted of measuring the noise of an advance turboprop at cruise in close proximity to the turboprop and on the ground. Measured and predicted ground noise levels will be presented in this paper. Participants in the En Route Noise Test were NASA LeRC, the FAA, and NASA LaRC.

EXPERIMENT DESCRIPTION

The test airplane was NASA LeRC's PTA airplane which has a 2.7 m (9 ft) diameter, eight-bladed, tractor-configured advanced turboprop mounted on its left wing. The test airplane was instrumented to measure the near-field turboprop noise levels, as well as, engine and other pertinent parameters. During the microphone array flyovers, the test airplane was tracked with a C-band beacon.

The En Route Noise Test was performed at the White Sands Missile Range in New Mexico in April 1989. Eighty-eight PTA airplane passes or runs over the ground microphone array were recorded. The array was an eight element, linear microphone array with an inter-element spacing of 122 m (400 ft). The completed

test matrix is illustrated in Table I. The majority of the runs were performed at altitudes of 4.6 and 9.2 km at a tangential tip speed of 240 meters per second (bpf of 226 Hz) and a nominal power setting of 90 percent. Seventeen runs were flown at other tip speeds in the range of 190 to 260 m/s. Meteorological profiles were measured during the flyovers from ground level up to 12 km.

PTA SPEED, M	ALTITUDE, km AGL			
	.6	2.7	4.6	9.2
.5	4	4	23	
.7			19	32
.77				6

Table I. Completed test matrix.

DATA ANALYSIS

The basic analysis used in the results presented in this paper is ensemble-average time histories[1]. Data from the eight ground mounted digital microphones (SR=2344 sps) are high-pass filtered at 80 Hz and then shifted based on the airplane ground speed to give all eight individual microphone time histories a common source emission time base. Each individual microphone time history consists of a series of 1/2-second root mean square pressure levels. The shifted time histories are then averaged. An ensemble-average time history has less variability than a single microphone time history and increased statistical confidence.

RESULTS

Data Variability.- To investigate long-term, between day, data variability, peak Overall Sound Pressure Level (OASPL) for each run was calculated from the ensemble-average time histories. No corrections were applied for deviations from a nominal flight path and no runs were rejected. The peak levels were averaged for like test conditions on a daily basis. Results are given in Table II for the 4.6 and 9.2 km runs with a tip speed of 240 m/s. Average OASPL valves ranged from 61 to

75 dB. In general, the repeatability within a particular test day was good. The standard deviation of the average OASPL of the 11 similar runs which were flown in a 90 minute period during the 6th test session was .7 dB. However, the average levels for the same test condition varied from day to day. For the 9.2 km, .7 M test condition, there was an 11 dB difference in average levels across days. For the same test condition and runs, a boom microphone on the PTA aircraft exhibited a range of 3 dB in the blade passage frequency noise level. The ground measured OASPLs were dominated by the blade passage frequency sound pressure level. This indicates, as expected, that the variability observed in the ground measurements is largely due to propagation. Another observation is that on the 3rd day the .5 M, 4.6 km average levels are greater by 3 dB than the .7 M, 4.6 km average levels.

		TEST SESSION							
TEST CONDITION	KEY	1	2	3	4	5	6	7	8
9.2 km, .7 M	AVG, dB	60.7	69.0	60.7	65.1			67.4	72.1
	σ, dB	1.4	.6	.2	.9			2.2	.8
	No.	2	4	4	4			3	4
4.6 km, .7 M	AVG, dB	74.8	72.6	67.6	69.7	74.8			74.0
	σ, dB	1.8	.5	1.3	.9	1.5			1.9
	No.	2	2	4	4	3			4
4.6 km, .5 M	AVG, dB	72.2		70.6	70.2	74.7	74.3		
	σ, dB	.6		.9	.2	.1	.7		
	No.	2		4	3	2	11		

Table II. Averaged ensemble-average time history peak OASPL.

Comparison To Ray Tracing.- Figure 1 is a comparison of a ray tracing predicted time history to an ensemble-average time history. The measured data are from a 9.2 km, .7 M run with a tip speed of 240 m/s. Included in the figure are the ensemble-average 80 percent confidence bounds. The acoustic source used in the ray tracing propagation model was an ANOPP[2] prediction based on nominally measured advanced turboprop operating conditions. An amplitude correction was applied to the predicted source levels for each run type based on the difference between a predicted and measured boom microphone amplitude for each run. A radiosonde weather profile was used in the two-dimensional ray tracing model which incorporates the effect of the wind by calculating an effective sound speed which

includes the component of the assumed horizontal wind in the vertical plane containing the airplane and the receiver. This comparison between measured and predicted time histories is fair. The peak level is overpredicted by 4 dB, and there is a small time shift in the prediction.

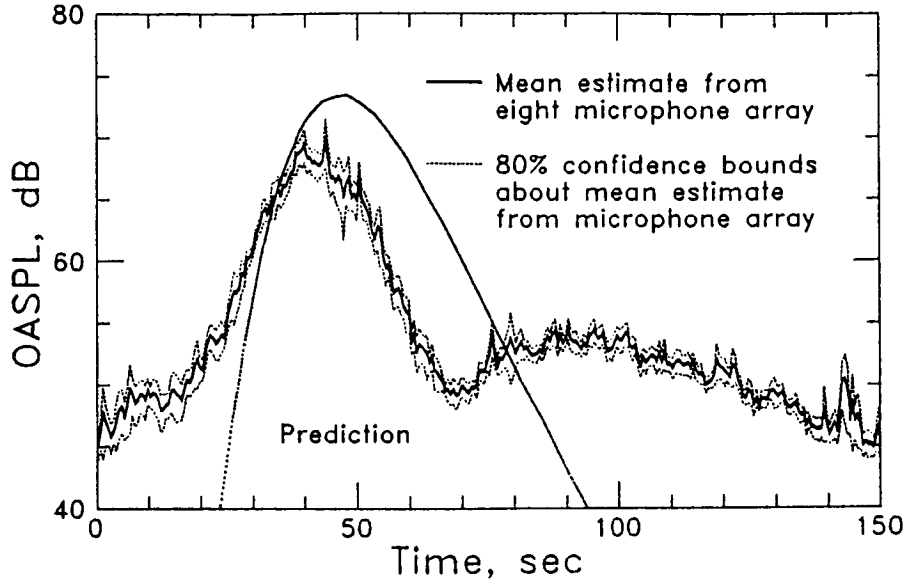

Figure 1. Ray trace prediction compared to ensemble-average time history.

Prediction Error.- To illustrate prediction error, the measured versus predicted overall SPLs for the 9.2 km, .7m; 4.6km, .7 m, and the 4.6 km, .5 m runs are plotted, respectively, in figures 2a through 2c. The dashed line in the plots is the perfect agreement line. The middle solid line is a regression line, and the 80% confidence levels about the regression line are represented by the two remaining solid lines. For the first two test conditions, 9.2 km and 4.6 km with a .7 m, the perfect agreement line falls within the 80% regression confidence bounds. There is an approximately 2 dB underpredicted basis in the 4.6 km, .5 m results. The reason for the basis is not currently known. The procedure for estimating source levels is being carefully reviewed. In general, the agreement between measurement and prediction is judged to be good.

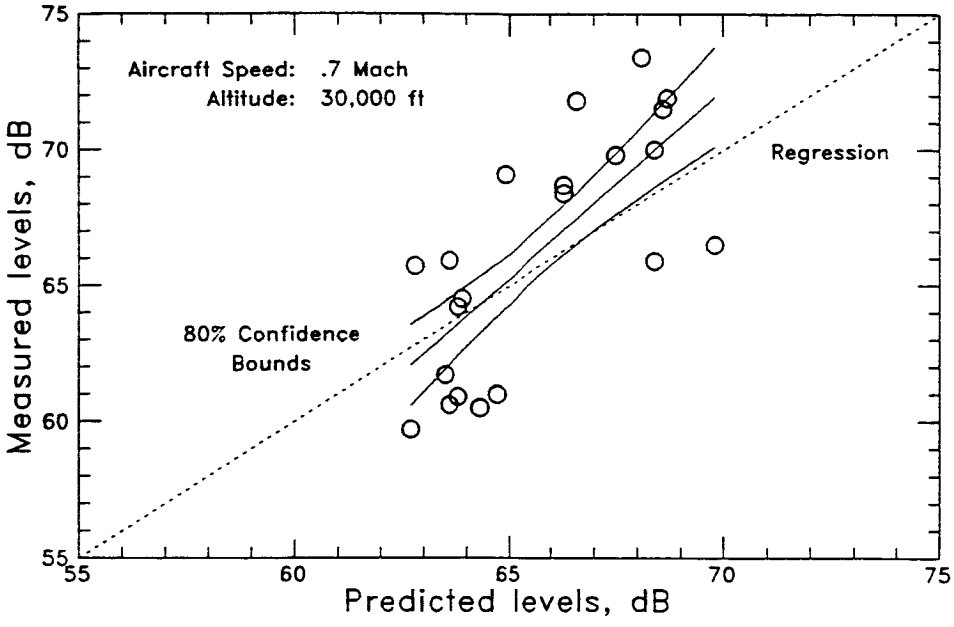

Figure 2a. Prediction error result for Mach .7, 30,000 ft. altitude condition.

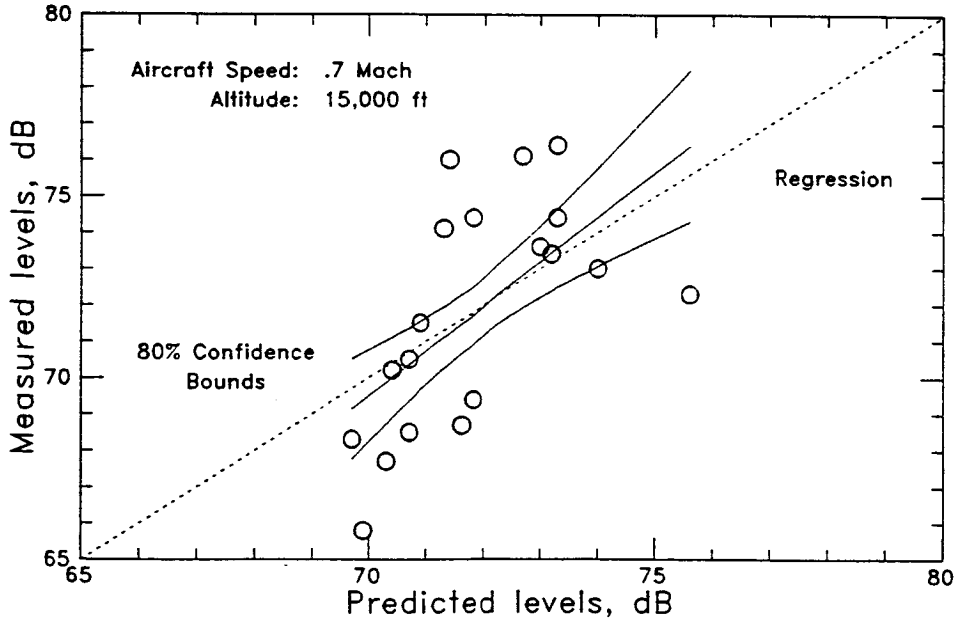

Figure 2b. Prediction error result for Mach .7, 15,000 ft. altitude condition.

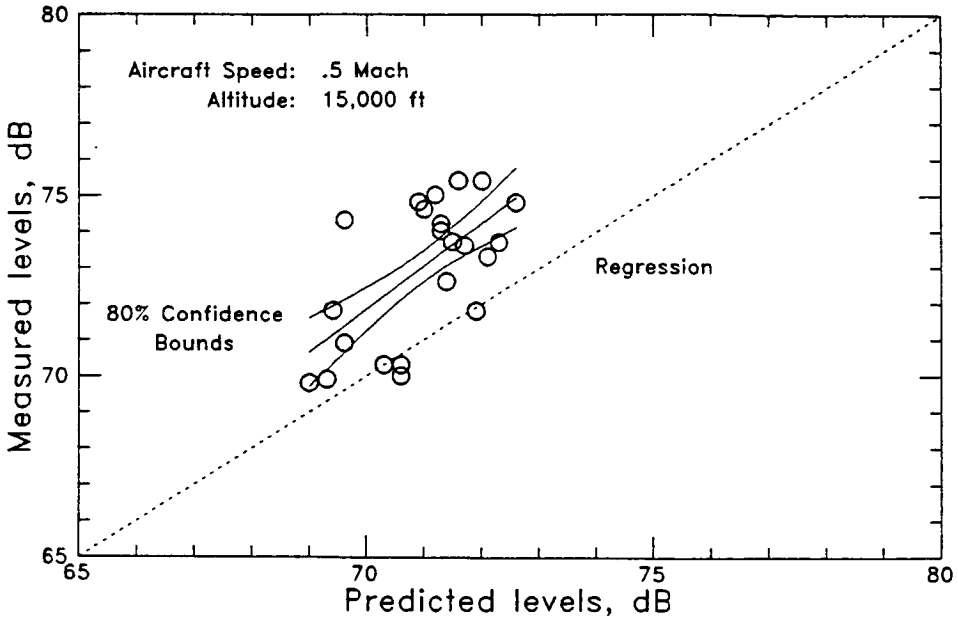

Figure 2c. Prediction error result for Mach .5, 15,000 ft. altitude condition.

SUMMARY

A flight experiment was conducted to investigate the propagation of advanced turboprop noise from cruise altitudes. The experiment was designed to use ensemble averaging and to measure weather profiles concurrently with the acoustic measurements. Data repeatability of ensemble-average Overall Sound Pressure Levels was good within a particular test day. Day to day average level variations existed. A two-dimensional ray tracing propagation model coupled with an empirically amplitude corrected predicted source noise directivity predicted the observed day to day average variability trends. Future research is aimed at understanding short-term, within a day, variability.

REFERENCES

1. O. Kipersztok: Uncertainty of Flyover Noise Data, AIAA Paper 83-0701, April 1983.

2. Aircraft Noise Prediction Program Theoretical Manual, NASA TM 83199, June 1986.

INFRASONIC OBSERVATIONS OF LARGE-SCALE HE EVENTS

Rodney W. Whitaker, J. Paul Mutschlecner,
Masha B. Davidson, and Susan D. Noel

Los Alamos National Laboratory

INTRODUCTION

The Los Alamos Infrasound Program has been operating since about mid-1982, making routine measurements of low frequency atmospheric acoustic propagation. Generally, we work between 0.1 Hz to 10 Hz; however, much of our work is concerned with the narrower range of 0.5 to 5.0 Hz. Two permanent stations, St. George, UT, and Los Alamos, NM, have been operational since 1983, collecting data 24 hours a day. For the purposes of this discussion, we will concentrate on our measurements of large, high explosive (HE) events at ranges of 250 km to 5330 km. Because our equipment is well suited for mobile deployments, we can easily establish temporary observing sites for special events. The measurements in this report are from our permanent sites, as well as from various temporary sites. In this short report we will not give detailed data from all sites for all events; rather, we will present a few observations that are typical of the full data set.

The Defense Nuclear Agency sponsors these large explosive tests as part of their program to study airblast effects. A wide variety of experiments are fielded near the explosive by numerous Department of Defense (DOD) services and agencies. Our measurement program is independent of this work; we use these tests as energetic known sources, which can be measured at large distances. Ammonium nitrate and fuel oil (ANFO) is the specific explosive used by DNA in these tests. Table I gives the test names, dates, charge weights, and number of our infrasonic stations operated for each test. All tests were fired at White Sands Missile Range, NM.

BACKGROUND

The basic sensor for our work is the Globe 100 microphone. A series of porous hoses is used to reduce the noise from the low-level local wind. Figure 1 shows a microphone and associated noise-reducing hoses, which can be thought of as a modification of the Daniel's tube used for lower frequency work (reference 1). During periods of quiet background, this sensor can easily detect signals down to a few tenths of a microbar. In our frequency

domain, there are natural as well as man-made sources of infrasound, some of which are described in Chapter 9 of reference 2. However, this background is not saturated with confusing signals, which simplifies the detection problem considerably.

An infrasound array consists of 3 to 6 sensors placed in a regular pattern. We employ standard, time-delay, and sum beamforming techniques to process the recorded data. The present algorithm is a modified version of one due to Young and Hoyle (reference 3). Generally, 20-seconds of data are processed at a time, followed by a 50% shift and continued processing. For each 20-second window, the beamformer provides the correlation coefficient, trace velocity, and azimuth of the highest correlation signal, as well as the power spectrum for that interval. Longer intervals of data can be summarized in the manner illustrated in figure 2, where 60 minutes of data are shown. The presence of a signal is easily seen as the fixed azimuth line from 16:36 UT to 16:43 UT.

Signal energy propagates in the atmospheric sound ducts created by the ambient temperature structure, or by a combination of temperature and wind. When propagation is in the same direction as the upper atmospheric winds, total refractions occur between 40 km and 60 km altitudes. The upper atmospheric winds are seasonal in nature, blowing to the east in winter and to the west in the summer (reference 4). It is important to note that at these altitudes the wind speed can be a significant fraction of the sound speed; therefore, the wind profile must be included correctly in any calculational work. The simplification of an effective sound speed profile is not appropriate for these propagation paths.

OBSERVATIONS

Before discussing specific time series for two events, a few general comments will be useful. We use the concept of an average velocity to broadly classify the observed propagation paths. Here, average velocity is just the great circle source to receiver distance divided by travel time. With wind propagation, the strongest signals arrive with an average velocity of 0.29 km/s. Ray tracing results confirm that this corresponds to total refractions at 40 km to 60 km altitudes. Higher average velocities indicate lower paths, and conversely. The stations north and northwest of White Sands, Los Alamos and St. George, often observe a first arrival with an average velocity of 0.34 km/s. This must be energy that travels at or very near the surface; we will for the moment refer to this as the surface wave.

The seasonal winds have a significant effect on observed pressures. A propagation path in the direction of the wind will result in a larger pressure than along a path directed against the wind. We apply a correction for this effect, which normalizes amplitudes to a zero wind condition. This procedure is described in reference 5.

For the Minor Scale test we had two arrays at Barking Sands, Kauai, HI, at a distance of 5330 km, our most distant detection. One array operated at our standard frequency range, while the other operated at lower frequency, about 0.01 Hz to 0.1 Hz. Both arrays detected the event, but the detection at the lower frequency was much better, as expected for such large distances.

Figure 3 presents single channel time series from four sites for the Misty Picture event. Each panel is composed of 12 minutes of data in three, four minute windows. The time above each window is the time at the start of the window. Average velocities, m/s, are written below specific features for easy reference. For Los Alamos, note the surface wave at 342.5 m/s. For these time series, the data are well correlated with the source azimuth from first arrival to the end of the record shown.

Figure 4 is the same as figure 2 but is for the Misers Gold event. The surface wave at Los Alamos is evident with a 339.2 m/s average velocity. Again signal energy is well-correlated with source azimuth from first arrival until the end of the displayed record. These two figures illustrate the character of the observations for these energetic events. Strong multiple arrivals are common, with total durations on the order of 10 minutes. The surface wave is common at 250 km north, and has been observed at 750 km to the northwest.

In figure 5, power spectra contours are shown for the Misty Picture event as observed at St. George, UT. Contours of power are given as functions of time and frequency. Four major arrivals are seen from 18:56:30 to 19:03:00, with the largest powers concentrated below 1.2 Hz. Note that the major arrivals have frequency contributions across the whole band, from 0.2 Hz to 3.0 Hz.

For the purpose of examining pressure as a function of range, we have found it useful to place all the data on a common scale by the use of scaled range. In figure 6, we give the peak-to-peak amplitude of the largest signal (wind corrected) as a function of scaled range. The scaled range is the actual range divided by $(2W)^{1/2}$, where W is the charge weight in tons, the factor of

2 is the standard factor for surface explosions, and the exponent is that appropriate for the cylindrical geometry of the ducted paths. The least squares slope is -1.4, showing only a modest increase in loss over the cylindrical value of -1.0.

During the conference, a few of the participants (Drs. Raspet, Attenborough, and West) suggested that the surface wave was likely a creeping wave, as described by Pierce (reference 6). Following the discussion in reference 6, we have estimated the attenuation for such waves and find an attenuation coefficient of 0.1 km^{-1}. Over the shorter path of 250 km, this gives a huge loss, sufficiently large, we believe, to rule out this explanation.

We wish to acknowledge the support of the Department of Energy Office of Arms Control for the work supported here.

TABLE I - EXPERIMENTS

Event	Date	Weight Tons	Sites
Millrace	9/16/81	600	1
Pre Direct Course	10/7/82	24	2
Direct Course	10/26/83	600	4
Minor Scale	6/27/85	4800	4
Misty Picture	5/14/87	4800	5
Misers Gold	6/01/89	2400	8

REFERENCES

1. Daniels, F. B.: Noise Reducing Line Microphone for Frequencies Below 1 cps. JASA 31, 529-531, 1959.

2. Gossard, Earl E.; Hooke, William H.: Waves in the Atmosphere. Elseview Sci. Pub. Co., 1975, Ch. 9.

3. Young, Jessie M.; Hoyle, Wayne A.: Computer Programs for Multidimensional Spectra Array Processing. NOAA Technical Report ERL 345-WPL43, 1975.

4. Webb, Willis L: Structure of the Stratosphere and Mesosphere. Academic Press, 1966.

5. Mutschlecner, J Paul; Whitaker, Rodney W.: The Correction of Infrasound Signals for Upper Atmospheric Winds. Fourth International Symposium on Long Range Sound Propagation, NASA CP-3101, 1990.

6. Pierce, Allan D.: Acoustics: An Introduction to Its Physical Principles and Applications. McGraw-Hill, Inc. 1981.

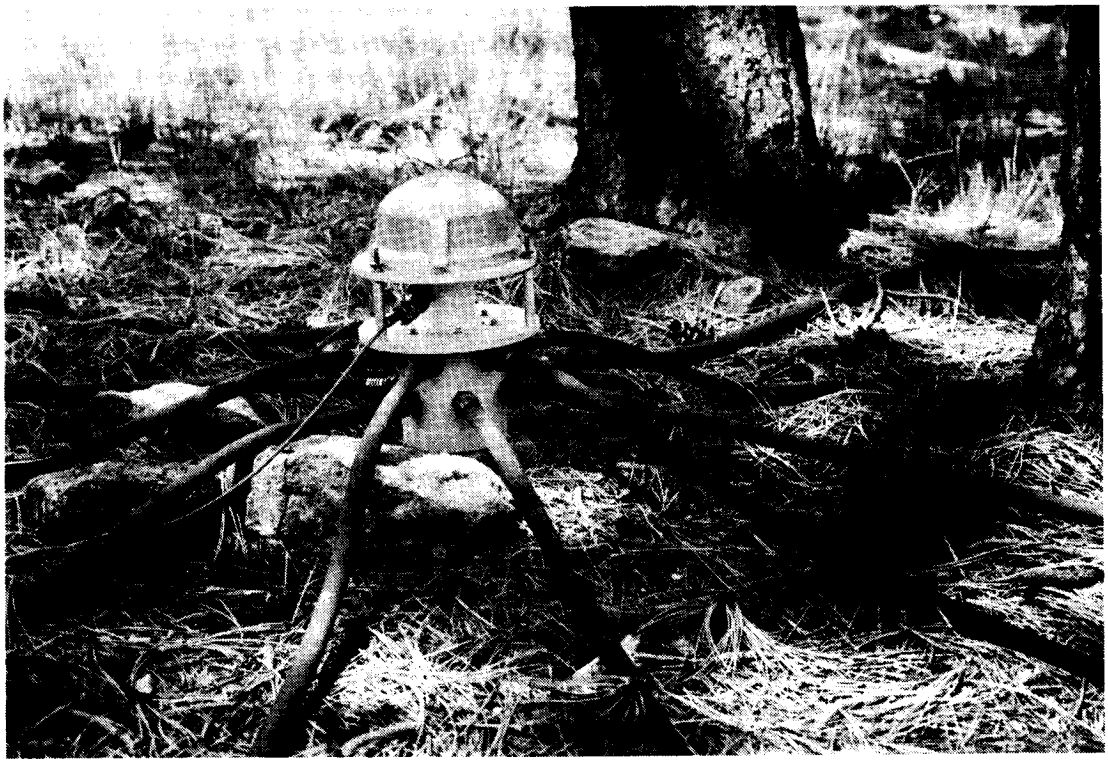

Figure 1. Infrasound microphone and noise reducing porous hoses.

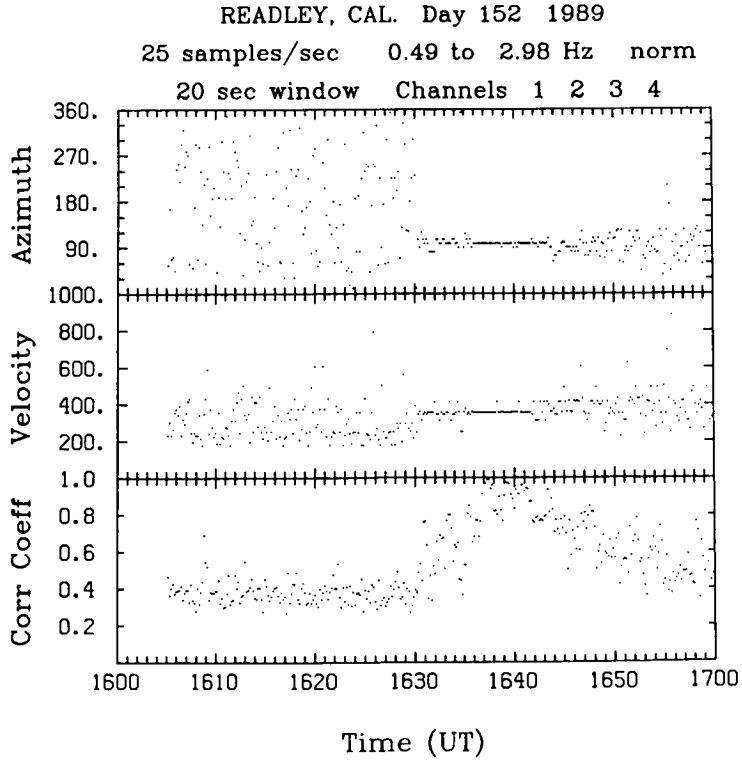

Figure 2. Summary of beamformer array processing program showing correlation coefficient, trace velocity, and azimuth as functions of time. Data are for Miser's Gold event observed at Readley, Ca.

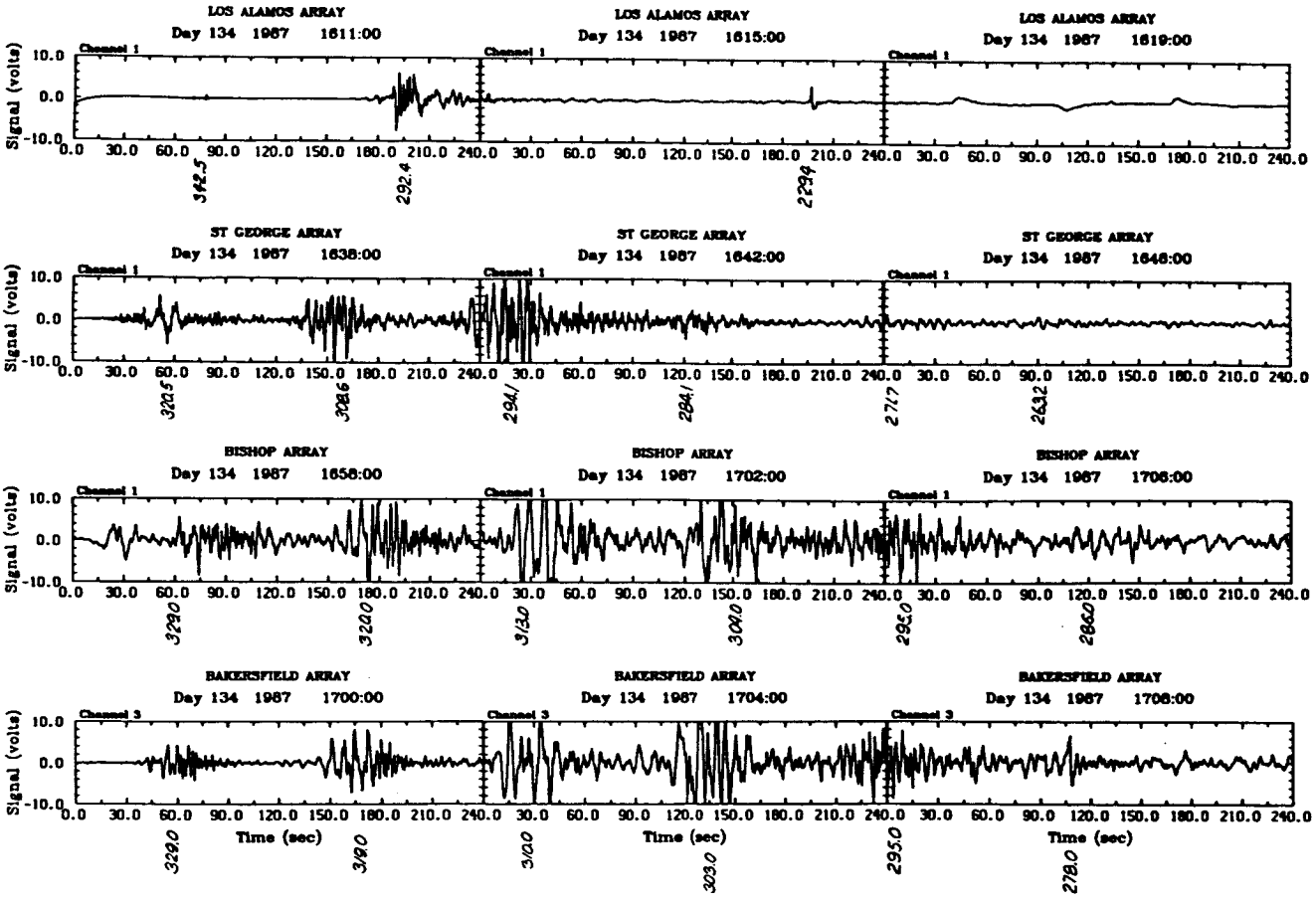

Figure 3. Samples of observed Misty Picture time series from four stations. The Bishop and Bakersfield stations were in California.

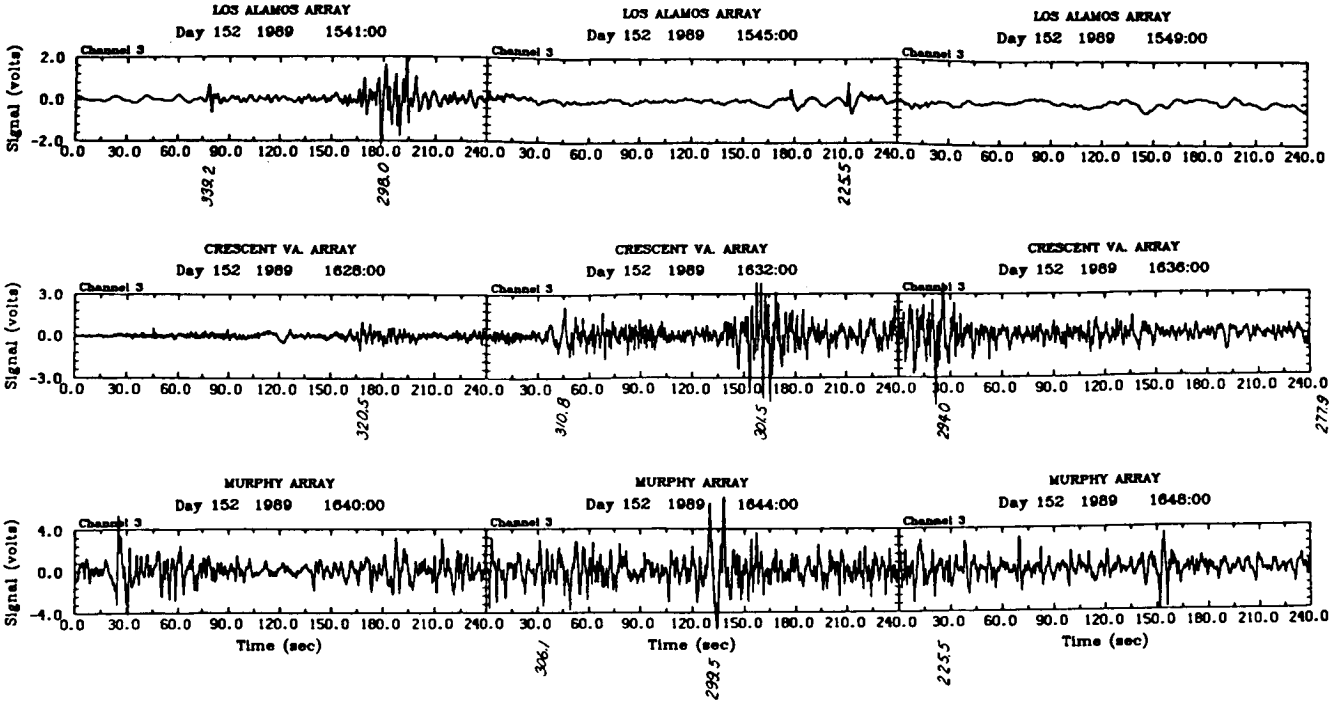

Figure 4. Samples of observed Miser's Gold time series from three stations. Crescent Valley is in Nevada, and Murphy is in Idaho.

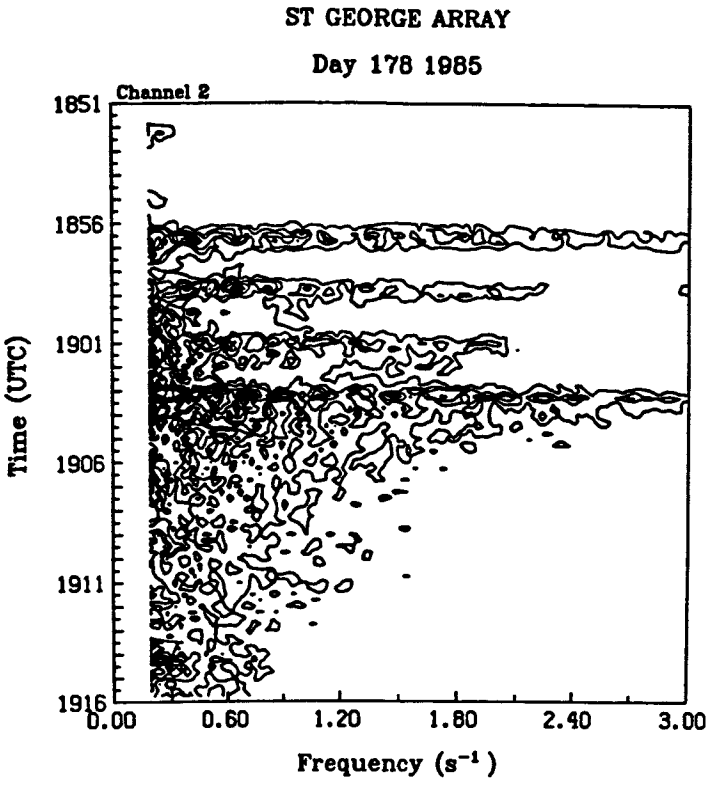

Figure 5. Power spectra contours for Misty Picture from the St. George, UT array.

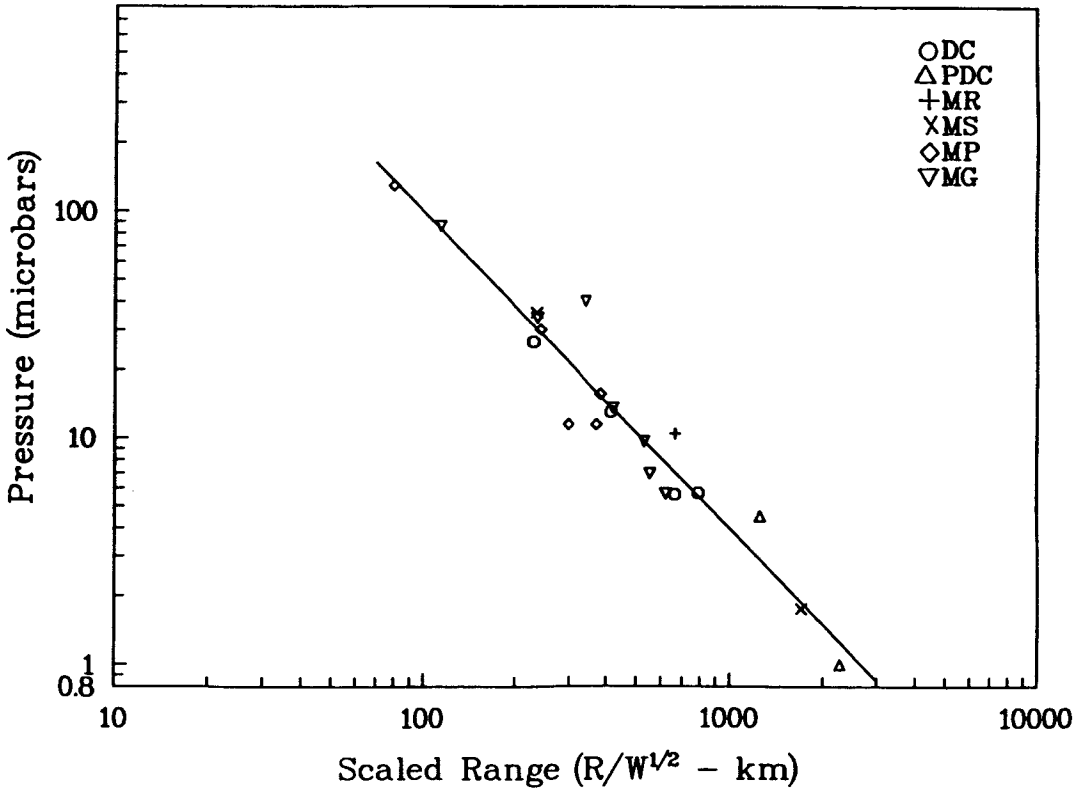

Figure 6. Peak to peak amplitude vs scaled range for the six HE events.

THE CORRECTION OF INFRASOUND SIGNALS FOR UPPER ATMOSPHERIC WINDS

J. Paul Mutschlecner and Rodney W. Whitaker
Los Alamos National Laboratory

INTRODUCTION

Infrasound waves propagate in the atmosphere by a well known mechanism produced by refraction of the waves, return to earth, and reflect at the surface into the atmosphere for subsequent bounces (see e.g. reference 1). Figure 1 illustrates this phenomenon with results from a ray trace model. In this instance three rays are returned to earth from a region centered at about 50 kilometers in altitude and two from a region near 110 kilometers in altitude. The control of the wave refraction is largely dominated by the temperature-height profile and inversions; however, a major influence is also produced by the atmospheric wind profile. Figure 2 illustrates the considerable ray differences for rays moving in the wind direction (to the right) and in the counter direction (to the left). It obviously can be expected that infrasonic signal amplitudes will be greatly influenced by the winds in the atmosphere. The seasonal variation of the high altitude atmospheric winds is well documented (see e.g. reference 2). Figure 3 illustrates this with average statistics on the observed zonal wind in the region of 50 $\pm$ 5 kilometers in altitude. The results are based upon a survey by Webb (reference 2); Webb terms this parameterization the Stratospheric Circulation Index (SCI). The very strong seasonal variation has the ability to exert a major seasonal influence on infrasonic signals. It is our purpose to obtain a method for the correction of this effect.

METHODOLOGY

There are two possible approaches to the determination of a procedure for the correction of infrasound signals for the effects of winds. The first of these is by modeling of infrasonic propagation in the presence of various wind profiles. We are currently taking this approach with both a ray-trace model and a normal mode model and hope to show results in the near future. The second approach is to derive a correction method empirically from a sufficiently large and consistent data set. This is the method which we report upon here. The results given here are preliminary in nature and we present only a simplified outline of the procedures. As indicated in Section IV, more extensive work in the near future will provide comprehensive results. In the meantime, we have been applying the results to our measurements (see reference 3).

A large data set, which appears to be appropriate for the empirical work, is given in reference 4. It consists of infrasonic observations by the Sandia National Laboratory of atmospheric nuclear tests conducted at the Nevada Test Site (NTS) during the period 1951 to 1962. The observations were made at nine stations surrounding NTS as shown in figure 4. While several of the stations are probably too close to the source region to be useful, at least six stations appear to be appropriate. A total of 80 events are presented by Reed and cover an explosive yield range from 1/2 to 74 kilotons (HE equivalent). The measurements were made by a standard set of microbarographs.

This consistently measured and analyzed set of signals, observed at many times of the year, presents a unique set of data for our purposes.

ANALYSIS AND RESULTS

Since the atmospheric nuclear data are for a variety of yields, and also have effects due to some variation in height of burst, it is necessary to scale all data for these two factors. Reed has done this with a $W^{0.4}$ scaling law (W = kilotons HE equivalent) and a height-of-burst functional relation. While some discussion of both of these scaling relations is appropriate, the preliminary nature of the present work leads to use of Reed's corrections.

Figure 5 illustrates the resulting scaled data for the St. George, Utah, station as a function of date. The symbols refer to various test series, unimportant here, and the line is an eye-fitted relation. Amplitudes are scaled to a 1 kiloton explosion. The very strong seasonal effect is the major feature of the data; the much lower amplitude during the summer period presumably results from the winds contrary to wave propagation to St. George during summer. It is unfortunate that there are no data for the period in mid winter, January - December. Examination of Reed's results shows that the seasonal variation changes markedly with station direction from the test site: northern and southern stations show a much weaker effect than does St. George. This follows from the fact that those stations are only slightly affected by the zonal wind and are primary affected by the much weaker and less variable meridional winds. This supports the hypothesis that we see primarily the seasonal wind effect in the data variation.

High altitude winds are conventionally measured by rocketsonde (and now by satellite). The absence of rocketsonde observations for the period covered by the NTS data leads us to use the statistical SCI data of reference 2 as a first-order estimator of the atmospheric wind. The eye-fitted lines for each station (e.g. figure 5) were used to estimate signal amplitudes at monthly intervals. Figure 6 illustrates the result for St. George, where the wind

velocity component directed from NTS to St. George is plotted against the amplitude. Similar relations are determined for each station, using the wind vector toward the station based upon meridional and zonal SCI values. The results are reasonably consistent among the stations; however, the nearly east or west stations, such as St. George, are probably more dependable because of the strong zonal wind variation there.

The averaged result of the analysis is,

$$A = A_o \, 10^{kV}$$

where A = observed amplitude (mbars)

A_o = corrected "zero-wind" amplitude (mb)

k = 0.018 s/meter

V = SCI vector from source to observer meters/s.

The relation permits us to correct all observations for the wind to derive consistent "zero-wind" amplitudes.

COMMENTARY ON RESULTS

We have applied the method described here to a wide variety of observations. Where possible, we have used rocketsonde or satellite observations of the wind profile, deriving from these an effective SCI wind vector amplitude. Since the actual wind can vary widely from the statistical SCI, use of statistical values is less dependable. As an example of the use of the method, we show its application to a set of observations of signals from a set of earthquakes which were observed at our St. George array, with the exception of the earthquake at M_b = 7.8, which is from reference 5. All amplitudes have been scaled to a distance of 1000 kilometers by use of the factor $(R/1000)^{1.15}$, where R is the actual range in kilometers. Figure 7 shows the amplitudes uncorrected for wind against the body magnitude, M_b, for each earthquake. The bars on some observations indicate the range of interpretation of peak amplitude. Figure 8 shows the same set of data but with the amplitudes corrected by our method; only statistical SCI winds were employed. Clearly the effect on the relationship is very large; there is also the impression that the connection between amplitude and M_b may be

clearer. However, a mechanism is not now known, so this evidence is circumstantial. The smallest earthquake, at M_b = 4.6, is an aftershock and may not be in the same class as the others.

We have not completed our analysis of the nature of the wind effect on amplitudes and therefore can only speculate on the correction method and its form. It is clear that two mechanisms can change the amplitude with change in the wind profile: (1) the number of rays captured at a return layer will vary depending upon the wind, (2) the distribution of rays on the surface will depend on the wind profile (e.g., see figure 2). Modeling should help in the understanding of the correction form.

It should be noted that all of the work reported here applies to those signals resulting from returns from a 50 kilometer high level. We believe that signals resulting from the 110 kilometer level require an additional correction and have formulated a tentative correction formulation. Such signals, in general, will occur only with near zero wind, or counterwind, conditions.

FUTURE EFFORTS

We have reported here on our preliminary results. We are now working on an improved analysis. This will include the following:

1. A comprehensive statistical analysis of the data set resulting in an improved formulation;

2. Modeling of the effect to better understand its physical basis;

3. A detailed investigation of the "counterwind" signal circumstances, using appropriate data and modeling.

We wish to acknowledge the support of the Department of Energy Office of Arms Control for the work supported here.

REFERENCES

1. Gossard, Earl E.; Hooke, William H.: Waves in the Atmosphere. Elsevier Sci. Pub. Co., 1975, Ch. 9.

2. Webb, Willis L: Structure of the Stratosphere and Mesosphere. Academic Press, 1966.

3. Whitaker, Rodney W.; Mutschlecner, J. Paul; and Davidson, Masha B.: Infrasonic Observations of Large Scale HE Events. Fourth International Symposium on Long Range Sound Propagation, NASA CP-3101, 1990.

4. Reed, Jack W.: Climatology of Airblast Propagation from Nevada Test Site Nuclear Airbursts. Sandia Laboratories Research Report, SC-RR-69-572, 1969.

5. Young, Jessie M.; and Greene, Gary E.: Anomalous Infrasound Generated by the Alaskan Earthquake of March 28, 1964. J. Acoust. Soc. of Am., 71 (2), February 1982.

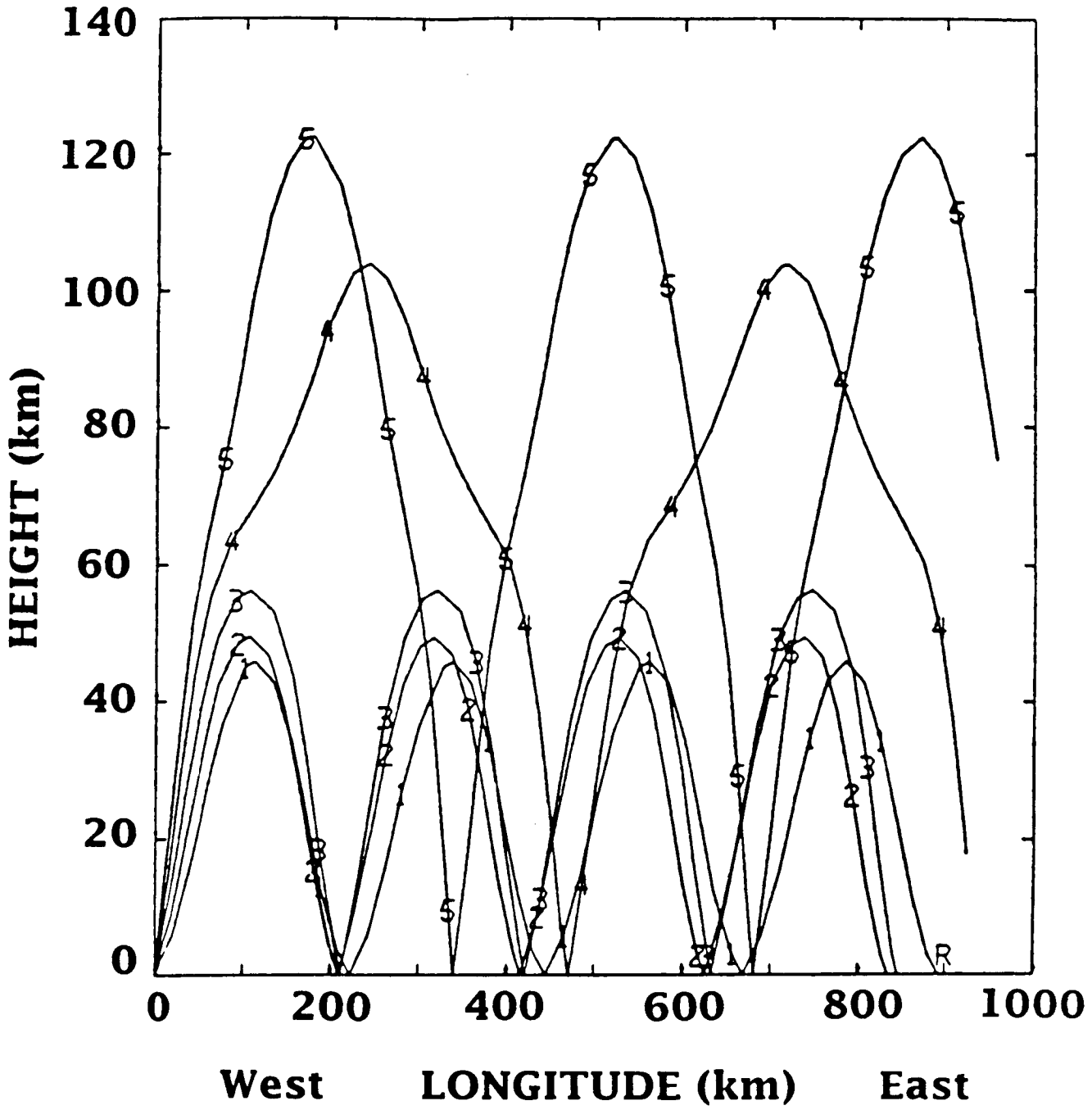

Figure 1. Results of a ray trace model showing five sample rays. Rays 1, 2, 3 are refracted and returned from a region near 50 kilometers and rays 4 and 5 from near 110 kilometers.

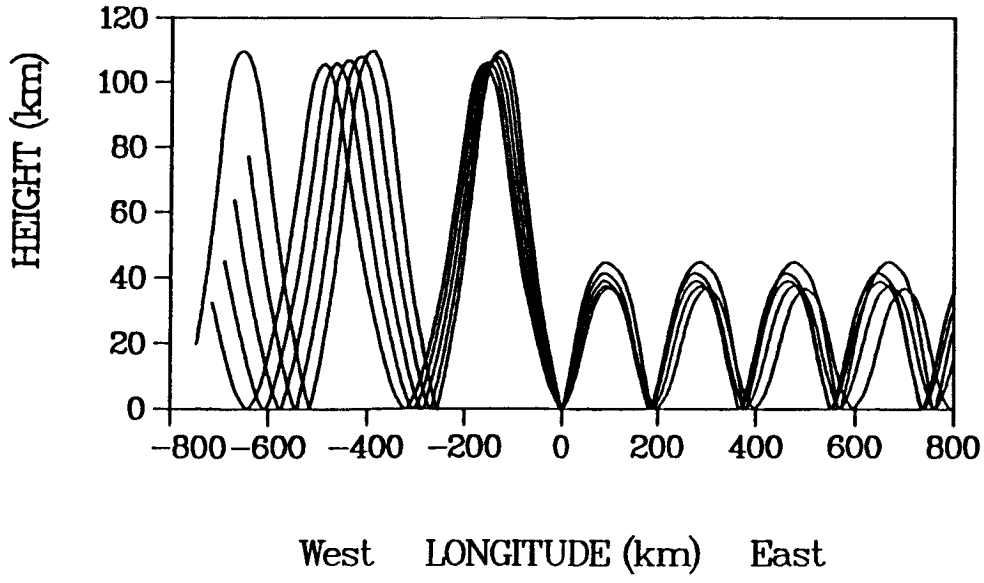

Figure 2. Ray tracing results for propagation with the wind (to the right) and against the wind (to the left).

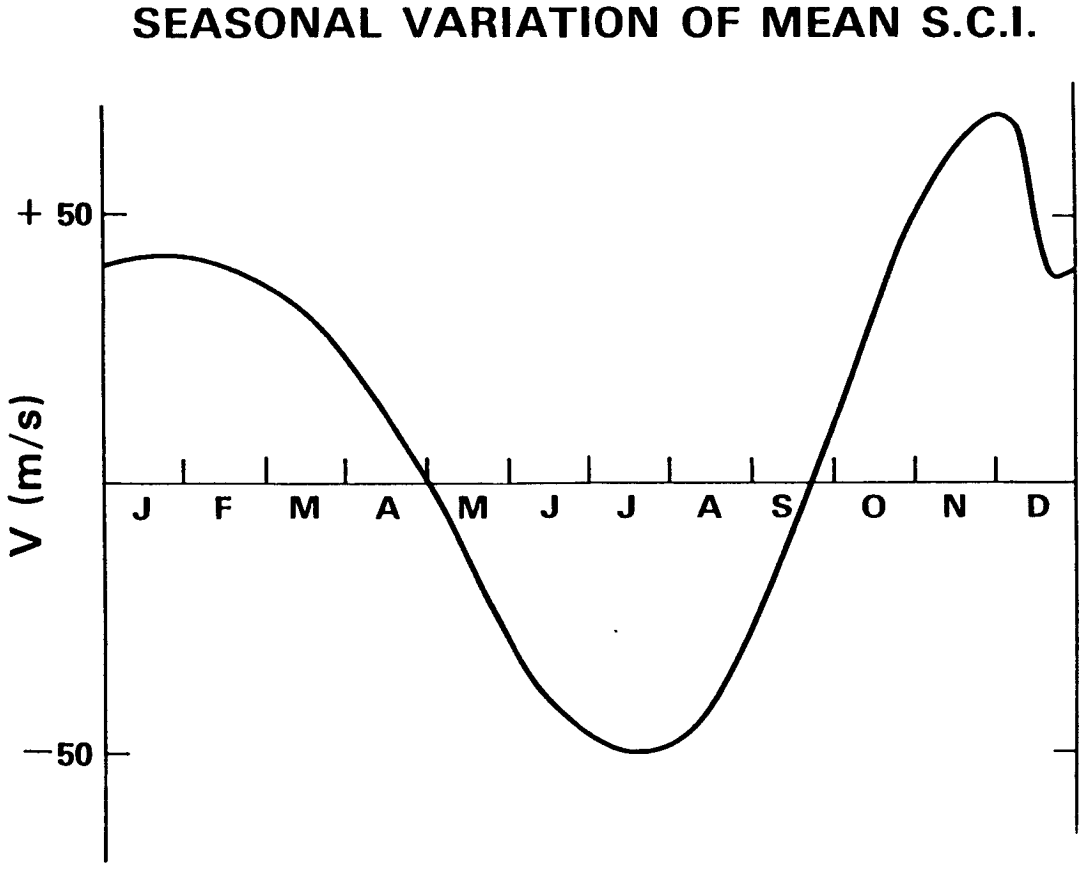

Figure 3. This illustrates the seasonal variation of the average SCI wind at White Sands.

Sandia Network

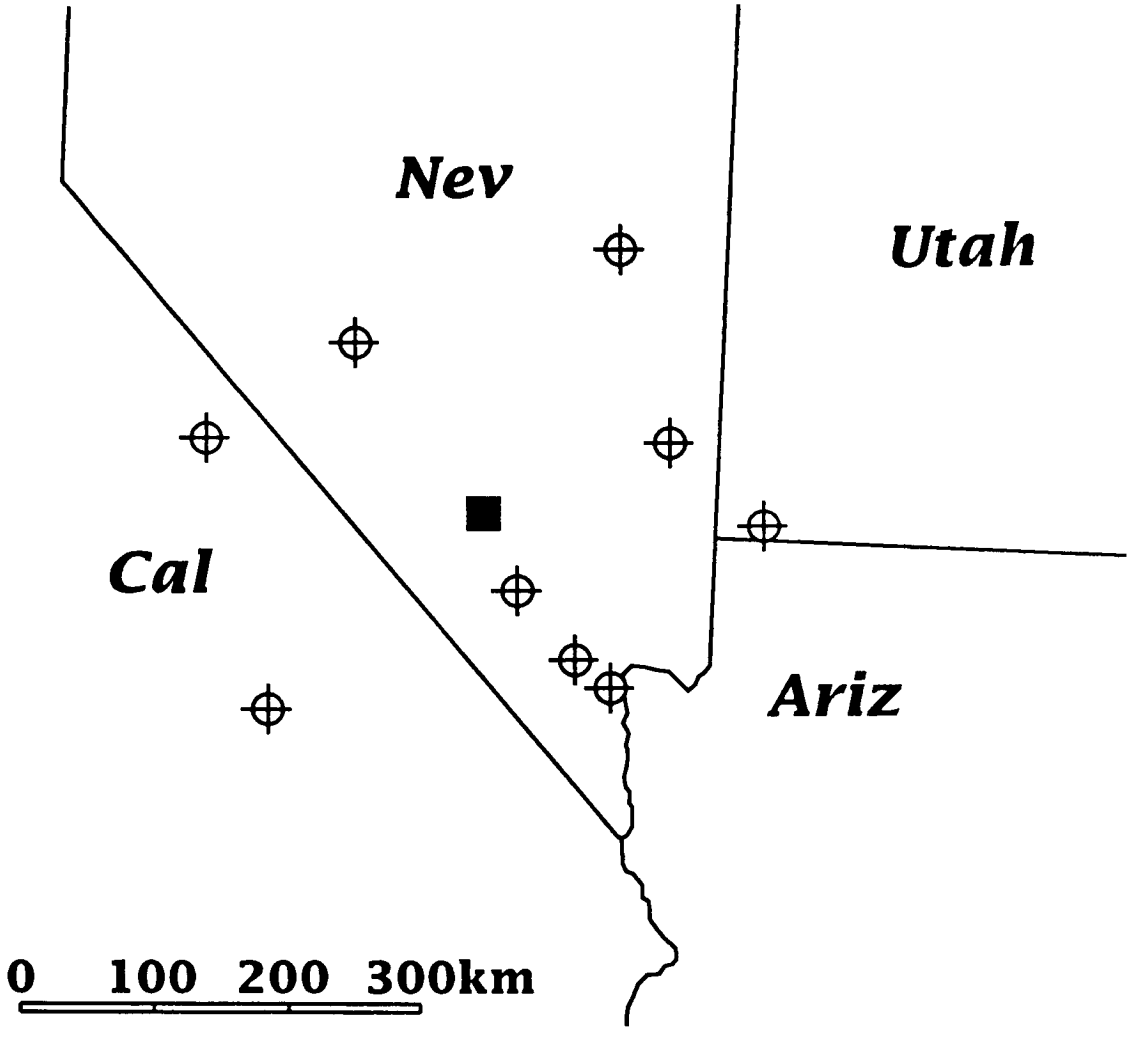

Figure 4. The Sandia Scientific Laboratory network of microbarographs (crossed circles) surrounding the Nevada Test Site (square).

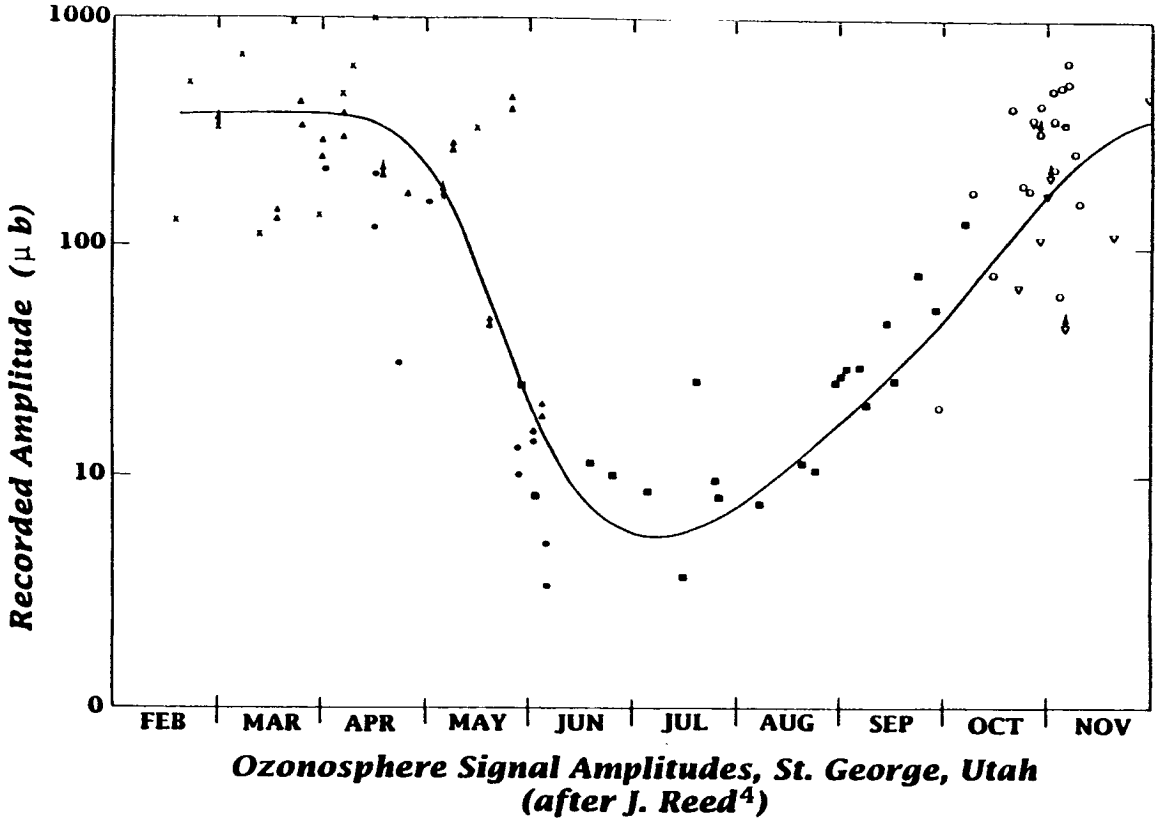

Figure 5. Nuclear atmospheric burst scaled signal amplitudes recorded at the St. George, Utah, microbarograph station against date.

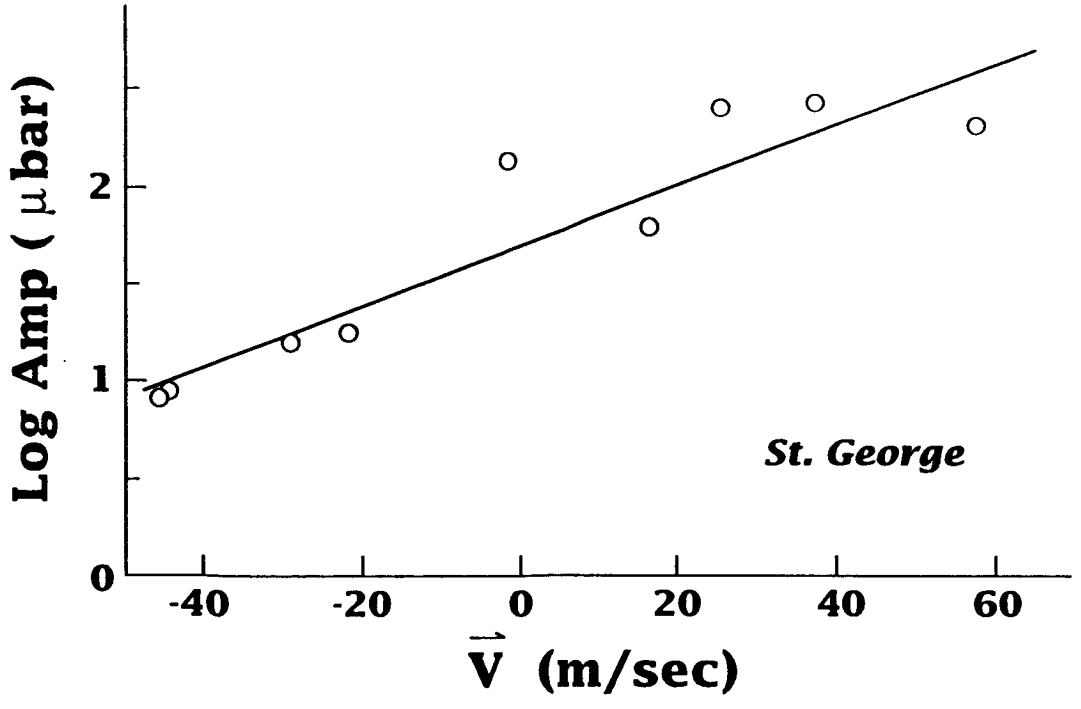

Figure 6. Monthly average values of nuclear atmospheric burst scaled signal amplitude versus statistical SCI velocity for St. George.

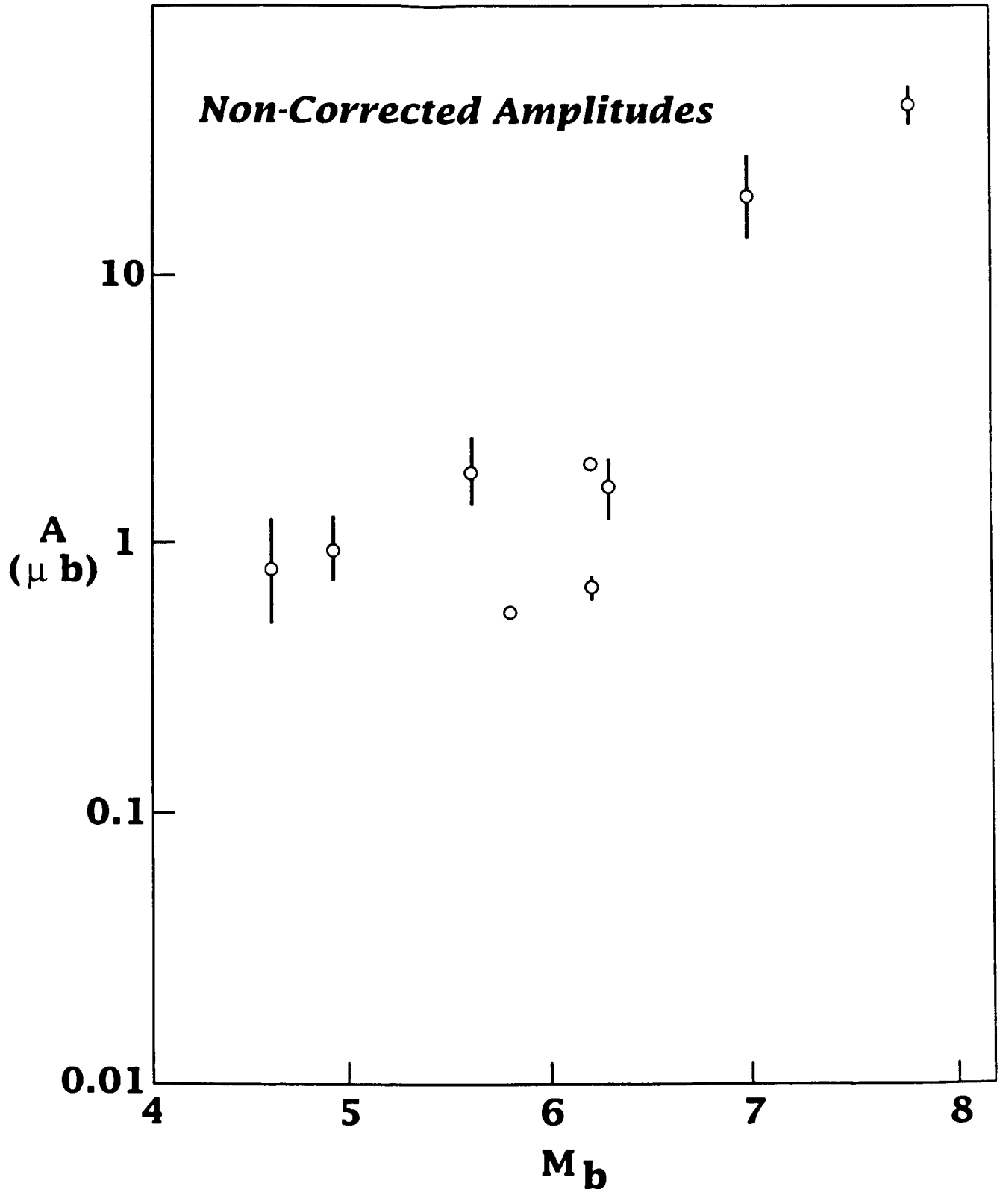

Figure 7. Scaled amplitudes of earthquake infrasonic signals versus earthquake body magnitude, M_b. Uncorrected for wind.

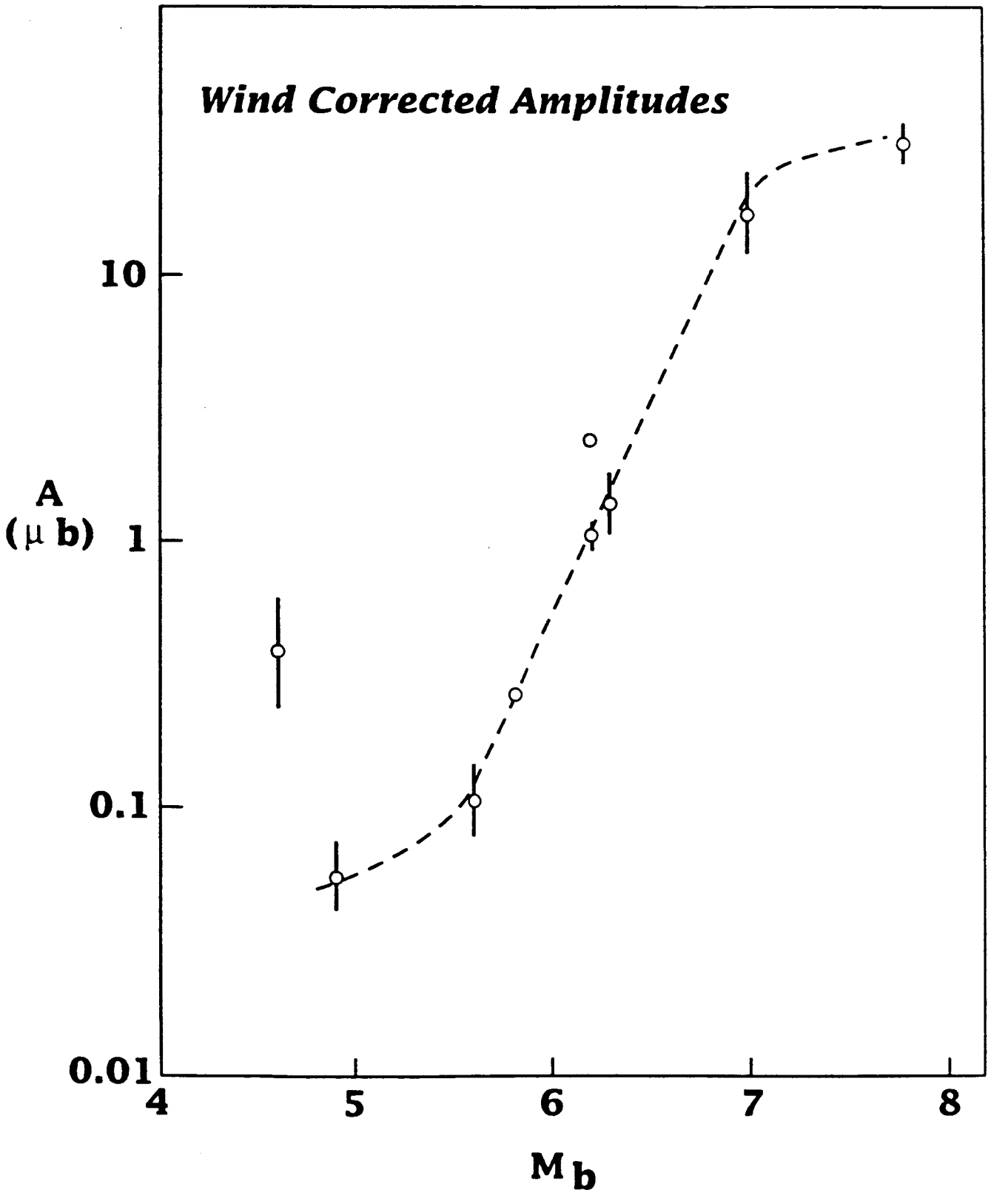

Figure 8. Same data as in Figure 7, but corrected for wind.

Meteorological Effects on Long-Range Outdoor Sound Propagation

Helmut Klug

University of Oldenburg, P.O.B. 2503, FB 8
D-2900 Oldenburg, FRG

I. INTRODUCTION

Measurements of sound propagation over distances up to 1000 m were carried out with an impulse sound source offering reproducible, short time signals. Temperature and wind speed at several heights were monitored simultaneously; the meteorological data are used to determine the sound speed gradients according to the Monin-Obukhov similarity theory. The sound speed profile is compared to a corresponding prediction, gained through the measured travel time difference between direct and ground reflected pulse (which depends on the sound speed gradient). Positive sound speed gradients cause bending of the sound rays towards the ground yielding enhanced sound pressure levels. The measured meteorological effects on sound propagation are discussed and illustrated by ray tracing methods.

II. SOUND SPEED PROFILES

Wind speed and temperature are functions of elevation above ground. They are interrelated and can be described by the Monin-Obukhov similarity theory /1/ using two parameters, the friction velocity u_* and the scaling temperature T_*. The Monin-Obukhov Length L is a stability parameter for the turbulent atmospheric surface layer:

$$L = (T_m/gk)(u_*^2/T_*)$$

T_m: representative temperature, g: acceleration due to gravity, k: von Kármáns constant (0.41).

The sound speed profile can be described by

$$c(z) = c(z_0) + a'(ln(z/z_0) + \psi(z/L)) \qquad (1)$$

where $a' = u_*/k + 0.6T_*/k$ and z_0 is the roughness length.

For the stable case (positive temperature gradient, strongest bending of sound rays towards the ground), $\psi(z/L) = 5z/L$, and the sound speed gradient is:

$$dc/dz = (a'/z)(1+5z/L) \qquad (2)$$

Examples of measured temperature and wind speed profiles are shown in Fig. 1. The parameters u_* and T_* are calculated from those measured data by least square methods /2/. In the unstable case wind speed and temperature almost remain constant in larger elevations (no sound speed gradient), while in the stable case there is still an increase in wind speed and temperature. Close to the ground the profiles are 'logarithmic' in both cases.

III. ACOUSTICALLY MEASURED SOUND SPEED GRADIENTS

Measured travel time differences between direct and ground reflected sound can be used to estimate the sound speed profile during the measurement. The geometrical time difference Δt_g is:

$$\Delta t_g = \Delta D/c = [\sqrt{(h_s + h_r)^2 + D^2} - \sqrt{(h_s - h_r)^2 + D^2}]/c \qquad (3)$$

c: sound speed ; h_s: source height; h_r: receiver height.

The sound speed profile c(z) causes an additional time difference $\Delta t'$, the total time difference Δt between direct and ground reflected sound is:

$$\Delta t = \Delta t' + \Delta t_g \qquad (4)$$

For small deviations of the actually curved ray path from the geometrical path the travel time of the ground reflected pulse can be estimated to be for the stable case /3/:

$$T_{refl} = \int c(z)^{-1} ds = Dc(z_0)^{-2} [c(z_0) - a' ln(z'/z_0) + a' - 2.5a'z'/L] + \Delta t_g \qquad (5)$$

where $z' = h_s = h_r$. The travel time of the direct pulse at height z' is:

$$T_{dir} = D/c(z') = D/[c(z_0) + a' ln(z'/z_0) + 5a'z'/L]$$

$$= Dc(z_0)^{-2}[c(z_0) - a ln(z'/z_0) - 5a'z'/L] \qquad (6)$$

and the travel time difference is:

$$\Delta t = T_{refl} - T_{dir} = [a'(1 + 2.5z'/L)]D/c(z_0)^2 + \Delta t_g. \qquad (7)$$

Two measurements of the travel time difference at different heights z' are necessary to determine the parameters a' and L.

Close to the ground or for the nearly neutral case (z/L becomes 0) the sound speed profile becomes 'logarithmic',

$$c(z) = c(z_0) + a ln(z/z_0) \quad \text{and} \quad dc/dz = a/z, \qquad (8)$$

the parameter a can be calculated from the measured time difference for only one source-receiver height:

$$a = \Delta t' c(z_0)^2/D \qquad (9)$$

IV. SOUND PROPAGATION MEASUREMENTS

The impulse sound source /4/ used for the acoustical measurements consists of a capacitor (100 μF, 3.5 kV), which is discharged over a spark gap. A reproducible short pulse (less than 1 ms) is radiated spherically (sound pressure level 150 dB at 1 m distance). As an example Fig. 2 shows a measured time signal close to the sound source. The time delay between direct and ground reflected pulse (here 8 ms) is mainly caused by geometry. A reference signal monitored in an unechoic room at 6.25 m distance to the sound source is used to calculate the SPL re free field for each frequency.

Two examples of downwind sound propagation measurements (8 August 1988 and 3 November 1988) are shown in the following. Measurements for several geometries done in the afternoon (unstable conditions) were repeated a few hours later under stable conditions (positive temperature gradient). The resulting meteorological effects are discussed.

August-measurement

For a distance of 250 m the measured time signal is shown in Fig. 3 a (temperature and wind speed profile see Fig. 1 c). The travel time difference Δt_g resulting from geometry is 3.7 ms. The measured time difference Δt (determined from the magnitude of the autocorrelation function of the measured sound pressure signal) is 5.3 ms (see Fig. 3b), the additional time delay $\Delta t'$ = 1.6 ms being due to meteorological effects (wind speed and temperature). It can be used (eq. 8,9) to calculate the sound speed gradient:

$$a = \Delta t' c(z_0)^2/D = 0.7 \text{ m/s}; \quad dc/dz = a/z = 0.7 \text{ 1/s}$$

A few hours earlier (meteorological conditions see Fig. 1 b) a time difference Δt = 4.6 ms was measured for the same geometry, yielding a parameter a = 0.4 m/s.

For a source and receiver height of 12.5 m there is only a small change in the measured SPL due to meteorological effects (Fig. 4 a). The interference pattern is shifted a little towards lower frequencies for the evening measurement, the sound pressure level increasing about 1 dB. For source and receiver situated closer to the ground (2 m, Fig. 4 b) the different meteorological conditions yield an evident shift of the 'ground dip' to lower frequencies. For a distance of 1000 m (h_s: 12.5 m and 5 m; h_r: 5 m, Fig. 5) no 'ground dip' occurs in the measured frequency range.

November-measurement

Fig. 6 a-d show SPL's for different geometries and two meteorological conditions. For $h_s = h_r$ = 5 m and 100 m distance (SPL see fig. 6 a) a time difference Δt = 1.7 ms was measured at 13.40, increasing to Δt = 2 ms two hours later (wind speed about 2 m/s in both cases, but negative temperature gradient in the first and positive temperature gradient in the second case). The time difference Δt_g due to geometry is 1.5 ms, $\Delta t'$ increases from 0.2 ms to 0.5 ms, the sound speed gradient in the late afternoon is more than twice as large as in the early afternoon.

The meteorological effects are strongest for low source heights and for large distances. The 'ground dip' is shifted towards lower frequencies with increasing sound speed gradient. If source and receiver are closer to the ground than in Fig. 6 a ($h_s = h_r$ = 1.5 m, D = 100 m, Fig 6 b) an evident 'ground dip' around 400 Hz occurs which is reduced for the stable measurement. Fig. 6 c shows a measurement at 825 m distance (h_s = 1.5 m, h_r = 5 m). The broken line is the calculated SPL using a single-parameter impedance model (see /5/) and a flow resistivity typical for grass covered ground (no sound speed gradient assumed). The positive sound speed gradient reduces the ground dip. For the stable case

(strongest sound speed gradient) the SPL is increased some 20 dB around 500 Hz. Fig. 6 d shows the SPL for a source height of 5 m. The measured SPL is larger than that for a source height of 1.5 m.

A ray tracing simulation for the 825 m measurement under stable conditions (Fig. 6 d) is shown in Fig. 7. Multiple reflections at the ground and focussing effects (see /6/) should result in larger sound pressure levels. Indeed, the sound pressure level is increased about 10 dB for the stronger sound speed gradient. The measured time signals corresponding to the spectra in Fig. 6 d also show the expected differences (see Fig. 8). While for the 'unstable' measurement direct and ground reflected sound arrive almost at the same time, a lot of ground reflected pulses with enhanced pressure levels are observed for the 'stable' measurement yielding a signal of more than 10 ms length. Calculations with ray tracing methods /7/ for the stable meteorological condition predict a travel time difference between the direct ray (which arrives first) and the latest multiply reflected ray of 13 ms, in good agreement with the measurement.

In Fig. 9 the sound speed gradient is plotted as a function of elevation above ground. Curve (a) represents the gradient calculated from the acoustical measurement, curve (b) is a best fit to the measured wind speed and temperature values. Good agreement is achieved close to the ground where the sound speed profile has a 'logarithmic' shape. With increasing height the curves differ due to the influence of the stability (z/L is not small compared to 1 in eq. (2)).

V. CONCLUDING REMARKS

Sound speed gradients determined from acoustical measurements represent integrated values during the actual travel time and along the actual sound path. Meteorological data in order to determine sound speed gradients, on the other hand, are measured locally and require several sensors (wind speed and temperature) of high accuracy close to the propagation area.

Downwind sound propagation (comparable wind speeds) is extremely sensitive to the stability of the atmospheric surface layer. Positive temperature gradients (stable conditions) yield a positive sound speed gradient even at large elevations, where negative temperature gradients (unstable conditions) yield a negligible sound speed gradient. Close to the ground the sound speed profile has a 'logarithmic' shape and the sound speed gradient can be described by one parameter a, which can be calculated from the measured travel time difference between direct and ground reflected sound.

The bending of sound rays towards the ground is strongest under stable conditions. The 'ground dip' is diminished and shifted to lower frequencies yielding negligible excess attenuation in the frequency range relevant for noise propagation. Focussing effects and multiple reflections lead to enhanced sound pressure levels.

/References/

/1/ *Monin, A.S.; Yaglom, A.M.:* Statistical Fluid mechanics:Mechanics of turbulence, Vol. 1, MIT Press, Cambridge, 1979.

/2/ *Nieustadt, F.:* The computation of the friction velocity u_* and the temperature scale T_* from Temperature and wind velocity profiles by least square methods, 235-246, Boundary-Layer-Meteorology 14, 1978.

/3/ *Klug, H.:* Schallimpulse als Meßsonde zur Bestimmung meteorologischer Einflüsse auf die Schallausbreitung, Dr.-Thesis, University of Oldenburg, 1990.

/4/ *Radek, U.; Klug, H., Mellert, V.:* Impulsive sound source of high intensity for outdoor sound propagation measurements, Proc. 13 th ICA, Vol. 2, 23 -26, Belgrad 1989.

/5/ *Attenborough, K.:* Acoustic impedance models for outdoor sound propagation. J. Sound and Vibration 99 (4), 521 -544, 1985.

/6/ *Mellert, V.; Klug, H.; Radek, U.:* Acoustic probing of meteorological and acoustical parameters in outdoor sound propagation, Proc. 13 th ICA, Vol. 2, 27 - 30, Belgrad 1989.

/7/ *Thompson, R. J.:* Ray theory for an inhomogeneous moving medium, JASA 51, 1675 - 1682, 1972.

Fig. 1: Measured wind speed and temperature profiles in the atmospheric surface layer (+). The solid line fits the measured values using the Monin-Obukhov similarity functions.

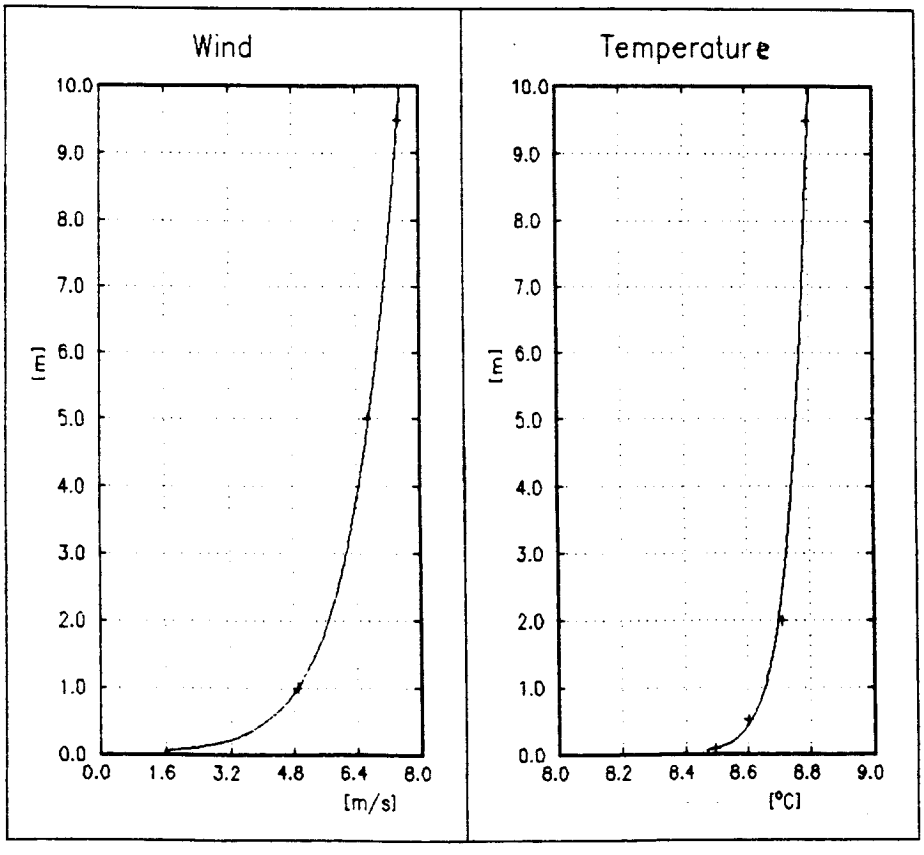

Fig. 1 a) nearly neutral (logarithmic wind profile)

24 November 1988
Time: 16.00

u_*: *0.46 m/s*

T_*: *+ 0.025 K*

L: *+422 m*

z_0: *0.01 m*

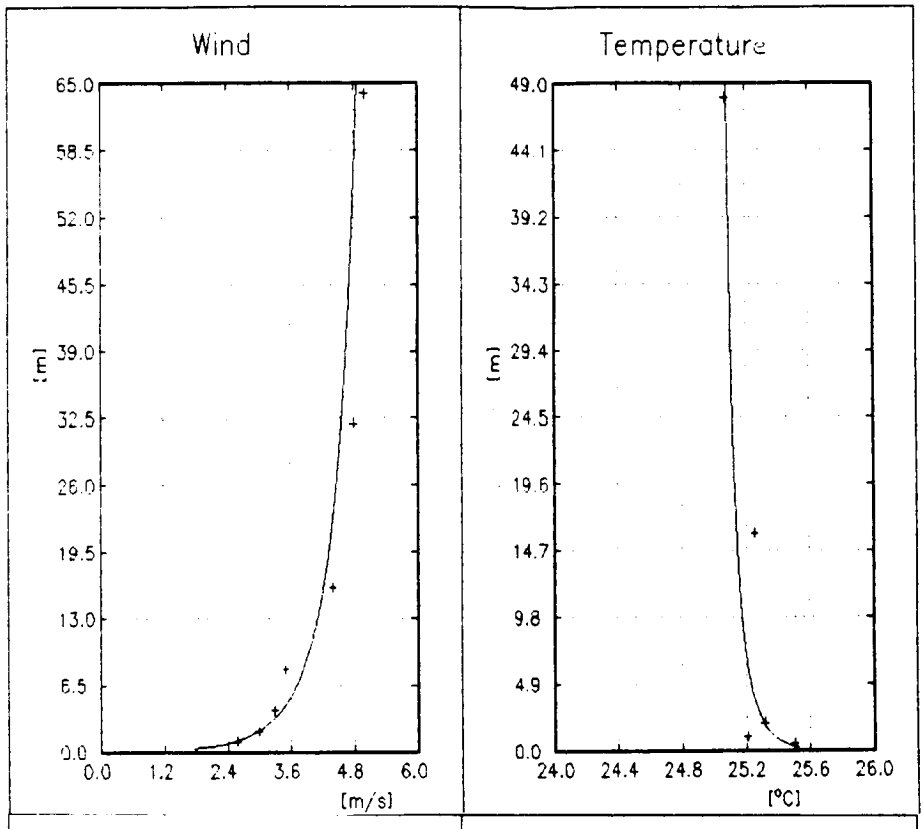

Fig. 1 b) unstable

8 August 1988
Time: 16.00

u_*: *0.28 m/s*

T_*: *- 0.043 K*

L: *- 134 m*

z_0: *0.02 m*

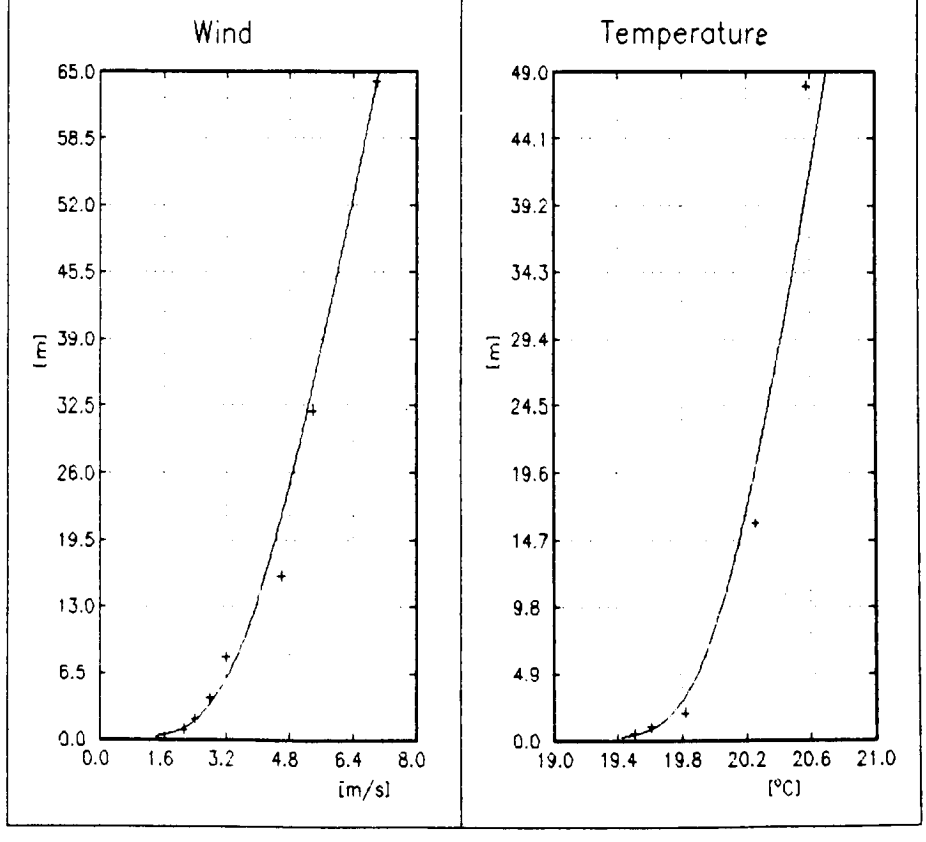

Fig. 1 c) stable

8 August 1988
Time: 21.00

u_*: *0.22 m/s*

T_*: *+ 0.057 K*

L: *+ 63 m*

z_0: *0.03 m*

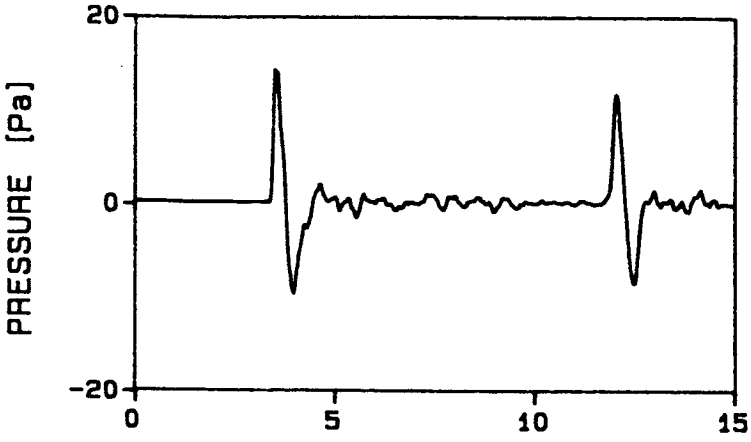

Fig. 2 : Measured time signal
h_s = 30 m; h_r = 2 m
horizontal distance: 34 m.

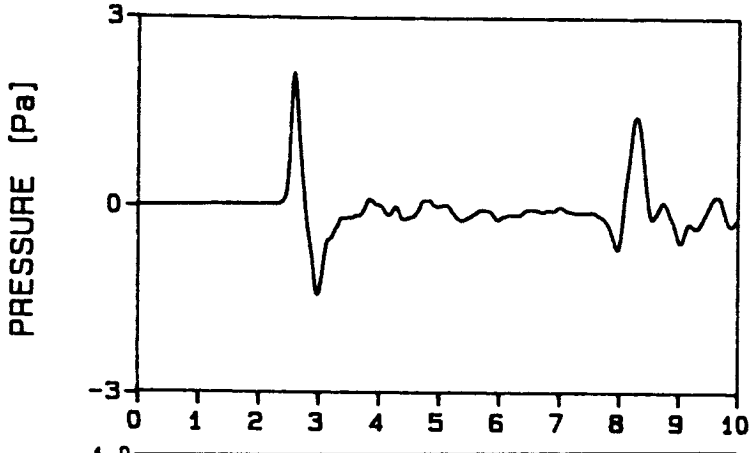

Fig. 3 a: Measured time signal
h_s = h_r = 12.5 m; distance: 250 m
(stable conditions)

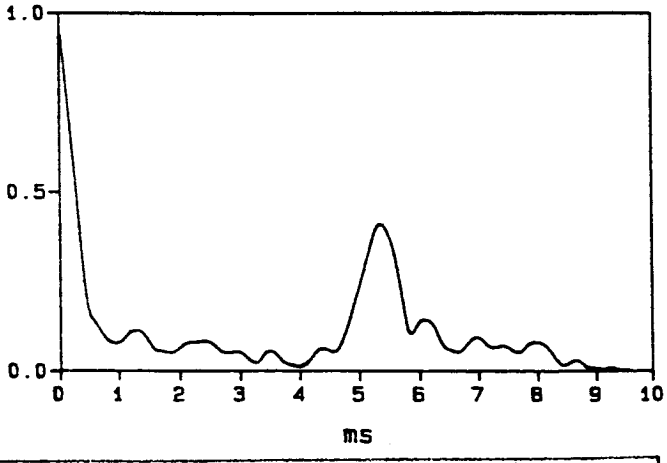

Fig. 3 b: Autocorrelation function of the signal in a .
The maximum at 5.3 ms shows the time difference between direct and ground reflected pulse

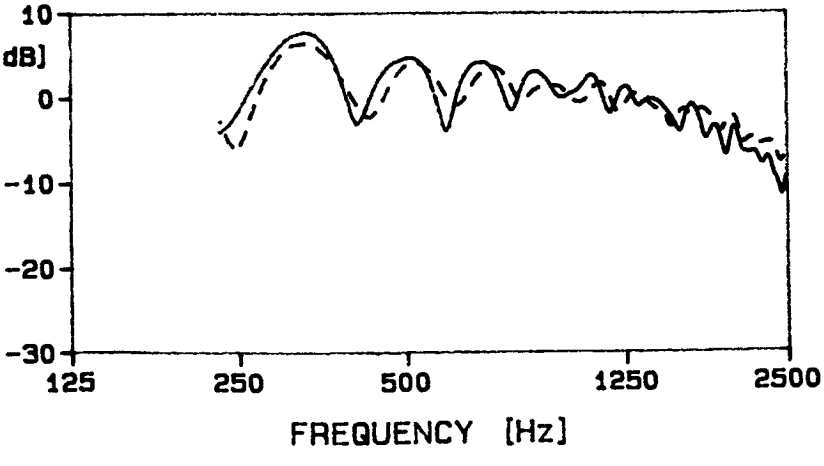

Fig.4 a: SPL re free field
(12.5 m, 12.5 m, 250 m)
——— ***stable conditions***
– – – – ***unstable conditions***

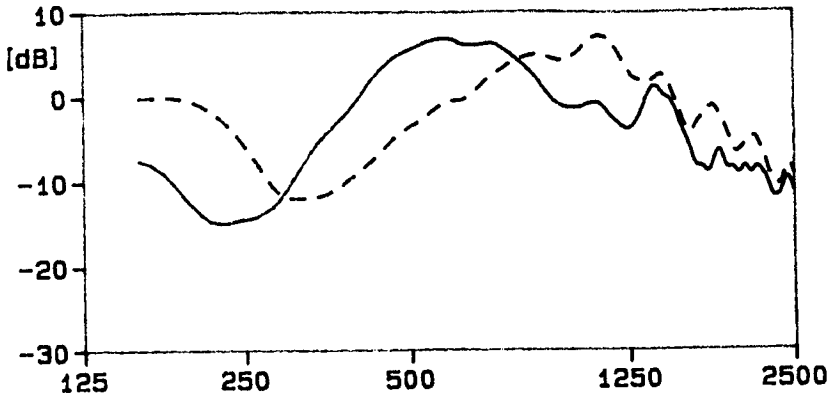

Fig. 4 b: SPL re free field (2 m, 2 m, 250 m)
——— *stable conditions*
- - - - *unstable conditions*

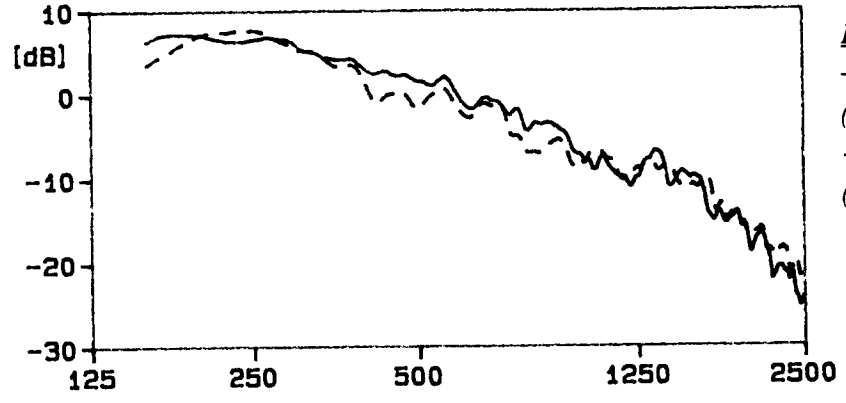

Fig. 5: SPL re free field;
——— *stable conditions (12.5 m, 5 m, 1000 m)*
----- *stable conditions (5 m, 5 m, 1000 m)*

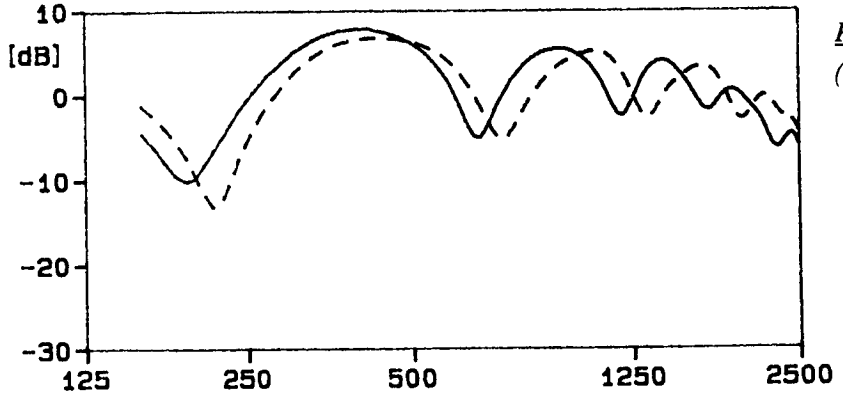

Fig.6 a: SPL re free field; (5 m, 5 m, 100 m)
——— *stable conditions*
- - - - *unstable conditions*

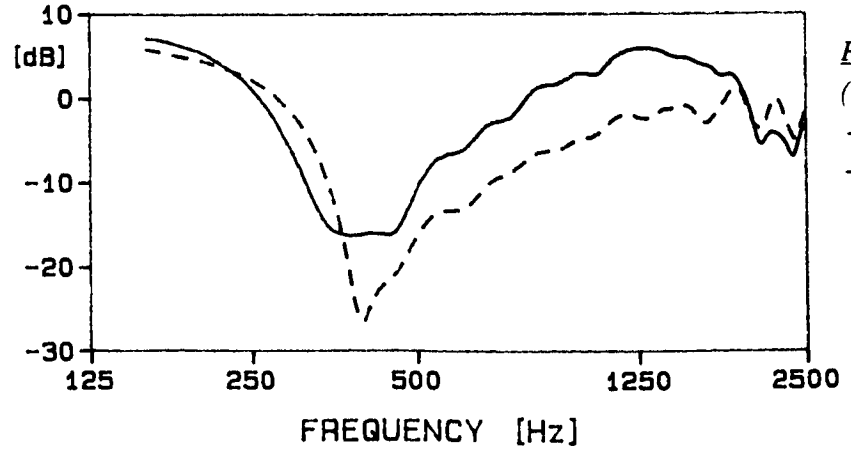

Fig.6 b: SPL re free field (1.5 m, 1.5 m, 100 m)
——— *stable conditions*
- - - - *unstable conditions*

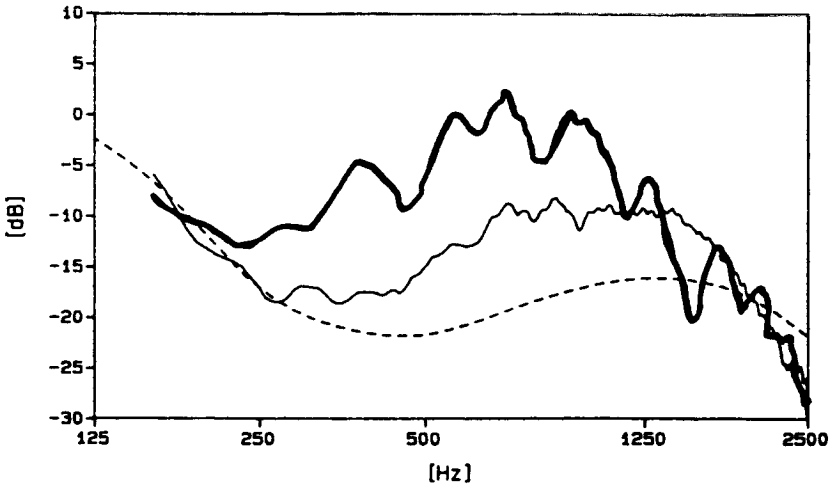

Fig.6 c: SPL re free field (1.5 m, 5 m, 825 m)
----- *calculatet* (σ = 225 000 $kgs^{-1}m^{-3}$)
stable conditions
unstable conditions

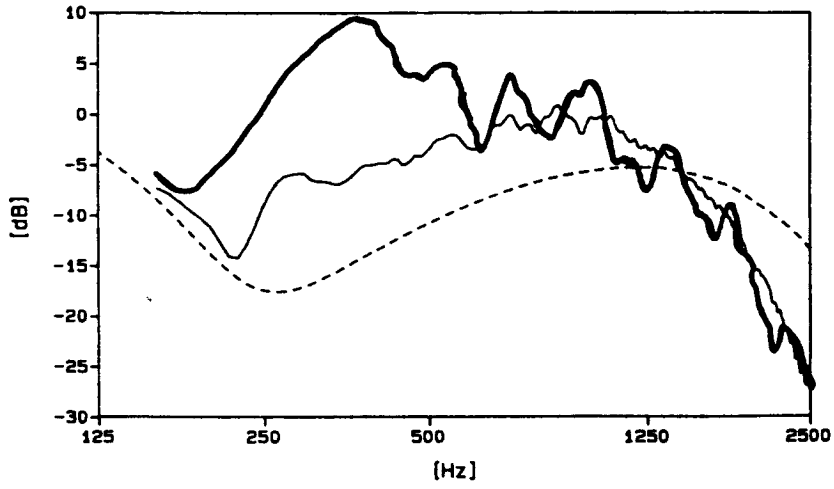

Fig.6 d: SPL re free field (5 m, 5 m, 825 m)
----- *calculatet* (σ = 225 000 $kgs^{-1}m^{-3}$)
stable conditions
unstable conditions

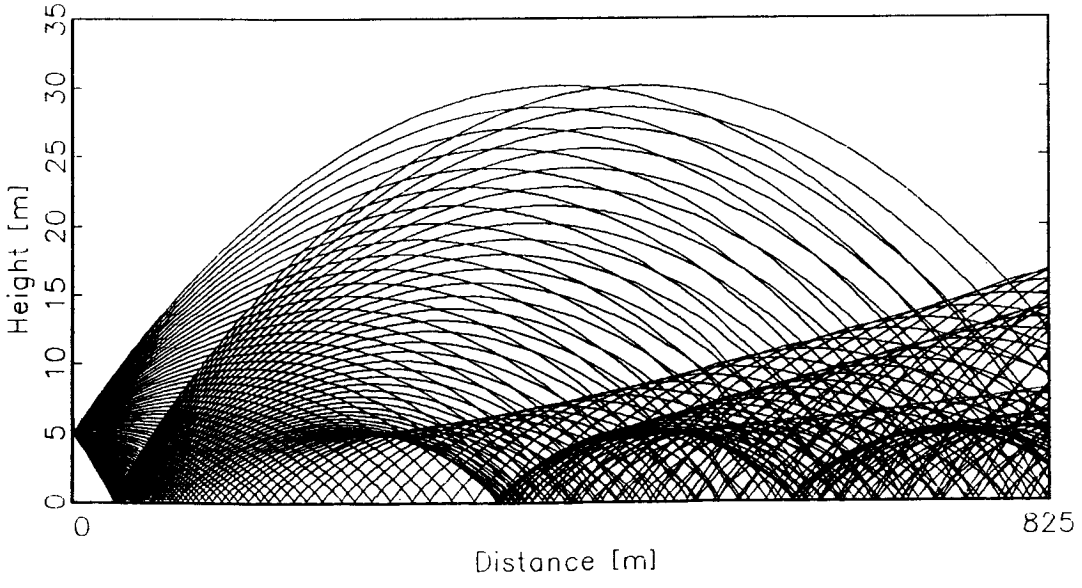

Fig. 7: ray pattern plot according to measurement 6 d (stable conditions; $u_* = 0.16$, $T_* = 0.07$, $L = 28$ m, determined from measured meteorological data)

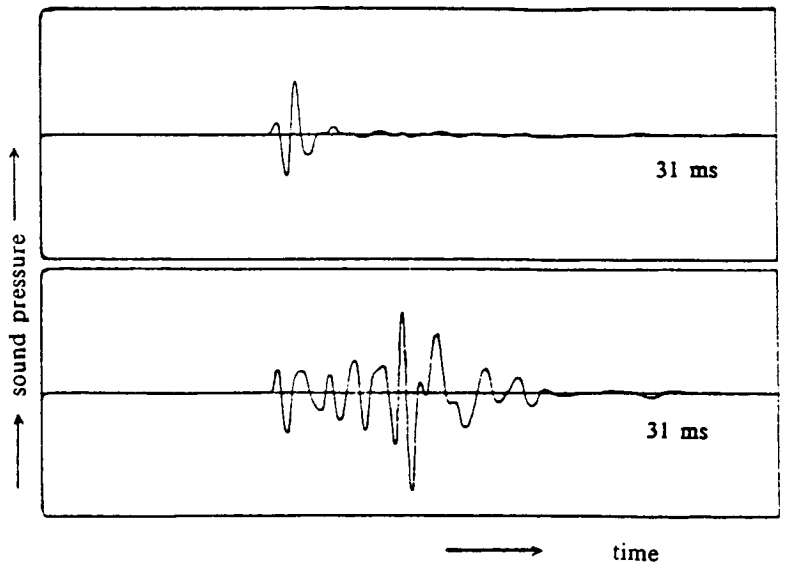

Fig. 8: Measured time signals
above: unstable conditions
below: stable conditions

Fig. 9: Sound speed gradient [1/s]
as a function of elevation above ground
a) measured acoustically (Fig. 3)
b) determined by meteorological measurements
(Fig. 1 c)

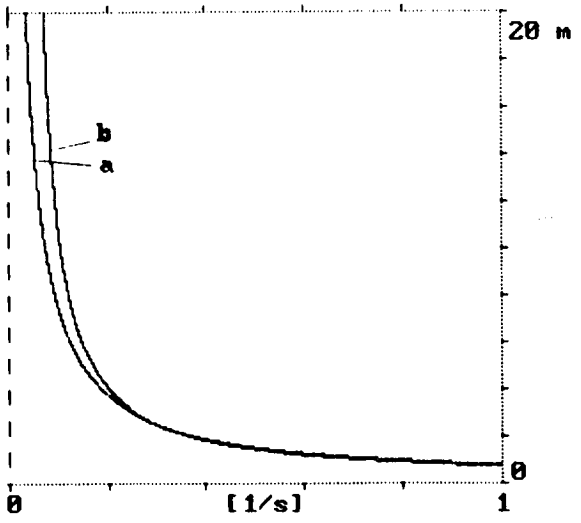

Effect of Wind and Temperature Gradients on Received Acoustic Energy *

Richard K. Brienzo
Lincoln Laboratory, Massachusetts Institute of Technology
Lexington, Massachusetts 02173

Abstract

The effect of refraction due to wind and temperature gradients on energy received from low flying aircraft is examined. A series of helicopter and jet flyby's were recorded with a microphone array on two separate days, each with distinctly different meteorological conditions. Energy in the 100-200 Hertz band is shown as a function of aircraft range from the array, and compared with the output of the Fast Field Program.

I. Introduction

This paper examines the effect of wind and temperature gradients on energy received at a microphone array from a series of aircraft flyby's. Of interest is the energy contained between 100 and 200 Hertz, the frequency band used in our acoustic detection and tracking algorithms.

One aspect of this work is to estimate our ability to detect and track low flying aircraft, or conversely, to assess the vulnerability of aircraft to acoustic detection and tracking. Propagation characteristics, which are largely influenced by wind and temperature gradients, must be taken into account if we are to make accurate predictions.

To illustrate the impact that wind and temperature gradients can have, received energy as a function of aircraft range has been calculated from aircraft flyby's on two separate days, each with distinctly different meteorological conditions. Sound speed profiles, derived from wind and temperature data collected during the experiments, are used to generate ray plots. Visualization of the ray paths helps to explain features seen in the experimental data.

To predict detection range or tracking ability for a given set of meteorological parameters, we must estimate acoustic energy as a function of distance from the source. To this end, the output of a propagation model, the Fast Field Program, is compared to the experimental results.

* This work was sponsored by the Department of the Air Force.

II. Experiment

Aircraft flyby's, depicted in Figure 1, were recorded on two different days (designated as Day 1 and Day 2). Results presented here are from a helicopter on Day 1, and a jet aircraft on Day 2. Both aircraft flew in a straight line at a constant altitude past a nine element microphone array. Ground truth TSPI (Time SPace Information) of the aircraft's position and velocity, corrected for acoustic propagation time, was also recorded during each flyby. Details are given in Table 1.

Array data were sampled at 2048 samples/second during the experiment and recorded directly to magnetic tape. The array consisted of nine GenRad 1962-P42 microphones with standard Sennheiser windscreens. Microphones were placed in notched wooden blocks on the ground in a tri-delta configuration (reference 1). The array was used with a wideband direction finding program (reference 2) to aid in determining whether received energy was signal from the aircraft, or noise. This is discussed further in Section IV.

Meteorological data (temperature, wind speed and direction, and relative humidity) were recorded to a height of 300 meters before and after the experiment using a tethered balloon. These parameters were also recorded on the ground throughout both experiments. Meteorological data were stored every 10 seconds during the experiment. The wind was from the South (190 degrees) on Day 1, and from the North (15 degrees) on Day 2. Headings of 345 and 165 degrees put the aircraft approximately into the wind, or with the wind.

The helicopter was louder when it was inbound to the array, so only incoming portions of the helicopter data are analyzed. There were two runs incoming from the North (345 degrees), and two runs incoming from the South (165 degrees). The closest point of approach (CPA) from each direction was 90 and 230 meters.

The jet was louder outbound from the array, so only outgoing portions of those runs are used. Three runs outgoing to the North (345 degrees), and three runs outgoing to the South (165 degrees) are analyzed. The CPA for these runs varied from 140 meters to 716 meters.

III. Data

Array data

The array time series for one of the helicopter runs at its CPA is shown in Figure 2a. This same time series is displayed in Figure 2b after bandpass filtering between 100 and 200 Hertz. The spectra from two of the channels are shown in Figure 3. These spectra show the strong harmonic structure that is typical for helicopters.

Array time series for the jet are shown in Figures 4a and 4b. The jet spectrum from two of the channels are shown in Figure 5. These figures illustrate the broadband spectra that is typical of jets.

The drop in power level in both Figures 3 and 5 at about 750 Hertz is due to the antialiasing filter. A rise in energy below 50 Hertz in the spectra of Figure 5 is due to wind noise.

Environmental data

Meteorological data collected from a tethersonde was used to calculate sound speed as a function of height. Data taken during one of the balloon raisings on Day 1 is shown in Figure 6. There was a normal temperature lapse above 50 meters, with the wind out of the South. Sound speed profiles for Day 1 at 345 degrees (looking North of the array) and 165 degrees (looking South of the array) are shown in Figure 7.

On Day 2, the wind was from the North (Figure 8). The wind speed initially increased up to 70 meters, then decreased with height, up to 300 meters. This unusual wind profile, along with a temperature inversion, led to the sound speed profile in figure 9.

IV. Analysis

Energy as a function of range

Received energy is calculated for each one-second segment (2048 points) of the array time series. This corresponds to a spatial average of about 30 meters for the helicopter, and 240 meters for the jet. The power spectrum for each channel is first calculated using a Hanning window and 2048 point fft's. After integrating the power spectra between 100 and 200 Hertz, the values for all channels are averaged. The level calculated for that one-second segment is then matched to the corresponding TSPI range, yielding energy received at the array when the aircraft was at that particular range.

Separating signal from noise

It is not always clear if acoustic energy received at a microphone is signal from an aircraft, or wind noise. Whether it is signal or noise will depend upon the propagation conditions (for example, the presence of a shadow zone), the level of wind noise, and the distance from the aircraft to the microphone. Discriminating between signal and noise is important when comparing the output of a propagation model to experimental data; we do not want to ascribe propagation effects to our experimental data when no signal is there to model. To ensure that we were only looking at signal from the aircraft, the array time series was used with a wideband direction finding algorithm (reference 2) to classify the received energy as signal or noise.

The direction finding algorithm outputs the energy arriving along a specified number of directions. The direction from which the maximum energy arrives is the detected azimuth of the source. Energy and azimuth pairs for other directions are output in order of

decreasing received energy. For energy to be selected as signal from the aircraft, we require the detected azimuth to be close to the azimuth reported by the TSPI (ground truth) data. In addition, we require that energy coming from the direction of the detection be larger than energy coming from other directions, otherwise we are probably measuring ambient noise. All energy versus range data reported in the next section have been screened using the above criteria.

Received energy data

To help in understanding features in the received acoustic energy data, raytraces were calculated (reference 3) using the sound speed profiles from Figures 7 and 9, and are shown along with the energy versus range plots. The ray plot for the case when the helicopter was incoming from the North on Day 1 (calculated from the sound speed profile in Figure 7a) is shown in Figure 10a.

If the aircraft is considered to be at zero range and an altitude of 40 meters on the ray plot, then the number of rays intersecting the ground at any range gives an indication of the acoustic energy that would be received at that distance from the aircraft. Since the sound speed decreases with height (Figure 7a), rays leaving the aircraft bend upward, and a shadow zone is formed at about one kilometer from the source.

The received acoustic energy as a function of range for runs in which the helicopter was incoming from the North is given in Figure 10b. Each data point represents the energy averaged over one second in the 100 - 200 Hz. band. To provide a reference, a solid curve representing spherical spreading is shown along with the experimental data. As suggested by the raytrace, there is a larger decrease in received energy than predicted by spherical spreading past one kilometer, where the shadow zone begins. Note that the energy level drops significantly in the shadow zone, but does not go to zero, as ray theory predicts.

The raytrace and energy plot for runs in which the helicopter was incoming from the South are shown in Figure 11. In this case, the sound speed increased with height (Figure 7b), causing the rays to be bent downward. Energy received past about one kilometer is less than that predicted by spherical spreading since much of the energy is refracted downward at short ranges; rays are more spread out at longer ranges than would be the case for spherical spreading. Other factors, such as directivity of the source, and the ground effect, are likely to be present as well.

The raytrace (calculated from the velocity profile in Figure 9a) and energy plot for outgoing runs to the North on Day 2 (jet) are given in Figure 12. The raytrace suggests a received energy somewhat higher than indicated by spherical spreading at short ranges where the rays are refracted downward, and less received energy at longer ranges where the rays are refracted upward. Comparison of the experimental data and the spherical spreading curve shows this to be the case.

When the aircraft was South of the array, an initial decrease in sound speed up to 80 meters in height (Figure 9b) caused shallow angle downgoing rays to be bent upward,

creating a small shadow zone. Past 80 meters, there was a general increase in sound speed with increasing height, which caused the rays to be bent downward. The steep drop in received energy (Figure 13b) between one and three kilometers corresponds to the shadow zone seen in the raytrace. There is an increase in energy between four and six kilometers as rays leaving the source with an upward angle were refracted back downward.

V. Comparison with FFP

Sound speed profiles in Figures 7 and 9 were used as input to the Fast Field Program (references 4-6). As seen in Figures 14 and 15, agreement between the model output and general features in the experimental data is quite good. In particular, note that the FFP output closely models the experimental data in the shadow zones seen beyond one kilometer in Figure 14a, and between one and three kilometers in Figure 14b.

VI. Summary

Measurements of acoustic energy from a series of aircraft flyby's were presented. Features in the experimental data were explained in terms of the propagation characteristics present at the time. Sound speed profiles, from meteorological data taken during the experiment, were used as input to the Fast Field Program. The FFP was seen to provide an excellent prediction of the general features found in the experimental data. The large difference between the experimental results and simple spherical spreading emphasizes the need for accurate and detailed meteorological data.

References

1. D.P. McGinn, T.E. Landers, "AVSE Acoustic Measurement Instrumentation and Techniques", Project Report CMT-69, Lincoln Laboratory, MIT (1985).

2. S. H. Nawab, F.U. Dowla, R.T. Lacoss, "Direction Determination of Wideband Signals", IEEE ASSP-33, 1114-1122 (1985).

3. H. Weinberg, "Generic Sonar Model", NUSC Technical Document 5971D, Naval Underwater Systems Center, New London, CT (June 1985).

4. Fast Field Program (FFP), U.S. Army Construction Engineering Research Laboratory, P.O. Box 4005, Champaign, IL 61824-4005.

5. S.W. Lee, N. Bong, W.F. Richards, R. Raspet, "Impedance formulation of the fast field program for acoustic wave propagation in the atmosphere", J. Acoust. Soc. Am., 79(3), 628-634 (1986).

6. S.J. Franke, G.W. Swenson, Jr., "A Brief Tutorial on the Fast Field Program (FFP) as Applied to Sound Propagation in the Air", Applied Acoustics 27, 203-215 (1989).

Table 1.

Day	Aircraft	Heading (degrees)	Velocity (m/sec.)	Wind speed (m/sec.)	Wind direction (degrees)
1	helicopter	345/165	30	1.3	190
2	jet	345/165	240	2.9	15

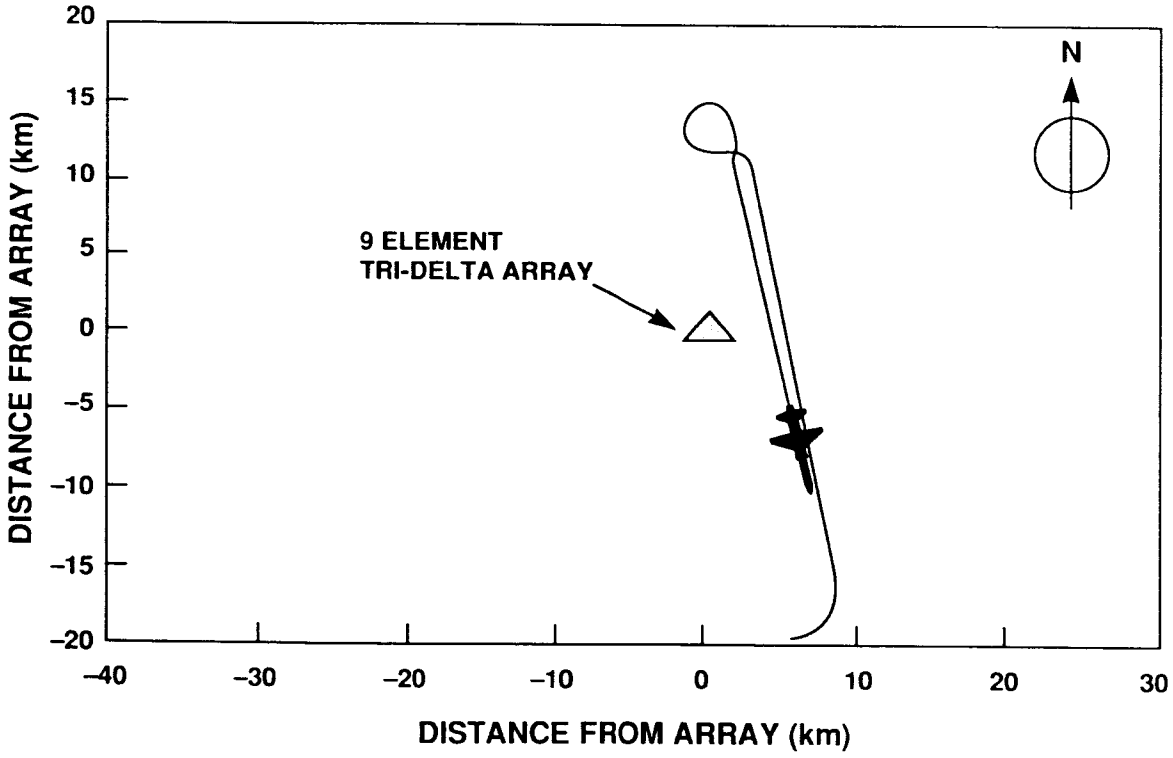

Figure 1. Aircraft flyby.

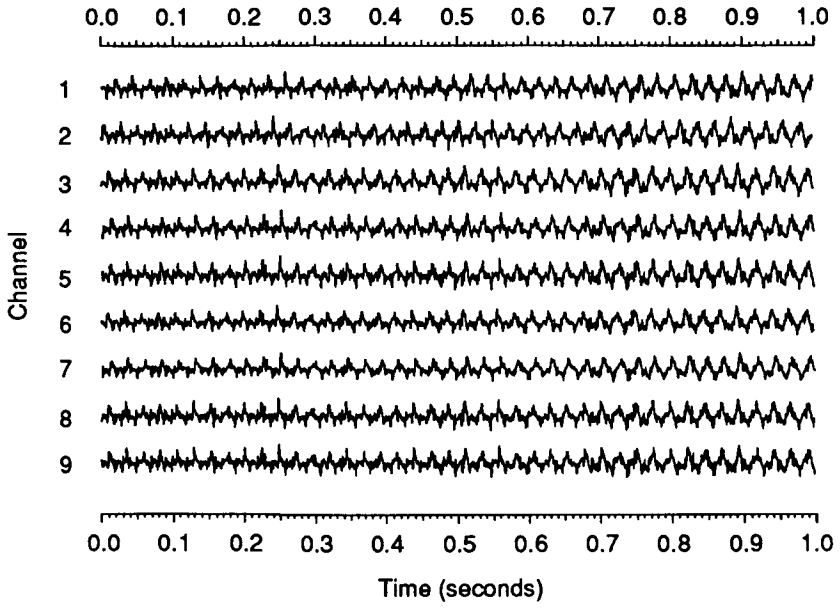

a) unfiltered time series.

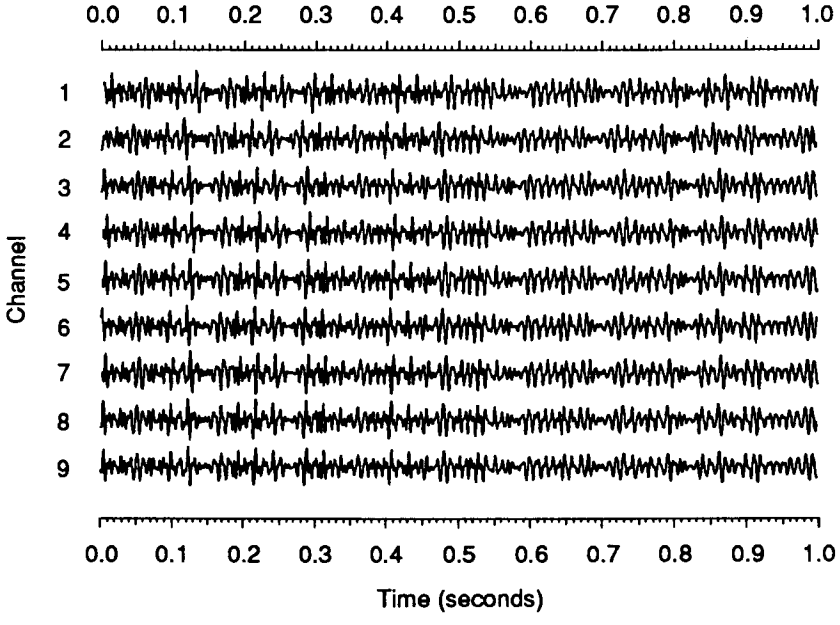

b) bandpass filtered time series [100 - 200 Hz.]

Figure 2. Helicopter time series at closest point of approach (90 meters).

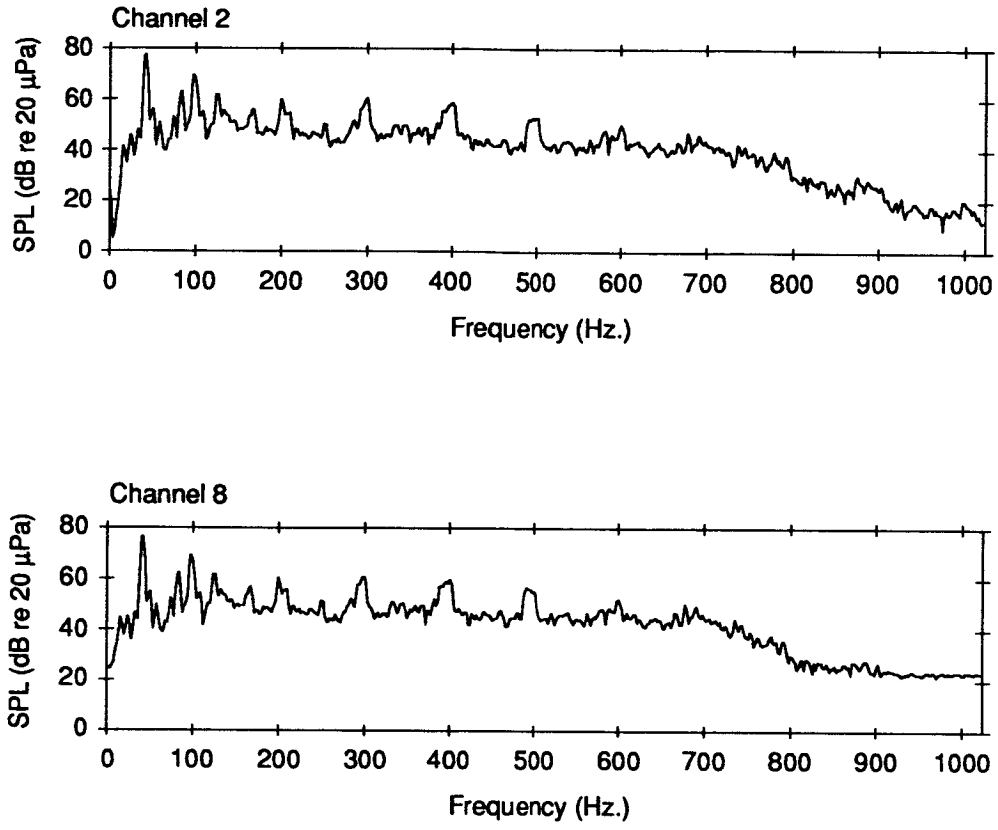

Figure 3. Helicopter spectra at closest point of approach (90 meters).

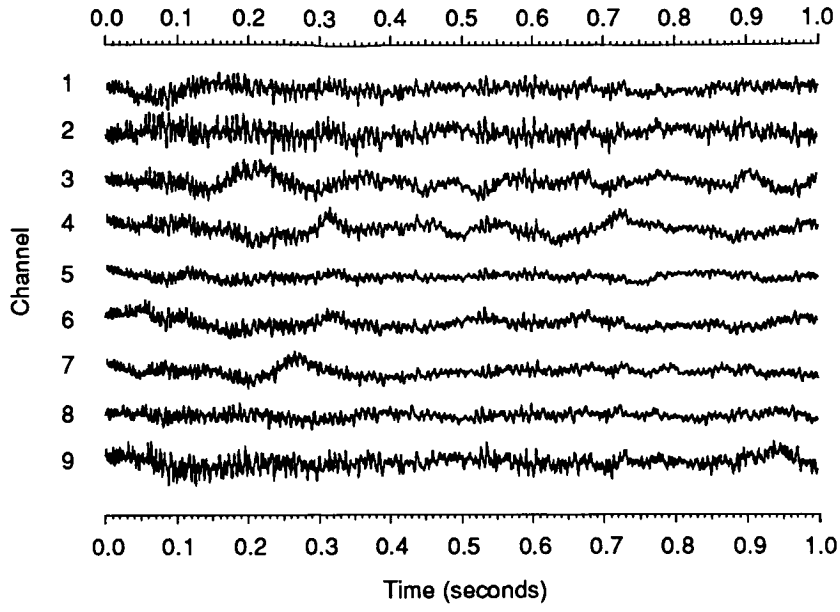

a) unfiltered time series.

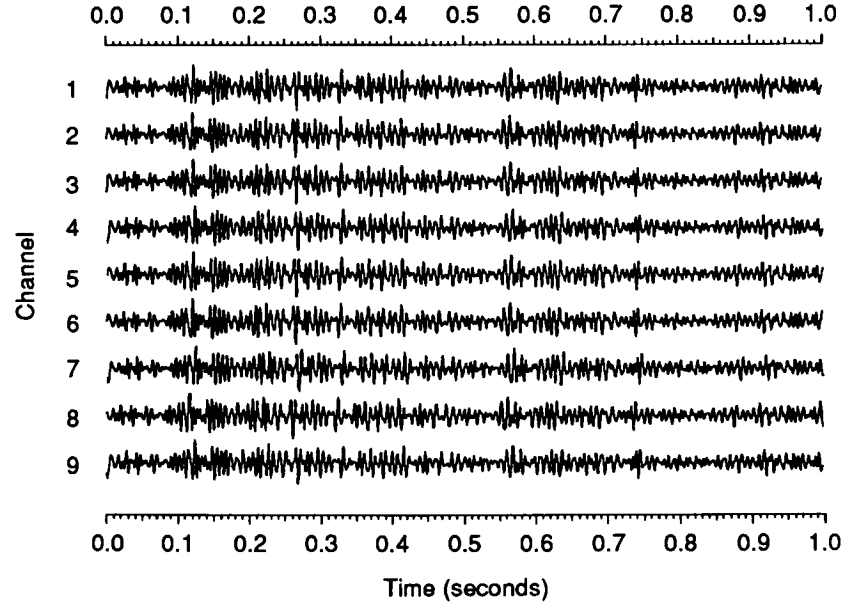

b) bandpass filtered time series [100 - 200 Hz.].

Figure 4. Jet time series at closest point of approach (716 meters).

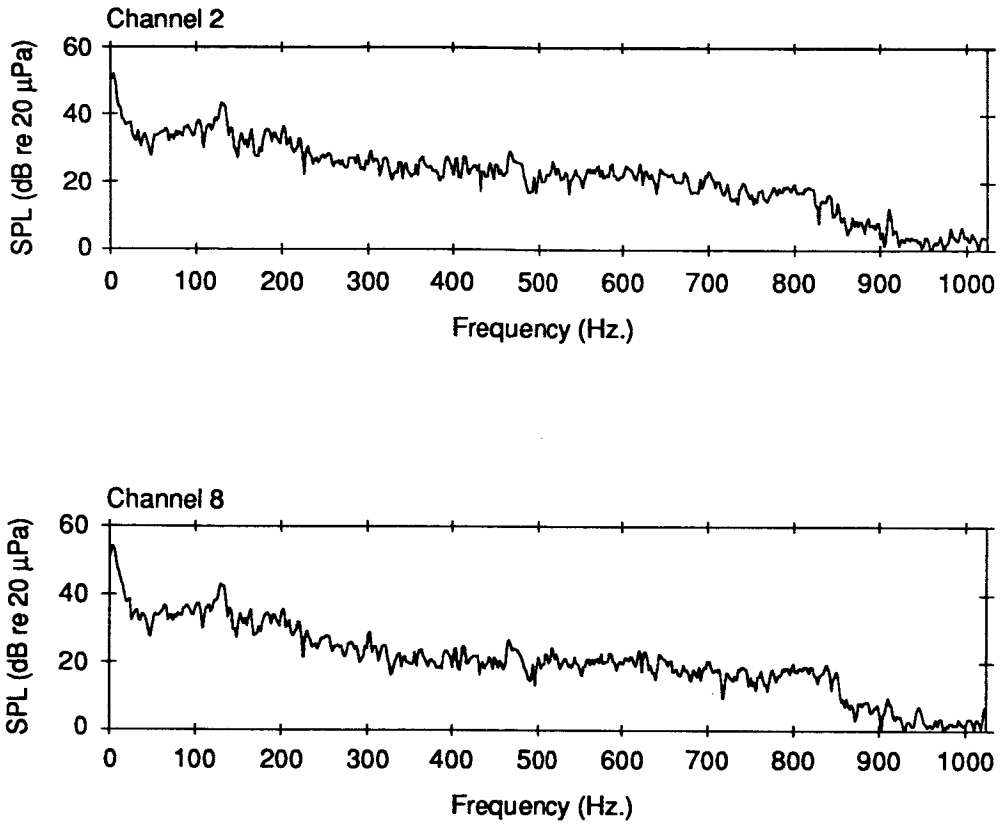

Figure 5. Jet spectra at closest point of approach (716 meters).

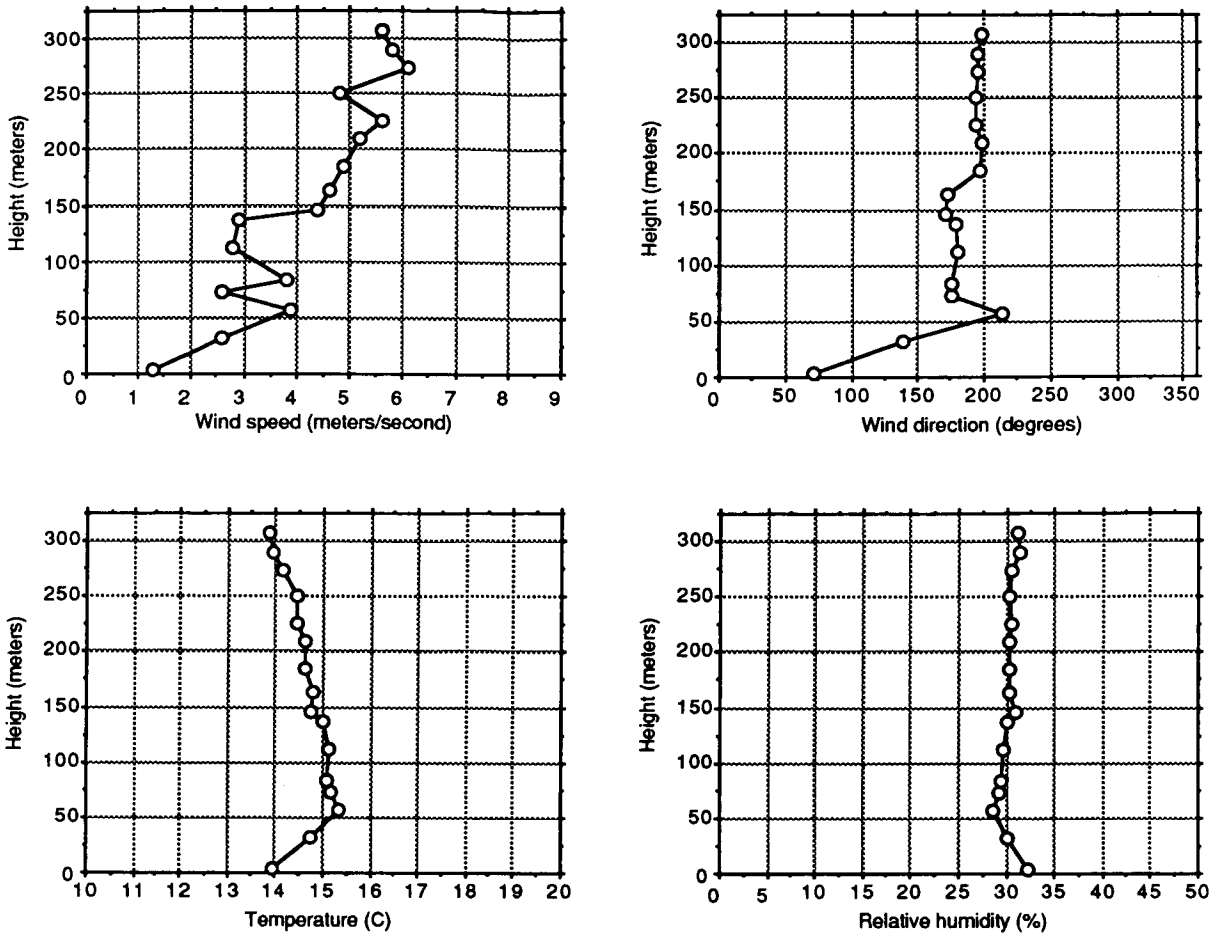

Figure 6. Day 1 meteorological data.

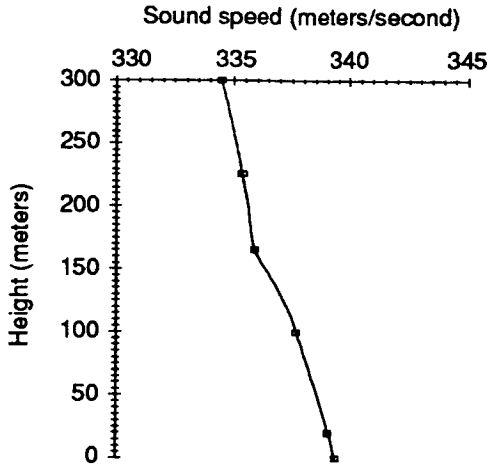

a) North of the array (345 degrees).

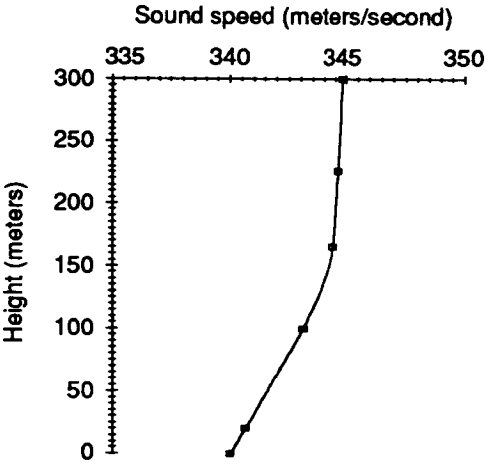

b) South of the array (165 degrees).

Figure 7. Sound speed profiles on Day 1.

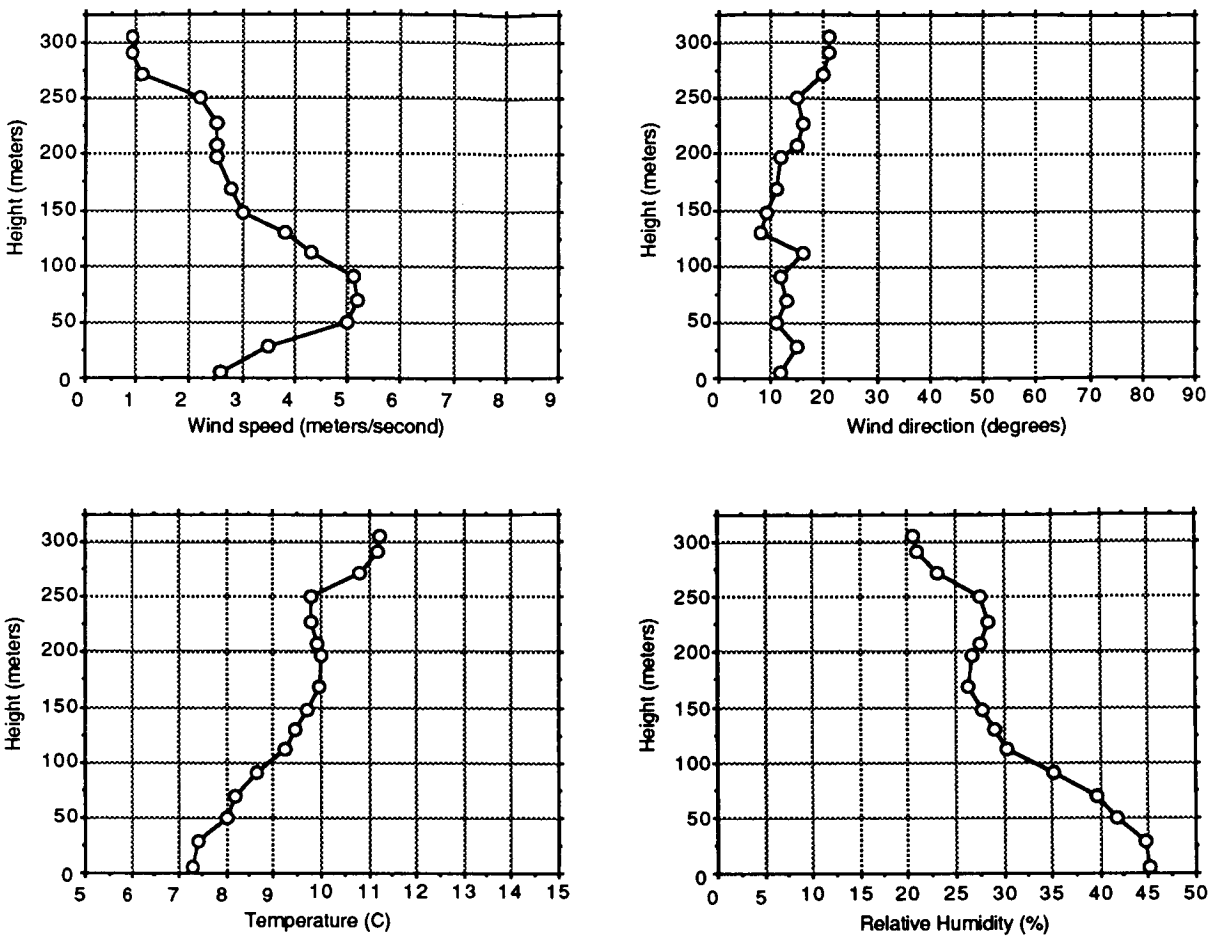

Figure 8. Day 2 meteorological data.

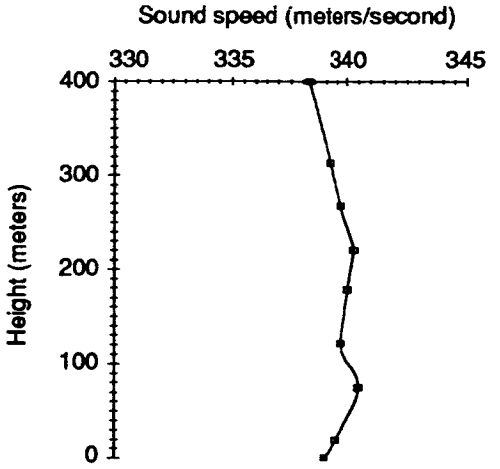

a) North of the array (345 degrees).

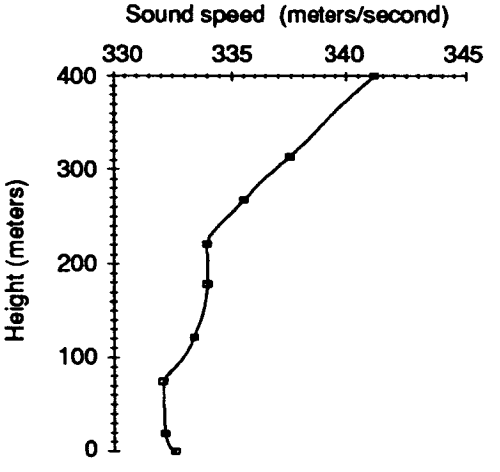

b) South of the array (165 degrees).

Figure 9. Sound speed profiles on Day 2.

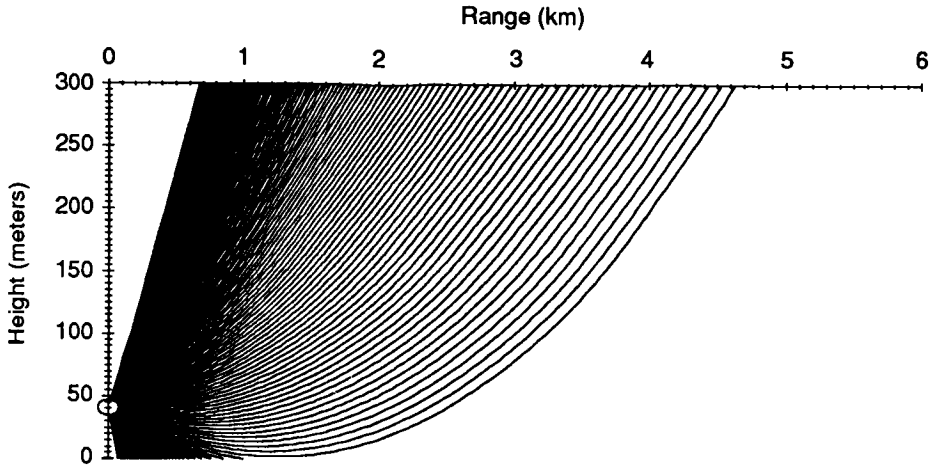

a) raytrace calculated from the velocity profile in Figure 7a.

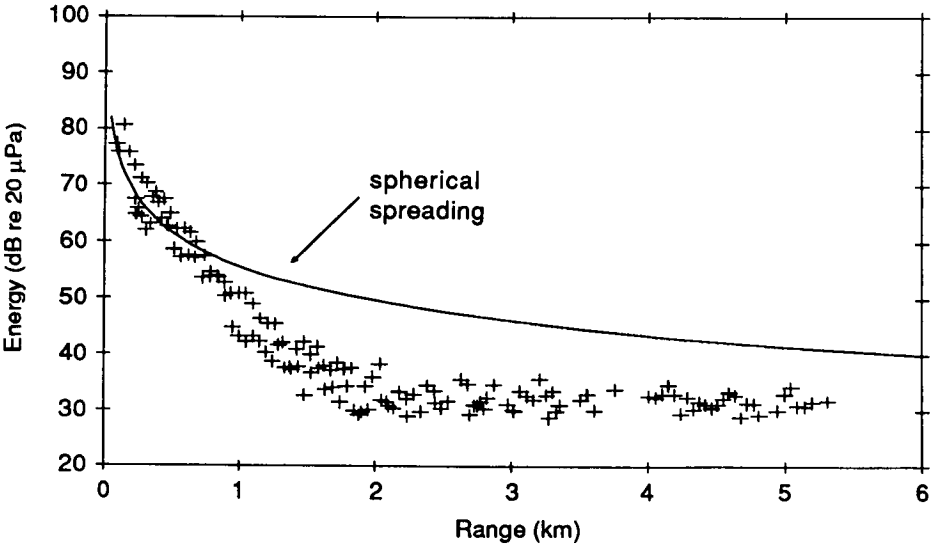

b) experimental data.

Figure 10. Helicopter incoming from the North (Day 1).

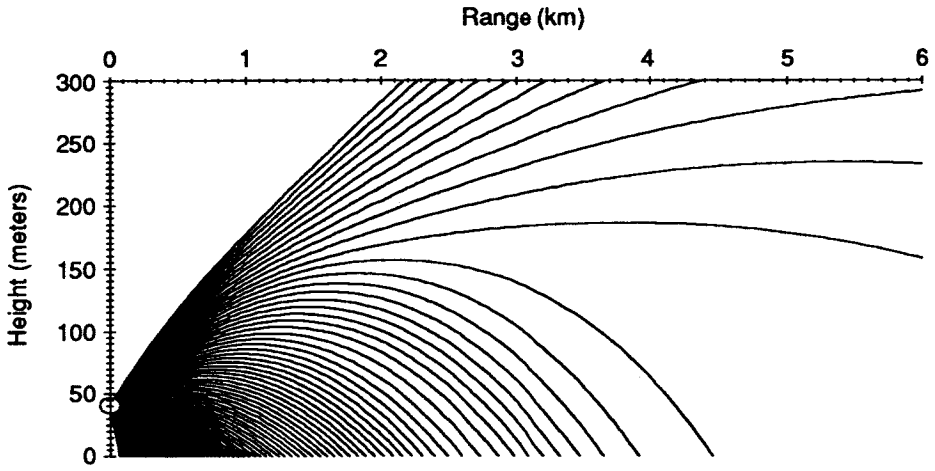

a) raytrace calculated from the velocity profile in Figure 7b.

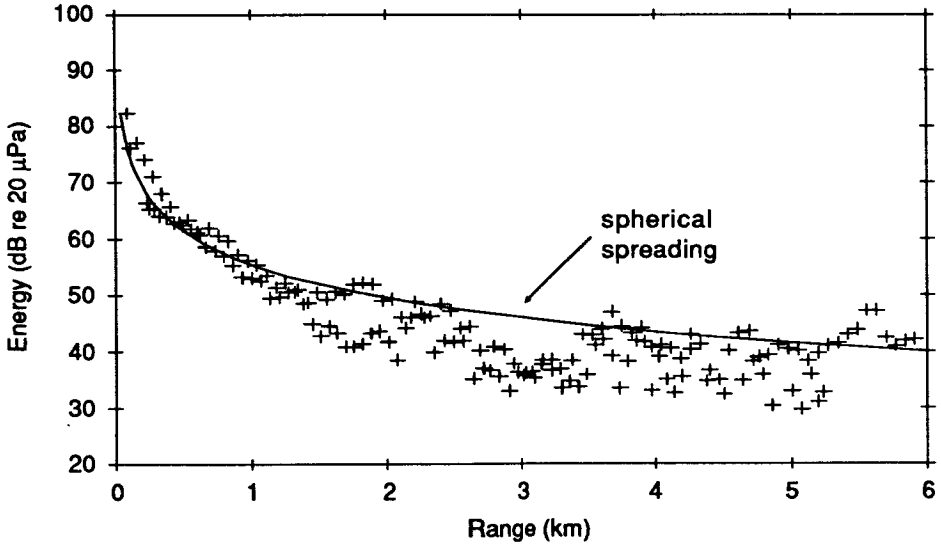

b) experimental data.

Figure 11. Helicopter incoming from the South (Day 1).

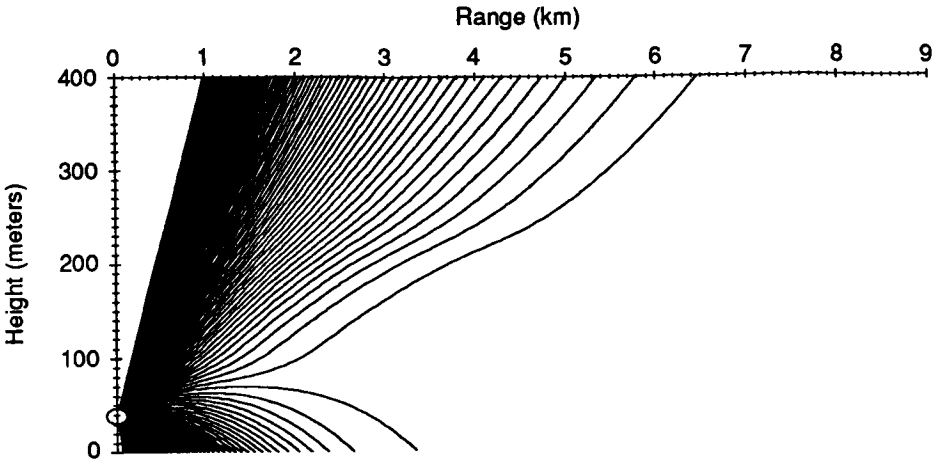

a) raytrace calculated from the velocity profile in Figure 9a.

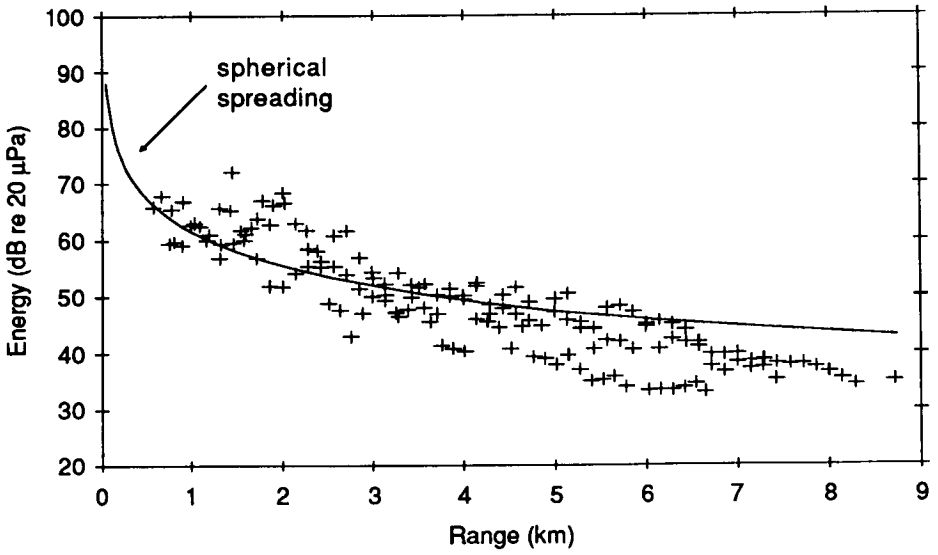

b) experimental data.

Figure 12. Jet outgoing to the North (Day 2).

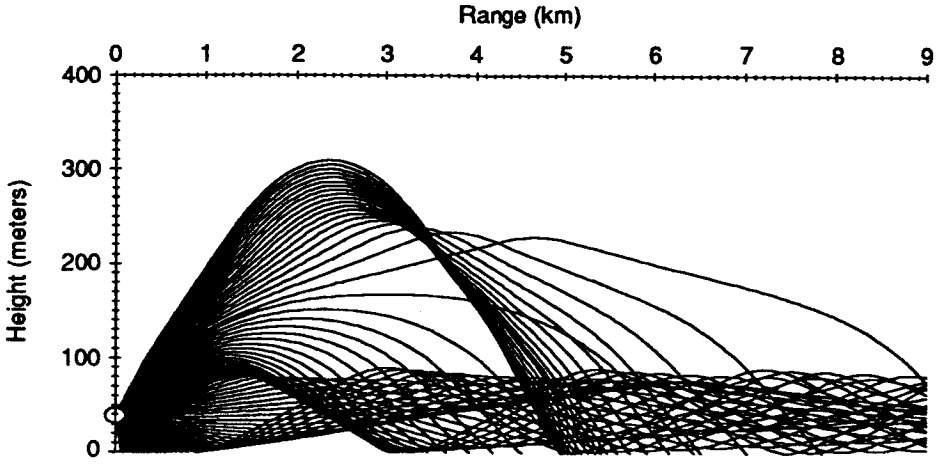

a) raytrace calculated from the velocity profile in Figure 9b.

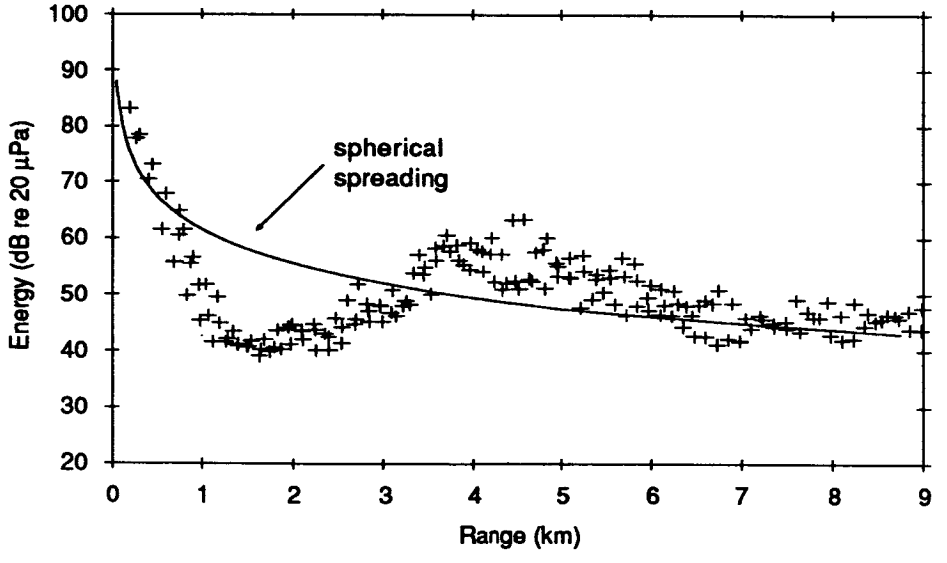

b) experimental data.

Figure 13. Jet outgoing to the South (Day 2).

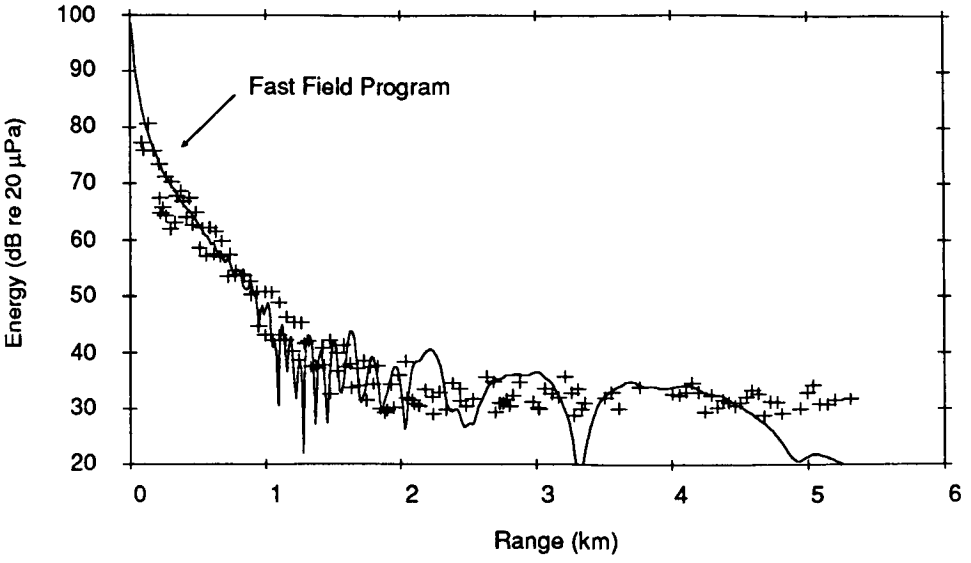

a) helicopter incoming from the North.

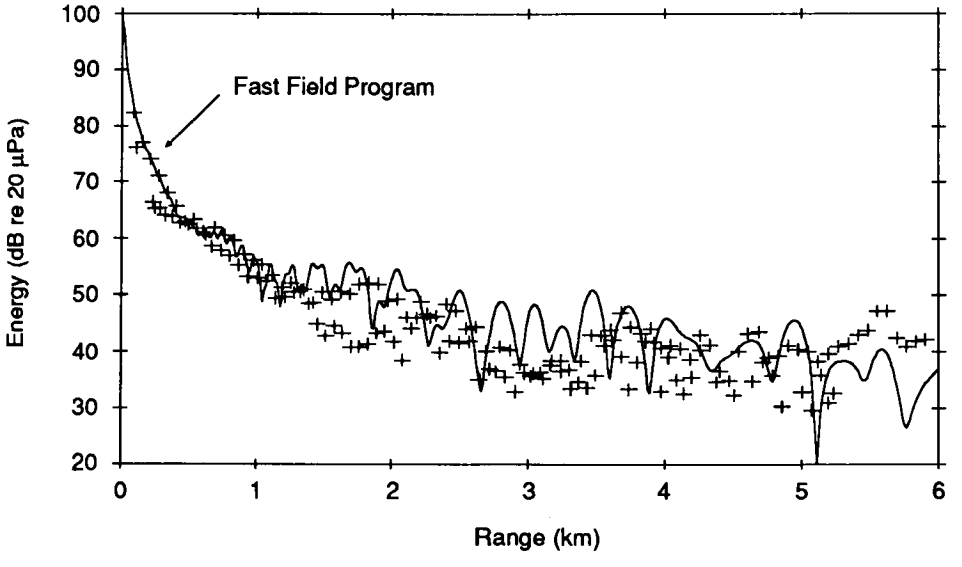

b) helicopter incoming from the South.

Figure 14. Comparison of Day 1 experimental data with the FFP.

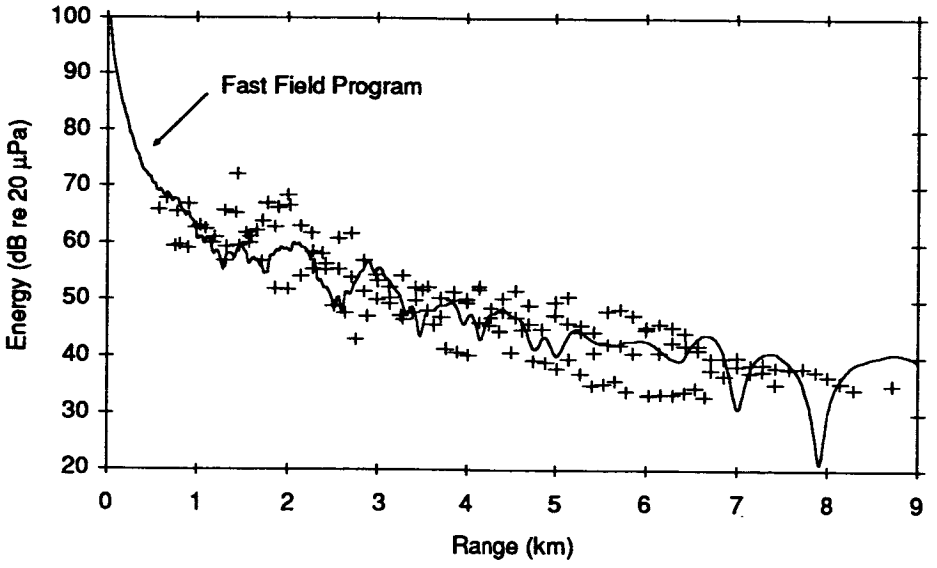

a) jet outgoing to the North.

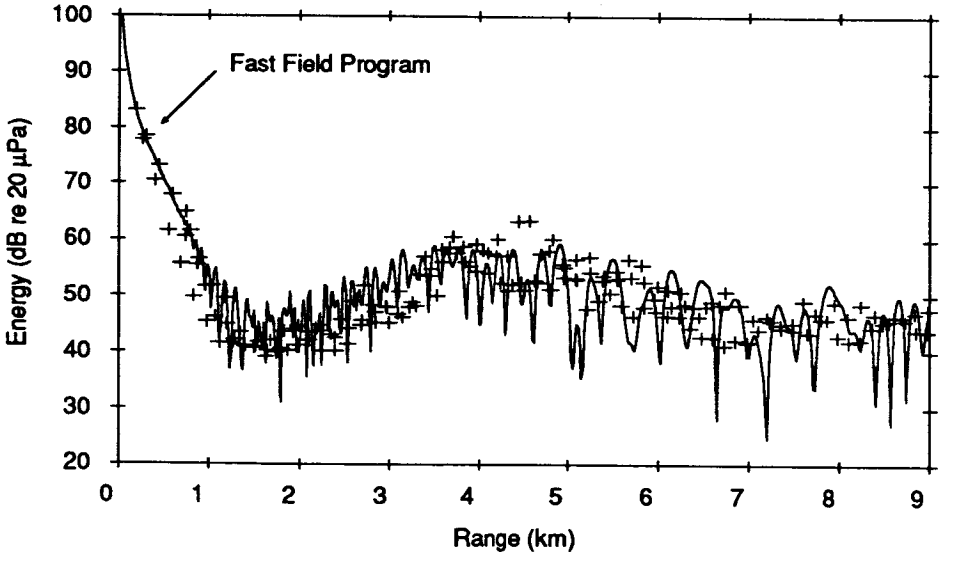

b) jet outgoing to the South.

Figure 15. Comparison of Day 2 experimental data with the FFP.

COMPARISON OF FFP PREDICTIONS WITH MEASUREMENTS OF A LOW-FREQUENCY SIGNAL PROPAGATED IN THE ATMOSPHERE

D. Keith Wilson and Dennis W. Thomson
Department of Meteorology,
The Pennsylvania State University

SUMMARY

An experimental study of low-frequency propagation over a distance of 770 m was previously reported [J. Acoust. Soc. Am. Suppl. 1 **86**, S120 (1989)]. For that study, sound speed profiles were reconstructed entirely from surface-layer micrometeorological data. When the acoustic data were compared with theoretical predictions from a fast field program (FFP), it was found that the FFP underpredicted sound levels measured in a shadow zone. In this paper, the effect on the predictions of including meteorological data for heights greater than the surface layer, i.e., wind profiles measured by a Doppler sodar, is discussed. Vertical structure of turbulence is simulated by stochastically perturbing the mean profiles, and the agreement between the acoustic data and FFP predictions is improved.

INTRODUCTION

Previous studies of fluctuations in acoustic signals propagated in the atmosphere have typically been concerned with time scales of a few seconds or less. The purpose of such experiments was primarily to study scattering by turbulence with sizes on the order of the acoustic wavelength.

The experiment described in this paper was designed to study temporal variability on a much longer time scale. The level of a low-frequency signal was monitored for several periods lasting between two and six days, with the sound level being recorded at one minute intervals. The atmospheric phenomena affecting acoustic signals on these time scales are large-scale turbulence (e.g., thermals), diurnal evolution of the atmospheric boundary layer, and synoptic-scale weather systems.

Along with monitoring of the acoustic signal, a wide variety of micrometeorological data were logged. One use of these micrometeorological data was the reconstruction of half-hour mean sound speed profiles. The sound speed profiles were used in a propagation model, the fast field program (FFP).

In an earlier paper presented at the fall 1989 meeting of the Acoustical Society of America [1], comparisons of acoustic data with predictions from the FFP were presented. The agreement between the data and predictions was found to be reasonably good, so long as the receiver was not in a shadow zone. For a receiver in a shadow, the disagreement

was up to 20 dB.

In the first section of this paper, the earlier paper will be summarized. In particular, the experimental procedures and the method originally used in the profile reconstructions will be discussed. In the second section, the profile reconstruction is extended to include data recorded by a Doppler sodar. The new method uses the generalized inverse to construct a least squares fit to the meteorological data. In the third section, stochastic perturbations are added to the profiles, in order to model the vertical structure of turbulence.

SUMMARY OF PREVIOUS RESULTS

Experimental Procedures

All of the experimental data were collected at the Pennsylvania State University's Rock Springs Agronomy Research Center. The propagation path was over crop area which had been planted with corn and soybeans, although the crops had been harvested prior to the experimental runs.

The basic experimental plan was quite simple: a 27.7 Hz source was continuously monitored at a distance of 770 m by one or two microphones, which were connected to a computerized data logging system. The source consists of four identical boxes, each approximately 1 cubic meter in size and having two fifteen-inch diameter moving-coil loudspeakers. The boxes were made to resonate at low frequency by drilling suitably-sized ports. The final operating frequency of 27.7 Hz was chosen because it was approximately the mean of the resonance frequencies of the individual boxes. The loudspeakers were driven by two Altec 400-watt stereo amplifiers. The sound pressure level at a reference microphone (General Radio 1560), located 8 meters from the source, was measured using a Hewlett-Packard 3561 single-channel spectrum analyzer, and logged to floppy disk via an HP 9186 microcomputer.

The set-up at the remote receiving station was quite similar. The sound pressure level at the two remote microphones (General Radio 1560) was monitored with a Hewlett-Packard 3562A dual-channel spectrum analyzer. The microphones were 0.6-2.0 m from the ground. Fifteen FFT's* were performed on the microphone signals each minute and averaged by the spectrum analyzer. The total power in the band 27.7 $\pm$ 1.0 Hz was calculated with an HP 9186 microcomputer and logged to floppy disk.

Preliminary investigations were performed in September 1988. The first extended experimental run took place during 13-16 October 1988. At this time the ground had not yet frozen, and was dry at the surface. The experiment then was repeated three times in February 1989, and once in March 1989.

To facilitate comparison of the various experimental runs, the sound level at the 8 m reference microphone was used to normalize the data. The first step in the normalization process was to compute an estimated sound pressure level at a distance of 1 m from the middle of the source. By assuming that the spreading from the source to the reference

*fast Fourier transforms

microphone was approximately spherical, the 1 m reference SPL could be found by adding 18 dB to the 8 m measurement. All of the acoustical data at the 770 m microphone were then normalized by subtracting the 1 m reference level. No additional compensation was made for cylindrical or spherical spreading losses between the 1 m reference and the remote microphones.

Meteorological Measurements

The surface layer measurements regularly logged at Rock Springs are extensive. Only those measurements which are most useful for interpretation of the acoustical data are discussed in this section.

One of the most sensitive and versatile instruments at Rock Springs is the Kaijo Denki DAT-300 ultrasonic anemometer-thermometer. This device, positioned ten meters above the ground, samples the wind velocity and temperature at a frequency of 20 Hz. Data from the ultrasonic anemometer-thermometer are also used to compute a number of turbulence statistics; among these are the covariance of the vertical wind component w with the horizontal wind component u, and the covariance of the vertical wind component w with the temperature T. These covariances are basic to the study of momentum and heat transfer processes in the surface layer.

In addition to the ultrasonic anemometer-thermometer, many other anemometers and thermometers with slower sampling rates are maintained. Cup anemometers and vanes are positioned at 2 m and 6.4 m. A device that is particularly useful in the reconstruction of temperature profiles is the "temperature difference probe," which continually senses the temperature difference between thermistors placed at 1.9 and 8.9 m. The thermistors are coupled in a bridge which ensures accurate evaluation of the temperature difference. This device is preferrable to the use of separate thermometers placed at different heights, because the latter method is sensitive to errors in the absolute calibration of the separate thermometers.

The data from the anemometers and thermometers are averaged for a half hour before being logged. Thus, with the current procedures, a half hour is the minimum interval for reconstruction of sound speed profiles.

A Doppler acoustic sounder (sodar) is also available for mapping temperature structure and wind profiles at heights greater than the instrumentated towers. The temperature structure information can be used to monitor the inversion height, to observe the presence of stable layers in the boundary layer, and to observe the passage of thermal plumes. The sodar was programmed to have a height resolution of fifty meters, with wind data being recorded every ten minutes.

Reconstruction of Sound Speed Profiles

Height-dependent sound speed profiles are required as input to refraction models such

as the FFP. It is highly desirable to be able to reconstruct useful profiles from only surface-layer data and remote measurements. Balloon launches are comparatively expensive.

In the literature on atmospheric acoustics, sound speed profiles have typically been determined in two ways. The first method, which might be called the "direct" method, consists of measuring the wind velocity and temperature at a large number of heights. In practice the direct method is, of course, costly if separate sensors are used at each height. It is also extremely sensitive to calibration of the individual sensors. A related option would be to use one set of moving sensors, although this procedure is complicated by the presence of turbulent fluctuations in the fields [2].

A second and more commonly used method, which might be called the "logarithmic" method, consists of measuring wind velocity and temperature at two heights. The measurements are then fit with a logarithmic sound speed profile. The problem with the logarithmic method is its accuracy: the sound speed profile is only approximately logarithmic, unless conditions are near neutral.

The method described here to reconstruct sound speed profiles is based on surface layer similarity scaling theory. It is similar to the logarithmic method, in that sensors are required at only two heights. With surface-layer similarity scaling, however, the analysis does not need to be limited to neutral conditions. One of the best summaries of surface-layer scaling theories is Stull [3], Chapter 9. Much of the following material is presented in more detail by Stull.

The type of scaling used in this paper is due to Monin and Obukhov. The meteorological profiles are written as functions of z/L, where z is the height from the surface and L is called the Monin-Obukhov length, which can be written

$$L = \frac{\overline{T_o}}{g\kappa}\frac{u_*^2}{T_*}. \tag{1}$$

In the above, g is gravitational acceleration, $\kappa = 0.4$ is the von Karman constant, $\overline{T_o}$ is the mean surface temperature in Kelvin,

$$u_* = \sqrt{-\overline{w'u'}} \tag{2}$$

is the *friction velocity*, and

$$T_* = -\frac{\overline{w'T'}}{u_*} \tag{3}$$

is the *surface-layer temperature scale.* The covariances are evaluated in the surface layer.

Note that if $\overline{w'T'}$ is positive, which is the case for statically unstable conditions, then $T_* < 0$ and $L < 0$. In fact, for unstable conditions, $-0.5L$ is approximately the height at which buoyant production of turbulence begins to dominate over mechanical (shear) production (Stull, p. 182). The limit $z/L \to 0$ represents neutral conditions. When $L > 0$, conditions are stable. In this case z/L indicates the extent to which mechanical turbulence is suppressed by the static stability in the mean temperature profile.

The rates of change of mean wind and temperature are written

$$\frac{\partial \overline{u}(z)}{\partial z} = \frac{u_*}{\kappa z}\phi_M\left(\frac{z}{L}\right), \tag{4}$$

$$\frac{\partial \overline{T}(z)}{\partial z} = -\gamma_d \overline{T}(z) + \frac{T_*}{\kappa z}\phi_H\left(\frac{z}{L}\right), \tag{5}$$

where the scaling functions ϕ are determined through a combination of theory and data regression.

When Eqs. 4 and 5 are integrated, the results can be written:

$$\overline{u}(z) = \frac{u_*}{\kappa}\left[\ln\left(\frac{z}{z_o}\right) - \psi_M\left(\frac{z}{L}\right)\right], \tag{6}$$

$$\overline{T}(z) = \overline{T}(z_t) - \gamma_d(z - z_t) + \frac{T_*}{\kappa}\left[\ln\left(\frac{z}{z_t}\right) - \psi_H\left(\frac{z}{L}\right)\right], \tag{7}$$

where z_o is the *aerodynamic roughness length*, and z_t is the *thermal roughness length*. For unstable conditions, $L < 0$,

$$\phi_M\left(\frac{z}{L}\right) = \phi_H\left(\frac{z}{L}\right)/0.74 = \left(1 - 13\frac{z}{L}\right)^{-1/3}. \tag{8}$$

When these functions are integrated, it can be shown that

$$\psi_M\left(\frac{z}{L}\right) = \psi_H\left(\frac{z}{L}\right)/0.74 = \frac{3}{2}\ln\left[\frac{(1+\phi_M^{-1}+\phi_M^{-2})}{3}\right] - \sqrt{3}\tan^{-1}\left(\frac{1+2\phi_M^{-1}}{\sqrt{3}}\right) + \frac{\pi}{\sqrt{3}}. \tag{9}$$

For stable conditions ($L > 0$), the ϕ-functions are much simpler:

$$\phi_M\left(\frac{z}{L}\right) = 1 + 4.7\left(\frac{z}{L}\right), \quad \phi_H\left(\frac{z}{L}\right) = 0.74 + 4.7\left(\frac{z}{L}\right). \tag{10}$$

Integration yields:

$$\psi_M\left(\frac{z}{L}\right) = \psi_H\left(\frac{z}{L}\right) = -4.7\left(\frac{z}{L}\right). \tag{11}$$

When a plant canopy or other roughness elements are present, the effective ground plane should be shifted upward by an amount d, called the *displacement height*. This is an extrapolated height at which the wind speed is approximately zero. It is possible to estimate z_o and d from the height of the roughness elements (plant canopy, buildings, etc.). According to Panofsky and Dutton [4],

$$z_o \simeq \frac{1}{8} \times \text{canopy height}, \tag{12}$$

$$d \simeq \frac{2}{3} \times \text{canopy height}. \tag{13}$$

There are now three unknowns in the wind and temperature profile equations: u_*, T_*, and the surface temperature, $T(z_t)$. This means that three independent measurements are required. In the original reconstruction procedure, these consisted of the temperature at two heights, say z_1 and z_2, and the wind velocity at one height, z_3. Solving Eq. 6 for u_* and evaluating at z_3, we have

$$u_* = \frac{\kappa \overline{u}(z_3)}{\ln[(z_3 - d)/z_o] - \psi_M[(z_3 - d)/L]}, \tag{14}$$

Solving 7 for T_*, evaluating at z_2 and z_1, and subtracting the z_2 equation from the z_1 equation, z_t is eliminated and we have

$$T_* = \frac{\kappa[\overline{\Delta T} + \gamma_d(z_2 - z_1)]}{\ln[(z_2 - d)/(z_1 - d)] - \psi_H[(z_2 - d)/L] + \psi_H[(z_1 - d)/L]}. \tag{15}$$

Since L is a function of u_* and T_*, these equations actually contain u_* and T_* on both sides. However, the ψ functions are small compared to the logarithmic term, and the equations may be solved by first neglecting the ψ functions, and then iterating until values for u_* and T_* have been converged upon. The solution is normally well behaved so long as there is good mixing in the surface layer. When local values of L are less than about 5, this method does not converge to a solution.

Once the wind and temperature profiles have been determined, an effective sound speed can be computed by adding the component of the wind velocity in the direction of propagation to the actual sound speed. An example of the sound speed profile evolution for 8 March 1989 is shown as Fig. 1. For this figure, L was assigned a value of 5 if there was no convergence to a solution. This was necessary during most of the nighttime hours.

Comparison with Acoustic Data

When the data shown in Fig. 1 were used in a fast field program (written by one of the authors, D. K. Wilson), the predictions shown in Fig. 2 result. For this figure, the acoustic data are plotted as half-hour means, so that the averaging periods of the acoustic data and meteorological measurements coincide. The sound speed profile was partitioned at 0.8, 1.4, 3, 6, 12 and 24 m. The ground was modelled as a rigid porous medium, with static flow resistivity of 200 000 mks rayls/m, tortuosity 2.5, and porosity 0.3.

Notice that, prior to 0800 and after 2000, the FFP predictions agree fairly well with the experimental data. During the daytime hours, however, the agreement is very poor. Examination of the profile reconstructions shows that the predictions are in good agreement so long as the sound speed increases with height, i.e., the receiver is in a surface sound channel. When the receiver is in an acoustic shadow zone, the FFP predicts a much greater propagation loss than actually occurs.

INCLUSION OF SODAR WIND PROFILES

The original method of reconstructing the profiles, discussed in the previous section, used only surface-layer data. This raises the question of whether incorporation of data for heights above the surface layer could improve the predictions.

Recall that a Doppler sodar was in operation during the experiment. The sodar monitors wind profiles at heights above 50 m. In this section, a new method for reconstructing the profiles, which incorporates the sodar data, is discussed. Unfortunately, the reconstruction procedure is much more difficult when the sodar data are included. The main reason is that the problem is now over-determined: there are more experimental data than parameters in the model.

Let us formulate the problem as follows. We arrange the meteorological data (surface-layer winds and temperatures, and Doppler sodar profiles), as a column vector $\mathbf{d}$. The model parameters, u_*, T_* and the surface temperature, comprise the column vector $\mathbf{m}$. Retaining just the first term in the Taylor series, the *forward* problem can be written

$$\mathbf{d}' \approx \mathbf{G}\mathbf{m}', \tag{16}$$

where the primes indicate the fluctuation about the actual value, and

$$G_{ij} = \frac{\partial d_i}{\partial m_j}. \tag{17}$$

The derivates can be evaluated, for example, by numerically differentiating Eqs. 6 and 7.

What we desire, however, is a solution to the *inverse* problem; that is, we want the model parameters in terms of the data. Some operator $(\mathbf{G})^{-1}$ must be constructed, so that

$$\mathbf{m}' \approx (\mathbf{G})^{-1}\mathbf{d}'. \tag{18}$$

Construction of such operators belongs to the field of inverse theory. An excellent introduction can be found in Chapter 12 of Aki and Richards [5]. The problem is not trivial, because $\mathbf{G}$ is not normally an invertable matrix.

For the profile reconstructions, a *weighted generalized inverse* was chosen. The generalized inverse gives a least squares solution to the overdetermined problem. The weighting was necessary because the Doppler sodar measurements are not as reliable as the surface-layer measurements. Weighting was accomplished by multiplying $\mathbf{d}$ and $\mathbf{G}$ by diagonal matrices, whose eigenvalues are interpreted as the variance associated with each datum. The surface-layer measurements were assigned a variance of one-tenth the Doppler sodar measurements.

Since the modeling equations are nonlinear, the model parameters are determined by iterating the inverse problem. The model parameter estimate after the $i+1$ iteration is

$$\mathbf{m_{i+1}} = (\mathbf{G})_\mathbf{i}^{-1}(\mathbf{d} - \mathbf{d_i}) + \mathbf{m_i}. \tag{19}$$

When there is good turbulent mixing (typically, the wind at 10 m > 3 m/s), the new method converges to a solution within ten iterations. However, the new method, like the older one, does not converge to a solution if the atmosphere is very stable. An example reconstruction using the new method, for 1548 on 8 March 1989, is shown in Fig. 3. The wind profile is on the left, and the temperature profile on the right. These profiles are typical of a convective boundary layer: the wind profile has a logarithmic shape, and the temperature decreases at a rate of one degree Celsius per 100 meters (the dry adiabatic lapse rate) outside of the surface layer.

In Fig. 2, FFP predictions generated from the new method are compared with the older one. The sound speed profile is partitioned into layers at 5, 10, 20, 35, 50, 75, 100, 125, 150, 175 and 200 m. The Doppler sodar data do not have a very significant effect on the predictions. In fact, the predicted levels are in even poorer agreement with the measurements than before.

STOCHASTIC PROFILE RECONSTRUCTIONS

Because the relationship between the meteorological profiles and the acoustic predictions is nonlinear, *the prediction from the mean sound speed profile is not necessarily the same as the mean prediction from the actual ensemble of profiles.* Due to turbulent fluctuations, the actual sound speed profile varies about the mean. In this section an attempt is made to reconstruct an ensemble of realistic profiles; that is, an ensemble of profiles which include the fluctuating turbulent part.

The reader may object to the neglect of the horizontal turbulent structure; whether a more realistic model for the horizontal structure would have much effect on the predictions remains to be determined. It should be kept in mind that the horizontal scale of turbulence is typically 100-500 m. (Ref. [3]) The vertical scale, however, is on the order of the height from the ground. For the purposes of acoustic predictions, it could be that a horizontally stratified atmosphere is a more realistic model than homogeneous turbulence. In any case, state-of-the-art modeling of homogeneous turbulence is discussed by Gilbert and Raspet [6], and the results of those authors are very similar to the results which will be given here.

Stull [3], and Panofsky and Dutton [4], discuss parameterizations for the variances for atmospheric turbulence. The following are in basic agreement with the equations presented in those two sources: For stable conditions, ($\sigma_u^2 = \overline{u'u'}$):

$$\sigma_u u_* = 2.4, \tag{20}$$

$$\sigma_T T_* = 3.5. \tag{21}$$

For unstable conditions,

$$\sigma_u / u_* = \left(12 - \frac{0.5 z_i}{L}\right)^{1/3}, \tag{22}$$

$$\sigma_T / T_* = -2.0 \left(1 - \frac{10z}{L}\right)^{-1/3}, \tag{23}$$

where z_i denotes the lower boundary of the stable layer, which caps the boundary layer.

In the reconstructions of turbulence presented here, the fluctuations were assumed to have a jointly Gaussian distribution. The fluctuations at the various heights in the discretized profiles were assumed to have a correlation length given by

$$\ell = \kappa z. \tag{24}$$

It is a straightforward procedure to generate random numbers for a jointly Gaussian distribution on a computer, and the details of the technique will not be discussed here.

As an example, the mean sound speed profile which was determined for 1548 on 8 March 1989 is shown on the left of Fig. 4, and an ensemble of five stochastically-modified profiles is shown on the right.

Predictions generated from the stochastically-modified profiles are shown in Fig. 2. Agreement with the experimental data is improved, although the FFP still predicts a greater propagation loss than was actually measured. For each prediction appearing on the graph, ten profiles were generated. FFP predictions from each of these profiles were then averaged. Since the standard deviation of each ensemble of FFP predictions is about 10 dB, we can expect to be within about 3 dB (≈ 10 dB$/\sqrt{10}$) of the mean when ten profiles are averaged. Fluctuations resulting from this error are obvious in Fig. 2. Obviously, it would be desirable to average many more profiles, but this would increase the computational time unreasonably. For example, since the data shown on the figure required about 24 hours of CPU time on a VAX Workstation, ten days of CPU time would be required to reduce the error to 1 dB.

CONCLUDING REMARKS

The modeling of meteorological profiles, and their use in predicting sound levels, was emphasized in this paper. Validity of Monin-Obukhov length similarity scaling was assumed in the modelling. The parameters needed for scaling were determined entirely from surface-layer measurements and remotely-sensed data, by performing a nonlinear inversion on mean meteorological data. The inversion technique presented in this paper, based on the generalized inverse, is flexible and works well when the problem is over-determined.

Unfortunately, the inversion is not successful under the conditions of a very stable boundary. Monin-Obukhov model breaks down in this case, and no simple and accurate method for modeling profiles in the absence of good turbulent mixing have yet been developed. If realistic forward models can be developed for the stable boundary layer, the inversion technique presented in this paper could be easily modified, and should converge to a solution.

The fast field program generates predictions for propagation in a horizontally-stratified medium. Therefore, only the effect of the vertical structure of turbulence on sound prop-

agation (and not the effect of the horizontal structure) can be modeled using the FFP. Nonetheless, since the horizontal scale of turbulence is typically much greater than the vertical scale, it still might be possible to model turbulence with sufficient realism using the FFP. In this paper, an initial attempt at turbulence modeling within the constraints of the FFP was made. Agreement between FFP predictions and acoustical measurements was improved, although at the cost of an order-of-magnitude increase in computational time.

REFERENCES

[1] Wilson, D. K.; and Thomson, D. W.: Experimental Studies of Low-Frequency Propagation Over Flat Terrain. Presented at the Fall 1989 meeting of the Acoustical Society of America, 27 November-1 December 1989, St. Louis, Missouri.

[2] Daigle, G. A.; Embleton, T. F. W.; and Piercy, J. E.: Propagation of sound in the presence of gradients and turbulence near the ground. *J. Acoust. Soc. Am.* **79**, 613-627, 1986.

[3] Stull, R. B.: *An Introduction to Boundary Layer Meteorology.* Kulwer, Dordrecht, 1988.

[4] Panofsky, H. A.; and Dutton, J. A.: *Atmospheric Turbulence: Models and Methods for Engineering Applications.* Wiley & Sons, New York, 1984.

[5] Aki; and Richards: *Quantitative Seismology.* W. H. Freeman, San Francisco, 1980.

[6] Gilbert, K. E.; and Raspet, R.: Calculation of turbulence effects in an upward refracting atmosphere. Presented at the Fall 1988 meeting of the Acoustical Society of America, 14-18 November 1988, Honolulu, Hawaii.

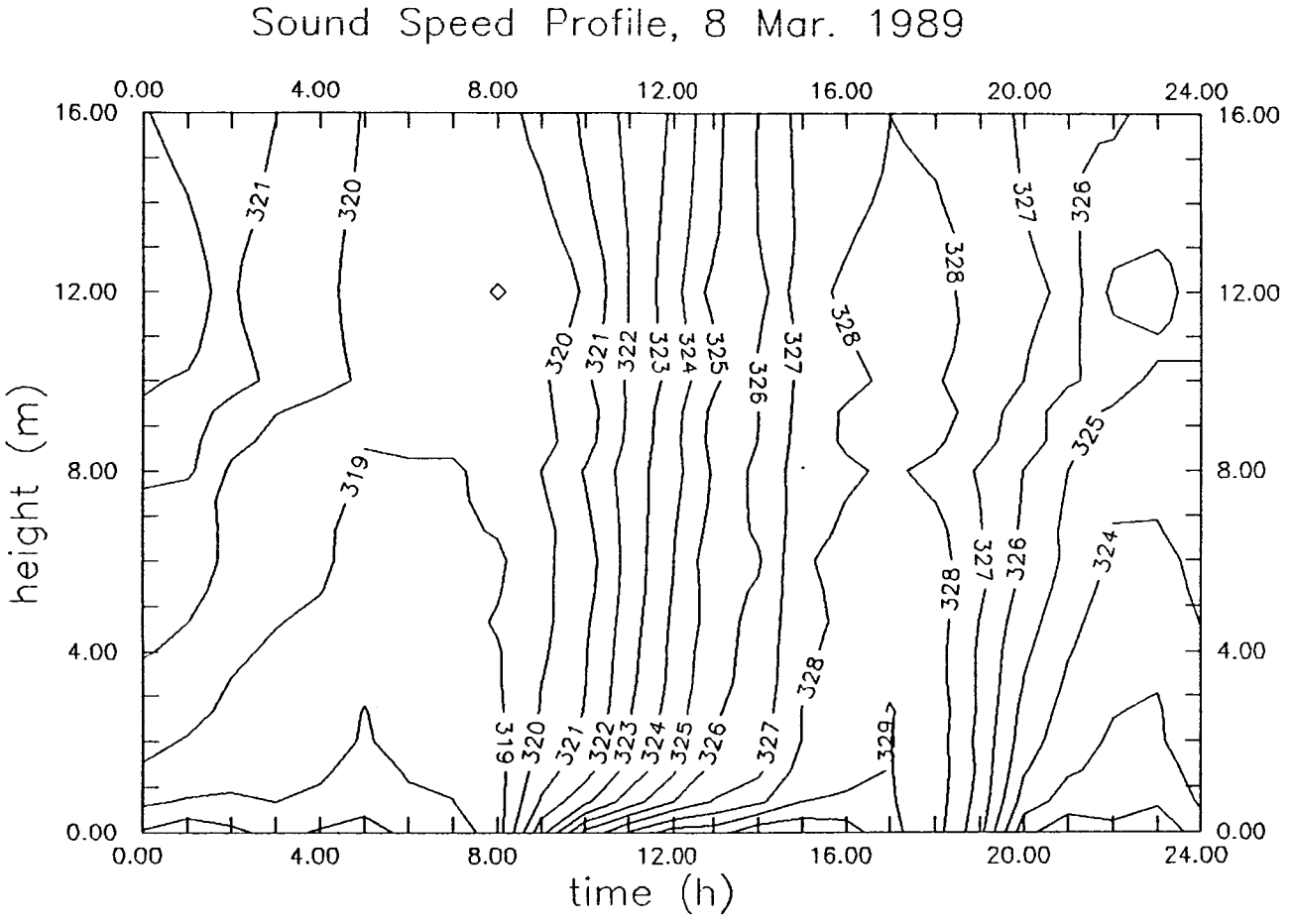

Fig. 1 Evolution of the sound speed profile on 8 March 1989. The profiles were reconstructed from measurements of the wind vector at 10 m, and the temperature at 1.9 and 8.9 m.

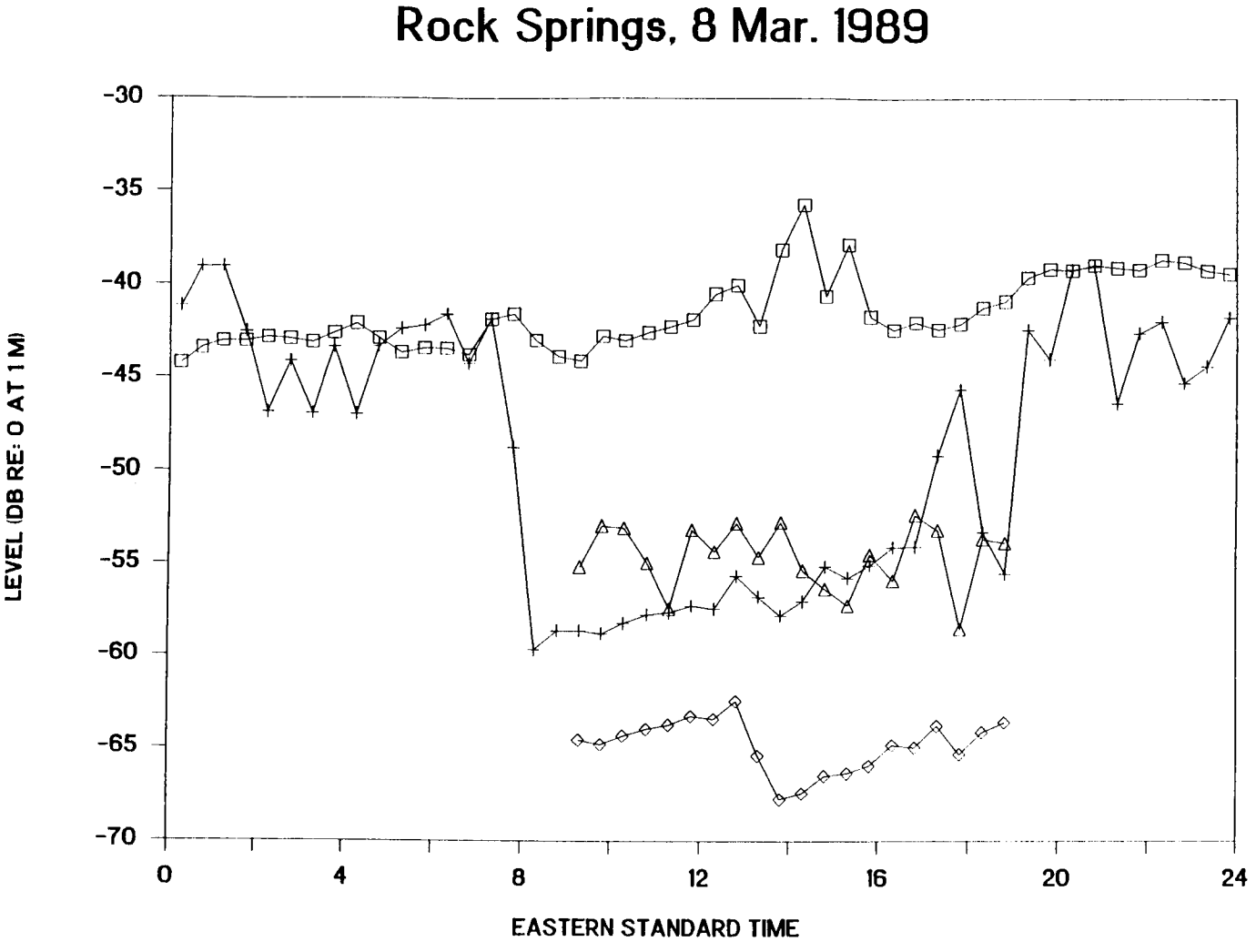

Fig. 2 Comparison of experimental data and FFP predictions. The data (marked with a square) generally exceed the predictions. Predictions marked with a plus sign were generated from the sound speed profiles shown in Fig. 1. Predictions marked with a diamond include sodar wind profiles in the SSP reconstructions. Predictions marked with a triangle include sodar data and turbulence modeling.

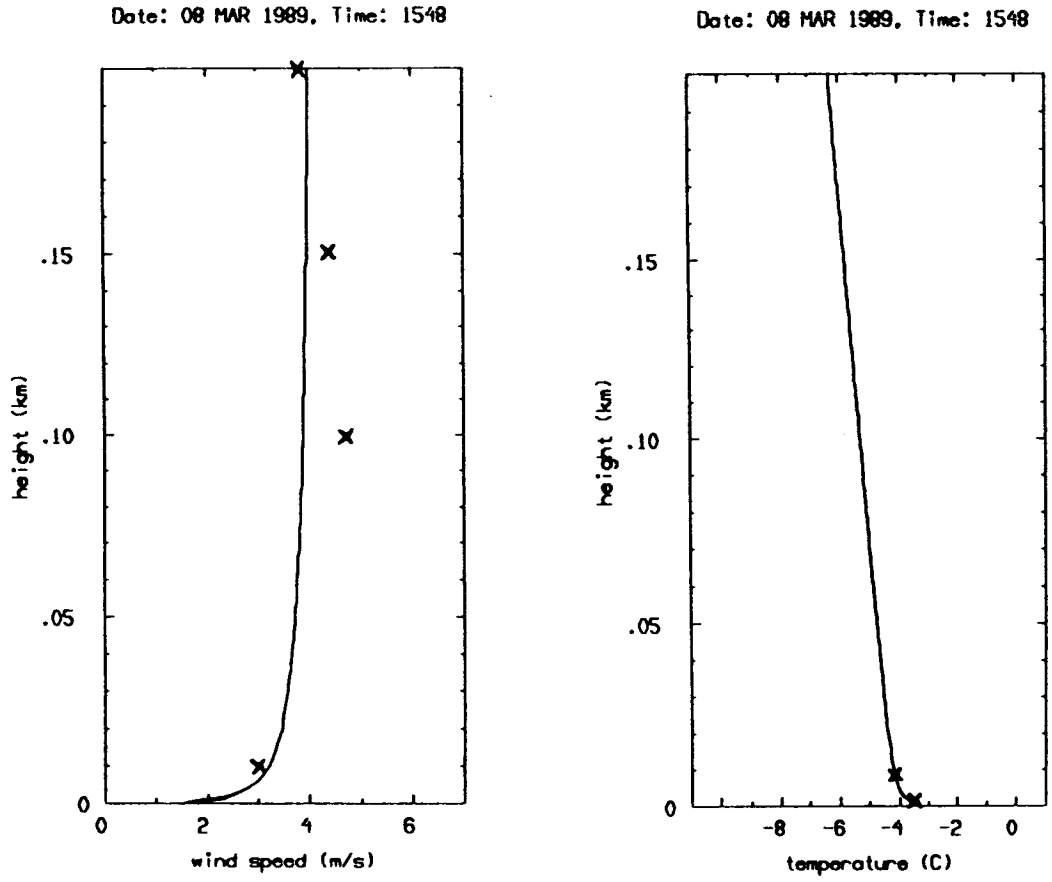

Fig. 3 Reconstruction of meteorological profiles for 1548 on 8 March 1989. Marked on the wind profile (left) are the sonic anemometer measurement at 10 m, and the sodar gates at 100, 150 and 200 m. Marked on the temperature profile (right) are the measurements at 1.9 and 8.9 m.

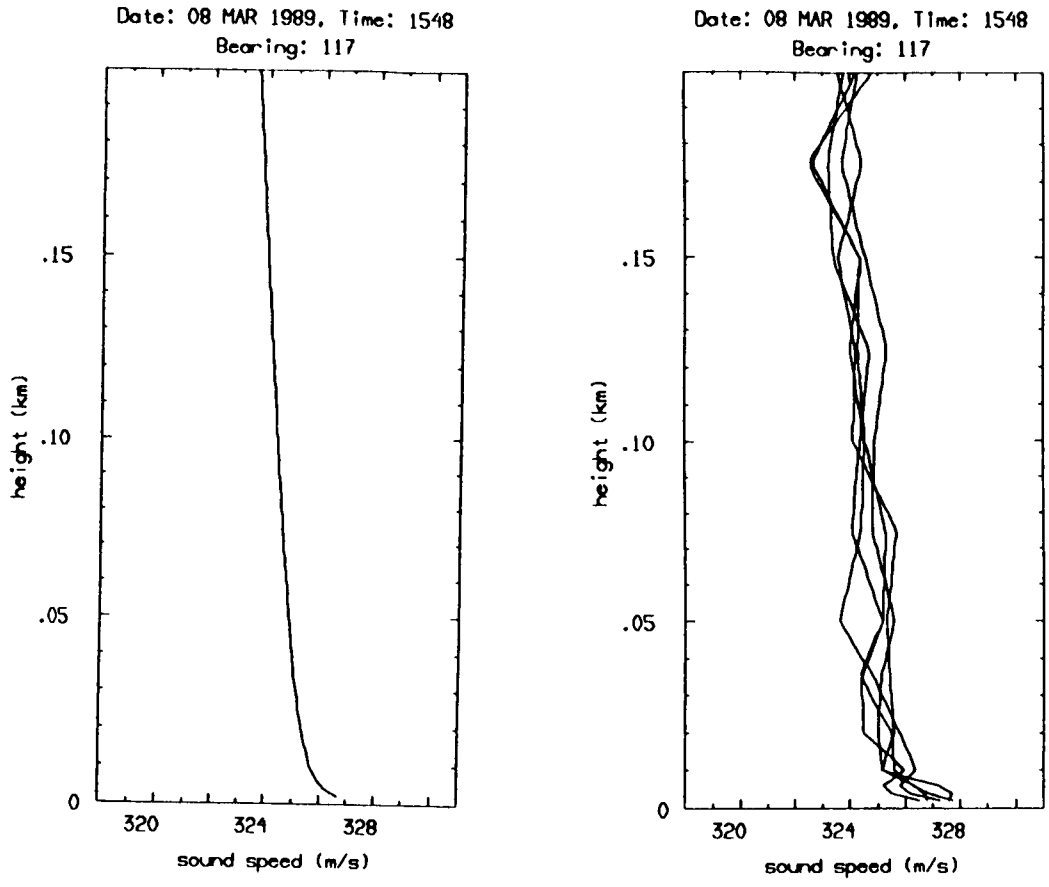

Fig. 4 On the right is the unperturbed sound speed profile for 1548 on 8 March 1989. At left, an ensemble of five stochastically-reconstructed profiles, modeling the vertical structure of turbulence, is shown.

NEW CORRECTION PROCEDURES FOR THE FAST FIELD PROGRAM WHICH EXTEND ITS RANGE

M. West, Department of Applied Acoustics
R. A. Sack, Department of Mathematics and Computer Science
University of Salford, Lancashire, England

SUMMARY

An FFP algorithm has been developed based on the method of Lee et al* for the prediction of sound pressure level from low frequency high intensity sources. In order to permit accurate predictions at distances greater than 2km, new correction procedures have had to be included in the algorithm. Certain functions, whose Hankel transforms can be determined analytically, are subtracted from the depth dependent Green's function. The distance response is then obtained as the sum of these transforms and the FFT of the residual k dependent function. One procedure, which permits the elimination of most complex exponentials, has allowed significant changes in the structure of the FFP algorithm, which has resulted in a substantial reduction in computation time.

1. INTRODUCTION

Sound pressure levels at large distances from a point source close to the ground have been predicted using ray based procedures[1] in enhanced zones and residue calculations[2] in strong shadow zones. In the published literature (see references 1 and 2) these predictions have been shown to be approximately valid. The errors for the predictions in the enhanced zone increase when ground reflections become important and when landing ray densities become small. In the shadow zone errors increase when the sound speed gradient becomes small. Both the above procedures are inaccurate or inoperable in the transition regions between shadow and enhancement.

Since the publication of the first paper on the FFP[3] for atmospheric sound propagation this method has been increasingly used for sound pressure level prediction. This has largely occurred because the FFP can operate irrespective of whether there are shadow or enhanced or even mixed conditions present. Moreover the FFP can take proper account of ground reflection.

The most widely known FFP algorithm, the CERL–FFP, stems from the method of Lee et al[4], which was a development of the algorithm described in Raspet et al's first paper[3].

Starting from reference 4 we have reworked the analysis to enable us to produce our own FFP algorithm, structured in such a way that we could incorporate a variety of corrections in k space and thereby extend the range of validity of the result in the transformed (real) space.

* Lee et al. J. Acoust. Soc. Am., 79, 1986, pp 628–634.

In section 2 of this paper a brief description is given of the development of our first prototype algorithm. A survey of previously published k spectral corrections applied to the first prototype is given in section 3. Section 4 describes our second algorithm which is based on a 'γ averaging' procedure and section 5 describes a technique adopted for speeding up the computation. In the last section, 7, a comparison between the FFP and our other model's predictions is given for a realistic case.

2. DEVELOPMENT OF THE FIRST FFP ALGORITHM

2.1 Sign Convention

Lee et al[4] replaced the system of atmospheric strata by an analogue electrical network. In our reworking of the model we found that this was not necessary and that retention of acoustic equations for pressure and particle velocity ensured greater clarity. In addition our analysis showed that great care had to be exercised with the signs used in the ladder calculation.

Raspet[3] correctly drew attention to the need for different signs for the characteristic admittance dependent on the direction of the particle velocity, which gives the correct sign for the characteristic admittance of top stratum, $Y_{co} = + i\gamma_o/\omega\rho_o$ where γ_o is the propagation constant and ρ_o is the density and for the characteristic admittance of the ground $Y_{cM} = + 1/Z$ where Z is the usual ground impedance.

None of the published papers on the FFP, including the most recent ones (see Franke et al[5]), make it clear that the signs used in the ladder admittance calculation must be chosen in accordance with the direction in which the calculation is performed. The equation for calculating an admittance (Y_{new}) at the stratum interface nearer to the source from the admittance at the stratum's other interface (Y_{old}) is

$$Y_{new} = Y_{cm} \frac{\epsilon \tanh \gamma_m \ell_m + Y_{old}/Y_{cm}}{1 + \epsilon\ (Y_{old}/Y_{cm})\ \tanh \gamma_m \ell_m} \qquad (1)$$

where the characteristic admittance for layer m, is $Y_{cm} = \epsilon\ i\gamma_m/\omega\rho_m$, γ_m being the propagation constant, ρ_m the density and ℓ_m the stratum thickness; ϵ is +1 when working upwards and −1 when working downwards. We note that the ϵ's cancel in (1) so that the same equation can be used whether working above or below the source interface. However in view of ϵ in the top semi-infinite layer being set to +1 the admittance calculated just above the source interface, $Y(z_s)^-$, has opposite sign to that calculated just below that height, $Y(z_s)^+$.

The z dependent Green's function at the source, $P(z_s)$, is obtained from the known discontinuity in particle velocity at that location. Using our sign convention and noting the opposite signs of $Y(z_s)^+$ and $Y(z_s)^-$ a negative sign must appear in the denominator of $P(z_s)$.

$$P(z_s) = \frac{-\ (2i/\omega\rho_s)}{Y(z_s)^+ - Y(z_s)^-} \qquad (2)$$

Likewise performing the calculation of the Green's function at the detector, $P(z_D)^*$ and retaining the above convention for ϵ, the equation for calculation of p at the stratum interface nearest the source (P_{new}) from that at that stratum's other interface (P_{old}) becomes

$$P_{new} = P_{old} \left\{ \cosh \gamma_m \ell_m + \epsilon \sinh \gamma_m \ell_m \left[\frac{Y_{old}}{Y_{cm}} \right] \right\} \qquad (3)$$

irrespective of whether the receiver is above or below the source.

2.2 Ground Impedance

The early FFP algorithms used the Delany Bazley[6] model for the ground impedance. Attenborough has suggested that his four parameter model[7] be used instead since this gives much smaller and more realistic impedance values at the low frequencies of interest in this study.

2.3 Damping Coefficient

The k spectrum calculated with the above ladder procedure has a large spike at the k value closest to ω/c_0 where c_0 is the sound speed for the top semi-infinite top layer and also a number of subsidary spikes at k values nearest to ω/c_m. These infinities produce errors when the Fourier transform is performed. A global damping is usually introduced, preferably by subtracting a small imaginary quantity $i\mu$ from k, where μ is typically 10^{-4}. The transform is corrected for the effect of the damping by multiplying it by $e^{\mu r}$

This procedure effectively produces different damping effects on each spike dependent on their proximity to the nearest k sample point. The k sampling errors are therefore only partially removed.

3. APPLICATION OF PUBLISHED k SPECTRAL CORRECTIONS

3.1 Candel and Crance's k Shift Procedure

Candel and Crance[8] proposed a method which ensured the k sample intervals were chosen so that the main peaks all occurred well away from the sample points. Thereby the transform errors arising from the presence of spikes in the k spectrum were substantially reduced.

We set up an algorithm to readjust the k sampling interval, Δk, until the 5 main spikes were more than a limiting distance ($\Delta k/10$) from the nearest k sample point. The method requires a full ladder calculation for typically 1/8th of the total k range centred on $k_0 = \omega/c_0$ for each setting of Δk. This can be time consuming when large numbers of strata are considered.

The method worked well for large Δk values when the total number of k samples, N, was less than 1k. For the larger N values required for ranges greater than 2km it became increasingly difficult to ensure the main spikes were distanced more than the above limiting value from the sample points.

* *The term k spectrum in this paper refers to $F = k\ P(z_D)$ which is the function to be Fourier transformed.*

3.2 The Richards and Attenborough[9] Tail Remover

The k spectrum very often has a non zero asymptotic value or tail as k goes to infinity. This tail invariably occurs when source and receiver are approximately the same height above ground.

Introduction of a cut-off for the spectrum at a value k_{max} produces large ripples in the transform which increase with range and with the proximity of k_{max} to ω/c_o.[3] In this study we set k_{max} at a value where the change in F was less than a prescribed limit, but this remained unsatisfactory.

The k spectral tail can be removed by subtracting the function g(k) given by Richards and Attenborough[9] from F(k).

$$g(k) = (A + e^{-kz_s})\ (1 - e^{-\delta k}) \qquad (4)$$

where z_s is the source height and $A = |F\ (k_{max})|$ and δ is the derivative of $|F\ (k)|$ at small k. g(k) has an exact Hankel transform which is added to the Fourier transform of F (k) − g (k). The above tail remover does not have the correct phase at small k and this produces a small error in the transform.

Experiments with functions, with exact Hankel transforms which mimic the F (k) behaviour at small k and near the main spike are in progress.

In Figure 1 the attenuation for a source and receiver 2m above an impedance ground at 50Hz is shown with and without the tail remover.

4. MODIFIED FFP ALGORITHM USING 'γ' AVERAGING[1]

For the large ranges of interest in this study very small Δk values must be used therefore the Candel and Crance method does not work. A novel technique for obtaining a k spectrum which can be more reliably transformed has been developed.

The γ averaging procedure is most easily understood by considering a single step in the admittance calculation for one stratum, index m, as described in section 2. Writing equation (1) in matrix form

$$\begin{bmatrix} P \\ U \end{bmatrix}_{new} = M_m \begin{bmatrix} P \\ U \end{bmatrix}_{old} \qquad (5)$$

where the matrix M_m has elements which are functions of k and are usually evaluated at a single k sample value, say k_r.

$$M_m = \begin{bmatrix} \cosh \gamma_m \ell_m & \epsilon Z_{cm} \sinh \gamma_m \ell_m \\ \dfrac{\epsilon \sinh \gamma_m \ell_m}{Z_{cm}} & \cosh \gamma_m \ell_m \end{bmatrix} \qquad (6)$$

where $\gamma_m = \sqrt{k_r^2 - \omega^2/c_m^2}$

For Fourier integrals of smoothly varying functions $F(k)$ (which have to be approximated by a discrete Fourier transform), the optimal sampling is at equidistant k_r values. These $F(k)$ samples can be assumed to approximate the contribution to the integral over the interval $k_r - \Delta k/2$ to $k_r + \Delta k/2$. In the presence of integrable infinities a different averaging process must be used.

The simplest method follows from changing the integration variable in the above interval from k to γ; then elementary averaging leads to (6) with $\gamma_m\ (k_r)$ replaced by

$$\bar{\gamma}_m = [\gamma_m\ (k_r - \Delta r/2) + \gamma_m\ (k_r + \Delta r/2)]/2$$

We employ this averaging method for those intervals where γ^2 changes sign.

Provided c_m is real (no damping) the values of γ_m in the integrand are either pure imaginary or pure real and so are the γ_m values at all sample points except those where the above averaging is employed. Hence the hyperbolic functions in (6) can be replaced by real trigonometric or hyperbolic functions, the full complex functions being required at the above critical points only. A speed up by a factor of 3 was obtained by this procedure over that using (6) in its general complex form. This high speed algorithm cannot be used if artificial damping is present.

5. k SPACE INTERPOLATION

In order to obtain predictions out to large distances the number of k samples, N, for a given k_{max} must be increased. As the major part of the computation lies in the determination of the z dependent kernel at each k value, we can achieve considerable improvements in calculation speed by interpolating $F(k)$ where it varies smoothly. This applies to all regions of the spectrum lying outside the range spanned by ω/c_m for all layers (typically $k_{max}/8$). It was found that $F(k)$ only needed to be evaluated every 8th point in the smooth region.

For most cases linear interpolation of $F(k)$ is adequate. However at very large ranges fluctuations occur in the transform due to the small discontinuities in the slope of the interpolated $F(k)$. These errors can be reduced by using cubic interpolation.

6. STRATUM QUANTISATION ERROR

In Figure 2 the predicted attenuation above an impedance ground is shown for two different stratum configurations with the same small linear sound speed gradient (0.01 s^{-1}). For the solid curve all strata above 30m are taken as 27m thick and for the dotted curve as 54m thick. It is clear that the undulations in the dotted curve are much bigger than for the solid curve. This occurs because the FFP uses mid stratum sound speed averages for the whole of each stratum. This produces a stratum sampling error which gets worse the thicker the strata and the larger the sound speed gradient. There are two remedies: one is to use many very fine strata that increases the amount of computation, the other is to use linear sound speed variations in each stratum and use a modified procedure employing Airy functions[10].

7. COMPARISON OF THE FFP PREDICTIONS WITH RAY/RESIDUE MODEL PREDICTIONS

In Figure 3 the attenuation predicted by the FFP for a lapse–inversion–lapse meteorology is compared with that obtained by a hybrid method. This latter method combines the predictions from a ray based model for the enhanced regions with

those from a residue model for the shadow regions. The advantages of using the FFP are apparent in this figure. The residue model overpredicts the shadow attenuation and the ray model is restricted to giving predictions only in the region where there are ray landing points. Neither of these models can properly deal with the transitional region between shadow and enhancement.

REFERENCES

1. Walkden, F. and West, M. Prediction of Enhancement Factor for Small Explosive Sources in a Stratified Moving Atmosphere. J. Acoust. Soc. Am. 84 (1), 1988, pp 321-326.

2. West, M; Walkden, F. and Sack, R. A. The Acoustic Shadow Produced by Wind Speed and Temperature Gradients Close to the Ground. Applied Acoustics, 27 (3), 1989, pp 239-260.

3. Raspet, R; Lee, S. W; Kuester, E; Chang, D. C; Richards, W. F; Gilbert, R and Bong, N. A Fast Field Program for Sound Propagation in a Layered Atmosphere above an Impedance Ground. J. Acoust. Soc. Am., 77, 1985, pp 345-352.

4. Lee, S. W; Bong, N; Richards, W. F. and Raspet, R. Impedance Formulation of the Fast Field Program for Acoustic Wave Propagation in the Atmosphere. J. Acoust. Soc. Am., 79, 1986, pp 628-634.

5. Franke, S. J. and Swenson, G. W. A Brief Tutorial on the Fast Field Program (FFP) as Applied to Sound Propagation in the Air. Applied Acoustics 27 (3), 1989, pp 203-215.

6. Delany, M.E. and Bazley, E. N. Acoustical Properties of Fibrous Absorbent Materials. Applied Acoustics 3, 1970, pp 105-116.

7. Attenborough, K. Acoustical Impedance Models for Outdoor Sound Surfaces. J. Sound Vib., 99 (4), 1985, pp 521-544.

8. Candel, S. M. and Crance, C. Direct Fourier Synthesis of Waves in Layered Media and the Method of Stationary Phase. J. Sound Vib., 74 (4), 1981, pp 477-498.

9. Richards, T. L. and Attenborough, K. Accurate FFT-Based Hankel Transforms for Predictions of Outdoor Sound Propagation. J. Sound Vib., 109 (1), 1986, pp 157-167.

10. Wilson, D. K. Propagation in a Stratified Atmosphere and Solution with the FFP-L Program. Internal Report, The Pennsylvania State University, April 1990.

ACKNOWLEDGEMENT

The authors gratefully acknowledge the financial support of the Ministry of Defence.

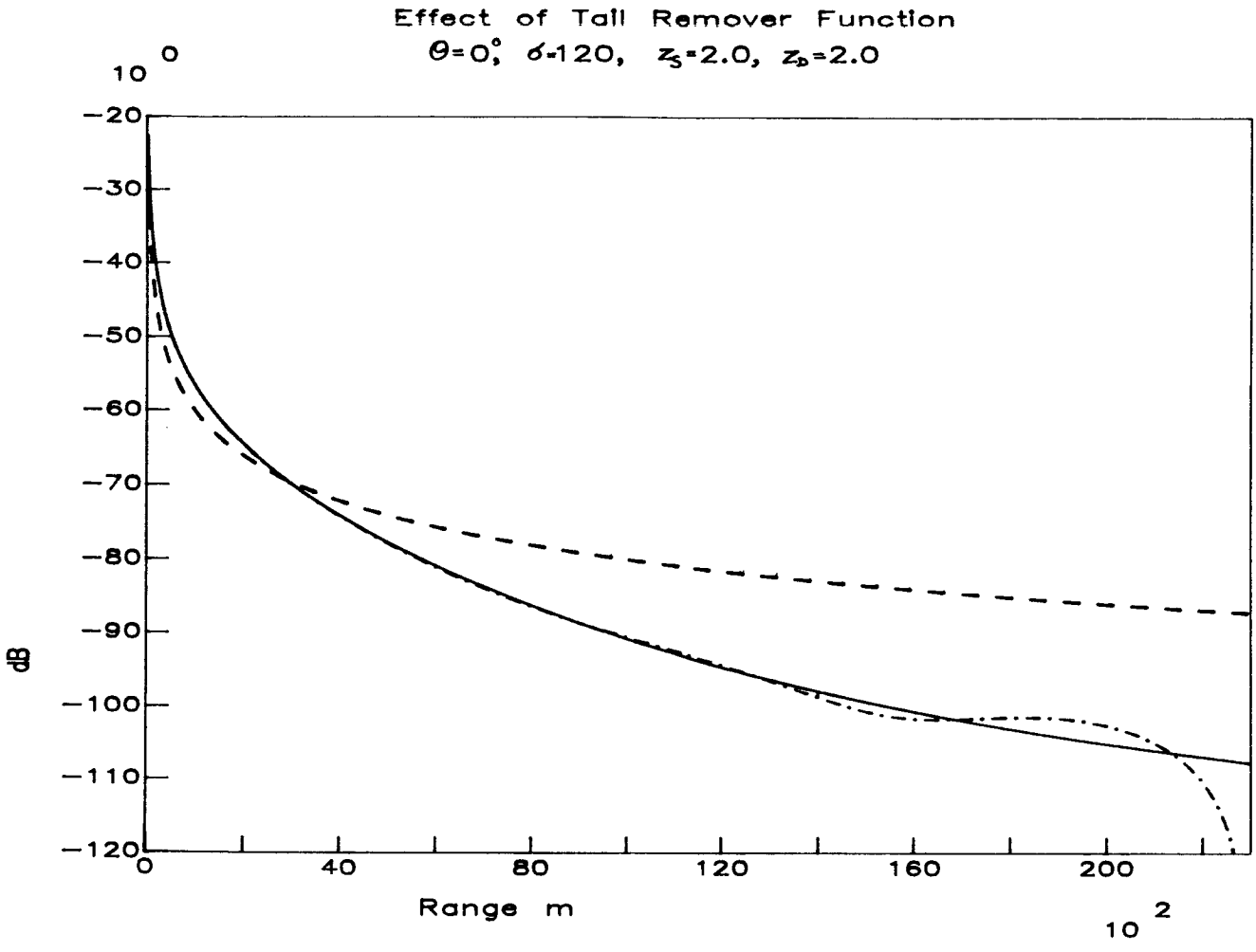

Figure 1 Effect of the Richards–Attenborough Tail Remover Function. Still air and an impedance ground.

Dashed line – free field

Solid line – with tail remover

Dashed–dotted line – without tail remover

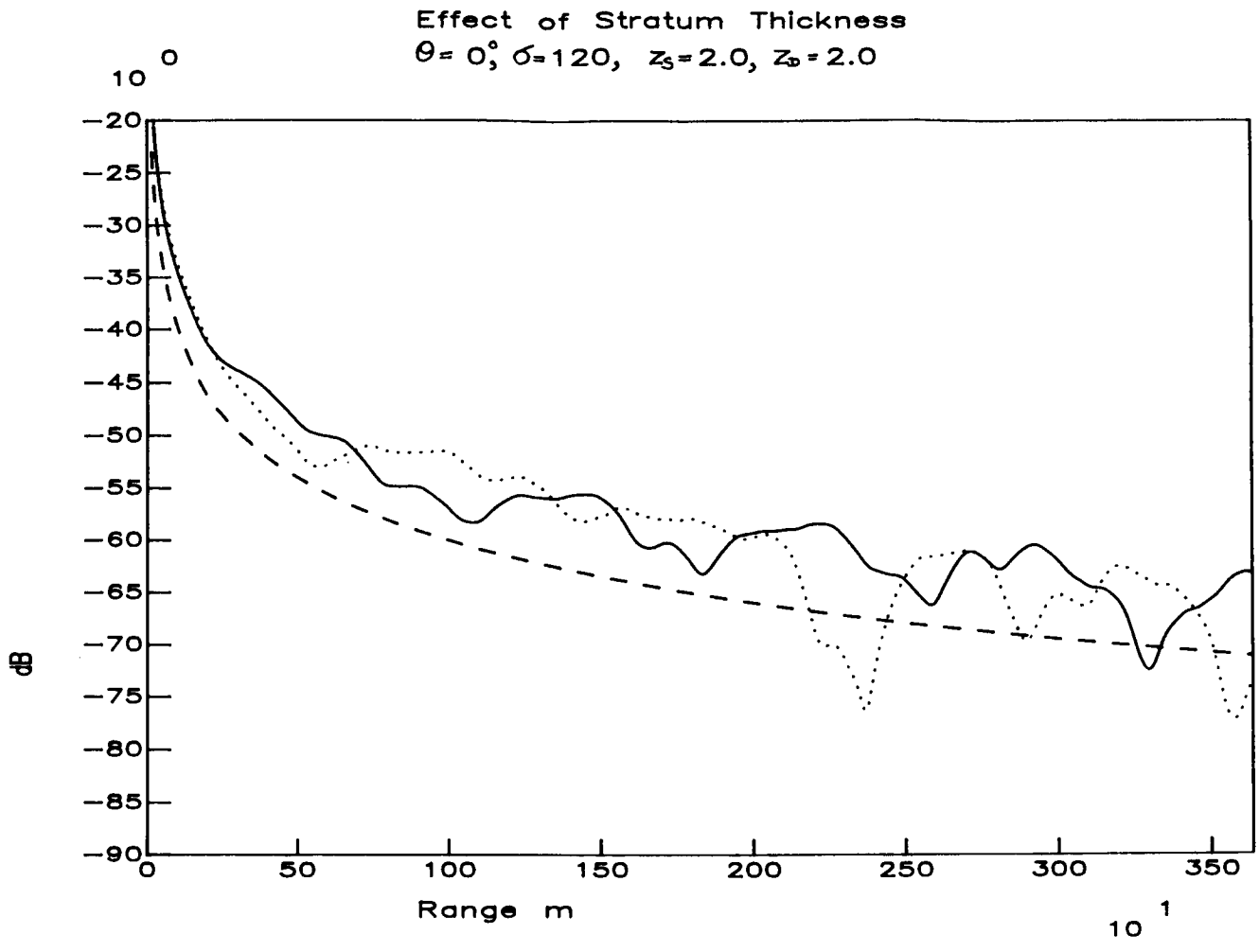

Figure 2 Effect of Stratum Thickness
Sound speed gradient 0.01 and an impedance ground.

Dashed line	–	free field
Solid line	–	27m thick strata above 30m
Dotted line	–	54m thick strata above 30m

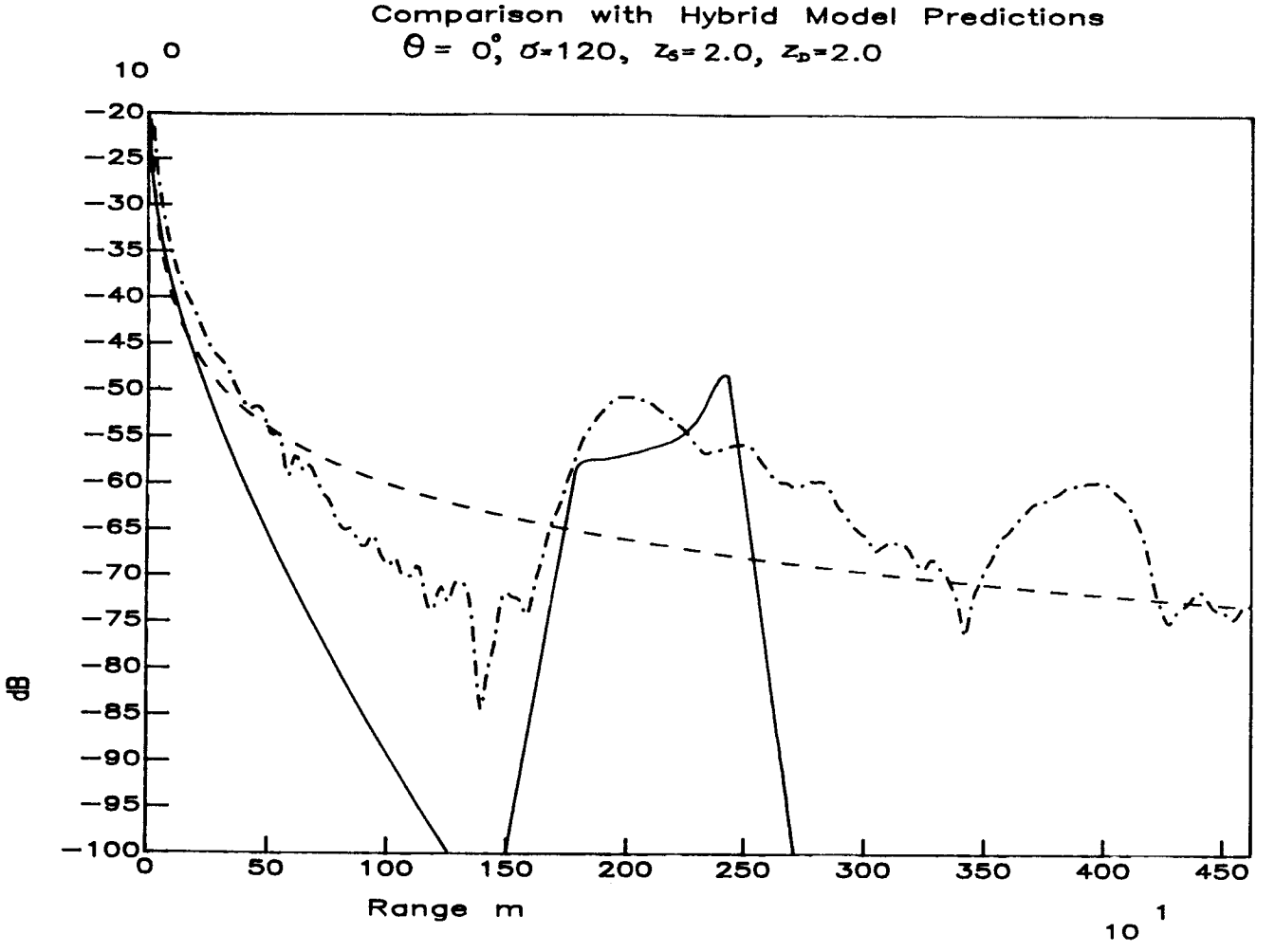

Figure 3 Comparison of FFP Predictions with those from a Hybrid Model. Sound speed gradient up to 100m −0.1, from 100m to 200m +0.1 and above 200m −0.05 and an impedance ground.

Dashed line	–	free field
Solid line	–	hybrid model prediction
Dashed–dotted line	–	FFP prediction

DISTORTED-WAVE BORN APPROXIMATION CALCULATIONS FOR TURBULENCE SCATTERING IN AN UPWARD-REFRACTING ATMOSPHERE *

Kenneth E. Gilbert, Xiao Di, and Lintao Wang
National Center for Physical Acoustics

University of Mississippi
University, Mississippi

ABSTRACT

Weiner and Keast observed that in an upward-refracting atmosphere, the relative sound pressure level versus range follows a characteristic "step" function. The observed step function has recently been predicted qualitatively and quantitatively by including the effects of small-scale turbulence in a parabolic equation (PE) calculation. [Gilbert *et al.*, J. Acoust. Soc. Am. **87**, 2428-2437 (1990)]. The present paper compares the PE results to single-scattering calculations based on the distorted-wave Born approximation (DWBA). The purpose is to obtain a better understanding of the physical mechanisms that produce the step-function. The PE calculations and DWBA calculations are compared to each other and to the data of Weiner and Keast for upwind propagation (strong upward refraction) and crosswind propagation (weak upward refraction) at frequencies of 424 Hz and 848 Hz. The DWBA calculations, which include only single scattering from turbulence, agree with the PE calculations and with the data in all cases except for upwind propagation at 848 Hz. Consequently, it appears that in all cases except one, the observed step function can be understood in terms of single scattering from an upward-refracted "skywave" into the refractive shadow zone. For upwind propagation at 848 Hz, the DWBA calculation gives levels in the shadow zone that are much below both the PE and the data.

INTRODUCTION

Weiner and Keast[1] and others[2,3] have observed that for sound propagation in an upward-refracting atmosphere, the relative sound-pressure level[4] versus range can be represented as a "step function" (Fig. 1). Recently the observed step function has been predicted qualitatively and quantitatively by parabolic equation (PE) calculations that include the effects of small-scale turbulence.[5]

Figure 2 shows gray-scale plots of the PE calculation without turbulence and with turbulence. The upward-refracted wave is called the "skywave."[6] In the plots with turbulence the skywave is still present although it has been noticeably modified by turbulence. For a

* This work was supported by the Office of Naval Research

source and receiver near the ground, the average relative sound pressure level inside the skywave (region 1 in Fig. 1) is approximately 0 dB (spherical spreading) with or without turbulence. However, the region below the skywave (region 3 in Fig. 1) is dramatically affected by turbulence. Without turbulence a deep shadow zone is predicted by the PE calculation. With turbulence, sound is scattered from the skywave into the shadow zone, producing a relative sound pressure level that is fairly uniform on the average. The region between the skywave and shadow zone (region 2 in Fig. 1) is a transition region. The horizontal extent of region 2 is a strong function of the strength of upward refraction. It is evident that, for a gray-scale plot with turbulence in Fig. 2, a horizontal "cut" through the plot at a particular receiver height will give a step function.

Although the gray-scale plots of the PE calculations give a good qualitative picture for understanding the step function, the PE calculations do not allow a simple physical explanation of the observed quantitative behavior of the relative sound pressure level versus range. For example, what causes the observed constant relative sound pressure level (spherical spreading) at long ranges? In the present paper a simpler calculation is presented which is based on single scattering out of the upward-refracted skywave. The simpler calculation, which uses the distorted-wave Born approximation (DWBA),[7] is compared to the PE calculation and to the data of Weiner and Keast. The objective is to gain insight into the physical mechanisms that produce the observed step function.

I. THEORY

A. Atmospheric model

We want to compare the DWBA calculations to the PE calculations reported in Ref. 5. Hence we use the same atmospheric model as in Ref. 5 and assume that the effects of turbulence can be adequately represented by small fluctuations in the index of refraction. The total index of refraction is thus written as a steady deterministic part $n_d(\vec{R})$ plus a fluctuating stochastic part $\mu(\vec{R},t)$ where $\vec{R} = (x,y,z)$ and t is time. With this approximation for turbulence, the wavenumber is given by

$$k(\vec{R},t) \;=\; k_0\big[n_d(\vec{R}) + \mu(\vec{R},t)\big] \quad , \tag{1}$$

where k_0 is a reference wavenumber, $n_d \cong 1$, and $\mu \ll 1$. The deterministic part of the index of refraction n_d is assumed to vary only with the height above the ground z. It was computed from a logarithmic sound-speed profile of the form

$$c_d(z) = \begin{cases} c_0 + a\ ln(z/d), & z \geq z_0 \quad , \\ c_0 + a\ ln(z_0/d) & z < z_0 \quad , \end{cases} \tag{2}$$

where $c_0 = 340$ m/s, $z_0 = 0.01$ m, and $d = 6 \times 10^{-3}$ m. The refraction parameter a is $-.5$ m/s for crosswind propagation (weak upward refraction) and -2.0 m/s for upwind propagation (strong upward refraction). The deterministic parameters were chosen to fit the short-range data of Weiner and Keast.[1]

In the calculations reported here, the fluctuation μ is assumed at any instant of time to be a function of $\vec{R} = (x, y, z)$. In Ref. 5 the turbulence model was two-dimensional so that sound propagated only in the $x - z$ plane. As will be shown, for computing the average sound pressure level using a single scattering approximation, the two atmospheric models are equivalent.

In Ref. 5 the stochastic wavenumber in Eq. (1) was used directly to calculate "snapshots" of the acoustic field. Here, we want to compute average levels so we need the autocorrelation function for μ. The autocorrelation function is defined by

$$C(\vec{S}) \equiv \langle \mu(\vec{R} + \vec{S})\mu(\vec{R}) \rangle \quad , \tag{3}$$

where $\langle\rangle$ denotes an ensemble average over many realizations of μ. (We assume an ensemble average and time average are equivalent.) For small-scale turbulence near the ground, $C(\vec{S})$ can be approximated by a Gaussian autocorrelation function of the form

$$C(\vec{S}) = \mu_0^2 e^{-(S_x^2/l_x^2 + S_y^2/l_y^2 + S_z^2/l_z^2)} \quad , \tag{4}$$

where μ_0 is the root-mean-square value of μ, and l_x, l_y, and l_z are the correlation lengths in the x, y and z directions, respectively. In numerical calculations isotropic turbulence was assumed ($l_x = l_y = l_z = l$). The input values for μ_0 and l ($\mu_0 = 1.42$ x 10^{-3}, and $l = 1.1$ m) were taken from measurements reported by Daigle.[8]

B. Ground impedance model

The ground was modeled as a flat, locally reacting plane with an angle-independent complex impedance. Impedance values were obtained from the empirical formulas of Delaney and Bazley[9] using an effective flow resistivity of 300 rayls/cm. The resulting impedance values were $7.19 + i8.20$ and $5.17 + i5.57$ at 424 Hz and 848 Hz, respectively.

C. Distorted-wave Born approximation (DWBA) calculations

We consider a point source with angular frequency ω in a turbulent atmosphere. At a particular instant in time the solution for a point source (Green's function) in a turbulent atmosphere satisfies

$$\nabla^2 G(\vec{R}, \vec{R}') + k_0^2 (n_d + \mu)^2 G(\vec{R}, \vec{R}') = -4\pi\delta(\vec{R} - \vec{R}') \quad , \tag{5}$$

where $\vec{R}'$ is the source location, and $\vec{R}$ is the receiver location. In the absence of turbulence ($\mu = 0$) the Green's function G_0 is given by

$$\nabla^2 G_0(\vec{R}, \vec{R}') + k_0^2 n_d^2 G_0(\vec{R}, \vec{R}') = -4\pi\delta(\vec{R} - \vec{R}') \quad , \tag{6}$$

where G_0 is a refracted wave (i.e., a distorted wave) if n_d varies with height. In this section we shall consider both an undistorted spherical wave and a wave distorted by upward refraction.

An integral equation for G which goes to G_0 in the absence of turbulence can be written as

$$G(\vec{R},\vec{R}') = G_0(\vec{R},\vec{R}') + \frac{1}{4\pi}\int G_0(\vec{R},\vec{R}'')\delta k^2(\vec{R}'')G(\vec{R}'',\vec{R}')d^3\vec{R}'' \quad , \tag{7}$$

where $\delta k^2 = k_0^2(n_d+\mu)^2 - k_0^2 n_d^2 \cong 2\mu k_0^2$, since $n_d \cong 1$ and $\mu \ll 1$.

Equation (7) allows us to write the total solution, G, as the solution in the absence of turbulence, G_0, plus an integral which gives the turbulent contribution. However, since the unknown G appears in the integral, Eq.(7) is as difficult to solve exactly as is the original differential equation. When δk^2 is "small enough" the full solution G that appears in the integral can be approximated by G_0. The approximation $G \cong G_0$ is generally known as the "Born approximation". When G_0 is a refracted wave the approximation is often called the "distorted-wave Born approximation" or "DWBA."[7]

Writing the turbulent contribution as δG , using $G \cong G_0$, and $\delta k^2 \cong 2\mu k_0^2$ we have

$$\delta G = \frac{k_0^2}{2\pi}\int G_0(\vec{R},\vec{R}'')\mu(\vec{R}'')G_0(\vec{R}'',\vec{R}')d^3\vec{R}'' \quad . \tag{8}$$

We want to calculate the time average of $|G|^2$, which we assume is the same as an ensemble average. Denoting the average value of $|G|^2$ as $\langle|G|^2\rangle$ and assuming a random phase between G and δG we have

$$\langle|\,G\,|^2\rangle = \langle|\,G_0\,|^2\rangle + \langle|\,\delta G\,|^2\rangle \quad , \tag{9}$$

where

$$\begin{aligned}\langle|\,\delta G\,|^2\rangle = \frac{k_0^4}{4\pi^2}\int & G_0^*(\vec{R},\vec{R}''')G_0^*(\vec{R}''',\vec{R}')\langle\mu(\vec{R}''')\mu(\vec{R}'')\rangle \\ & \times G_0(\vec{R},\vec{R}'')G_0(\vec{R}'',\vec{R}')d^3\vec{R}'''d^3\vec{R}'' \quad .\end{aligned} \tag{10}$$

Now $\langle\mu(\vec{R}''')\mu(\vec{R}'')\rangle = C(\vec{S})$ where C is the autocorrelation function and $\vec{S} = \vec{R}''' - \vec{R}''$. Transforming from the variables ($\vec{R}''$, $\vec{R}'''$) to the variables ($\vec{R}''$, $\vec{S}$) gives

$$\begin{aligned}\langle|\,\delta G\,|^2\rangle = \frac{k_0^4}{4\pi}\int & G_0^*(\vec{R},\vec{R}''+\vec{S})G_0^*(\vec{R}''+\vec{S},\vec{R}')C(\vec{S}) \\ & \times G_0(\vec{R},\vec{R}'')G_0(\vec{R}'',\vec{R}')d^3\vec{S}\;d^3\vec{R}'' \quad .\end{aligned} \tag{11}$$

For the sake of illustration we first consider an undistorted spherical wave in free space, i.e., we take $G_0(\vec{R},\vec{R}'') = \exp(ik_0|\vec{R}-\vec{R}''|)/|\vec{R}-\vec{R}''|$. For $|\vec{R}'| = 0$ (source at the origin) and $|\vec{R}''| >> |\vec{S}|$, the Green's function $G_0(\vec{R}''+\vec{S},\vec{R}'=0)$ can be approximated as

$$G_0(\vec{R}''+\vec{S},\vec{R}'=0) \cong \frac{e^{ik_0|\vec{R}''|}}{|\vec{R}''|}e^{i\vec{k}\cdot\vec{S}} \quad , \tag{12}$$

where the $\vec{k} = k_0\hat{n}$, and $\hat{n} = (\vec{R}''/|\vec{R}''|)$. Similarly the Green's function $G_0(\vec{R},\vec{R}''+\vec{S})$ can be approximated as

$$G_0(\vec{R},\vec{R}''+\vec{S}) \cong \frac{e^{ik_0|\vec{R}-\vec{R}''|}}{|\vec{R}-\vec{R}''|}e^{-i\vec{k}'\cdot\vec{S}} \quad , \tag{13}$$

where $\vec{k}' = k_0\hat{n}'$, and $\hat{n}' = (\vec{R}-\vec{R}'')/|(\vec{R}-\vec{R}'')|$. With these approximations for the free-space Green's functions, we have

$$\langle|\,\delta G\,|^2\rangle = \frac{k_0^4}{4\pi^2}\int \frac{1}{|\vec{R}''|^2}\frac{1}{|\vec{R}-\vec{R}''|^2}e^{i(\vec{k}'-\vec{k})\cdot\vec{S}}C(\vec{S})d^3\vec{S}d^3\vec{R}'' \quad . \tag{14}$$

We now define a scattering function $\sigma(\vec{q})$ as

$$\sigma(\vec{q}) \equiv \int e^{i\vec{q}\cdot\vec{S}}C(\vec{S})d^3\vec{S} \quad , \tag{15}$$

where $\vec{q} = \vec{k}' - \vec{k}$. Then Eq. (14) becomes

$$\langle|\,\delta G\,|^2\rangle = \frac{k_0^4}{4\pi^2}\int \frac{1}{|\vec{R}''|^2}\sigma(\vec{q})\frac{1}{|\vec{R}-\vec{R}''|^2}d^3\vec{R}'' \quad . \tag{16}$$

In Eq. (16) we can identify $1/|\vec{R}''|^2$ as the sound intensity I_{inc} incident on the scattering volume and $1/|\vec{R}-\vec{R}''|^2$ as the scattered intensity I_{scat} that reaches the receiver. Hence we can write

$$\langle|\,\delta G\,|^2\rangle = \frac{k_0^4}{4\pi^2}\int I_{inc}(\vec{R}'')\sigma(\vec{q})I_{scat}(\vec{R}'')d^3\vec{R}'' \quad . \tag{17}$$

Equation (17) has a useful physical interpretation (see Fig. 4). The average intensity of the sound reaching the receiver from a particular volume of space is proportional to the product of the incident intensity reaching the volume, the scattering strength of the volume, and the scattered intensity. The Appendix gives an analytic result for Eq. (17) for small-angle scattering.

In order to take upward refraction into account we use the following prescription: In Eq. (17) we replace the incident intensity $I_{inc} = 1/|\vec{R}''|^2$ and the scattered intensity $I_{inc} = 1/|\vec{R} - \vec{R}''|^2$ with $I_{inc} = |G_{PE}(\vec{R}'')|^2$ and $I_{scat} = |G_{PE}(\vec{R}, \vec{R}'')|^2$, respectively, where G_{PE} denotes the Green's function without turbulence computed using the parabolic equation method described in Refs. 5 and 10. Writing the integrals in Cartesian coordinates we have

$$\begin{aligned} \langle \mid \delta G \mid^2 \rangle &= \frac{k_0^4}{4\pi^2} \int \mid G_{PE}(\vec{R}'')^2 \mid G_{PE}(\vec{R}, \vec{R}'') \mid^2 \\ &\times \exp\left[i(q_x S_x + q_y S_y + q_z S_z)\right] C(S_x, S_y, S_z) dx'' dy'' dz'' dS_x dS_y dS_z \quad . \end{aligned} \tag{18}$$

Since G_{PE} is azimuthally symmetric and $|\vec{R}''| >> |\vec{S}|$, we neglect the y-dependence in G_{PE} and integrate $\exp(iq_y S_y)$ over y and obtain the δ-function result obtained in the Appendix. (See Eqs. (A2) - (A4).) Also we set $q_x = 0$, as in the Appendix, and obtain

$$\begin{aligned} \langle \mid \delta G \mid^2 \rangle &= \frac{1}{x} \frac{k_0^3}{2\pi} \int x''(x - x'') \mid G_{PE}(\vec{R}'') \mid^2 \mid G_{PE}(\vec{R}, \vec{R}'') \mid^2 \\ &\times e^{iq_z S_z} C(S_x, 0, S_z) dS_x dS_z dx'' dz'' \quad . \end{aligned} \tag{19}$$

Using the general Gaussian autocorrelation function in Eq.(4) for the integrations over S_x and S_z, we have

$$\begin{aligned} \langle \mid \delta G \mid^2 \rangle &= \frac{\mu_0^2 k_0^3 l_x l_z}{2x} \int x''(x - x'') \mid G_{PE}(x'', z'') \mid^2 \\ &\times \mid G_{PE}(x, z; x'', z'') \mid^2 e^{-q_z^2 l_z^2/4} dx'' dz'' \quad . \end{aligned} \tag{20}$$

In the parabolic equation method the quantity actually solved for is $\Psi(r, z)$, where $G_{PE}(r, z) = [\exp(ik_0 r)/\sqrt{r}\ ]\Psi(r, z)$, and $r = \sqrt{x^2 + y^2}$. Since the integral is now two-dimensional, we can set y to zero and let $r = x$. Then in terms of $\Psi(x, z)$ we have

$$\begin{aligned} \langle \mid \delta G \mid^2 \rangle &= \frac{\mu_0^2 k_0^3 l_x l_z}{2x} \int \mid \Psi(x'', \ z'') \mid^2 \mid \Psi(x - x''; z, z'') \mid^2 \\ &\times e^{-q_z^2 l_z^2/4} dx'' dz'' \quad . \end{aligned} \tag{21}$$

In the numerical calculations we assumed the turbulence to be isotropic with a correlation length l. Hence we have finally

$$\begin{aligned} \langle \mid \delta G \mid^2 \rangle &= \frac{\mu_0^2 k_0^3 l^2}{2x} \int \mid \Psi(x'', z''); \ z, \ z'' \mid^2 \mid \Psi(x - x''; z, z'') \mid^2 \\ &\times e^{-q_z^2 l^2/4} dx'' dz'' \quad , \end{aligned} \tag{22}$$

where x'' goes from zero to x, and z'' goes from zero to infinity.

II. NUMERICAL CALCULATIONS

A. Comparison of DWBA calculations with PE calculations and with experiment

In Fig. 3 the DWBA calculations and the PE calculations are compared to each other and to the data of Weiner and Keast. The data is for octave bands of random noise between 300-600 Hz and 600-1200 Hz, respectively. In both the DWBA and the PE calculations, the frequency was taken to be $\sqrt{f_1 f_2}$ where f_1 and f_2 are the lowest and highest frequencies, respectively, in the octave bands considered. Section I gives the parameters for the atmospheric model and the ground impedance model used in the calculations. Note that the DWBA calculations and the data are for the average relative sound pressure level while the PE calculations are a "snapshot" of the relative sound-pressure level and not the average level. However, the trend in a particular PE calculation is generally fairly close to the average level predicted by the corresponding DWBA calculation.

The DWBA calculations, which include only single scattering from turbulence, give a good approximation to the average PE levels in all cases except for upwind propagation at 848 Hz. For upwind propagation at 848 Hz, the DWBA prediction deep in the shadow zone is much below both the PE and the data.

B. Discussion of numerical results

Some of the features of the curves in Fig. 3 can be understood in a straightforward way using the DWBA calculations. The deterministic (no turbulence) part of the Green's function is G_0 and the stochastic part due to turbulence is δG. Near the source (regions 1 and 2 in Fig. 1) we have $\mid G_0 \mid^2 \gg \langle \mid \delta G \mid^2 \rangle$ while at long ranges (region 3 in Fig.1) we have just the reverse. Consequently, near the source, the shape of a given curve for relative sound pressure level versus range is governed by the deterministic sound-speed profile so the level is essentially what one would obtain from a calculation without turbulence.

Since we have $\mid G_0 \mid^2 \ll \langle \mid \delta G \mid^2 \rangle$ at long range, the relative sound pressure level is due almost entirely to scattering from turbulence. In order to understand the long-range behavior of the curves in Fig. 3 we must make a more detailed analysis than was required at short range. As shown in the Appendix, the contribution to the relative sound pressure level from turbulence scattering in free space (with no refraction) diverges as the logarithm of the range. We expect similar behavior even with upward refraction over a finite impedance plane. Consider the situation in Fig. 4 where we have a scattering volume with an incident intensity I_{inc} and a scattered intensity I_{scat}. The sound intensity incident on the scattering volume is proportional to $1/r^2$ where r is the horizontal range to the receiver. The scattering volume itself is proportional to r^3. The scattered intensity reaching the receiver from the scattering volume, like the incident intensity, is proportional to $1/r^2$. For a fixed scattering angle, the average scattered intensity from the volume is thus proportional to $(1/r^2) \times (r^3) \times (1/r^2) = 1/r$. Hence, as shown in Eq. (A9), we expect the relative sound pressure level to increase as the logarithm of the horizontal range. This behavior at long range is seen in the DWBA calculation for crosswind propagation (weak upward refraction) at 424 Hz. When there is significant upward refraction the height of the scattering volume is not proportional to the range but increases more rapidly than linearly with range. As a result, the scattering angle is not fixed but

increases with increasing range. Since the scattered intensity is reduced at larger scattering angles, the relative sound pressure level versus range is "flattened" so that a nearly constant relative sound pressure level is reached at long ranges. Because of the flattening effect caused by an increasing scattering angle, a nearly constant relative sound pressure level is seen in the DWBA calculation for upwind propagation (strong upward refraction) at 424 Hz. A similar behavior is seen for crosswind propagation (weak upward refraction) at 848 Hz. The flattening effect with weak upward refraction at 848 Hz is apparently due to the greater sensitivity to the scattering angle at the higher frequency.

The DWBA calculation for upwind propagation (strong upward refraction) at 848 Hz falls off in the shadow zone much more rapidly than the PE calculation and the data. The major computational difference between the two calculations is that the PE calculation includes multiple scattering while the DWBA calculation does not. Hence the disagreement indicates that for upwind propagation at 848 Hz, multiple scattering is important. This interpretation is supported by a gray-scale plot for this case which shows the skywave greatly modified by turbulence so that the approximation $G \cong G_0$ is not valid.

III. SUMMARY AND CONCLUSIONS

We have compared distorted-wave Born approximation (DWBA) calculations to parabolic equation (PE) calculations and to the data of Wiener and Keast. In all cases except one, the DWBA calculations, which include only single scattering, predicted the step-function behavior of the relative sound pressure level versus range seen in both the data and the PE calculations. The important conclusion to be reached is that, in the presence of upward refraction, single scattering can give a relative sound pressure level that does not diverge as the logarithm of the range but rather is nearly constant at long range. Hence, in all cases except one, the observed step function can be understood in terms of single scattering from an upward-refracted skywave.

For upwind propagation (strong upward refraction) at 848 Hz, the DWBA calculation grossly underestimated both the data and the PE calculation. In this case, the single scattering approximation $G \cong G_0$ was not valid in the skywave. To accurately predict multiple scattering of sound into the shadow zone, one must have a good predictive model for sound propagation in the skywave itself. Hence, it would be valuable to have measurements not only for the sound scattered into the refractive shadow, but also for the sound field in the skywave.

APPENDIX: ANALYTIC EXPRESSION FOR FREE-SPACE SCATTERING FROM ANISOTROPIC TURBULENCE

To see the general behavior of Eq. (17) we can consider weak small-angle scattering in free space . For weak small-angle scattering we can use the Born approximation and obtain an analytic result for anisotropic turbulence.

For small angle scattering we can let $1/|\vec{R}''|^2 \cong 1/x''^2$ and $1/|\vec{R} - \vec{R}''|^2 \cong 1/(x - x'')^2$. We could integrate Eq. (17) directly using a particular autocorrelation function such as a Gaussian. However, to obtain a more general result that does not assume any particular autocorrelation function, it is convenient to return to the form in Eq. (14) which is written in terms of the autocorrelation function $C(S_x, S_y, S_z)$,

$$\langle | \delta G |^2 \rangle = \frac{k_0^4}{4\pi^2} \int \frac{1}{x''^2} \frac{1}{(x - x'')^2} e^{i(q_x S_x + q_y S_y + q_z S_z)} C(S_x, S_y, S_z)\, dx''\, dy''\, dz''\, dS_x\, dS_y\, dS_z \quad . \tag{A1}$$

For small angles we can approximate q_z as

$$\begin{aligned} q_z &\cong k_0 \left(\frac{1}{x''} + \frac{1}{x - x''}\right) z'' \\ &= k_0 \left[\frac{x}{x''(x - x'')}\right] z'' \quad . \end{aligned} \tag{A2}$$

Similarly,

$$q_y \cong k_0 \left[\frac{x}{x''(x - x'')}\right] y'' \quad . \tag{A3}$$

We now consider the integral over z'':

$$\begin{aligned} \int_{-\infty}^{+\infty} e^{iS_z k_0 [x/x''(x-x'')] z''}\, dz'' &= 2\pi\, \delta\left[k_0 \frac{x}{x''(x - x'')} S_z\right] \\ &= \frac{2\pi}{k_0} \frac{x''(x - x'')}{x} \delta(S_z) \quad . \end{aligned} \tag{A4}$$

The integral over y'' gives a similar result with S_z replaced by S_y. Inserting the results from integrating over z'' and y'' into Eq. (A1) and integrating over S_z and S_y, we have

$$\langle | \delta G |^2 \rangle = \frac{k_0^2}{x^2} \int e^{iq_x S_x} C(S_x, 0, 0)\, dx''\, dS_x \quad . \tag{A5}$$

We could integrate over S_x and define a special scattering function

$\sigma_{00} = \int C(S_x, 0, 0) \exp(iq_x S_x) dS_x$. However, we are considering small-angle propagation. Hence $\vec{q}$ is almost perpendicular to the propagation direction and we can therefore set q_x to zero. Thus, integrating in the region between the source and receiver we have

$$\begin{aligned} \langle | \delta G |^2 \rangle &= \frac{k_0^2}{x^2} \int_{-\infty}^{\infty} C(S_x,\ O,\ O)\ dS_x \int_0^x dx'' \\ &= \frac{k_0^2}{x} C_{00} \quad , \end{aligned} \tag{A6}$$

where

$$C_{00} = \int_{-\infty}^{\infty} C(S_x,\ O,\ O) dS_x \quad . \tag{A7}$$

For anisotropic turbulence having a Gaussian autocorrelation function (See Eq.(4)) we obtain

$$\langle | \delta G |^2 \rangle = \sqrt{\pi}\ \mu_0^2\ k_0^2\ l_x / x \quad . \tag{A8}$$

Thus for weak small-angle scattering in free space, the scattering due to turbulence falls off inversely with the range and depends on the correlation length only in the direction of propagation. Note that, written in terms of the relative sound pressure level (RSPL), the contribution from turbulence scattering diverges as the logarithm of the range.

$$\begin{aligned} RSPL &= 10 \log_{10} (x^2 \langle | \delta G |^2 \rangle) \\ &= 10 \log_{10} (\sqrt{\pi} \mu_0^2\ k_0^2\ l_x) + 10 \log_{10} (x) \quad . \end{aligned} \tag{A9}$$

REFERENCES

1. F. M. Weiner and D. N. Keast, "Experimental study of the propagation of sound over ground," J. Acoust. Soc. Am. **31**, 724-733 (1959).

2. P. H. Parkin and W. E. Scholes, "The horizontal propagation of sound from a jet engine close to the ground at Radlett," J. Sound. Vib. **1** (4), 1-13 (1964).

3. P. H. Parkin and W. E. Scholes, "The horizontal propagation of sound from a jet engine close to the ground at Hatfield," J. Sound.Vib. **2** (4), 353-374 (1965).

4. Reference 1 above reports the negative of the relative sound pressure level (excess attenuation). The relative sound pressure level in Ref. 1 is the level corrected for spherical spreading and atmospheric absorption and adjusted to be O dB at 30.5 m (100 ft.). We assume this level is the same as the sound pressure level relative to a free field.

5. K. E. Gilbert, R. Raspet, and X. Di, "Calculation of turbulence effects in an upward refracting atmosphere," J. Acoust. Soc. Am. **87**, 2428-2437 (1990).

6. J.E. Piercy, T.F.W. Embleton, and L.C. Sutherland, "Review of noise propagation in the atmosphere, " J. Acoust. Soc. Amer. **61**, 1403-1418 (1977).

7. L. S. Rodberg and Roy M. Thaler, *Introduction to the Quantum Theory of Scattering* (Academic Press, New York, 1967).

8. G.A. Daigle, "Effects of atmospheric turbulence on the interference of sound waves above a hard boundary," J. Acoust. Soc Amer. **64**, 622-630 (1978).

9. M.E. Delany and E.N. Bazley, "Acoustical properties of fibrous absorbent materials," Appl. Acoust. **3**, 105-116 (1970).

10. K.E. Gilbert and M.J. White, "Application of the parabolic equation to sound propagation in a refracting atmosphere," J. Acoust. Soc. Amer. **85**, 630-637 (1989).

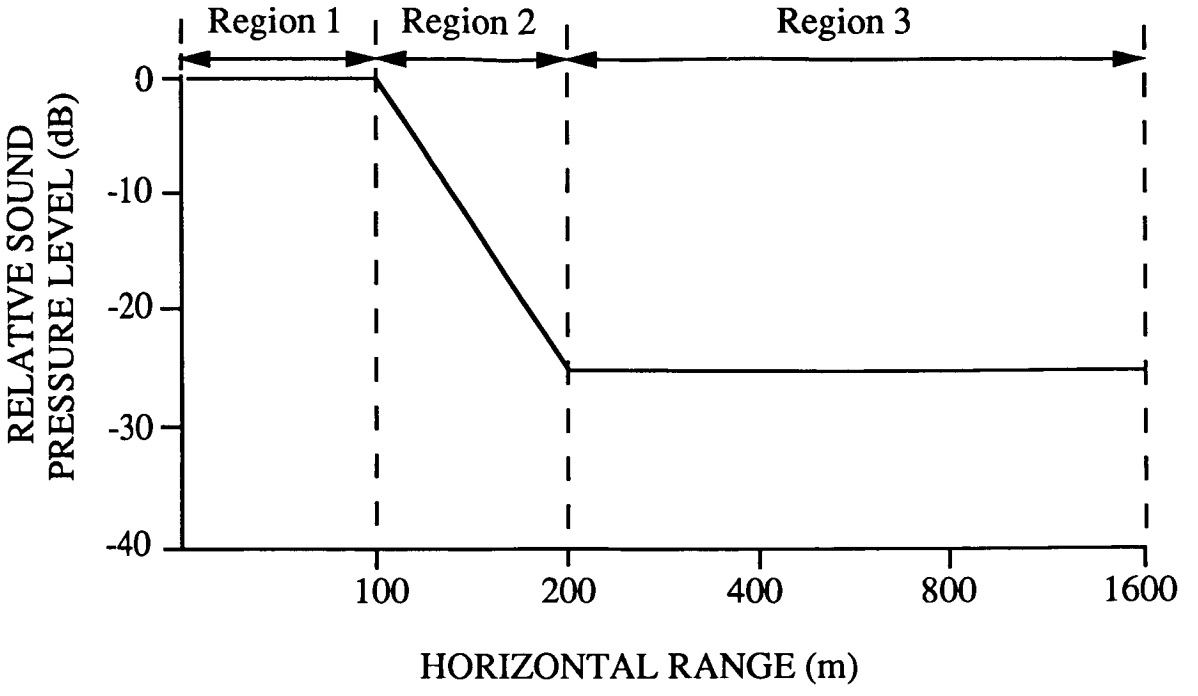

Fig. 1. Characteristic "step" function for the relative sound pressure level versus range for sound propagation in an upward-refracting atmosphere. (From Gilbert et al.[5])

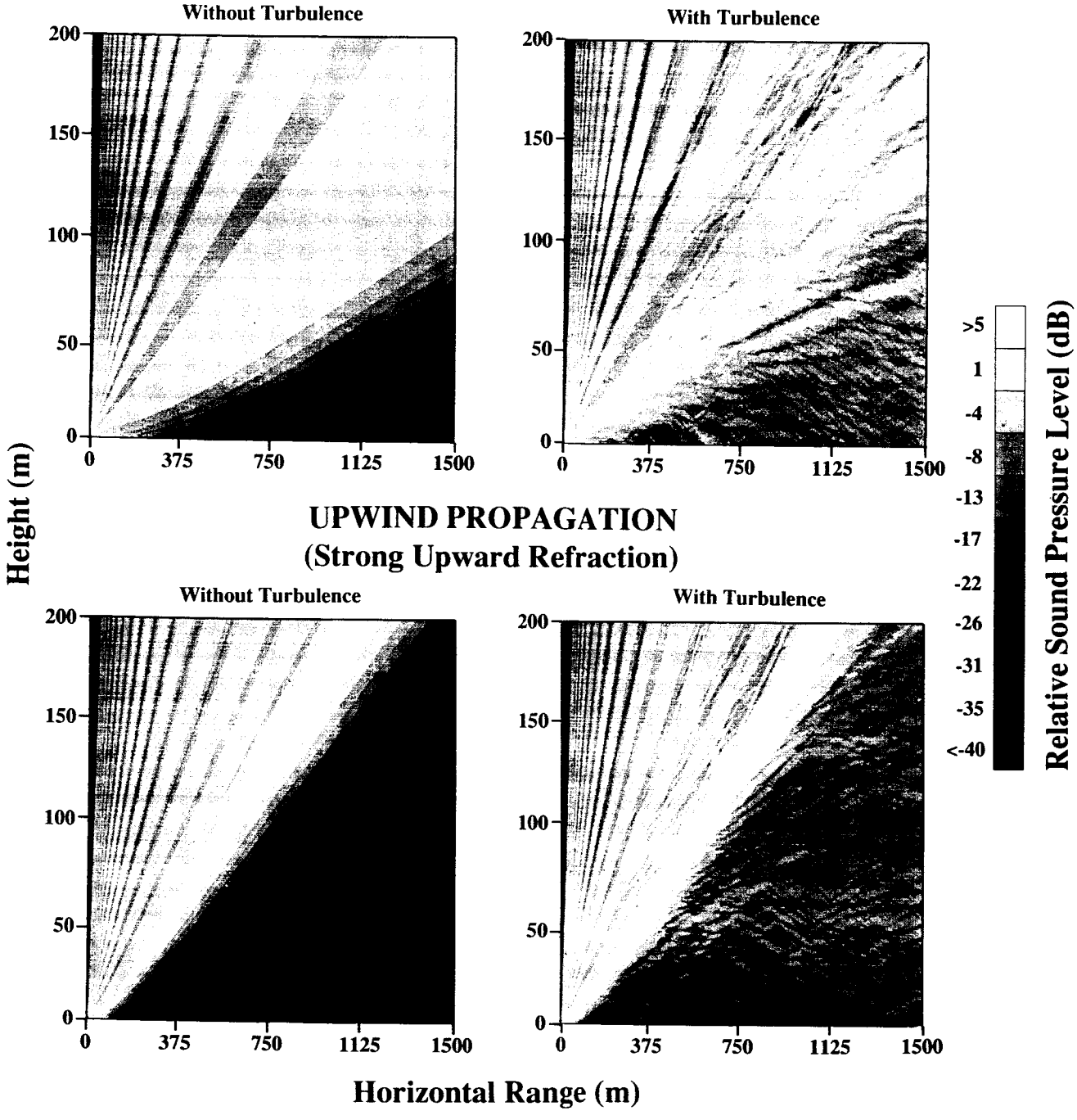

Fig. 2. Gray-scale plots of relative sound pressure level versus height and horizontal range for a non-turbulent atmosphere and a turbulent atmosphere. The frequency is 424 Hz, and the source height is 3.7 m (12 ft). Parameters for the atmospheric model and ground impedance model are given in the text. (From Gilbert et al.[5])

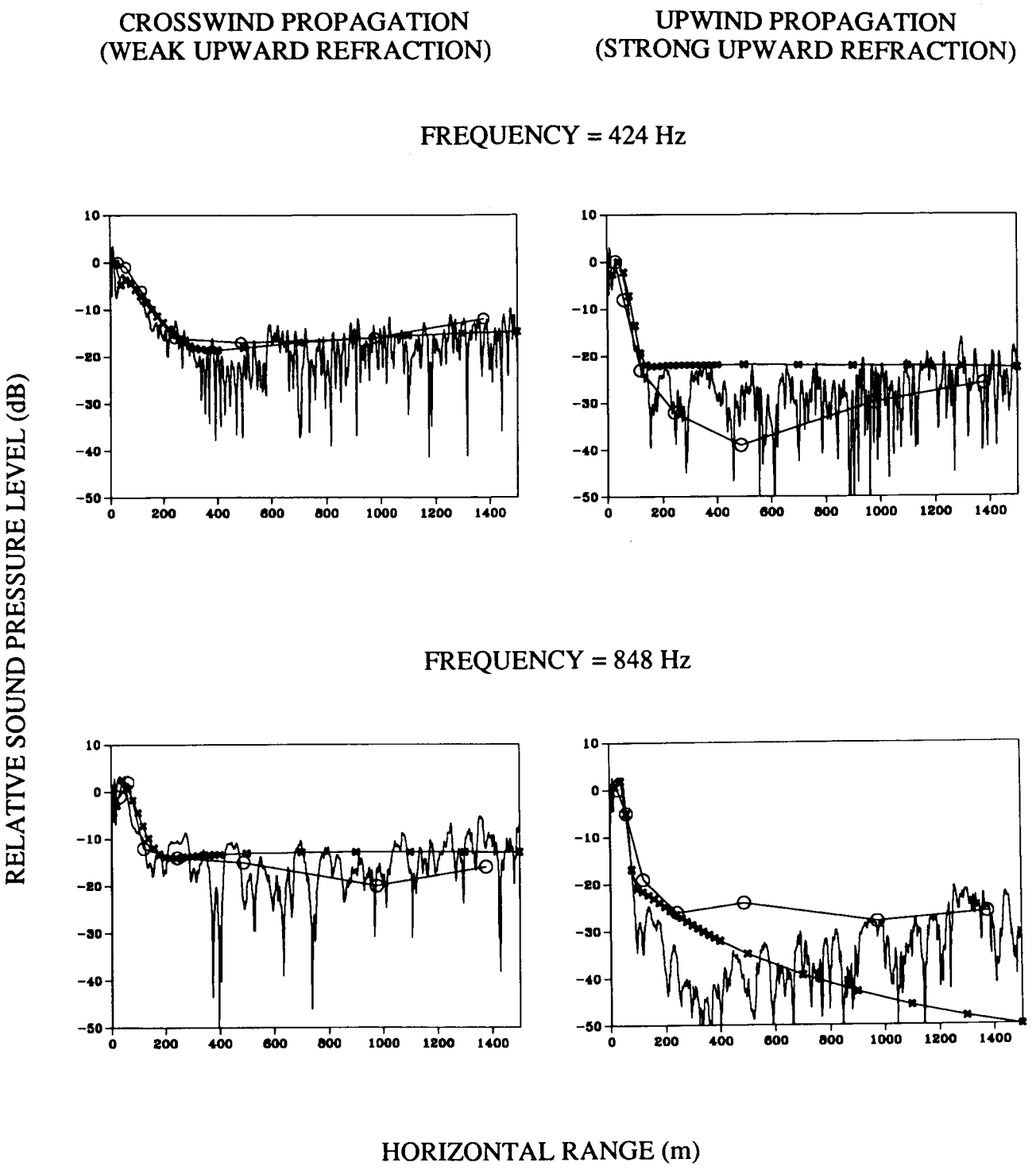

Fig. 3. Relative sound pressure level versus horizontal range for a refracting, turbulent atmosphere. The connected circles are the data of Weiner and Keast.[1] The solid lines are parabolic equation results from Ref. 5. The connected x's are distorted-wave Born approximation calculations. Parameters for the atmospheric model and ground impedance model are given in the text.

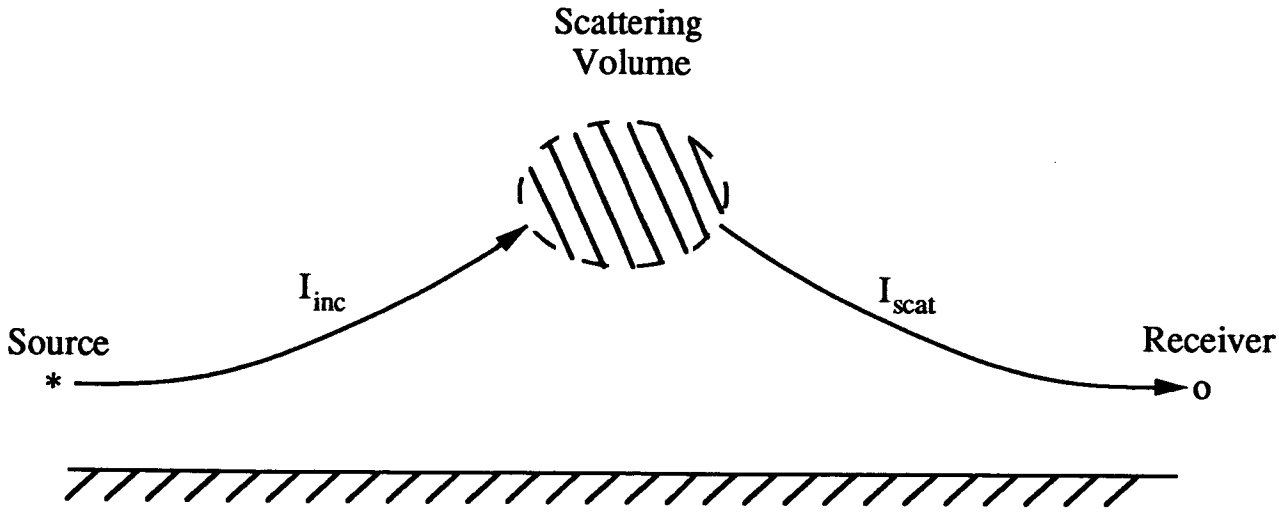

Fig. 4. Schematic representation of scattering from turbulence. The quantity I_{inc} is the average intensity incident on a particular scattering volume, and I_{scat} is the average scattered intensity. The total scattered intensity is obtained by integrating over the volume between the source and receiver.

WAVE PROPAGATION THROUGH RANDOM MEDIA:

A Local Method of Small Perturbations based on the Helmholtz Equation

Ralf Große, Universität Oldenburg, Postfach 2503, D-2900 Oldenburg, FRG

1 Introduction

Propagation of sound through the turbulent atmosphere is a statistical problem. The randomness of the refractive index field causes sound pressure fluctuations. Although no general theory to predict sound pressure statistics from given refractive index statistics exists, there are several approximate solutions to the problem. The most common approximation is the parabolic equation method. Results obtained by this method are restricted to small refractive index fluctuations and to small wave lengths. While the first condition is generally met in the atmosphere, it is desirable to overcome the second. This paper presents a generalization of the parabolic equation method with respect to the small wave length restriction.

2 Parabolic Equation Method

For the small wave length limit[1] the Helmholtz equation can be converted into a parabolic form (main propagation direction $\vec{e}_z$) /1/:

$$\left(2ik\frac{\partial}{\partial z} + \frac{\partial^2}{\partial x^2} + \frac{\partial^2}{\partial y^2} + k^2\mu(\vec{r})\right) \quad \psi(\vec{r}) = 0 \tag{1}$$

k = *wave number;* μ = *refractive index deviation;* ψ = *complex sound pressure*

The refractive index deviation μ is considered as a random function. Therefore equation (1) is a stochastic differential equation and the sound pressure ψ becomes a random function, too. Stochastically this equation is nonlinear, e.g. it contains a product of two random variables. For this reason the stochastic parabolic equation cannot be solved exactly. Further approximations are necessary. Several mathematical tools were applied to remove the stochastical nonlinearity, i.e. path integrals /2/, functional derivatives /3/, perturbation expansion methods /1/. Despite approximations used in the calculations looking different, the results are all the same.

The physical meaning of all these approximations becomes evident in the *local method of small perturbations* /1/. By this method the scattering volume is divided into slabs perpendicular to the main propagation direction. Each slab is chosen as thin as required by the validity limit of the first order perturbation expansion term (single scattering approximation, Born approximation). This distance clearly depends on the strength of the refractive index fluctuations. If these fluctuations are sufficiently small, the slabs are much thicker than one correlation length of the random medium. Therefore the slabs can be regarded as uncorrelated. Based on both assumptions - small refractive index fluctuations and a small wave length compared to the correlation length - the statistical independence of subsequent slabs can be proofed mathematically. Wave propagation through random media is described here as a Markov process.

[1]The wave length must be small compared to the size of a typical inhomogeneity of the medium. In statistical terms this size is expressed by the correlation length of the refractive index autocorrelation- function.

As a consequence of the Markov property slabs of finite thickness are no longer necessary. This results in a differential equation for the mean sound pressure which is linear in the stochastical sense as well[2]/1/:

$$\left(2ik\frac{\partial}{\partial z}+\frac{\partial^2}{\partial x^2}+\frac{\partial^2}{\partial y^2}+2ik\alpha\right) \; <\psi(\vec{r})>=0 \tag{2}$$

$$\alpha=\frac{<\mu^2>\, k^2 l}{4} \tag{3}$$

l = *correlation length*

Equation (2) can be solved easily:

$$<\psi(\vec{r})>=\psi_0(\vec{r})\; exp\{-\alpha z\} \tag{4}$$

ψ_0 = *free propagated incident wave*

The mean complex sound pressure decreases exponentially while the wave propagates through the random medium. This is an effect of decorrelation of the sound wave due to phase fluctuations. Different members of the statistical assembly interfere destructively because of their different phases.

The validity of result (4) - and of any other result obtained by the parabolic equation method - is restricted first by the validity of the parabolic wave equation (1) and second by the validity of the Markov assumption. Necessary conditions are the smallness of refractive index fluctuations and the smallness of the wave length (compared with the correlation length). In the next section the first condition is also assumed to be true. The small wave length assumption, however, will be replaced by the weaker condition of negligible backscattering. This will lead to a generalized Markov process and, consequently, to generalized results with respect to the wave length - correlation length ratio.

3 Generalized Local Method of Small Perturbations

While generalizing the parabolic equation method the main idea of the local method of small perturbations will be retained. The refractive index fluctuations are assumed to be small enough to justify the application of a single scattering approximation within a distance Δz in the scattering volume which is large compared to the correlation length. Again the scattering volume is divided into slabs of this size. Therefore subsequent slabs are uncorrelated as well. But contrary to the parabolic equation method the contribution of one slab will not be calculated from the parabolic equation but from the Helmholtz equation:

$$\left(\Delta+k^2(1+\mu(\vec{r}))\right)\; \psi(\vec{r})=0 \tag{5}$$

Δ = *Laplace operator*

Neglecting backscattering[3] yields a difference equation for the mean sound pressure:

$$<\psi(\vec{\rho}_n, n\Delta z)>=\left(\hat{G}_0+\hat{S}\right) \; <\psi(\vec{\rho}_{n-1},(n-1)\Delta z)> \tag{6}$$

[2]It is possible to derive similar equations for the higher statistical moments of ψ by the parabolic equation method, too. Only the first moment equation and its solution are presented here in order to compare them with the generalized results derived in section 3 of this paper. The decorrelation coeffecient α is calculated for an exponential autocorrelation function for comparison, too.

[3]Neglecting of backscattering is not an *assumption* of the parabolic equation method but a *consequence* of the small wave length limit. The parabolic equation implies that there are small scattering angles only and no backscattering at all.

$\vec{\rho} = (x, y)$; n = *number of slab*

$\hat{G}_0$ is the integral operator of the homogeneous Helmholtz equation ($\mu = 0$, free propagation) and $\hat{S}$ is an integral operator for the scattering within one slab. Since double scattering is the lowest order non-vanishing term, the kernel of $\hat{S}$ contains the autocorrelation function of the refractive index field:

$$\hat{S}\,(\vec{r}_n, \vec{r}) < \psi(\vec{r}) >= -k^4 \int d^3\vec{r}' \int d^3\vec{r}\, G(\vec{r}_n, \vec{r}')G(\vec{r}', \vec{r}) < \mu(\vec{r}')\mu(\vec{r}) > < \psi(\vec{r}) > \tag{7}$$

G = *Greens function of the Helmholtz equation*

The solving of equation (6) is somewhat different from that of the related parabolic equation problem. Here no wave length approximation helps to calculate the integrals. But for the case of a homogeneous refractive index autocorrelation function, equation (7) becomes a convolution product. It can be Fourier-transformed with respect to the variable $\vec{\rho}$, and this operation turns the operators $\hat{S}$ and $\hat{G}_0$ into simple functions $\tilde{S}$ and $\tilde{G}_0$. In the Fourier representation equation (6) reads:

$$<\tilde{\psi}\,(\vec{\kappa}, n\Delta z) >= \left(\tilde{G}_0 + \tilde{S}\right) <\tilde{\psi}\,(\vec{\kappa}, (n-1)\Delta z) > \tag{8}$$

$\vec{\kappa}$ = *2-dimensional spatial frequency*

By Fourier-transformation the $\vec{\rho}$-integrations are already performed and only the z-integrations are left. They can be performed, too, if the z-dependence of the medium autocorrelation function is known. For the sake of simplicity this dependence is assumed to be exponential[4]. After z-integration the scattering contribution of one slab is seen to be proportional to the slabs thickness Δz. Therefore equation (8) can be written as ($\tilde{S} = \tilde{s}\ \Delta z$):

$$<\tilde{\psi}\,(\vec{\kappa}, n\Delta z) >= \left(\tilde{G}_0 + \tilde{s}\ \Delta z\right) <\tilde{\psi}\,(\vec{\kappa}, (n-1)\Delta z) > \tag{9}$$

The effect of all slabs is obtained by iteration:

$$<\tilde{\psi}\,(\vec{\kappa}, n\Delta z) >= \left(\tilde{G}_0 + \tilde{s}\ \Delta z\right)^n \tilde{\psi}_0\,(\vec{\kappa}, 0) \tag{10}$$

Regarding a sufficiently large number of slabs yields ($z = n\,\Delta z$):

$$<\tilde{\psi}\,(\vec{\kappa}, z) >= \tilde{\psi}_0\,(\vec{\kappa}, z)\ exp\{\tilde{s}\,(\vec{\kappa})\, z\} \tag{11}$$

For the special case of an isotropic exponential autocorrelation function $\tilde{s}$ becomes:

$$\tilde{s}\,(\kappa) = \frac{<\mu^2> k^4}{4aa_l(a_l - a)} \tag{12}$$

$$a = \sqrt{k^2 - \kappa^2} \quad , \quad a_l = \sqrt{(k + i/l)^2 - \kappa^2} \tag{13}$$

To compare (11) and (12) with the corresponding parabolic equation method results (4) and (3), the incident wave ψ_0 is assumed to be a plane one. Then the Fourier-transformation of (11) results in:

[4]For more complicated functions the z-integration can be performed numerically.

$$< \psi(\vec{r}) >= \psi_0(\vec{r})\ exp\{\tilde{s}\ (0)\, z\} \tag{14}$$

$$\tilde{s}\ (0) = \frac{< \mu^2 > k^2 l}{4} \frac{(ikl - k^2 l^2)}{(1 + k^2 l^2)} \tag{15}$$

The real part of $\tilde{s}(0)$ describes the decorrelation of the sound wave. It is a more general expression than (3) - only in the small wave length limit they are equal. Because of $\tilde{s}(0)$ being a complex number, a second effect is predicted by this method, which cannot be seen in the parabolic results. The imaginary part is a stochastic correction to the wave number k due to an increase of the mean propagation distance in the random medium. Only in the small wave length limit the scattering angles are small and the mean propagation distance corresponds to the z-extension of the scattering volume.

4 Conclusions

A generalized form of the local method of small perturbations has been presented in this paper. Working directly from the Helmholtz equation instead of the parabolic equation the *small angle scattering method* was replaced by a *forward scattering method.* By this method only one result was derived here: The first statistical moment of an incident plane wave scattered by a very weakly statistical homogeneous random medium with an exponential autocorrelation function. This result shows corrections to the corresponding parabolic equation method result.

It is possible to apply the method to more complicated problems, i.e. a difference equation for the second statistical moment can be derived by the same idea.

If the medium fluctuations become stronger, the thickness of one slab decreases. The slabs might be thicker than the correlation length, but not as much as assumed before. Then correlations between two slabs have to be taken into account. This leads to difference equations which connect statistical moments not only from one slab to the following, but to the next following, too.

The most valuable advantage of this method might be its suitability for numerical calculations. For any given medium autocorrelation function the scattering function $\tilde{s}$ can be obtained by Fourier-transformation. The incident wave is also Fourier-transformed. Then the algorithm given by equation (9) is applied iteratively until the desired propagation distance is covered. The final result is obtained by Fourier-transformation again.

The author wishes to thank Prof. K. Haubold, Prof. V. Mellert, Dr. M. Schultz-von Glahn and A. Sill for the valuable discussions during the whole work.

References

/1/ *Strohbehn,J.W., Modern theories in the propagation of optical waves in a turbulent medium* in: *Strohbehn,J.W. Laser beam propagation in the atmosphere* Berlin 1978

/2/ *Dashen,R., Path integrals for waves in random media*, J.Math.Phys. (5), 1979, 894–920.

/3/ *Tatarskii,V.I., The effects of the turbulent atmosphere on wave propagation* Jerusalem 1971

A Noise Assessment and Prediction System

Robert O. Olsen and John M. Noble
U.S. Army Atmospheric Sciences Laboratory
ATTN: SLCAS-AS-I
White Sands Missile Range, New Mexico 88002-5501

Abstract

A system has been designed to provide an assessment of noise levels that result from testing activities at Aberdeen Proving Ground, MD. The system receives meteorological data from surface stations and an upper air sounding system. The data from these systems are sent to a meteorological model, which provides forecasting conditions for up to three hours from the test time. The meteorological data are then used as input into an acoustic ray trace model which projects sound level contours onto a two dimensional display of the surrounding area. This information is sent to the meteorological office for verification, as well as the range control office, and the environmental office. To evaluate the noise level predictions, a series of microphones are located off the reservation to receive the sound and transmit this information back to the central display unit. The computer models are modular allowing for a variety of models to be utilized and tested to achieve the best agreement with data. This technique of prediction and model validation will be used to improve the noise assessment system.

Introduction

The U.S. Army has an active testing program for munitions and weapons located at Aberdeen Proving Ground, MD (APG). The results of these tests can cause high sound levels to impact on the local community. This problem has existed for a long period of time, but recently it has become more acute because of the development of the local communities adjacent to the Proving Ground. APG is actively engaged in a number of different programs to alleviate the noise problem. One of the approaches to mitigate noise complaints is to be able to better indicate when conditions could enhance the sound propagation at long distances due to the atmospheric structure. As a result of these concerns, the Noise Assessment and Prediction System (NAPS) was proposed utilizing sensors, models, and computers to predict the noise levels that might be encountered at an off-range site as a result of a particular test.

Objective and Approach

The objective of the NAPS development is to create an operational system for predicting noise intensities based upon present and forecasted diurnal meteorological conditions. The reason for specifying diurnal conditions is to limit the meteorological model to only those conditions that change with solar input. The meteorological model will not be used to forecast synoptic conditions, passage of fronts, etc; synoptic scale conditions accounted for utilizing standard weather forecast techniques and tools.

The NAPS development approach is to modify and adapt existing acoustic and meteorological prediction models for this noise prediction problem. The aim is to be able to have these models operate on a PC located at the meteorological office, providing the information to the various range offices responsible for testing. In order to provide timely information to the users, the results of the noise predictions will be made available to users every 15 to 20 minutes. Users will have an assessment of the current conditions and how they may vary within the next three hours.

These criteria required that both the acoustic and meteorological models be compact with short execution times in order to meet the required specifications. Therefore, it was initially decided to utilize a standard ray trace model[1,2] with modifications for its use to make predictions at APG. In the same vein, a 1-D planetary boundary layer model[3,4] was chosen and incorporated into NAPS.

In the development of NAPS, it was decided to utilize a SODAR which provides wind averages and the occurrence of wind shears at 15 minute intervals. The SODAR measurement coupled with other meteorological measurements from an instrumented mast at the test site and upper air data from a radiosonde would provide the required input data for the predictive meteorological model. To better aid the meteorologist and range personnel in determining the propagation conditions, the data are assimilated from the different sensors, processed through the various models to provide displays of the meteorological profile, the ray trajectories, or the contour of sound intensities overlaid on a terrain map of APG and presented at each users office. These computer displays aid in making the test scheduling and GO/NO GO decisions.

The next step in the development process is the evaluation of the system to determine its performance and fine tune the system to an operational performance level for use on a daily basis in support of the test programs at APG.

Data Requirements

The data requirements and operations for NAPS consist of a radiosonde measurement at 8:00 AM, to provide information on the atmospheric conditions up to 5 km. The number of radiosonde flights

depends on the synoptic conditions, ranging from a minimum of one release for no synoptic changes during the day to a number determined by the meteorologist monitoring the changing synoptic conditions. The radiosonde provides vertical profiles of temperatures, winds, and relative humidity from near surface to 5 km. The vertical profile can detect for occurrences of temperature inversion and wind shear conditions which can cause the sound to be refracted to the surface rather than being refracted upward.

Wind conditions within the planetary boundary layer (PBL) (surface to 1-2 km), whose height varies diurnally, are monitored by a SODAR. The SODAR is a remote sensor which provides 15 minute averages of winds and wind shears to approximately 600 meters. This permits a continual update of the atmosphere near the surface; the part of the PBL subject to the greatest changes during the progression of the day. As mentioned previously, there are two-meter meteorological masts located at each of the test locations. These measure surface temperature, winds, humidity, pressure, and solar radiation. In the future, plans call for adding a ten-meter mast. This would permit measurements of meteorological parameters at the two-meter and ten-meter levels. The two and ten-meter configuration will enable meteorologists to utilize similarity theory and other techniques to model the surface layer meteorological conditions. Again, the vertical extent of the surface layer varies and is dependent upon the solar radiation input, the type of surface and wind speed.

Data from the various sensors will be continually monitored by the meteorologist to ensure the accuracy of the observations. The data is then entered into NAPS to provide an assessment of the present conditions and how these conditions vary under the influence of diurnal and terrain conditions. Once the meteorological data is verified, it is provided as input into the acoustic propagation model (ray trace) to calculate ray trajectories and noise intensity contours. These are again examined by the meteorologist to verify that the predicted intensities at the different locations are reasonable and agree with the meteorological conditions. The meteorologist, after verifying the data is consistent, can now release the data to the range personnel to assist them in making a decision about upcoming tests.

Acoustic Models

NAPS provides an estimate of peak noise intensity from a blast source at ground level in all directions from the blast source. An essential feature of the model is its ability to account for variations in meteorological conditions in the calculation of sound propagation. In performing noise intensity estimates, acoustic ray traces are generated each 5^o (or multiples of 5^o) in azimuth, over a sufficient range of elevation angles to define the focusing and shadow regions in the area surrounding the blast. The NAPS model accounts for spherical spreading, absorption[5], focusing, shadow

zones, reflection of rays from water, interference of multiple rays arriving at the same location, the directional asymmetry of a blast, and the terrain elevation. Essential model inputs are the vertical temperature, vector wind speed, humidity structure of the atmosphere, the blast charge weight, blast location, and blast height.

Meteorological Model

The acoustic model requires input from meteorological sensors or meteorological parameters derived from a meteorological prediction model. NAPS is required to be able to predict favorable propagation conditions and when conditions are not favorable for the test. To accomplish this, a 1-D planetary boundary layer model was acquired and adapted to operate on a PC. The initial meteorological conditions are input to the model utilizing the surface meteorological data at the firing site, SODAR data from the adjacent location and the upper air data from the standard morning sounding or a sounding closest in time to the test period. The 1-D model generates a vertical profile of temperature, vector wind speed, and humidity from the surface to the top of the boundary layer.

The measured data from the sensors are merged into a single wind and temperature profile at the site. The profiles with additional meteorological measurements and the geostrophic winds at 850 mb are used as input into the 1-D Planetary Boundary Layer model. The model is then used to predict meteorological profiles at one hour intervals up to three hours in time. These profiles are then used as input into the ray trace model to predict acoustic intensity levels resulting from a particular test and firing.

System Description and Operation

The various components and sensors comprising the NAPS system are shown in figure 1. Data from the various sensors are linked to the PC in the Meteorological Station by either hardline or RF link. The data is ingested into the PC, evaluated, and then sound contours are predicted for a particular test. The meteorological data, both measured and predicted from the model, are transferred to the Range Control Office, where it is used as input into the same acoustic ray trace model as being run at the meteorological station. This permits the Range Control Office to share the same information that is available at the Meteorological Station. A view of the data flow in the system is shown in figure 2, where the data are used as input into the meteorological model. Examples of this output are shown in figures 3-6 which are the wind speed, direction, temperature and speed of sound, respectively. From this point, the data are input into the acoustic model with output from the acoustic model shown in figures 7 and 8 as ray trajectories generated at given azimuths. Also displayed are the speed of sound profiles showing the atmospheric structure which causes the rays to

be refracted either upward or downward. Sound level contours are generated by utilizing the ray traces at 5° increments from 0° to 360°. In addition, for post analysis and system evaluation, data from the off-post microphones are collected and put into the computer for inclusion in the graphic display for archiving with the meteorological data.

To demonstrate how NAPS would operate, meteorological data are used as an input into the acoustic model which produces the sound level contours shown in figure 9. These contours are generated from measured data and indicate what the sound intensity levels would be at the present time. The contours are elongated and could result in some loud noises impacting upon the local community. The next step is to determine how the situation might change in the next several hours. Prediction of the meteorological conditions for one and three hours later are made by the meteorological model and inserted into the acoustic model with the results shown in figures 10 and 11. In figure 10, one hour later, the changes in the contours are appreciable, with the overall contour shape becoming rounder. Three hours later, there are some changes in the contours, but these are not as significant compared to those showing the change from present time to one hour later. Reviewing the data, as it becomes available, indicates that the test might be delayed to an hour until conditions for testing have improved.

System Evaluation

The situation at APG is excellent for evaluating meteorological and acoustic models since the sound source characteristics[6,7] and locations are known; and there are a large number of atmospheric sensors located throughout APG. To verify the complaints and provide comparisons for NAPS, a noise monitoring system is used to provide measurements of the propagated sound levels. Figure 12 is a map which shows the location of the meteorological and acoustical sensors on and off APG. The asterisks in figure 12 indicate the seventeen microphone sites which are located off APG. These are set up to operate at a threshold of 108 db. When the noise exceeds this level, it is recorded and transmitted with the time of occurrence to a computer at range control and from here it is transmitted to the meteorological station. There are five surface meteorological masts sited on APG and three that are located off APG to the east, west, and north of the Proving Ground. In addition, there are two SODARS located approximately 12 miles apart which provide winds and wind shear heights; these are shown by the open circle. Upper air soundings are made at the meteorological station which is also indicated by an open circle located adjacent to the SODAR at the north end of APG. These sensors then provide detailed data on the meteorological conditions at APG, and the microphone monitoring system provides sound level intensities from those tests that exceed a level of 108 db.

This configuration of sensors and sources can provide a system for evaluating the acoustic predictions made by the ray trace model as well as the predictions of meteorological conditions made by the meteorological model.

As mentioned earlier, preliminary evaluations have been made of the NAPS prediction capability. An example of this is shown in figure 13 where there is a fair agreement between the predicted sound level contours and those levels measured by the microphones.

It is planned to evaluate the performance of the NAPS over a minimum of an annual cycle, since there are seasonal periods when the occurrence of high intensity off range are greatest. To be able to capture the required data, a NAPS data base management system is being developed. Figure 14 is a diagram of this system. There are two major parts to the system; one is located at APG, the NAPS operational site, and the other site is located at WSMR*, which is the prototype development site. The WSMR site will be used to test and evaluate the software and hardware before integration into the operational NAPS at APG. The data base will consist of data obtained at both sites, which have markedly different environments from each other. In the case of WSMR, the environment is a desert one, with low humidity, higher temperatures and greater solar radiation. The APG site is more a continental maritime site situated on the Chesapeake Bay. This site would be more humid, with lower temperatures and less solar radiation due to the presence of clouds, vegetation, and inclement weather. It will be interesting to compare similar type data from each of the sites. By analyzing data from both sites, it may be possible to gain further insight to local variations at each of the sites, thereby making the utilization of NAPS at other locations easier.

Summary

The NAPS was developed to predict sound level intensities resulting from testing at APG. NAPS utilizes standard in-situ meteorological sensors in addition to remote sensors. A ray trace acoustic model and a 1-D planetary boundary layer model are used to predict sound propagation conditions out to three hours based on the meteorological model. A data base is being developed to capture the acoustic and meteorological data and to utilize this data on evaluating and improving the sound intensity predictions. The data will include data from at least a years period to insure that NAPS has been evaluated and utilized under a variety of diurnal and seasonal conditions. After a thorough evaluation, the NAPS will become an operational system. The information learned by putting this type of operation at APG can then be used in installing the NAPS at other sites that may be having a noise problem which could be mitigated by taking into account the effects of the atmosphere on acoustic propagation.

***White Sands Missile Range**

References

1. N.H. Gholson, "An Analysis of Sound Ray Focusing," NWL-TR-2834, January 1973.

2. N.H. Gholson, "Evaluation and Utilization of the NWL Sound Intensity Prediction System," NWL-TN-T-4/74, Oct 1974.

3. Dalin Zhang, *A Verification of One-Dimensional Model Simulations of the Planetary Boundary Layer Over Dry and Moist Terrain*, M.S. Thesis, The Pennsylvania State University (1981).

4. Dalin Zhang and Richard A. Anthes, "A High-Resolution Model of the Planetary Boundary Layer–Sensitivity Tests and Comparisons with SESAME-79 Data," J. Appl. Meteor. **21**, 1594-1609(1982).

5. Acoustical Society of America, "Estimating Air Blast Characteristics for Single Point Explosions in Air with a Guide to Evaluation of Atmospheric Propagation and Effects," ANSI S2.20-1983, Acoustical Society of America.

6. P. Schomer, L. Little, and A. Hunt, "Acoustical Directivity Patterns for Army Weapons," CERL-IR-N-60, January 1979.

7. P. Schomer and R. Raspet, "Acoustical Directivity Patterns for Army Weapons: Supplement 2," CERL-TR-H-60, August 1984.

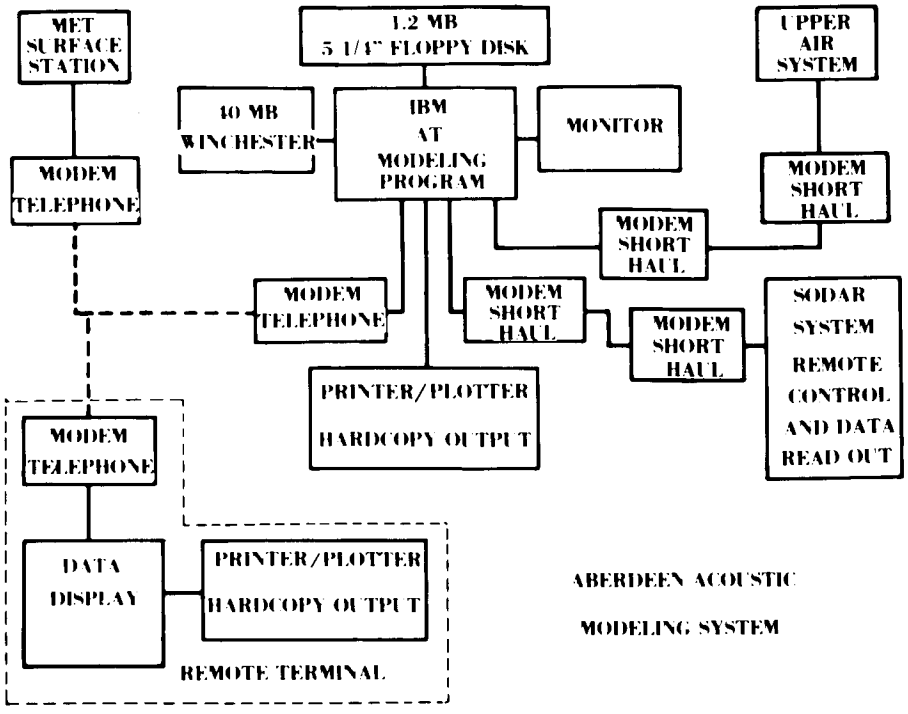

FIGURE 1. NOISE ASSESSMENT AND PREDICTION SYSTEM SENSORS AND INSTRUMENTATION.

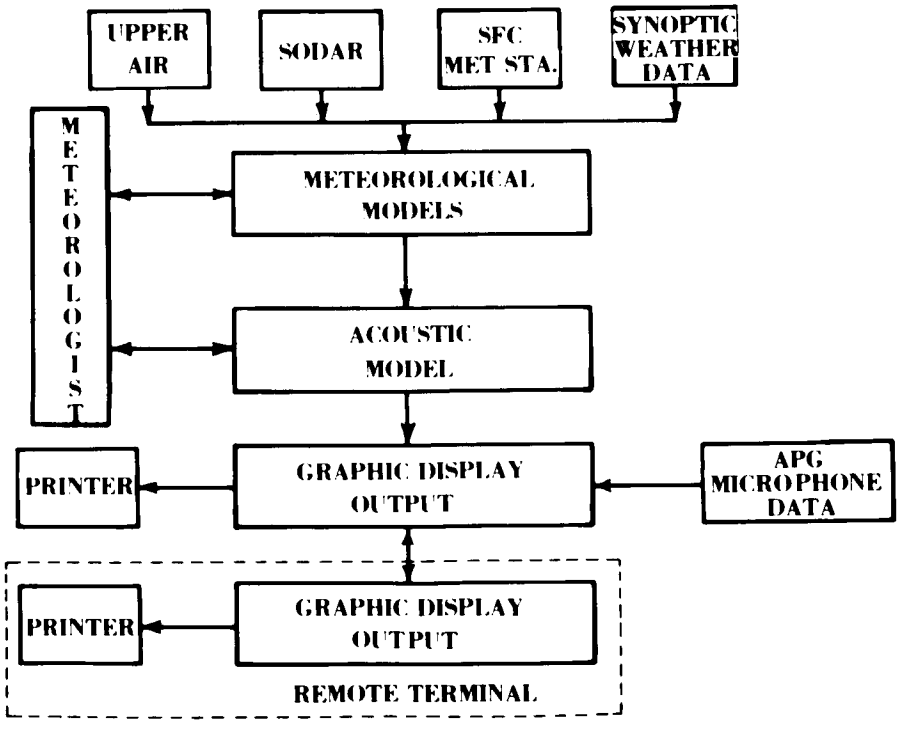

FIGURE 2. NOISE ASSESSMENT AND PREDICTION SYSTEM DATA FLOW.

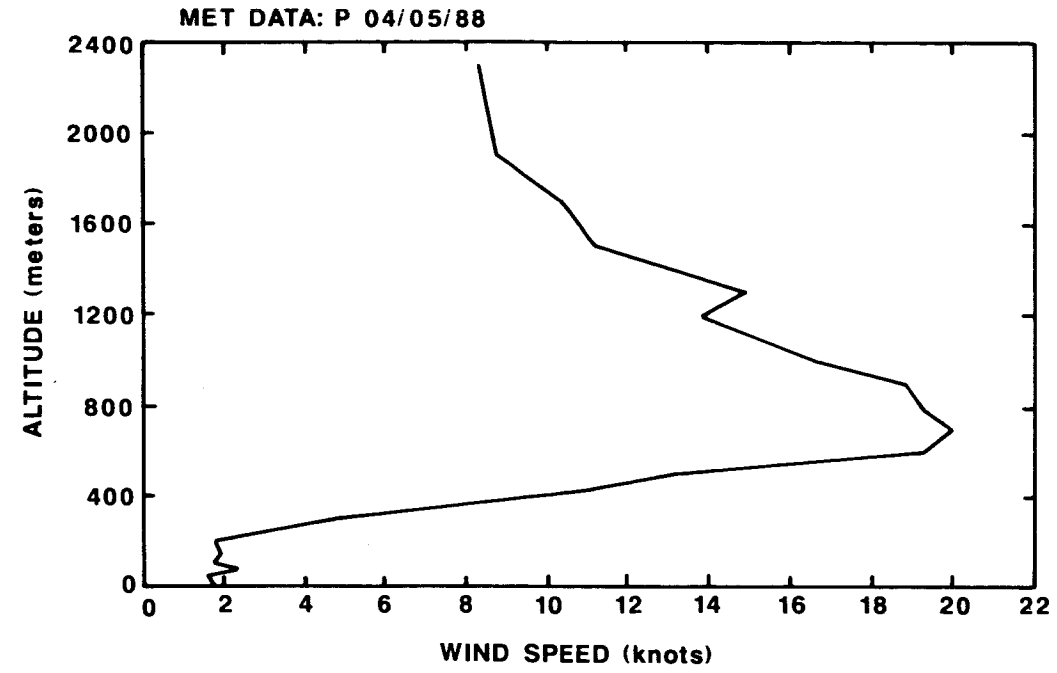

FIGURE 3. COMPUTER DISPLAY OF WIND SPEED PROFILE.

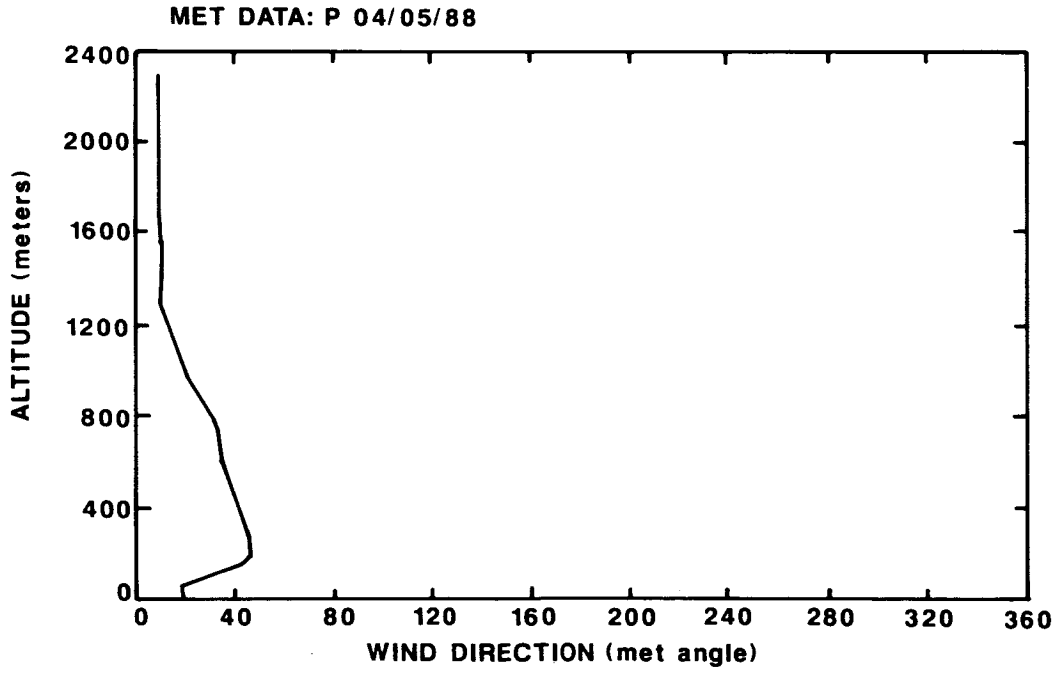

FIGURE 4. COMPUTER DISPLAY OF WIND DIRECTION PROFILE.

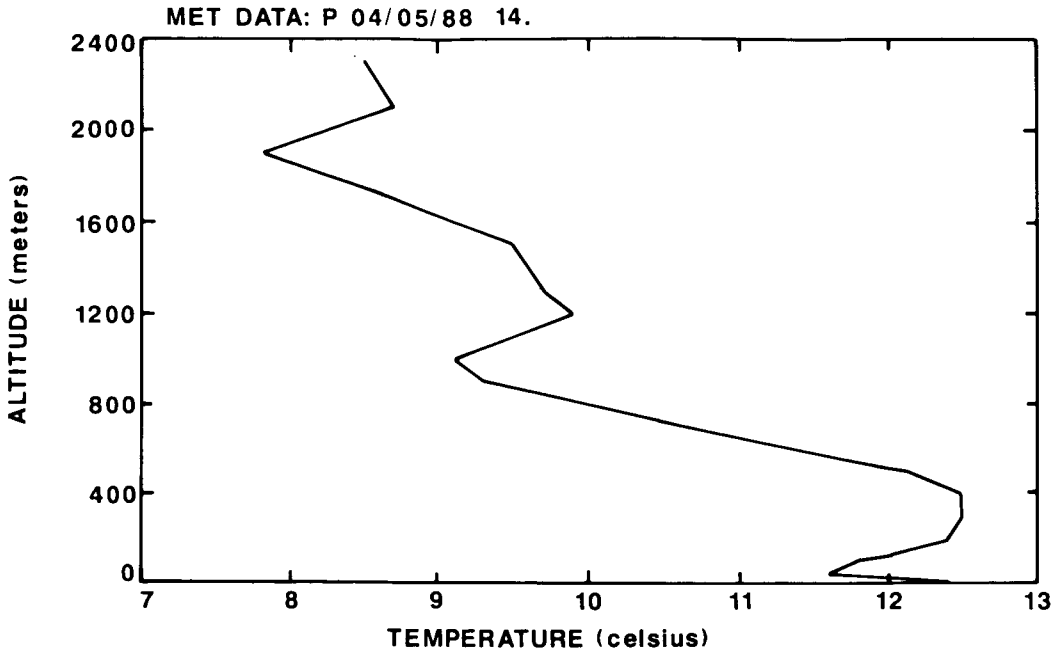

FIGURE 5. COMPUTER DISPLAY OF TEMPERATURE PROFILE.

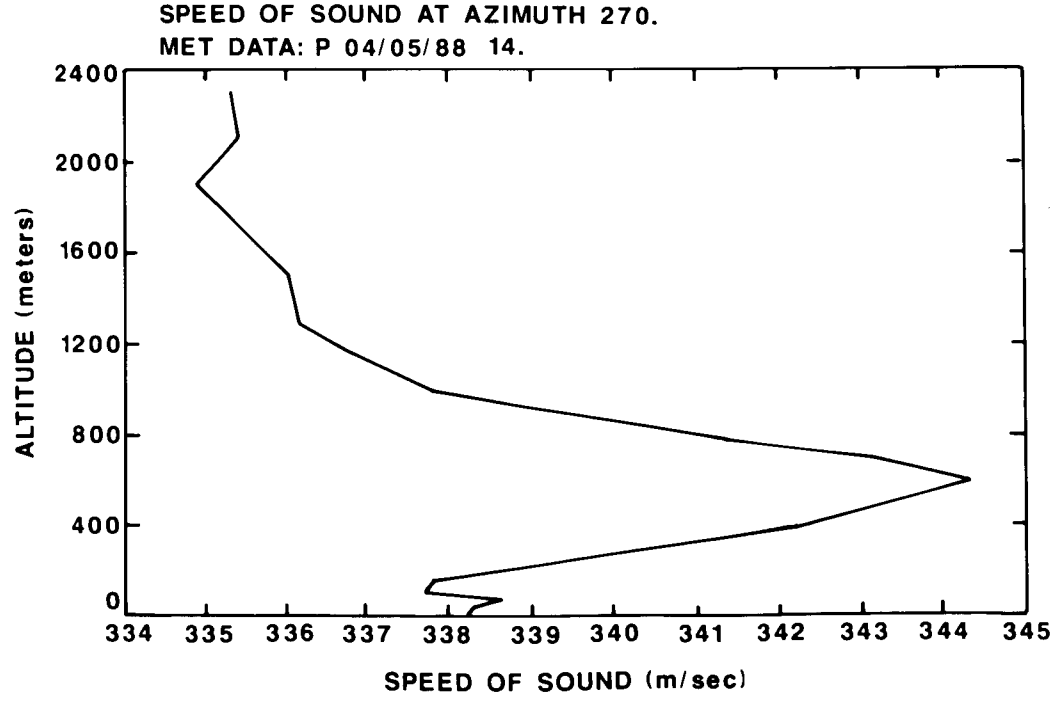

FIGURE 6. COMPUTER DISPLAY OF SOUND SPEED PROFILE.

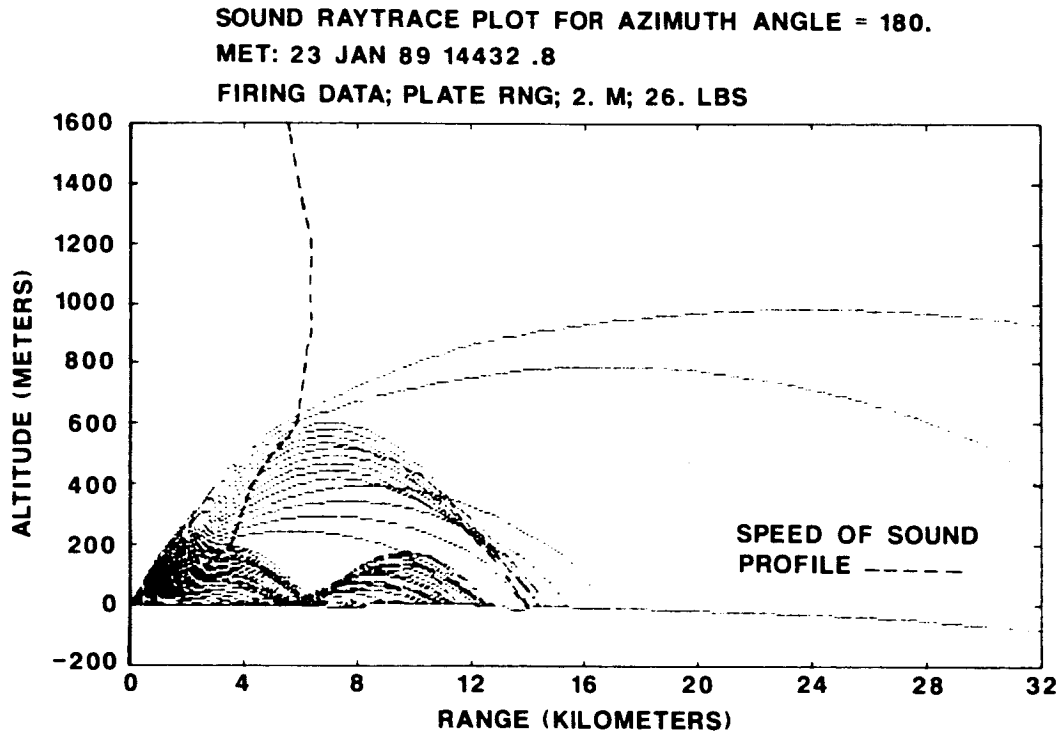

FIGURE 7. RAY TRACE WITH SOUND SPEED PROFILE.

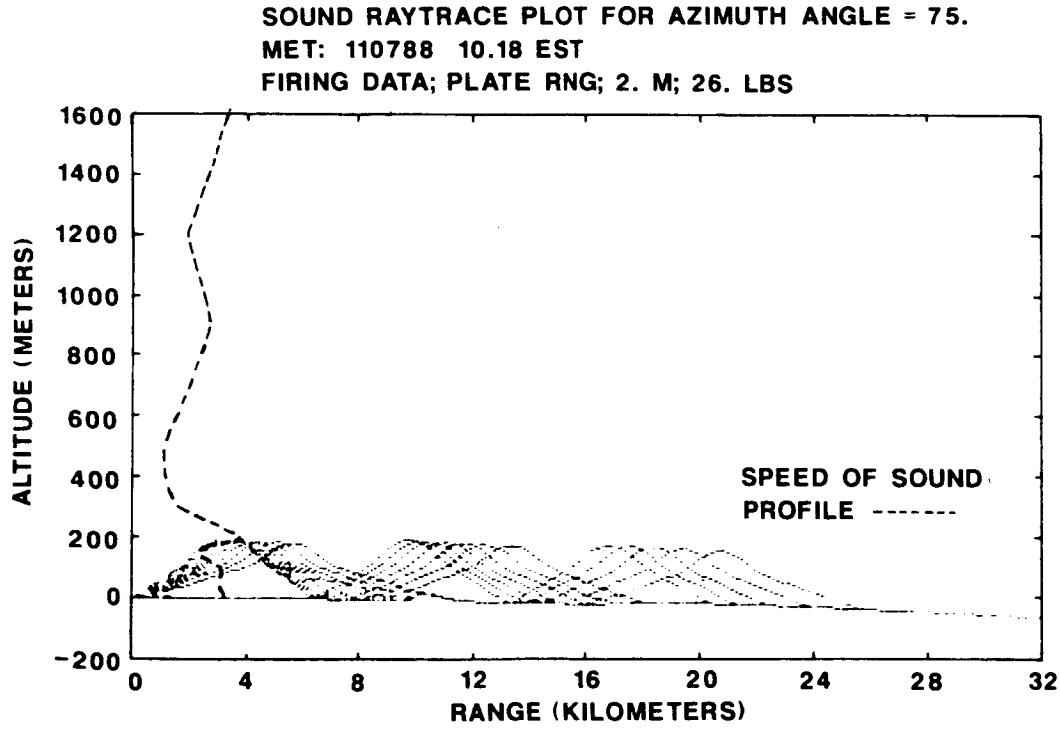

FIGURE 8. RAY TRACE WITH SOUND SPEED PROFILE.

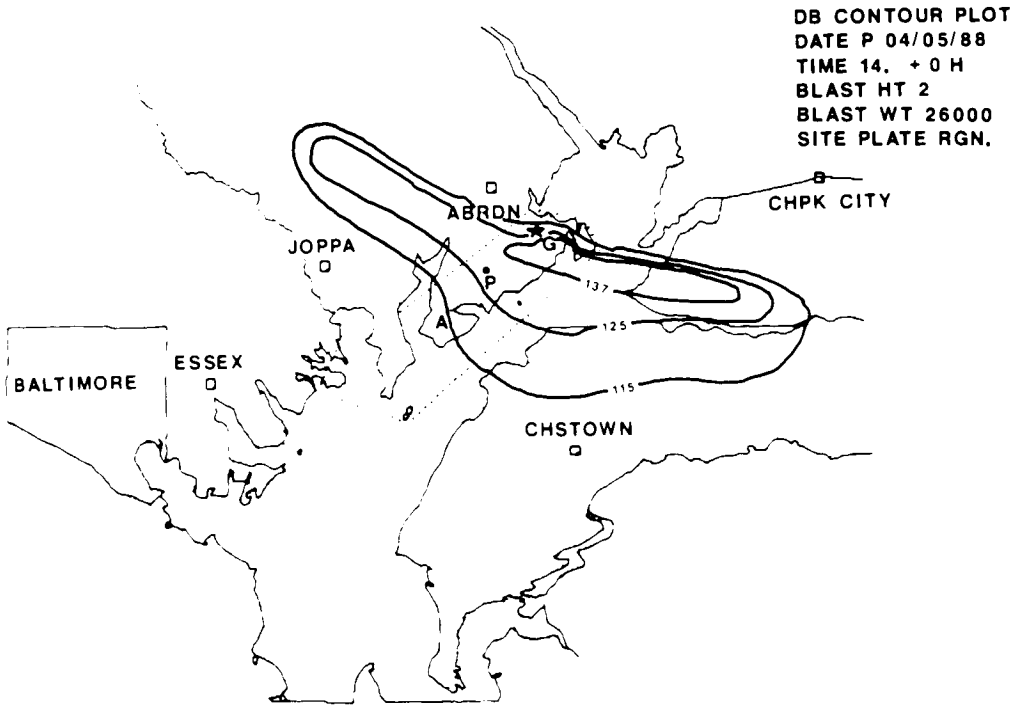

FIGURE 9. SOUND LEVEL CONTOURS DERIVED FROM METEOROLOGICAL MEASUREMENTS.

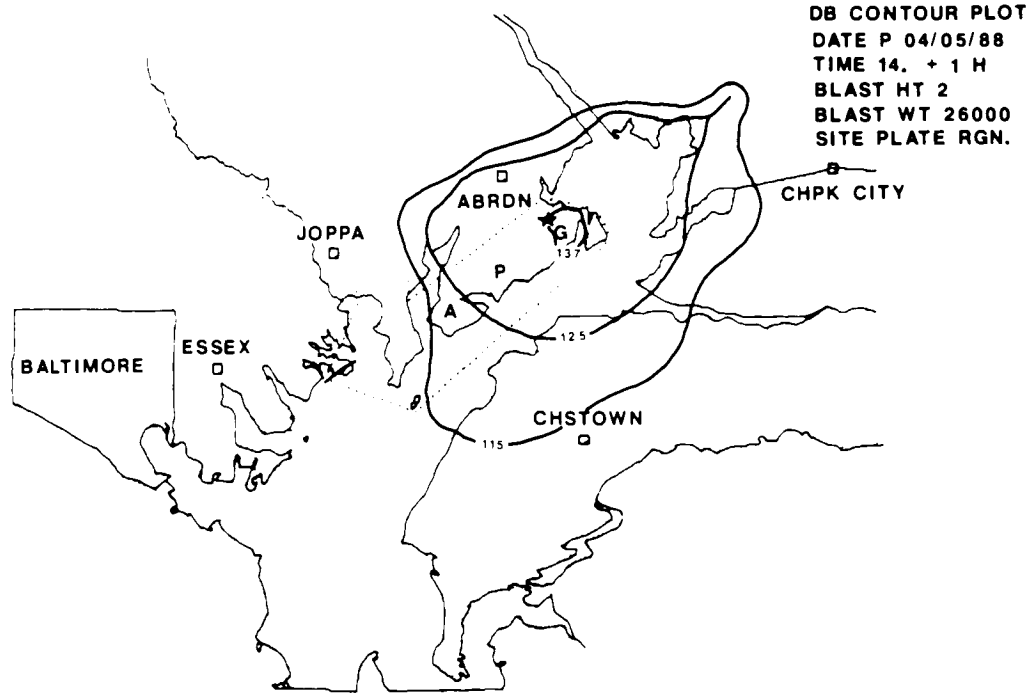

FIGURE 10. SOUND LEVEL CONTOURS DERIVED FROM PREDICTED METEOROLOGICAL CONDITIONS ONE HOUR LATER.

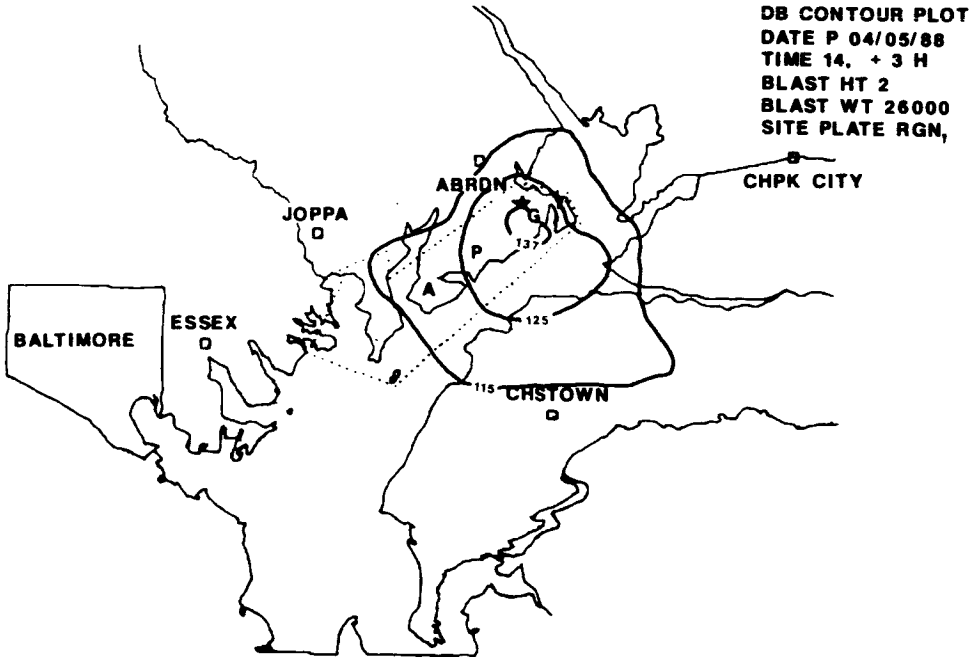

FIGURE 11. SOUND LEVEL CONTOURS DERIVED FROM PREDICTED METEOROLOGICAL CONDITIONS THREE HOURS LATER.

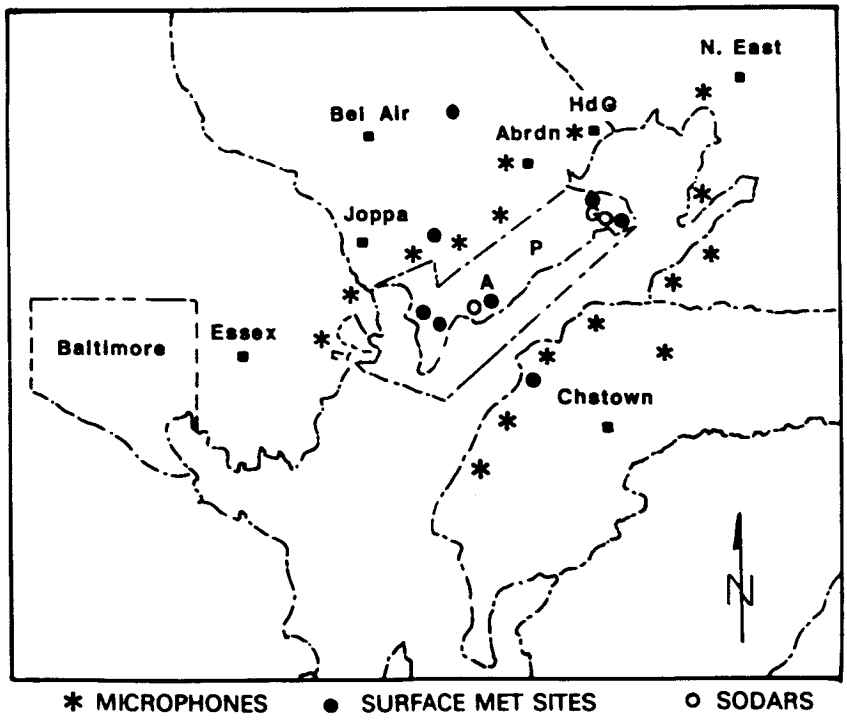

FIGURE 12. ACOUSTIC AND METEOROLOGICAL SENSOR LOCATIONS AT ABERDEEN PROVING GROUND.

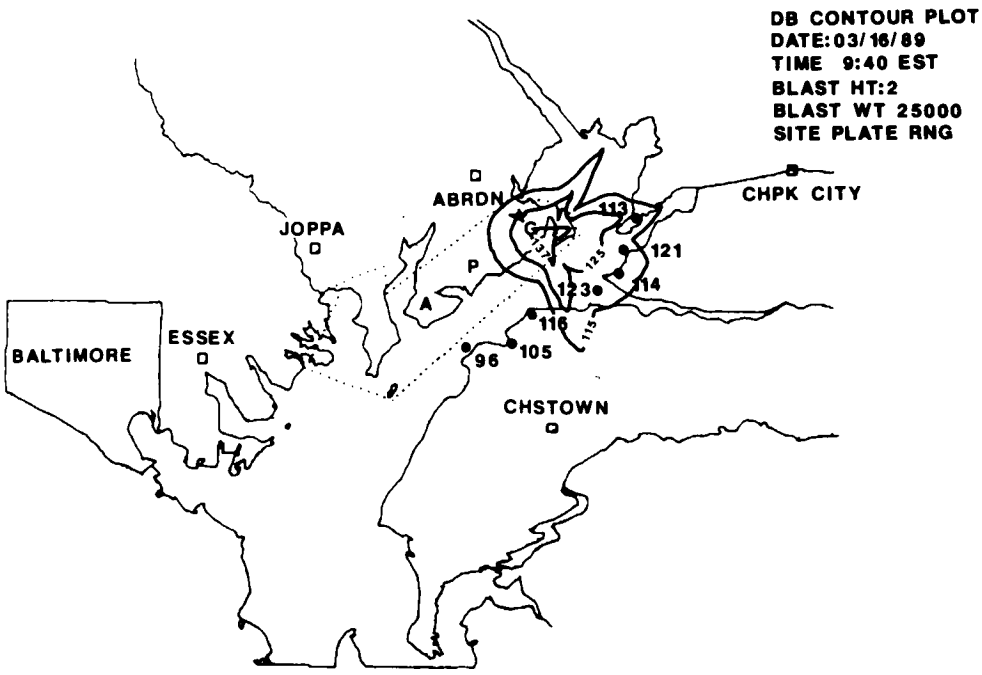

13. PREDICTED SOUND LEVEL CONTOURS COMPARED TO MEASURED SOUND LEVELS FROM MICROPHONE SYSTEM.

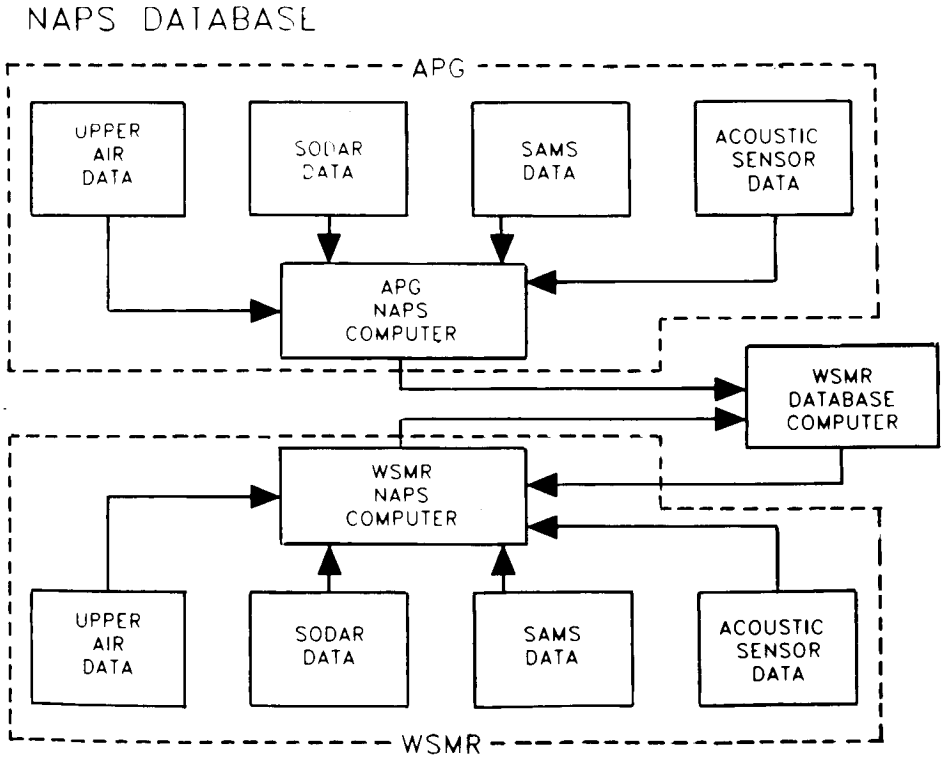

FIGURE 14. NOISE ASSESSMENT AND PREDICTION SYSTEM DATA BASE CONFIGURATION.

SCATTERING OF SOUND BY ATMOSPHERIC TURBULENCE: PREDICTIONS IN A REFRACTIVE SHADOW ZONE

Walton E. McBride
Planning Systems, Inc.
Slidell, LA 70458

Henry E. Bass, Richard Raspet, and Kenneth E. Gilbert
University of Mississippi
University, MS 38677

ABSTRACT

According to ray theory, regions exist in an upward refracting atmosphere where no sound should be present. Experiments show, however, that appreciable sound levels penetrate these so-called shadow zones. Two mechanisms contribute to sound in the shadow zone: diffraction and turbulent scattering of sound. Diffractive effects can be pronounced at lower frequencies but are small at high frequencies. In the short wavelength limit, then, scattering due to turbulence should be the predominant mechanism involved in producing the sound levels measured in shadow zones. No existing analytical method includes turbulence effects in the prediction of sound pressure levels in upward refractive shadow zones. In order to obtain quantitative average sound pressure level predictions, a numerical simulation of the effect of atmospheric turbulence on sound propagation is performed. The simulation is based on scattering from randomly distributed scattering centers ("turbules"). Sound pressure levels are computed for many realizations of a turbulent atmosphere. Predictions from the numerical simulation are compared with existing theories and experimental data.

INTRODUCTION

Solar heating of the ground produces strong temperature gradients in the air just above the surface of the Earth. Since the speed of sound is proportional to the square root of the temperature, sound will follow upwardly curved paths in every direction from a source. The stronger the temperature gradients involved, the shorter the distance to what is properly called a shadow zone, since no direct or reflected rays can penetrate into this region. Figure 1 is an illustration of an upward refractive shadow zone where the source is at a height h_s and the radius of curvature of the limiting ray is R_c. The edge of the shadow zone is delineated by the so-called limiting ray which grazes the ground.

In a similar fashion, sound traveling upwind is curved upwards due to the strong wind gradients near the ground and a shadow zone is also formed. In the case of wind, however, the effect is not isotropic because of the vector nature of the wind velocity and the rays are actually bent downward for the sound propagating downwind.

Two mechanisms contribute to the magnitude of the sound levels measured in shadow zones: diffraction and the turbulent scattering of sound. Pierce[1] describes the solution for a linear sound speed

gradient in terms of residue series for the pressure in the shadow zone. He examines the cases of a hard boundary and a pressure-release surface and gives approximate solutions when the source and receiver are above the creeping wave layer height, defined as $(R_c/2\ k_0^2)^{1/3}$, where R_c is the radius of curvature of the limiting ray and k_0 is the wavenumber.

Daigle et al.[2] made use of the above two approximate solutions in an effort to fit the data they collected over an asphalt airport runway and over a grass-covered strip near the runway, the latter approximating a pressure-release surface at frequencies greater than 500 Hz and the former approximating a hard boundary. They found that the hard boundary data was well explained by Pierce's approximate solution for that case and that the data up to 1000 Hz over the grass-covered ground was satisfactorily explained by Pierce's approximate solution for a pressure-release surface.

The approximate solution leads to large errors in the effective source levels for sources close to a pressure-release or finite impedance ground, as was the case with Daigle's data. A complete discussion of this problem can be found in the paper by Raspet and Franke.[3] In a later paper, Berry and Daigle[4] used the complete residue series solution and again compared the above data. They found that the data at 250 Hz still agreed well with the predictions of diffraction theory. But the data was well under-predicted by diffraction theory at 500 Hz and especially at 1000 Hz. The predictions from the full residue series solution are shown in Fig. 2, which is a reproduction of Fig. 13b of Ref. 4.

The role played by atmospheric turbulence in the insonification of shadow zones has escaped analytical formulation. In an effort to obtain a quantitative estimate of the extent to which atmospheric turbulence raises the sound levels in a shadow zone, Gilbert et al.[5] used a parabolic equation method to numerically simulate sound propagation in a turbulent atmosphere. They compared their predictions for upward refracting conditions with experimental results of Wiener and Keast.[6] The numerical predictions involved the calculation of the sound pressure magnitude for a particular realization or "snapshot" of turbulence, while the results of Wiener and Keast were expressed in terms of average sound pressure levels. Nevertheless, Gilbert et al. were able to duplicate the apparent range independence of excess attenuation characteristic of the experimental data at ranges as great as 1 km.

In this paper, we present the average sound pressure levels in an upward refractive shadow zone predicted by a scattering center based numerical simulation. The main features of the numerical solution are reviewed and the modifications necessary to adapt it to an upward refractive atmosphere are discussed. Sound levels are computed for over 500 realizations of the turbulent atmosphere. Predictions from the numerical simulation are then compared with experimental data taken by Daigle et al.[2]

MAIN FEATURES OF THE NUMERICAL SIMULATION

Although the details of the numerical simulation were given in an earlier paper,* the main features are repeated here so that the reader may have a better idea of the type of calculations involved. Following the model of de Wolf,[7] we construct an ensemble of isotropic, irrotational scattering centers which we call "turbules." If μ is defined as the change from unity of the index of refraction, a given turbule is assigned the refractive profile

*Walton E. McBride, Henry E. Bass, Richard Raspet, Kenneth E. Gilbert, "Scattering of sound by atmospheric turbulence," submitted to J. Acoust. Soc. Am., Feb. 1990.

$$\mu(r,s) = q_i\, e^{-r^2/s^2} \tag{1}$$

where q_i is the value of μ at the center of the spherically symmetric turbule and s is the $1/e$ contour of the scattering center and can be considered to be its effective size. The value of q_i and the probability distribution of turbule sizes depend in general on the particular functional form chosen for the correlation function of the fluctuations of the index of refraction. If the correlation function is chosen to have the Gaussian form,

$$\langle \mu_1 \mu_2 \rangle = \left\langle \mu^2 \right\rangle e^{-r^2/L^2}, \tag{2}$$

where $<\mu^2>$ is the variance and L is the correlation length, then the size spectrum is a delta function implying that all the turbules have the same size,

$$s = \frac{L}{\sqrt{2}}\,. \tag{3}$$

The value of q_i for this particular form of the correlation function is given by

$$q_i = \pm \left[\frac{8 \left\langle \mu^2 \right\rangle}{\pi \sqrt{\pi} \rho_N L^3} \right]^{1/2} \tag{4}$$

and is inversely proportional to the turbule number density ρ_N. An upper value of ρ_N of about half the overlap density is necessary so that the turbules will be separate entities. With single scattering, sound scattered from a particular turbule reaches the receiver downfield with negligible scattering by other turbules located between that particular turbule and the receiver. From Eq. (4) the product $q_i^2 \rho_N$ is a constant whose value depends on the independently measured micrometeorological variables $<\mu^2>$ and L. There is, therefore, a certain latitude in the value of ρ_N. Decreasing ρ_N will result in a greater value for $|q_i|$. Although a lesser number of turbules result from a decrease of ρ_N, the predictions of the numerical simulation are statistically steady as the turbule number density is decreased from an upper limit of half the overlap density.

Initially in the development of the simulation, the first Born approximation to scattering was used to determine the scattering effect of each turbule. In practice, the evaluation of the scattering integral is performed by assuming that both source and receiver are far away from the scattering region; thus first order terms in the phase are sufficient. Because some of the turbules in the numerical simulation are close to the source or receiver, second order terms in the phase were kept in the scattering integral. The total pressure at a receiver downfield is, then, the sum of the direct and scattered spherical waves. For only one turbule in free space, this is:

$$p(R) = \frac{e^{ikR}}{R} + \sqrt{\frac{\pi}{2}}\, q_i\, k^2\, s^3\, \frac{e^{ik(r_{st}+r_{tr})}}{r_{st} r_{tr}} \left(\frac{1}{1-ia}\right) e^{-Ck^2 s^2/4}, \tag{5}$$

where

$$C = \left(1-\cos\Theta_0\right)^2 + \sin^2\Theta_0 \left(\frac{1}{1-ia}\right), \tag{6}$$

and

$$a = \frac{ks^2}{2}\left(\frac{1}{r_{st}} + \frac{1}{r_{tr}}\right). \tag{7}$$

In the above equation, k is the wavenumber, s is the effective size of the turbule, Θ_0 is the angle between the incident and scattered directions, R is the distance between source and receiver, while r_{st} is the distance between source and turbule center, and r_{tr} is the distance between turbule center and receiver.

Note that the usual Born scattering term is recovered when a = 0 and the first term in Eq. (6) is dropped. Even with this improved evaluation of the Born scattering integral, the distance from turbule to source or receiver cannot be less than about twice the radius of the turbule. Consequently, "buffers" of a turbule's diameter were placed in front of the source and receiver where no turbules were allowed.

The numerical simulation using the first Born approximation to scattering was then compared to theoretical expressions due to Karavainikov[8] for the log-amplitude and phase variances of the pressure fluctuations. It was found that good agreement was reached whenever the wave parameter D (=R/kL^2) was greater than 1. As shown in Fig. 3, the log-amplitude variances as predicted by Karavainikov are independent of frequency when D < 1, a result also obtained by Bergmann using geometrical optics.

In an effort to reach better agreement in the geometrical optics region, the Rytov approximation used by Karavainikov was incorporated into the numerical simulation. The Rytov method consists of approximating the field at the receiver by

$$\vec{p}^{R}(\vec{r}) = \vec{p}_0(\vec{r})\, e^{\vec{\Psi}^{R}(\vec{r})}; \tag{8}$$

whereas the Born approximation is written:

$$\vec{p}^{B}(\vec{r}) = \vec{p}_0(\vec{r}) + \vec{\Psi}^{B}(\vec{r}). \tag{9}$$

There is a simple relationship between the first Rytov and first Born approximations:

$$\vec{\psi}^{R}_1(\vec{r}) = \frac{\vec{\Psi}^{B}_1(\vec{r})}{\vec{p}_0(\vec{r})}, \tag{10}$$

and it was, therefore, a simple matter to incorporate the first Rytov approximation into the numerical

simulation. The results are shown in Fig. 4 and good agreement is obtained throughout the range of the wave parameter D.

As can be seen from the above comparisons with Karavainikov's analytic curves, the first Rytov approximation is superior to the first Born approximation for an unbounded medium without refraction. When refractive conditions are introduced, however, the formation of shadow zones becomes possible. In the shadow zones, p_0 is 0 and the first Rytov approximation cannot be used. Recourse must be made to the first Born approximation and the wave parameter D must be greater than 1 for the numerical simulation to be valid in accordance with the results of Fig. 3.

The next step is the inclusion of the ground. An immediate consequence of the existence of a boundary is the presence of three additional paths by which sound can propagate to the receiver. There now exist four single scatter paths that connect the source and receiver:

1. source-turbule-receiver,
2. source-turbule-ground-receiver,
3. source-ground-turbule-receiver,
4. source-ground-turbule-ground-receiver.

The last three paths all interact with the ground and, therefore, a model of the effect of the ground on the sound wave was also included in the numerical simulation.

The algorithm proceeds as follows. Values of $<\mu^2>$ and L are given from independent micro-meteorological measurements. From these, the value of s and q_i are obtained using the above equations. A scattering space, which will enclose thousands of turbules, is defined with buffers in front of the source and receivers of widths equal to about the diameter of a turbule. The turbules are assigned positive or negative signs for their value of q_i. The sound pressure at the receiver is calculated for this particular arrangement of turbules, and the result is referred to as a realization. Then each turbule is given random, small increments in its Cartesian coordinates. The sound pressure at the receiver is recalculated, resulting in another realization. The process is repeated for as many realizations as are necessary for the statistics to stabilize. We have found that 500 realizations are sufficient. Average sound pressure levels can then be obtained from the 500 stored values of the sound pressure. It should be mentioned that any other desired statistical quantity can be obtained, such as structure and correlation functions, as well as the variances of the log-amplitude and phase fluctuations.

The inclusion of a sound speed gradient requires two modifications: the rays are now curved and the value of the wavenumber k is no longer constant along a ray. In order to obtain a closed form solution for the equation describing the rays, a linear sound speed gradient was assumed. As is well known, a consequence of this assumption is that the ray paths are arcs of circles.

Because of the curvature of the ray paths, each path must be tested to see whether the source and each turbule can be joined together, as well as each turbule and the receiver. If either segment of the total path cannot be linked, that particular turbule's contribution is discarded. It was found that about 15% of the turbules were eliminated in this way for the experimental data to be described later.

The last correction necessary is the calculation of an effective wavenumber k_e for each ray path. This required the computation of the length of each path, as well as the travel time along that path. Their

ratio gave an effective sound speed c_e along that path, and the effective wavenumber was then given by ω/c_e.

COMPARISON TO DATA

In order to implement the numerical simulation, the statistical properties $<\mu^2>$ and L of the turbulent atmosphere and the impedance of the ground are required. The former was given in the article by Daigle et al.[2] as $<\mu^2> = 6 \times 10^{-6}$ and L = 1.6 m. The impedance had to be approximated because the article mentioned above did not specify a particular impedance model. To estimate the impedance, a residue series solution developed by Raspet and Franke[3] was used to match the curves of Fig. 2 as closely as possible at all three frequencies. The particular impedance model used was a four parameter model developed by Attenborough.[9] A shape factor n' of .750, a shape factor ratio s_f of .875, a porosity Ω of .675, and a flow resistivity σ of 330 cgs rayls give the results shown in Fig. 5.

The numerical simulation was performed with the above parameter values for 500 realizations. Rms sound pressure values were computed and divided by the pressure doubling plus attenuation factor $(2e^{-\alpha R}/R)$ as was done in Daigle's presentation of his experimental data. The source was given a height of 0 m, and six receiver positions were used 230 m downrange at heights of 0.25 m, 0.50 m, 1.0 m, 2.0 m, 4.0 m, and 7.0 m in order to sample the vertical behavior of the sound pressure levels in the shadow zone. Because we are forced to use the first Born approximation when the receiver is in a shadow zone ($p_0 = 0$), the possible values of the wave parameter D must be checked to see that they will be greater than 1. Since $D = R/kL^2$ with R = 230 m and L = 1.6 m, it is sufficient to check the value of D for the greatest frequency of interest. With 1000 Hz, $k \approx 18.4$ and, therefore, $D \approx 5$ which is well above the minimum value of 1. The sound pressure levels predicted by the numerical simulation (expressed in dB) are compared to Daigle's experimental data in Fig. 6 for the three frequencies involved. Notice the similarity in shape which the curves representing the turbulent scattering contribution share with the curves that are typical of diffraction theory predictions. As can be seen by comparing Figs. 2 and 6, it appears that for this experiment the contributions from turbulent scattering and diffractive effects are about equal at 250 Hz. However, turbulent scattering becomes the major contributor at 500 Hz. At 1000 Hz, turbulent scattering is the predominant mechanism behind the increased sound pressure levels measured in the shadow zone.

CONCLUSION

Quantitative predictions for the average sound pressure levels in a refractive shadow zone have been presented. Good agreement was reached with experimental data collected by Daigle et al[2] in a shadow zone caused by temperature gradients. It seems that the use of a simple linear sound speed gradient is a good approximation to the real sound speed profile directly above the ground for the moderate ranges involved in this study. At the longer ranges investigated by Gilbert et al. it was necessary to use a logarithmic sound velocity profile to obtain accurate predictions.[5] The relative contributions of diffraction and turbulent scattering have been examined and graphically displayed. The dominant mechanism which dictates sound levels in shadow zones at higher frequencies is scattering due to turbulence.

ACKNOWLEDGMENTS

This work was supported in part by the Army Research Office. In addition, one of us (WEM) gratefully acknowledges support by the U.S. Army Construction Engineering Research Laboratory.

REFERENCES

1. A.D. Pierce, Acoustics: An Introduction to its Physical Principles and Applications, (McGraw-Hill, New York, 1981).

2. G.A. Daigle, T.F.W. Embleton, and J.E. Piercy, "Propagation of Sound in the Presence of Gradients and Turbulence Near the Ground," J. Acoust. Soc. Am. 79, 613-627 (1986).

3. R. Raspet and S.J. Franke, "Residue Series Solution of Impulse Noise Propagation into a Shadow Zone," J. Acoust. Soc. Am. 83, 1964-1967 (1988).

4. A. Berry and G.A. Daigle, "Controlled Experiments of the Diffraction of Sound by a Curved Surface," J. Acoust. Soc. Am. 83 (6), 2047-2058 (1988).

5. Kenneth E. Gilbert, Richard Raspet, and Xiao Di, "Calculation of Turbulence Effects in an Upward Refracting Atmosphere," J. Acoust. Soc. Am. 87, 2428-2437 (1990).

6. F.M. Wiener and D.N. Keast, "Experimental Study of the Propagation of Sound over Ground," J. Acoust. Soc. Am. 31 (6), 724-733 (1959).

7. D.A. de Wolf, "A Random-motion Model of Fluctuations in a Nearly Transparent Medium," Radio Science 18, 138-142 (1975).

8. V.N. Karavainikov, "Fluctuations of Amplitude and Phase in a Spherical Wave," Akust. Zh. 3, 175-186 (1957).

9. K. Attenborough, "Acoustical Impedance Models for Outdoor Ground Surfaces," J. Sound Vib. 99, 521-543 (1985).

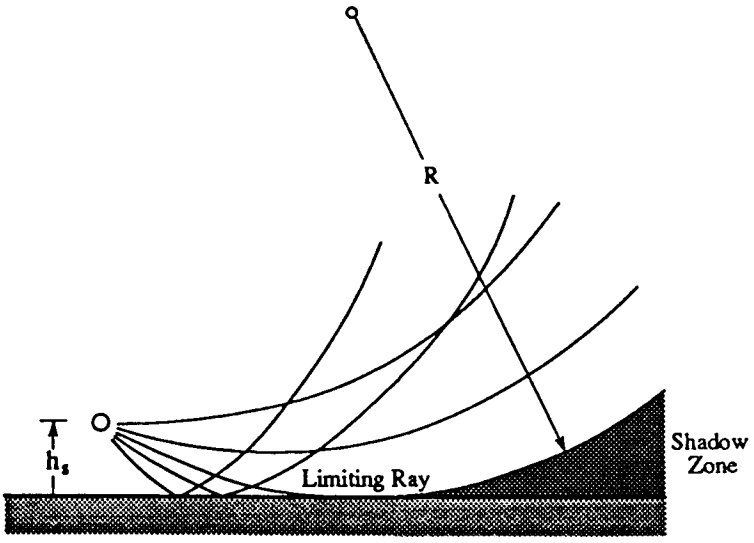

Fig. 1 Shadow zone formation for a sound speed profile that decreases linearly with height.

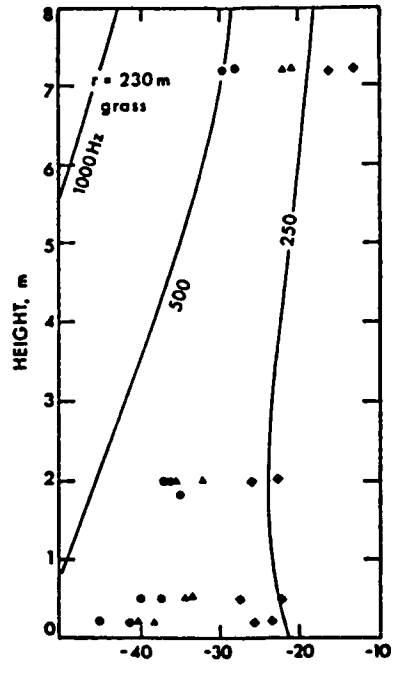

Fig. 2 Comparison of measured sound levels (points) with predictions based upon diffraction into the shadow zone, taken from Ref. 4. Solid circles are for 1000 Hz, triangles for 500 Hz, and diamonds for 250 Hz.

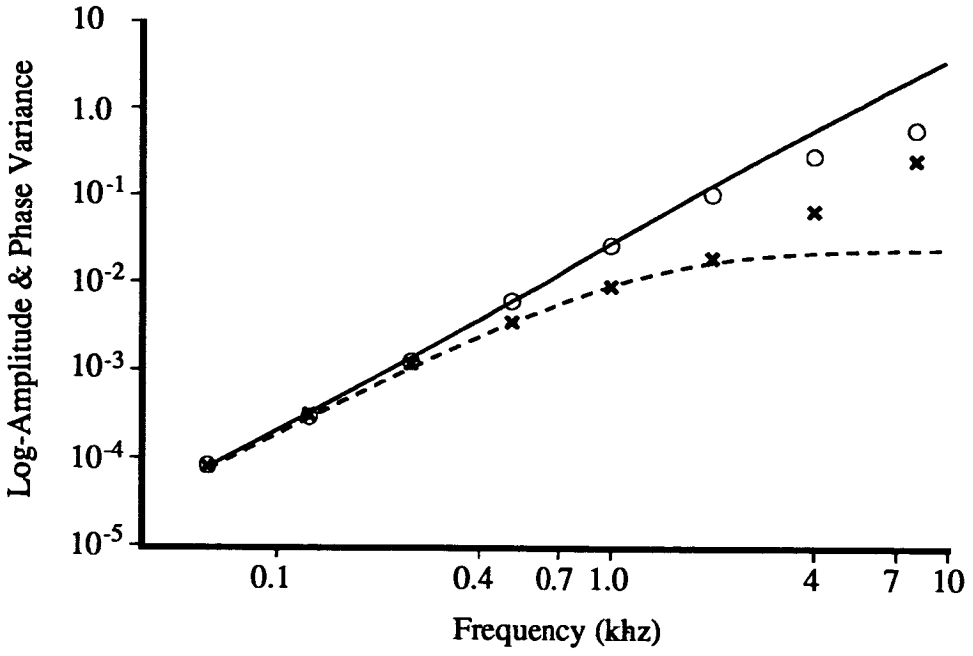

Fig. 3 Comparison of the numerical simulation using the first Born approximation (o for phase variances; x for log-amplitude variances) with Karavainikov's analytical results (——— for phase variances; --------- for log-amplitude variances).

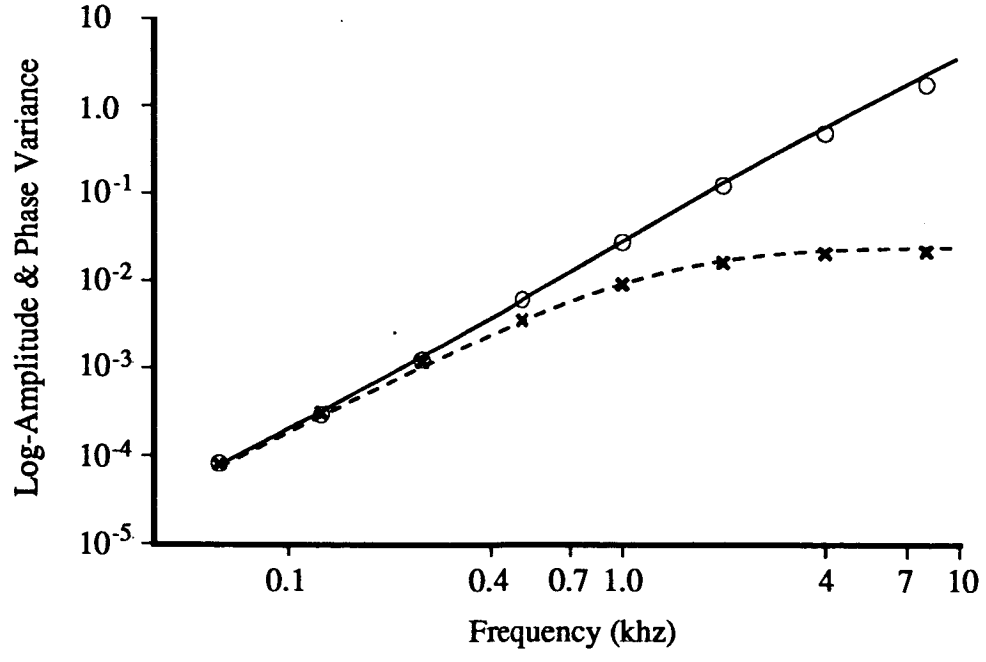

Fig. 4 Comparison of the numerical simulation using the first Rytov approximation (o for phase variances; x for log-amplitude variances) with Karavainikov's analytical results (——— for phase variances; --------- for log-amplitude variances).

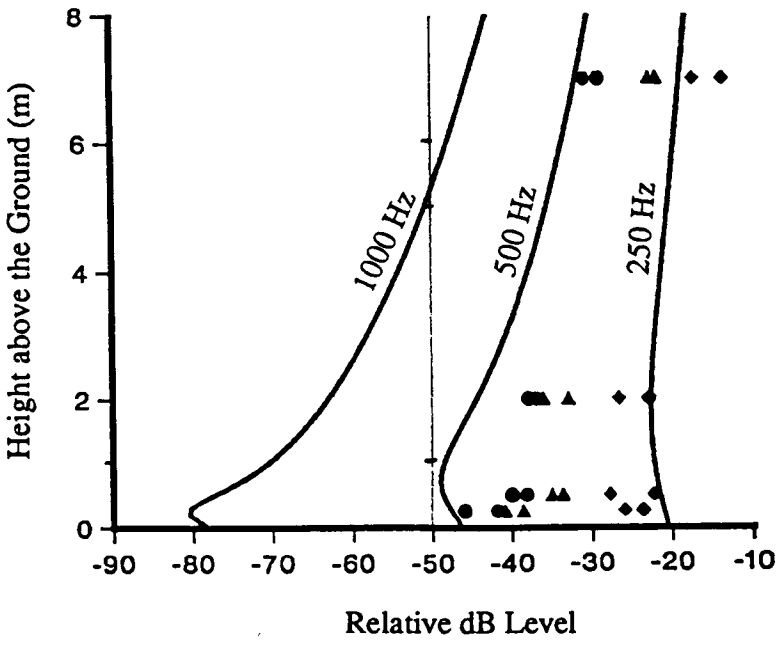

Fig. 5 Comparison of data with the prediction of diffraction theory using the residue series solution. Data points are described for Fig. 2.

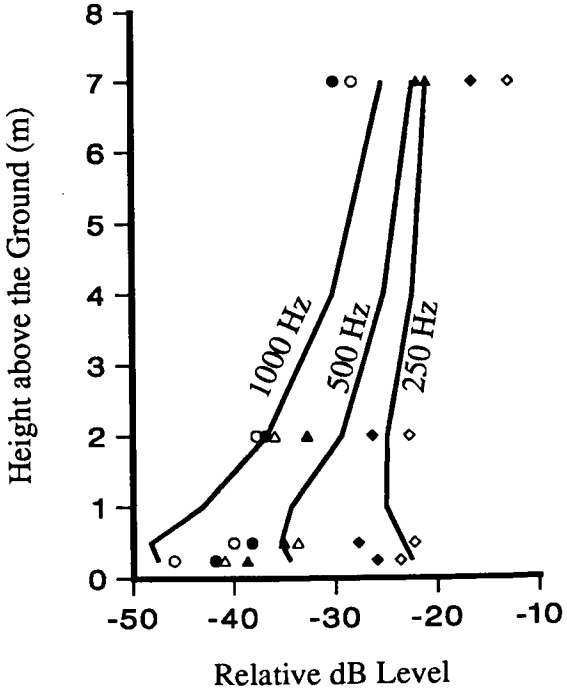

Fig. 6 Comparison of the prediction from the numerical simulation with experimental data taken in shadow zone. Experimental data is the same as in Fig. 5.

Effects of Large-Scale Wind Driven Turbulence on Sound Propagation

John M. Noble
U.S. Army Atmospheric Sciences Laboratory
ATTN: SLCAS-AS-I
White Sands Missile Range, NM 88002

Henry Bass and Richard Raspet
Physical Acoustics Research Group
Department of Physics and Astronomy
The University of Mississippi
University, MS 38677

Abstract

Acoustic measurements made in the atmosphere have shown significant fluctuations in amplitude and phase resulting from the interaction with time varying meteorological conditions. The observed variations appear to have short term and long term (1-5 minutes) variations at least in the phase of the acoustic signal. One possible way to account for this long term variation is the use of a large scale wind driven turbulence model. From a Fourier analysis of the phase variations, the outer scales for the large scale turbulence is 200 meters and greater, which corresponds to turbulence in the energy-containing subrange. The large scale turbulence is assumed to be elongated longitudinal vortex pairs roughly aligned with the mean wind. Due to the size of the vortex pair compared to the scale of our experiment, the effect of the vortex pair on the acoustic field can be modeled as the sound speed of the atmosphere varying with time. The model provides results with the same trends and variations in phase observed experimentally.

Effects of Large Scale Wind Driven Turbulence on Sound Propagation

Introduction

Random fluctuations in the acoustical index of refraction in the atmosphere is the result of the presence of turbulence. These random fluctuations in the acoustical index of refraction results in fluctuations of the amplitude and phase of an acoustic wave. The variations in the amplitude and phase show changes occurring over two different time scales. The short term variations correspond to turbule sizes on the order of 1 meter, while the long term variations seem to correspond to turbule sizes on the order of 100 m and greater.

The aim of this work was to develop a descriptive model for large scale wind driven turbulence and the effects of large scale turbulence on the sound field. The model will describe the shape and horizontal and vertical wind velocity profiles for the turbulence. Due to the size of the turbules in relation to the experiment conducted, a simple phase model was developed to perform phase variation calculations using the results from the large scale turbulence model.

Atmospheric Effects

Before the model for the large scale wind-driven turbulence is presented, lets first examine the dynamics of the atmosphere. In discussing the details of air flow, it is convenient to consider the atmosphere to be divided into a number of horizontal layers (figure 1). The region in which the atmosphere experiences surface effects through vertical exchanges of momentum, heat, and moisture is called the planetary boundary layer (PBL) or is sometimes referred to as the friction layer. Panofsky and Dutton[1] defines the depth of the PBL, h, as the thickness of the turbulent region next to the ground which is also called the mixing layer. Another height used to describe the thickness of the PBL in the daytime is the height z_i of the lowest inversion. Actually, h tends to be roughly 10% larger than z_i because the lowest part of the inversion is still turbulent, partly because of overshooting from below, partly because there is often strong wind shear in the inversion.

The lowest part of the PBL is called the surface layer. In this layer, the characteristics of turbulence and the vertical distribution of mean variables are relatively simple. There is no precise definition of the surface layer. Qualitatively, the surface variations of vertical fluxes can be ignored. Typically, the fluxes are large at the surface and decrease to zero near the top of the PBL.

The main problem is calculating the height of the lowest inversion z_i. This value is important since it represents the largest size an inhomogeneity can be in the atmosphere. According to Panofsky and Dutton[1], the horizontal wind speed fluctuations are related to z_i by

$$\frac{\sigma_u}{u_*} = (12 - 0.5\frac{z_i}{L_{mo}})^{1/3} \tag{1}$$

where u_* is the friction velocity and L_{mo} is the Monin-Obukhov length. If variations in the horizontal wind speed are due to purely mechanical turbulence, an alternate formula for u_* can be used for $z > z_o$:

$$u_* = \frac{uk}{ln(z/z_o)} \tag{2}$$

where k is the von Karmon constant (0.4), u is the horizontal wind speed at height z, and z_o is the roughness length. Substituting equation (2) into equation (1) and solving for z_i results in

$$z_i = 2L_{mo}[12 - (\frac{\sigma_u}{ku})^3 ln^3(z/z_o)] \tag{3}$$

This provides the height of the lowest inversion in terms of Monin-Obukhov length, the fluctuation of the horizontal wind speed, and the roughness length. The Monin-Obukhov length can be estimated using tables 1 and 2 knowing the surface wind, incoming solar radiation, and the roughness length (for table 2, the roughness length was 0.05 meters for the experiments[1]).

Experimental Procedure and Data Analysis

A series of line-of-sight propagation measurements were made over relatively flat open farm land. A run consisted of an eight minute record of signals received simultaneously at five transverse microphones mounted one meter above the ground and one microphone mounted near the source for a reference (figure 2). The sound source was driven by a tape with a prerecorded signal consisting of a mixture of eight tones centered at one octave spacings beginning at 62.5 Hz. This geometry is similar to the geometry Daigle[2,3] used in his experiments.

The meteorological data was collected using a series of three-cup anemometers and temperature probes at four heights; 3, 10, 30, and 110 ft. The data acquisition system provided a five minute period of wind speed, wind direction, and temperature as well as the maximum and minimum values during the five minute period. Measurements of the fluctuating wind speed and temperature data were also made using the techniques outlined by Johnson[4].

The Fourier transform of the amplitude and phase variations contains the spectrum of the fluctuations of the sound field due to turbules present

in the atmosphere. The spectral peaks are related to the scale of turbulence L by "Taylor's hypothesis of frozen turbulence" which relates the temporal and spatial turbulence scales by[5]

$$L = \overline{u}\tau \tag{4}$$

where $\overline{u}$ is the mean wind speed and τ is the characteristic time associated with the temporal measurements. Taylor's equation can be rewritten as

$$L = \frac{\overline{u}}{\nu} \tag{5}$$

where $\nu = 1/\tau$. Calculations of L show the different scales of turbulence present in the atmosphere during the experiment. Figure 3 is for a run where the wind speed is low. The spectrum shows several peaks which represent the different scales of turbulence present in the atmosphere for that run. Figure 4 is for a run where the wind speed is high. The only spectral peak present is one at a low frequency. This implies that the only scale of turbulence which is affecting the phase is on the order of a few hundred meters in size.

Some caution must be noted here about this type of analysis. The location of the low frequency peak may be a result of insufficient frequency resolution due to the length of the sample analyzed. A longer time sample might shift the low frequency peak to even lower frequencies.

The Fourier transform for the amplitude variations were also computed. There is not a spectral peak for the amplitude at the low frequency end of the spectrum. Large scale variations in the atmosphere cause changes in the sound field resulting in refractive variations instead of a scattering process as in small scale turbulence.

Large Scale Turbulence Model

The first problem is to obtain, from experimental measurements, a clear idea of the structure and motion of the turbulence. From now on, frequent references will be made to 'eddies' of the turbulent motion, a word intended to describe flow patterns with spatially limited distributions of vorticity and comparatively simple forms. Since the experimental data consists of point measurements, the identification of eddy types must be by informed guesswork followed by measurements designed to confirm the guess.

According to Tennekes,[6] there appears to exist in all turbulent shear flows more or less distinct large eddies with relatively long lifetimes. Townsend was the first to investigate the structure and dynamics of these large scale vortices.[7] Townsend was struck by the fact that in all turbulent shear flows he knew, the eddy viscosity K_m, nondimensionalized by appropriate length and velocity scales, turned out to be a number that is relatively independent of the flow considered. Townsend hypothesized that the large eddies must be responsible for this universality. According to

Townsend, the eddies are elongated longitudinal vortex pairs in the boundary layer, roughly aligned with the mean flow, figure 5.

The lifetimes of the eddies are greater than the length of time for data runs discussed here. For this analysis, they will be considered to be "permanent". Note that secondary circulations cause local regions of horizontal convergence near the surface. Those regions are the sites of vigorous turbulence production rates, and may be responsible for the generation of most of the Reynold stress in the boundary layers. Tennekes concludes that the eddies are capable of relatively long lifetimes because the mean shear is an adequate source of energy.

If a stream function $f(x,z)$ for a particular arrangement of eddies is known, there are several parameters of the eddy system which can be calculated. Stream functions are a type of function which describe the streamlines in a flow. Streamlines are regions where the velocity vectors of the fluid are tangent at a particular instant. The velocity distribution of the eddy can be calculated using[8]

$$u(x,z) = -\frac{\partial f(x,z)}{\partial z} \tag{6}$$

and

$$v(x,z) = \frac{\partial f(x,z)}{\partial x} \tag{7}$$

where $u(x,z)$ and $v(x,z)$ are the horizontal and vertical wind speeds respectively. The functional form of the stream function which represents an eddy pair is[7]

$$f(x,z) = A[cos(lx) + e^{-l^2/\alpha_x^2}]e^{-\frac{1}{4}\alpha^2 r^2} \tag{8}$$

where A is a constant specifying the intensity of the eddy pair, $\alpha^2 r^2 = \alpha_x^2 x^2 + \alpha_z^2 z^2$, l is the characteristic wavenumber of the eddy pair, and α_x and α_z are the horizontal and vertical wavenumbers for the eddy pair. The coordinates (x,z) are relative to the center of the eddy pair. Townsend uses a characteristic wavenumber for the eddy pair of $\pi\alpha_x$.

Using equations (6) and (7), the horizontal and vertical wind speed are

$$u(x,z) = B\alpha_z^2 z[cos(lx) + e^{-l^2/\alpha_x^2}]e^{-\frac{1}{4}\alpha^2 r^2} \tag{9}$$

and

$$v(x,z) = -B\{2lsin(lx) + \alpha_x^2 x[cos(lx) + e^{-l^2/\alpha_x^2}]\}e^{-\frac{1}{4}\alpha^2 r^2} \tag{10}$$

where $B = A/2$. Figure 6 is the horizontal wind speed versus height for x = 0 m, $\alpha_x = 0.0043\ m^{-1}$, $\alpha_z = 0.0087\ m^{-1}$, and $B = 2000\ m^2/s$. The negative height refers to a vertical position below the center of the eddy pair. Figure 7 is the horizontal wind speed versus range for z = -150 m using the same parameters as in the previous figure. The negative range refers to a horizontal position to the left of the center of the eddy pair.

For this work, the size and intensity of the eddy pairs were determined from meteorological data taken in the field. The standard deviation of the wind speed was calculated using a TSI hot wire anemometer. Using the standard deviation of the wind speed, the roughness length, the wind speed at height z, and estimating the Monin-Obukhov length from table 2, the height of the lowest inversion layer z_i is calculated using equation (3). This provides a maximum height of the eddy pair. The Fourier transform of the phase variation provides an estimate of the lower limit for the horizontal extent of the eddy pair. For the data analyzed, the average of the wind speed over five minutes at a given height remains essentially constant for successive five minute periods; the maximum and minimum variations in the wind speed must occur within that five minute period. Assuming that the eddy pair is carried by the mean wind, the maximum horizontal length scale is just the mean wind times five minutes.

The information known at this point allows α_x and α_z to be estimated. Next, the variational constant B of the eddy pair must be estimated. The value of B in equation (9) is varied until the fluctuation of the horizontal wind speed agrees with the maximum and minimum wind speeds recorded over a five minute period on the tower. With these three parameters estimated, the eddy pair model will provide the horizontal and vertical wind speed with range and height.

Determination of Eddy Pair Parameters

The meteorological data consisted of five minute averages with the maximum and minimum of the wind speed in that period. A direct calculation of the scale sizes of the eddy pairs can not be made since they typically passed the tower in less than five minutes. The procedure used to determine the eddy pair parameters outlined in the previous section is used for the experimental runs examined.

The first experiment to be examined is Run 2.1 of January 11, 1985. The important constants are the mean wind speed, the horizontal and vertical wavenumbers, and the constant, B, for the eddy pair. The mean wind speed is calculated from the meteorological profiles of the experimental runs by performing a curve fit to equation (2). The procedure to determine the horizontal and vertical wavenumbers is to use equation (3) for calculating the height of the first inversion layer and using this height to calculate the vertical height of the eddy pair. The curve fit to equation (2) provides values for the roughness length and the friction velocity. The horizontal wind speed fluctuation, σ_u, is determined from the hot wire measurements. Using the mean wind speed and incoming solar radiation, the Monin-Obukhov length can be estimated from table 2.

For the experiment in question, the day was overcast with a light wind of 3.3 m/s. Using tables 1 and 2 for incoming solar radiation and a surface wind speed of 3.3 m/s, the Monin-Obukhov length, L_{mo}, was estimated to be 20 meters. From analysis of the five minute wind speed measurements

with height, the horizontal wind speed fluctuation was 0.40 m/s. For the experiments discussed, the roughness length was estimated from table 3 to be 0.05 meters. Using these parameters, the height of the first inversion layer was calculated to be 450 meters using equation (3).

Using the condition that the eddy pair traverses past the tower within a five minute period, the maximum eddy pair size possible to traverse the field of propagation is 990 meters. If the dimensions of each eddy are 450 m, then the eddy pair has a horizontal length of 900 meters. This size is less than the maximum size constraint dictated by the five minute measurement period. Using equation (9), the horizontal and vertical wavenumbers (α_x and α_z) for the eddy pair are 0.125 m^{-1} and 0.025 m^{-1}.

To determine the constant B in equation (9), the maximum and minimum wind speed fluctuations within a five minute segment with height are compared with the wind speed fluctuations predicted by the model. The parameter B is varied until the predicted wind speed variations fit those observed for a five minute segment. For the date in question, the value of B which best fit the data is 200 m^2/s.

The next experimental run was Run 1.1 of December 13, 1984. This day differed from January in that the mean wind speed and horizontal wind speed fluctuations were much greater. The mean wind speed was 6.3 m/s while the horizontal wind speed fluctuation was 1.0 m/s. Table 6.6 in Panofsky and Dutton[1] is used to determine the value of L_{mo}. Using this table, the value of L_{mo} is estimated to be on the order of 100 to 150 m, which gives a value for z_i of 575 to 875 m.

Results From the Eddy Pair Model

Viewing the movement of the eddy pair on the scale of the geometry of the experiments, the variation of the sound speed in the atmosphere would appear to change slowly over the entire range of the experiment uniformly. Using a simple model of the wind speed in the atmosphere slowly varying from u_1 to u_2, the expected phase change can be calculated using

$$\Delta\varphi = \frac{2\pi f R}{c_o^2}(u_1 - u_2) \tag{11}$$

where R is the propagation distance, c_o is the sound speed at temperature T, and f is the frequency of the signal. A comparison between the magnitude of the phase change for the simple model and the experimental results is shown in table 3.

Conclusions

Experimental acoustic phase data definitely displays two variational time scales. The short term time variations can be attributed to the presence of small scale turbulence present in the atmosphere. The small scale turbulence does not account for the longer time variations in phase.

The large scale turbulence model is composed of pairs of vortices or eddies moving through the atmosphere at the mean wind speed. The scale parameters for the eddy pairs are determined from the available meteorological data composed of the maximum, minimum, and average wind speed over a five minute segment for four heights and meteorological theories of the behavior of the lower atmosphere. The constraint of the eddy pair moving through the field of propagation within five minutes is generally used as an upper bound for the dimensions of the eddy pair; however, it could be used as the size of the eddy pair if there is lack of available meteorological data.

The results of the eddy pair model were used to examine the phase fluctuations of the acoustic wave using a simple phase model. The input parameters for the model were determined from analysis of the acoustical and meteorological data collected in the experiments. The magnitude of the phase variations predicted using this model was found to be in very good agreement with the experimental results.

References

1. H.A. Panofsky and J.A. Dutton, *Atmospheric Turbulence: Models and Methods for Engineering Applications*, (Wiley, New York, 1984).

2. G.A. Daigle, J.E. Piercy, and T.F.W. Embleton, "Line-of-Sight Propagation Through Atmospheric Turbulence Near the Ground," J. Acoust. Soc. Am. **74**, 1505-1513(1983).

3. G.A. Daigle, T.F.W. Embleton, and J.E. Piercy, "Propagation of Sound in the Presence of Gradients and Turbulence Near the Ground," J. Acoust. Soc. Am. **79**, 613-627(1986).

4. M.A. Johnson, R. Raspet, and M.T. Bobak, "A Turbulence Model for Sound Propagation from an Elevated Source Above Level Ground," J. Acoust. Soc. Am. **81**, 638-646(1987).

5. G.A. Daigle, J.E. Piercy, and T.F.W. Embleton, "Effects of Atmospheric Turbulence on the Interface of Sound Waves Near a Hard Boundary ," J. Acoust. Soc. Am. **64**, 622-630(1978).

6. H. Tennekes, "Similarity Laws and Scale Relations in Planetary Boundary Layers," in *Workshop on Micrometeorology*, edited by Duane A. Haugen (American Meteorological Society, Boston, 1973), pp. 177-216.

7. A.A. Townsend, *The Structure of Turbulent Shear Flow* (Cambridge University Press, New York, 1976).

8. D.E. Rutherford, *Fluid Dynamics* (Interscience Publishers Inc, New York, 1966).

Table 1. Estimation of Turner Classes.

Surface Wind Speed (at 10m), m/s	Incoming Solar Radiation		
	Strong	Moderate	Light
<2	1	1	2
2-3	1-2	2	3
3-5	2	2-3	3
5-6	3	3-4	4
6<	3	4	4

Table 2. Estimation of L_{mo} for Various Turner Classes.

Turner Class	- Lmo
1	8-12 m
2	12-20 m
3	20-60 m
4	>60 m

Table 3. Results from the Simple Phase Model for Run 2.1 of January.

Frequency (Hz)	$\Delta\varphi_{mea}(deg)$	$\Delta\varphi_{pred}(deg)$
62.5	40°	41°
125.	72°	82°
250.	155°	163°

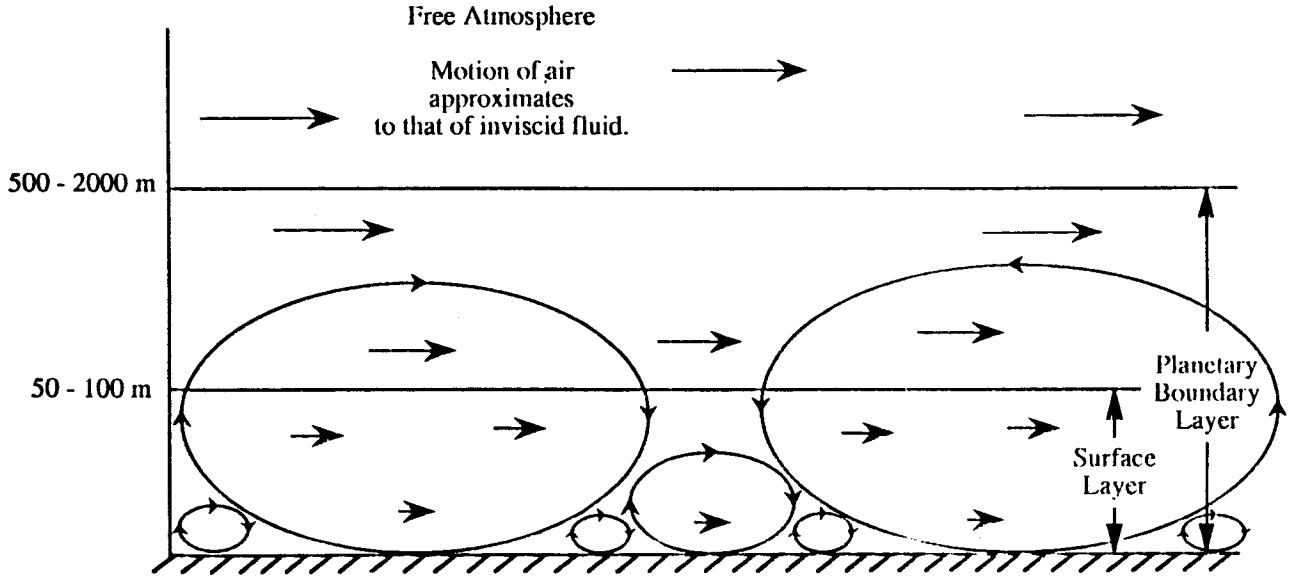

Figure 1. Breakdown of The Lower Atmosphere.

BONDVILLE, ILL.
JAN. 11, 1985
RUN 2.1

GEOMETRY

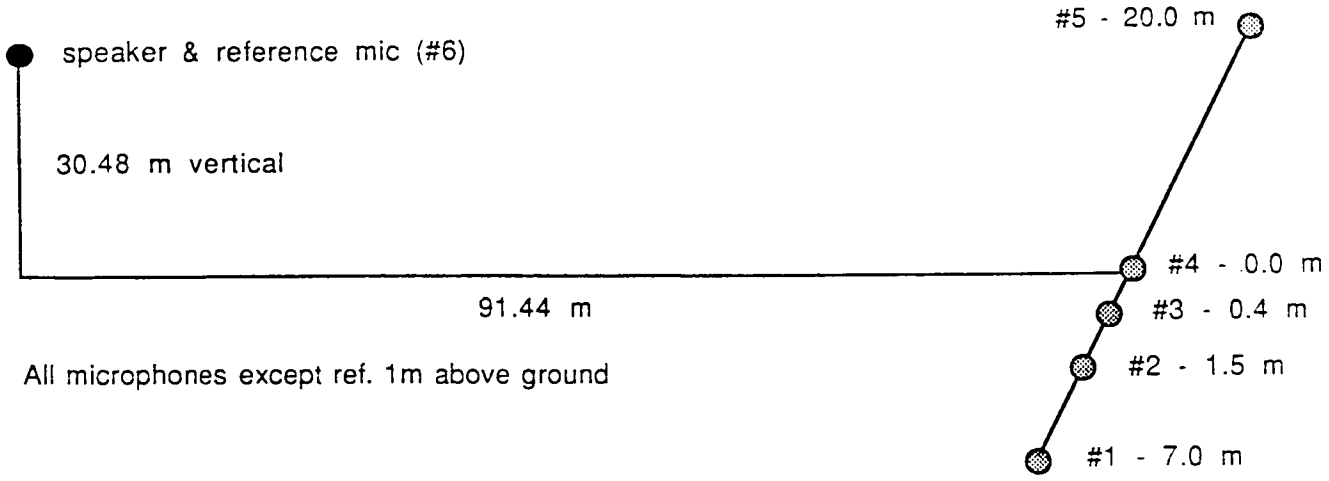

Transverse Distances		
1/2	-	5.5 m
1/3	-	6.6
1/4	-	7.0
1/5	-	27.0
2/3	-	1.1
2/4	-	1.5
2/5	-	21.5
3/4	-	0.4
3/5	-	20.4
4/5	-	20.0

Ch. #	Mic. #
1	2
2	3
3	4
4	7
5	5
6	ref
7	voice

Figure 2. Geometry For Jan. 11, 1985.

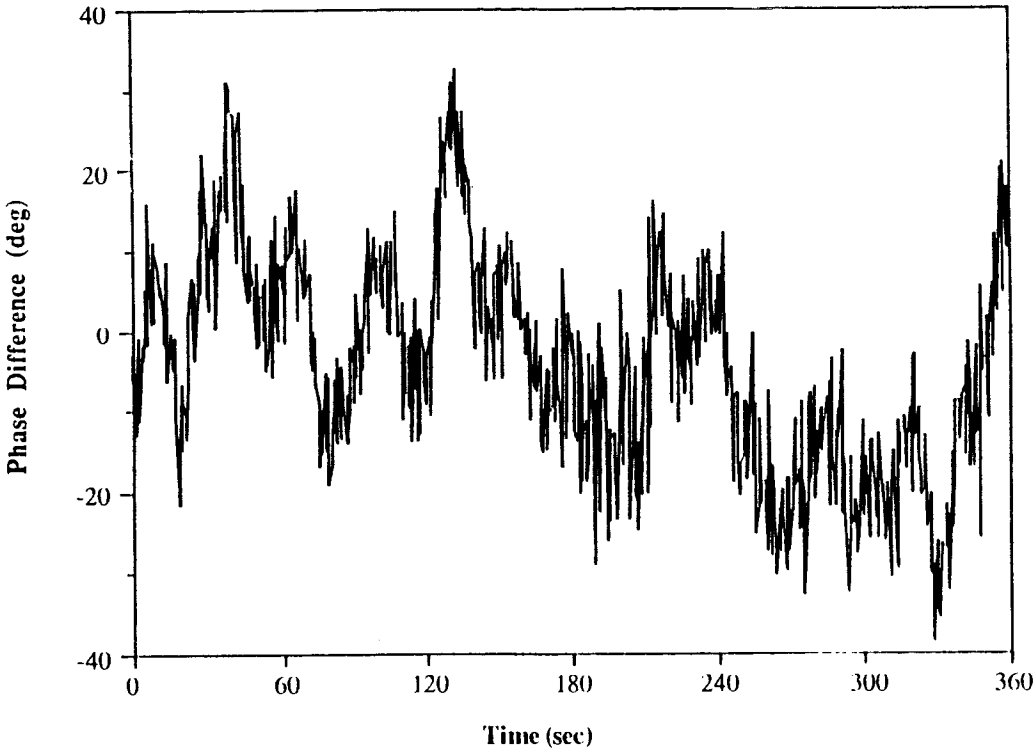

Figure 3a. Time Fluctuations for Low Wind Speed.

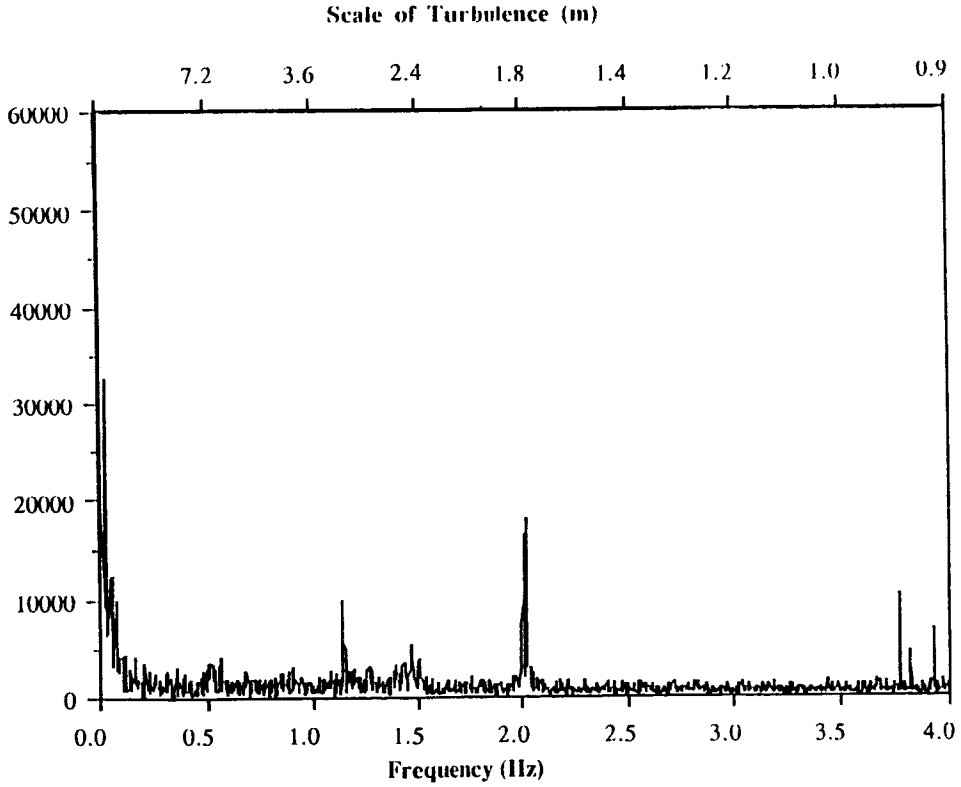

Figure 3b. Spectrum of Phase Fluctuations for Low Wind Speed.

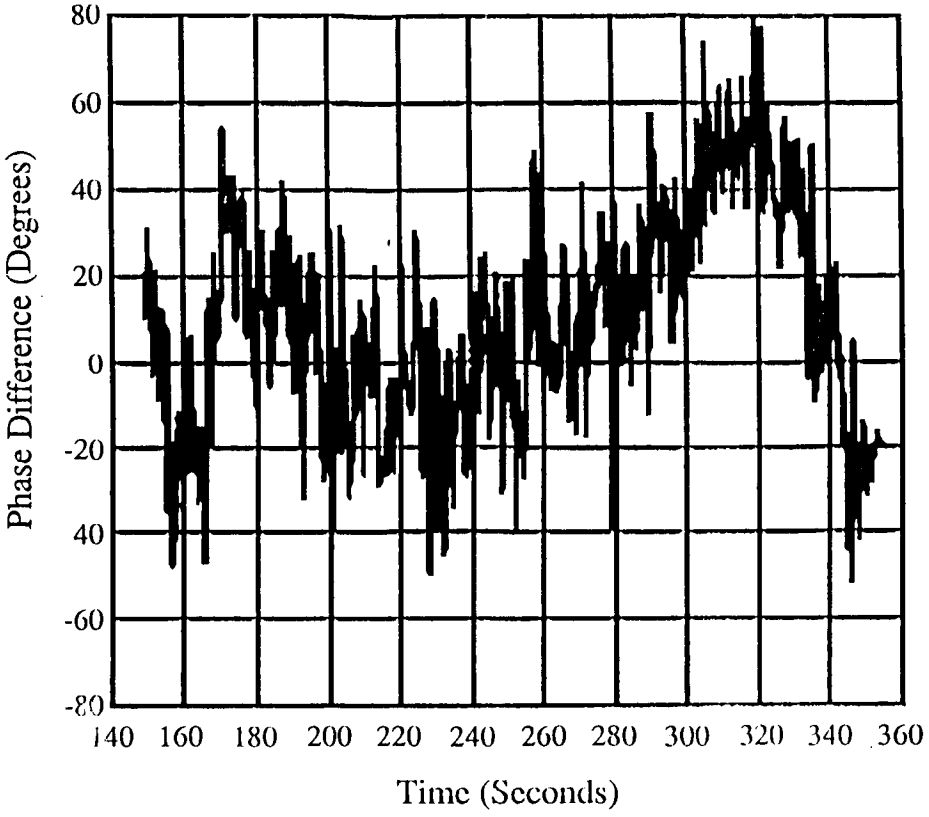

Figure 4a. Time Fluctuations for High Wind Speed.

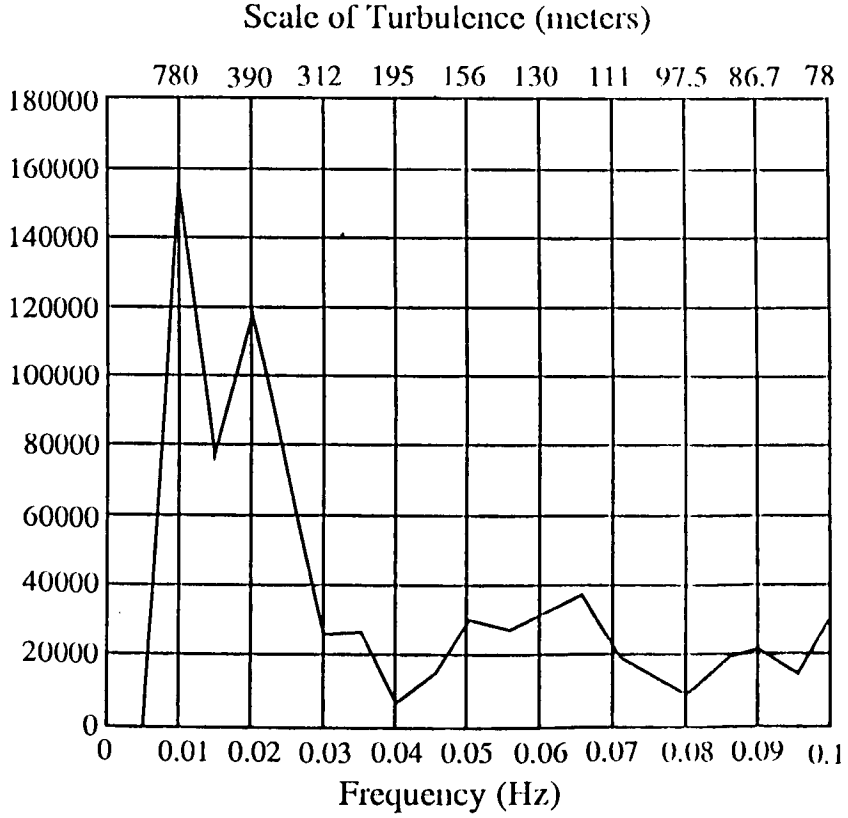

Figure 4b. Spectrum of Phase Fluctuations for High Wind Speed.

C-4

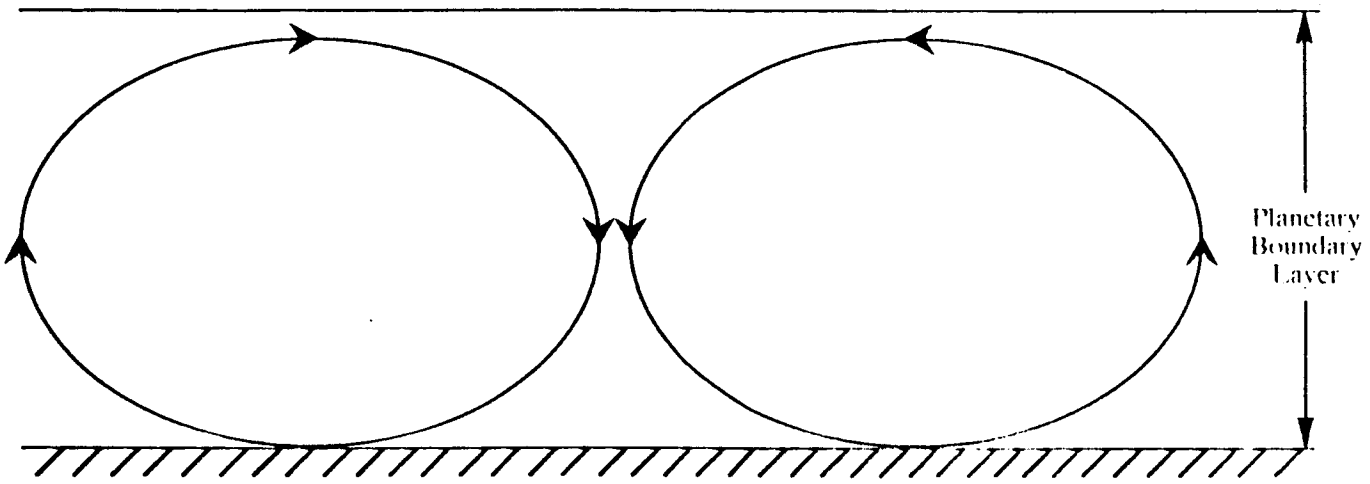

Figure 5. Illustration of Eddy Pair in the Planetary Boundary Layer.

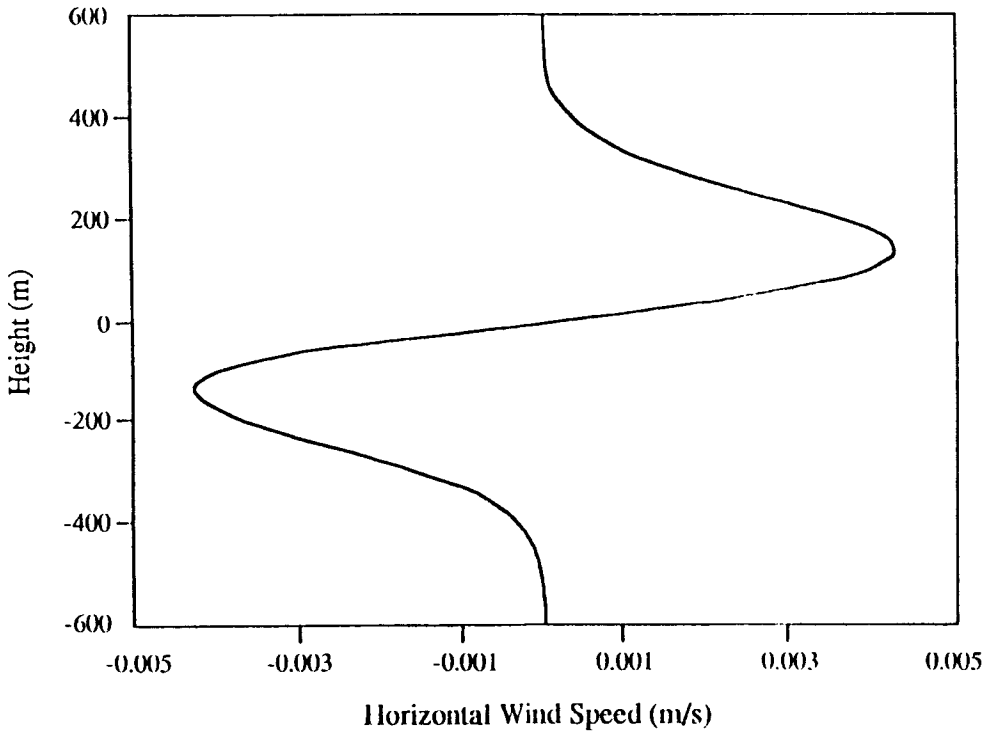

Figure 6. Horizontal Wind Speed vs. Height for $x = 0, \alpha_x = 0.0043\text{m}^{-1}$, $\alpha_z = 0.0087\text{m}^{-1}$, and $B = 2000\text{m}^2/s$.

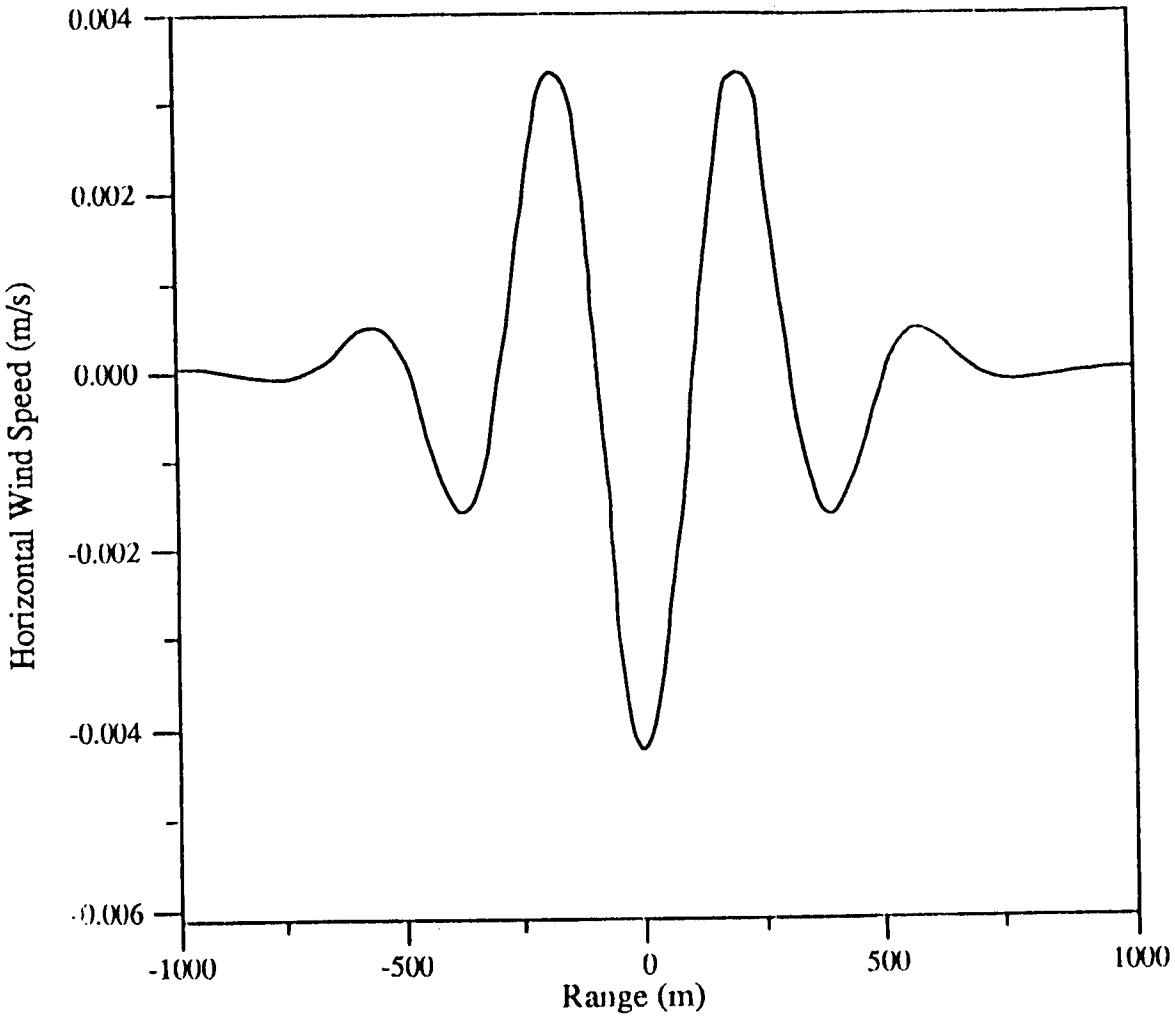

Figure 7. Horizontal Wind Speed vs. Range for $z = -150, \alpha_x = 0.0043\text{m}^{-1}$, $\alpha_z = 0.0087\text{m}^{-1}$, and $B = 2000\text{m}^2/s$.

NASA
National Aeronautics and Space Administration

Report Documentation Page

1. Report No.	2. Government Accession No.	3. Recipient's Catalog No.
NASA CP-3101		

4. Title and Subtitle
Fourth International Symposium on Long-Range Sound Propagation

5. Report Date
December 1990

6. Performing Organization Code

7. Author(s)
William L. Willshire, Jr., Compiler

8. Performing Organization Report No.
L-16875

9. Performing Organization Name and Address
NASA Langley Research Center
Hampton, Virginia 23665-5225

10. Work Unit No.
505-61-11-02

11. Contract or Grant No.

12. Sponsoring Agency Name and Address
NASA Langley Research Center
Hampton, Virginia 23665-5225

University of Mississippi
Oxford, Mississippi 38677

Open University of England
Milton Keynes, United Kingdom MK7 6AA

13. Type of Report and Period Covered
Conference Publication

14. Sponsoring Agency Code

15. Supplementary Notes

16. Abstract

Long-range sound propagation is an aspect of many acoustical problems ranging from en route aircraft noise to the acoustic detection of aircraft. Over the past decade, the University of Mississippi and the Open University of England, together with a third institution, have held a symposium approximately every 2 years so that experts in the field of long-range propagation could exchange information on current research, identify areas needing additional work, and coordinate activities as much as possible.

The Fourth International Symposium on Long-Range Sound Propagation, jointly sponsored by the University of Mississippi, the Open University of England, and the National Aeronautics and Space Administration (NASA), was held at the NASA Langley Research Center on May 16–17, 1990. Papers were given in the areas of: ground effects on propagation, infrasound propagation, and meteorological effects on sound propagation. This report is a compilation of the presentations made at the symposium along with a list of attendees, and the agenda.

17. Key Words (Suggested by Authors(s))	18. Distribution Statement
Long range Sound propagation Ground effects Infrasound Meteorological effects	Unclassified - Unlimited Subject Category 71

19. Security Classif. (of this report)	20. Security Classif. (of this page)	21. No. of Pages	22. Price
Unclassified	Unclassified	283	A13

NASA FORM 1626 OCT 86

NASA-Langley, 1990

For sale by the National Technical Information Service, Springfield, Virginia 22161-2171

National Aeronautics and
Space Administration
Code NTT-4

Washington, D.C.
20546-0001

Official Business
Penalty for Private Use, $300

SPECIAL FOURTH-CLASS RATE
POSTAGE & FEES PAID
NASA
Permit No. G-27

POSTMASTER: If Undeliverable (Section 158
Postal Manual) Do Not Return